Wind Tunnel Tests of the FFA-W3-241, FFA-W3-301 and NACA 63-430 Airfoils

Peter Fuglsang, Ioannis Antoniou, Kristian S. Dahl,
Helge Aa. Madsen

Abstract

This report deals with 2D measurements of the FFA-W3-241, FFA-W3-301 and NACA 63-430 airfoils. The aerodynamic properties were measured at $Re = 1.6\times10^6$. The VELUX open jet wind tunnel with a background turbulence intensity of 1% was used. The airfoil sections had a chord of 0.60 m and a span of 1.9 m and end plates were used to minimize 3D flow effects. The measurements comprised both static and dynamic inflow where dynamic inflow was obtained by pitching the airfoil in a harmonic motion. We tested the influence from vortex generators and leading edge roughness both individually and in combination.

The aerodynamic characteristics were measured and the agreement between calculations and measurements was fair for FFA-W3-241 but not good for FFA-W3-301 and NACA 63-430. In general calculations overestimated maximum C_L and sometimes underestimated minimum C_D. Maximum C_L for smooth flow was in good agreement with calculated maximum C_L for leading edge transition flow and this could serve as a worst case calculation. We determined the influence from vortex generators and they should always be applied on thick airfoils to increase maximum C_L. We determined the influence from leading edge roughness, which reduced maximum C_L and increased minimum C_D. Compared with the NACA 63-4xx airfoils, the FFA-W3 airfoils were found better suited for the inboard part of a wind turbine blade both with and without vortex generators.

Contents

Nomenclature

c	[m]	Airfoil chord
h	[m]	Jet height
k		Reduced frequency
Δp	[Pa/m]	Pressure loss
p	[Pa]	Static pressure
p_o	[Pa]	Total pressure head
q	[Pa]	Dynamic pressure
s		Airfoil surface coordinate
t	[s]	Pitch motion time
x		Coordinate in chord direction
y		Wake rake vertical coordinate, airfoil vertical coordinate

A	[°]	Pitch motion amplitude
C_D		Drag coefficient
C_L		Lift coefficient
C_M		Moment coefficient
C_N		Normal force coefficient
C_P		Airfoil pressure coefficient
C_T		Tangential force coefficient
Re		Reynolds number
T	[°C]	Air temperature
V	[m/s]	Velocity

α	[rad] [°]	Angle of attack
ε		Speed-up factor
ρ	[kg/m^3]	Air density
ω	[rad/s]	Pitch motion angular velocity

Subscripts

$1\text{-}3$	Pitot tube measurement
a	Airfoil section measurement
j	Jet outlet measurement
m	Mean value
min	Minimum value
max	Maximum value
p	Pressure measurement
t	Measured value (uncorrected)
w	Wake rake measurement
∞	Free stream reference for normalisation of airfoil forces

1 Introduction

This report concerns 2D wind tunnel measurements of the FFA-W3-241, FFA-W3-301 and NACA 63-430 airfoils. All three airfoils are relatively thick and have been used on the inboard part of different Danish wind turbine blades. The measurement program took place as a part of the EFP 95 'Blade design' project. The tests were carried out in the VELUX wind tunnel, which has an open test section. Pressure distribution measurements were taken on the airfoil section together with wake rake pressure measurements. The testing facility is described in detail in Fuglsang, 1998 [1].

There exist uncertainty on the flow conditions of the inboard part of a rotating wind turbine blade. Rotation and 3d effects complicate the flow and both measurements as well as numerical predictions are difficult to carry out accurately. The uncertainty is reflected both on the prediction of power and on the prediction of loads.

Another element of uncertainty is difficulties in the numerical prediction of the 2D flow of thick airfoils. Furthermore only few 2D measurements of thick airfoils exist at Reynolds numbers representative for wind turbine blades conditions such as Timmer and van Rooy, 1992 [2] and Timmer and van Rooy, 1993 [3]. It was therefore decided to carry out measurements of three thick airfoils that are typically used on Danish wind turbines.

The testing program included:
- Steady and quasi-steady inflow measurements where mean values were obtained for the airfoil aerodynamic coefficients. The angle of attack was changed in steps of 2° and a 20 s duration time series was obtained for each angle of attack. Alternatively the angle of attack was changed continuously at an average rate around 0.3°/s.
- Dynamic inflow was measured with the airfoil in pitching motion at amplitudes around ±2° and reduced frequencies around 0.1. The hysteresis effects on the aerodynamic coefficients were derived.

All tests were carried out at Reynolds number 1.6 million. The angle of attack range was between -5° and 30°.

The airfoils were tested under the following configurations:
- Smooth surface, referred to as 'smooth flow'.
- Vortex generators on the suction side to delay separation and increase the maximum lift coefficient, referred to as 'VG'.
- Leading edge roughness to simulate the change of the aerodynamic coefficients from dirt and dust accumulation, referred to as 'LER'.
- A combination of vortex generators and leading edge roughness, referred to as 'VGLER'.

2 Experimental set-up

The experimental set-up is briefly described in this chapter. A more complete description can be found in Fuglsang *et al.*, 1998 [1].

2.1 Testing facility

The VELUX wind tunnel is of the closed return type with an open test section with a cross section of 7.5×7.5 m and a length of 10.5 m, Figure 2-1. The cross section of the jet blowing into the test section is 3.4×3.4 m. The maximum flow velocity is 45 m/s.
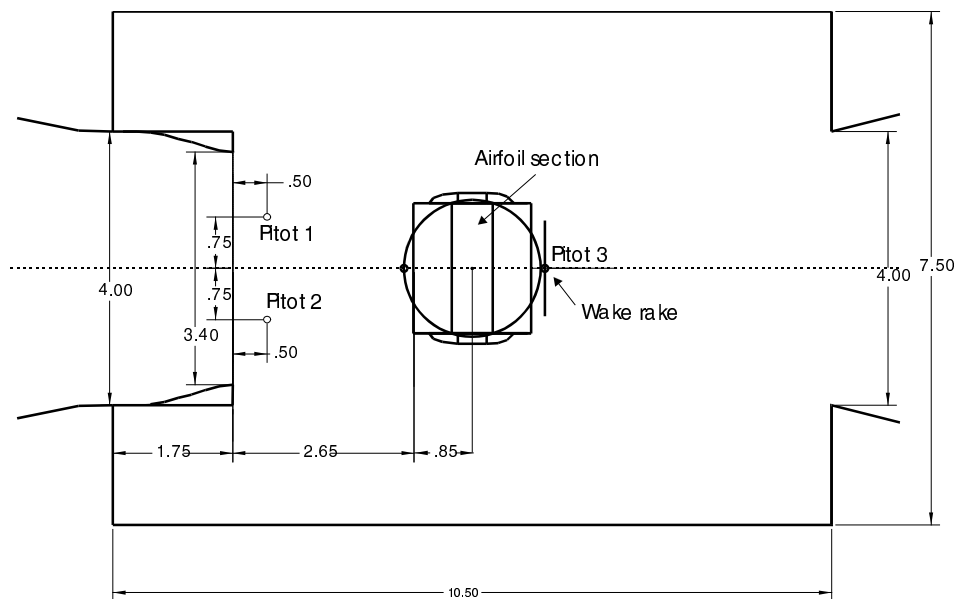

Figure 2-1 The wind tunnel test section with the test stand seen in a top view.

A test stand was built for 2D airfoil testing, Figure 2-2. The test stand was inserted in the tunnel test section. The airfoil section with a span of 1.9 m and a chord of 0.6 m was mounted 1.7 m from the tunnel floor and 3.2 m from the nozzle outlet. Endplates were fixed to the stand at the ends of the airfoil section to limit 3d effects.

Three Pitot tubes measured static and total pressure at different locations in the test section, Figure 2-1. These Pitot tubes were used to measure the wind tunnel reference pressures and to estimate the turbulence level and the stability of the wind tunnel flow.

Quasi-steady measurements at continuously varying angles of attack as well as dynamic inflow measurements were possible. Dynamic inflow was obtained by pitching the airfoil section at different reduced frequencies up to $k = 0.15$ and amplitudes between $\pm 2° < A < \pm 5°$ with the pitch axis was located at $x/c = 0.40$, see section 2.4.
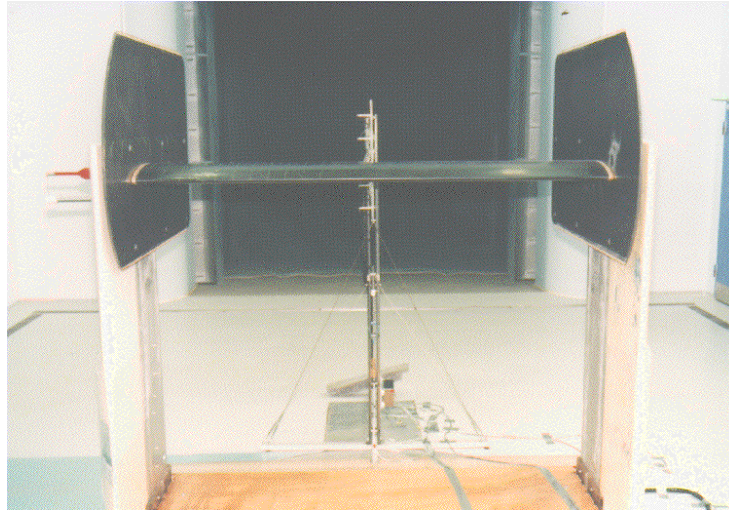
Figure 2-2 The test section with the test stand and the wake rake downstream of the airfoil section.

The wake rake consisted of 53 total pressure probes and five static tubes. The vertical span was 0.456 m, Figure 2-3. The distance between the airfoil trailing edge and the wake rake was 0.7 airfoil chords and the middle of the wake rake was placed at the height of the trailing edge at 0° incidence and behind the centre line of the airfoil section. The rake was not traversed in the horizontal or the vertical directions.
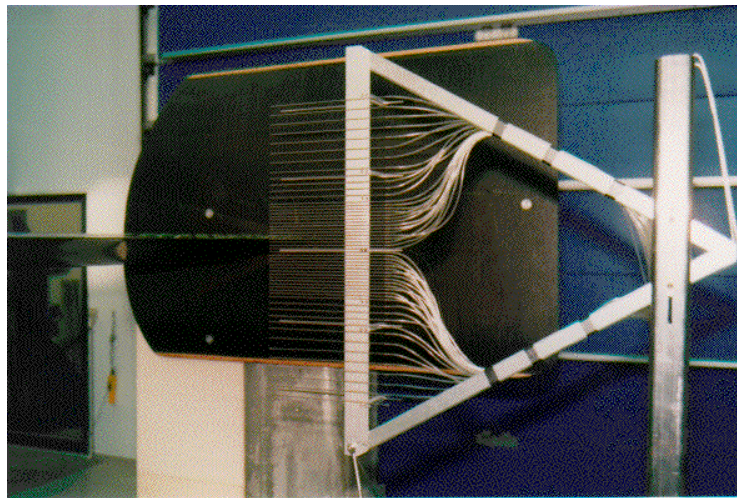

Figure 2-3 The wake rake seen from the side in front of an endplate.

The HyScan 2000 data acquisition system from Scanivalve Corp. was used. Two ZOC33 pressure-scanning modules recorded the pressure signals. For the airfoil surface pressures, 40 1psi and 24 2.5psi range sensors were used. For the wake rake and the pitot tubes, 10´´ H_2O sensors were used. The ZOC module for the airfoil pressures was mounted on the test stand side just outside the airfoil section. Equal length tubes were lead from the airfoil section through a hollow axis to the pressure module. The pressure module used for the wake and the pitot tube measurements was placed on the floor next to the wake rake. A ZOCEIM16 module was used for the acquisition of the electrical signals.

Risø-R-1041(EN)

A total of 134 signals were measured by the data acquisition system during the measurement campaigns:

- 64 airfoil surface static pressures, $p_a(s)$
- 5 wake rake static pressures, $p_w(y)$
- 53 wake rake total pressures, $p_{ow}(y)$
- 3 Pitot tube static pressures, p_{1-3}
- 3 Pitot tube total pressures, p_{o1-3}
- Angle of attack, α
- Air temperature, T
- Air density, ρ
- 2 strain gauges for recording shaft bending corresponding to the lift and drag forces experienced by the airfoil section.
- Electric motor frequency

2.2   Wind tunnel boundary corrections

Wind tunnel corrections should be applied for streamline curvature and down-wash. Horizontal buoyancy, solid and wake blockage could on the other hand be neglected because the test section configuration corresponds to an open jet, which is free to expand, Ray and Pope, 1984 [4]. The application of wind tunnel boundary corrections for the VELUX wind tunnel was verified in Fuglsang *et al.,* 1998 [1].

Streamline curvature is introduced to the flow, especially in the case of open test sections. Solid walls do not bound the flow, which is then free to diverge downstream of the airfoil section. The curvature of the flow induces drag and influences the effective angle of attack over the airfoil. In the case of the VELUX tunnel, the presence of the floor close to the jet bottom boundary will influence the streamline curvature and will introduce uncertainty on the wind tunnel corrections. This influence was assumed to be negligible and the applied corrections for streamline curvature do not account for it.

Down-wash is introduced to the flow when the jet dimensions exceed the airfoil section span. The airfoil section corresponds to a finite wing and trailing vortices appear at the ends of the span although reduced by the endplates. The trailing vorticity induces a down-wash velocity in the case a of positive lift coefficient. Thus due to the down wash the angle of attack is reduced and additional drag is induced.

Both down-wash and streamline curvature result in a change in the angle of attack due to the induction of a velocity normal to the flow direction and the airfoil section. It is assumed in this case that down-wash is insignificant compared with streamline curvature because of the presence of endplates.

For the correction of streamline curvature, the method of Brooks and Marcolini, 1984 [5] was used.

The corrected free flow angle of attack, α, is found from:

$$\alpha = \alpha_t - \frac{\sqrt{3\sigma}}{\pi} C_L - \frac{2\sigma}{\pi} C_L - \frac{\sigma}{\pi} (4 C_{Mt}) \; [rad]$$

(2-1)

Where

$$\sigma = \frac{\pi^2}{48} \cdot \left(\frac{c}{h}\right)^2$$

(2-2)

The drag coefficient, C_D, is calculated from:

(2-3)

$$C_D = C_{Dt} + \left[-\frac{\sqrt{3\sigma}}{\pi} C_L \right] C_L$$

The moment coefficient, C_M, is obtained:

$$C_M = C_{Mt} - \frac{\sigma}{2} C_L$$

(2-4)

For details see Fuglsang *et al.*, 1998 [1].

2.3   Wind tunnel flow conditions

In Fuglsang *et al.,* 1998 [1] the wind tunnel flow conditions is investigated and it is found that:

- The turbulence intensity at the test section inlet is 1%.
- Between the inlet and the airfoil section, there is a speed-up of, $\varepsilon_{j\text{-}a} = 6.9\%$, and a static pressure drop of $\Delta p_{j\text{-}a} = 15$ Pa/m.

The wind tunnel references for static, p_∞ and total pressures, p_{o_∞} were derived from Pitot 1 measurements, Figure 2-1. The flow acceleration between Pitot 1 and the airfoil section, $\varepsilon_{1\text{-}\infty} = 5.9\%$ and the static pressure drop between Pitot 1 and the airfoil section, $\Delta p_{1\text{-}\infty} = 15$ Pa/m were determined in Fuglsang *et al.,* 1998 [1] and they are taken into account at the calculation of p_∞ and p_{o_∞}.

2.4   Calculation methods

The airfoil pressure coefficient, $C_p(s)$, around the airfoil surface, s, is calculated from:

$$C_p(s) = \frac{p_a(s) - p_\infty}{q_\infty}$$

(2-5)

Where

$$q_\infty = p_{o\infty} - p_\infty$$

(2-6)

The normal force coefficient, C_N, and the tangential force coefficient, C_T, are found from integration of the $C_P(s)$ distribution along the *x*- and *y*-axis as seen

in Figure 2-4. The airfoil lift coefficient, C_L, and drag coefficient, C_D, are found by resolving C_N and C_T perpendicular to and parallel with the oncoming flow:

$$C_L = \cos(\alpha)C_N + \sin(\alpha)C_T$$

(2-7)

$$C_D = -\cos(\alpha)C_T + \sin(\alpha)C_N$$

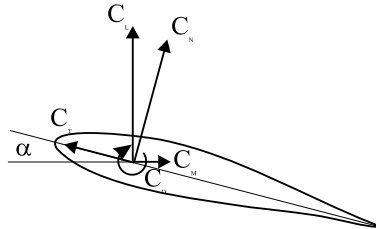The moment coefficient, C_M, is found from integration of $C_P(s)$ at $x/c = 0.25$.

Figure 2-4 Sign convention for aerodynamic coefficients.

The total airfoil drag is the sum of skin friction and pressure drag. By assuming a control surface, which surrounds the airfoil section, the total drag can be calculated from the balance of the momentum flux entering the control surface in front of the airfoil and the momentum flux exiting the control surface behind the airfoil section. The momentum profile entering is assumed uniform and is calculated from the wind tunnel free stream reference pressures. The momentum profile exiting is calculated from the pressures measured by the wake rake.

Assuming that the flow is 2D, the total wake drag coefficient, C_{Dw}, is calculated from Rae and Pope, 1984 [4]:

$$C_{Dw} = \frac{2}{c} \int_{y_{min}}^{y_{max}} \sqrt{\frac{p_o(y) - p(y)}{q_\infty}} \cdot \left(1 - \sqrt{\frac{p_o(y) - p(y)}{q_\infty}}\right) dy$$

(2-8)

In the analysis of dynamic loads, while the airfoil is in pitching motion, the pitching motion is defined:

$$\alpha = A\sin(\omega t) + \alpha_m$$

(2-9)

The pitching motion is related to the reduced frequency:

$$k = \frac{\omega c}{2V_\infty}$$

(2-10)

3 Airfoil sections and aerodynamic devices

The tested airfoils were the FFA-W3-241 and FFA-W3-301 airfoils from Björk, 1990 [6] and the NACA 63-430 airfoil. The latter was derived from the NACA 63-421 airfoil described in Abbot and von Doenhoff, 1959 [7] by linear scaling of the thickness distribution.

3.1   Airfoil sections

For all airfoil sections, the span was 1.9 m and the chord was 0.60 m. LM Glasfiber A/S manufactured the models and Risø carried out the instrumentation. Each model was manufactured in two pieces as an upper and a lower shell to facilitate instrumentation. The models were made of GRP in moulds. The pressure taps were holes drilled in the model surface with the exception of the leading and trailing edges where tubes were installed through the model surface, flush with the surface. At the model inside, metal tubes were mounted parallel to the drilled holes and flexible plastic tubes were connected to the metal tubes. When the instrumentation was completed the two shells were assembled and the pressure tubes were taken outside of the model through a hollow axis at one side of the airfoil.

The airfoil sections were equipped with 62 pressure taps of 0.5 mm inner diameter in the centre line region. The taps were placed along the chord at the centre line of the model in a staggered alignment to minimise disturbances from upstream taps. Additional taps were drilled close to the centre line as a back-up to taps at important positions, e.g., the trailing edges, and in order to allow measurements away from the centre line.

The position of the pressure taps on the model was decided by looking on the theoretical pressure distributions derived by numerical calculations. The distributions of the pressure taps reflect the expected pressure gradients and the tap spacing is dense at leading edge. There is higher concentration on the upper surface compared to the lower surface. After the model was permanently assembled the model dimensions and the tap positions were checked for compliance with the theoretical ones, with the help of a CNS flat-bed machine.

The location of the pressure taps for the different airfoils can be seen in Figure 3-1 to Figure 3-3, where the actual model coordinates are compared with the theoretical coordinates from [6] and [7].

Figure 3-1 shows the FFA-W3-241 airfoil model, where the agreement with theoretical coordinates is good at the leading edge region. There are only small deviations at the trailing edge.

Figure 3-2 shows the FFA-W3-301 airfoil model. The agreement with theoretical coordinates is good near the leading edge but the maximum thickness of the model is slightly less compared with the theoretical coordinates and the thickness is in general too low toward the trailing edge.

Figure 3-3 shows the NACA 63-430 airfoil where the agreement with the theoretical coordinates is good both at the leading and at the trailing edges.

In general the deviations which occurred between the actual and the theoretical shape of the airfoil cross sections are due to the gluing process when the two model shells are assembled.

The comparison of airfoil models with theoretical coordinates did not reveal any kinks in the surface or any large discrepancies. The observed deviations were minor offsets of the original coordinates, especially toward the trailing edge. For all airfoil models, it was concluded that this would not result in significant errors in the pressure distribution and in the derivation of aerodynamic loads.
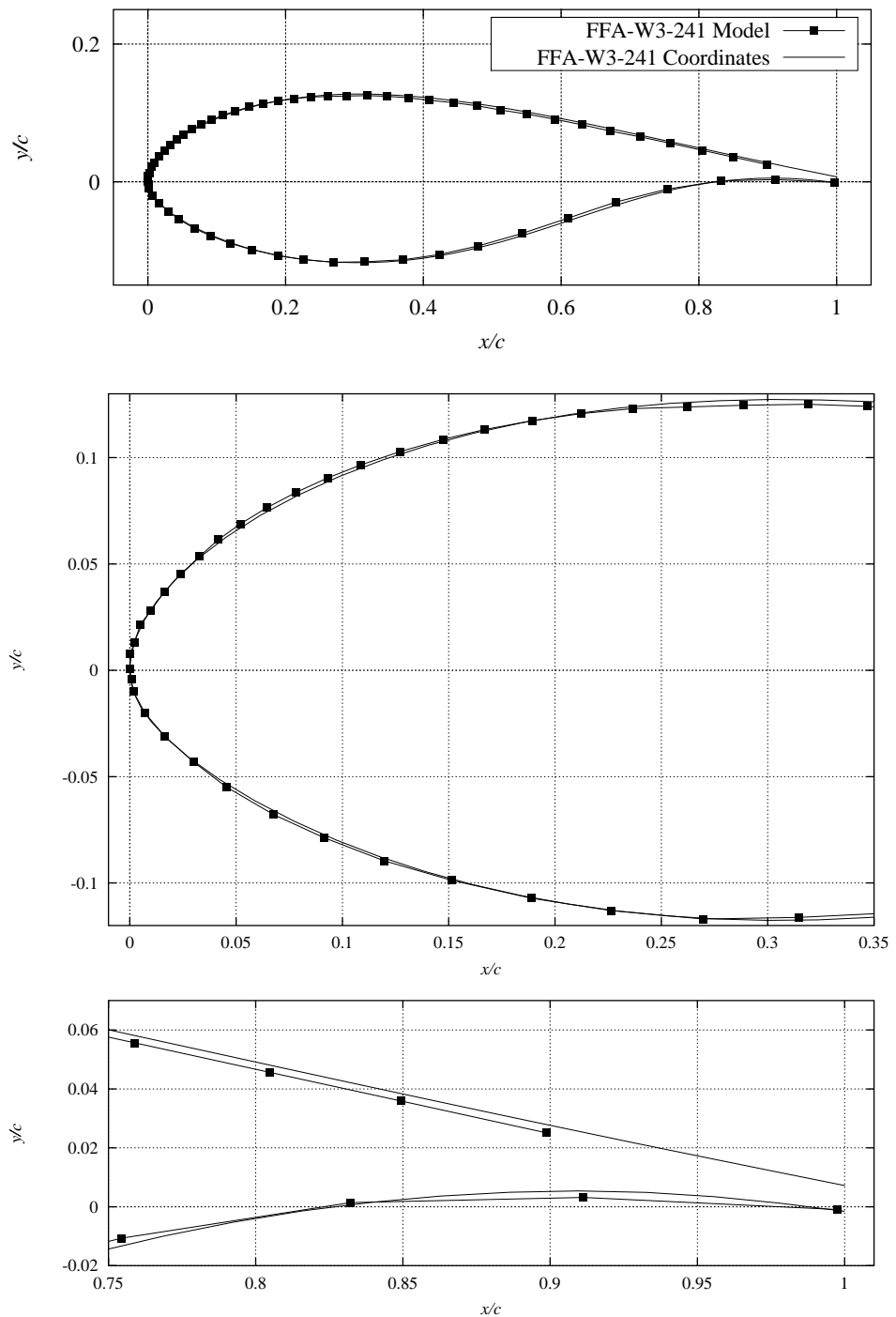
Figure 3-1 The actual FFA-W3-241 model coordinates compared with the theoretical coordinates from [6]. Each symbol corresponds to a pressure tap. The leading edge and the trailing edge regions are shown enlarged.
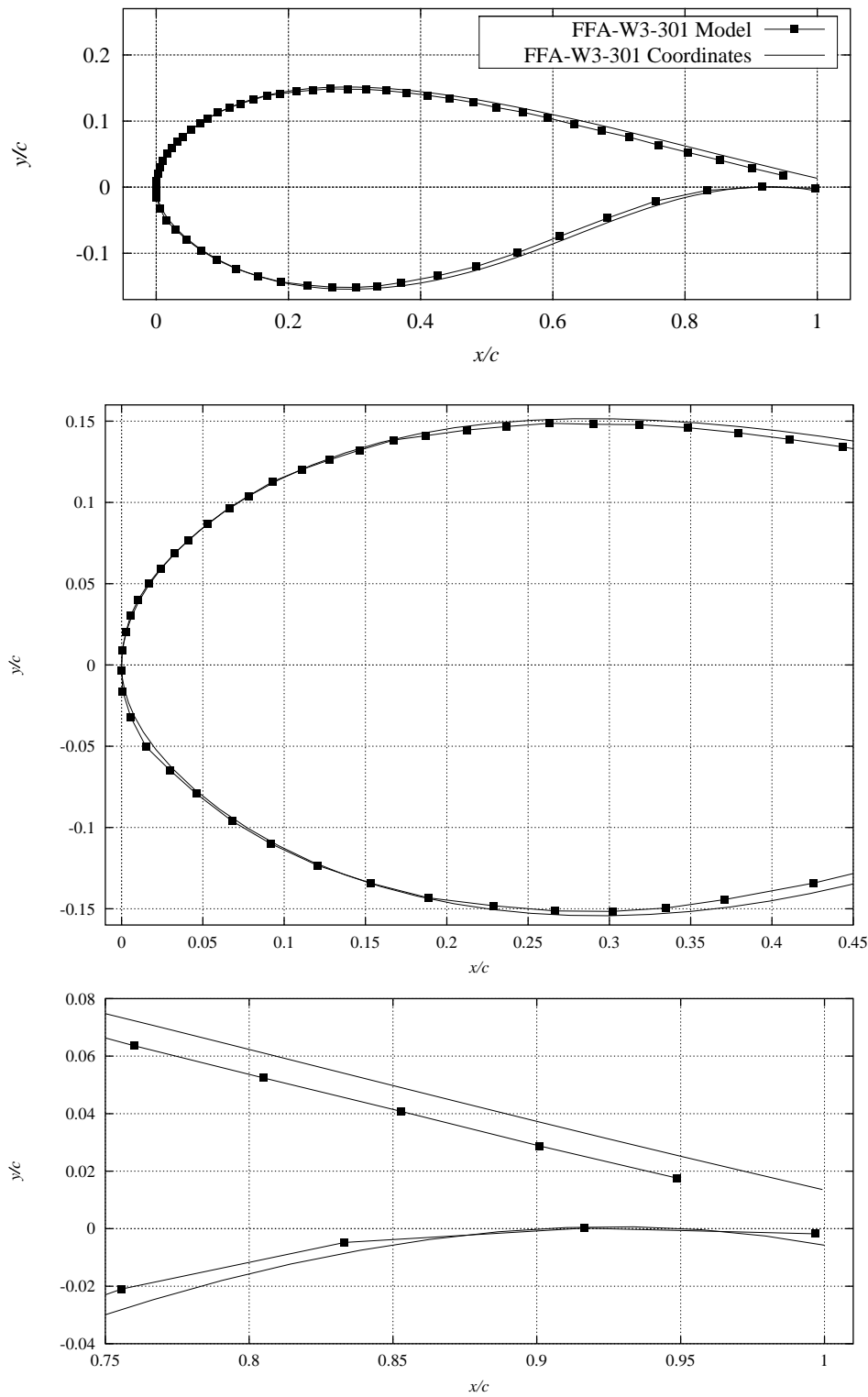
Figure 3-2 The actual FFA-W3-301 model coordinates compared with the theoretical coordinates from [6]. Each symbol corresponds to a pressure tap. The leading edge and the trailing edge regions are shown enlarged.
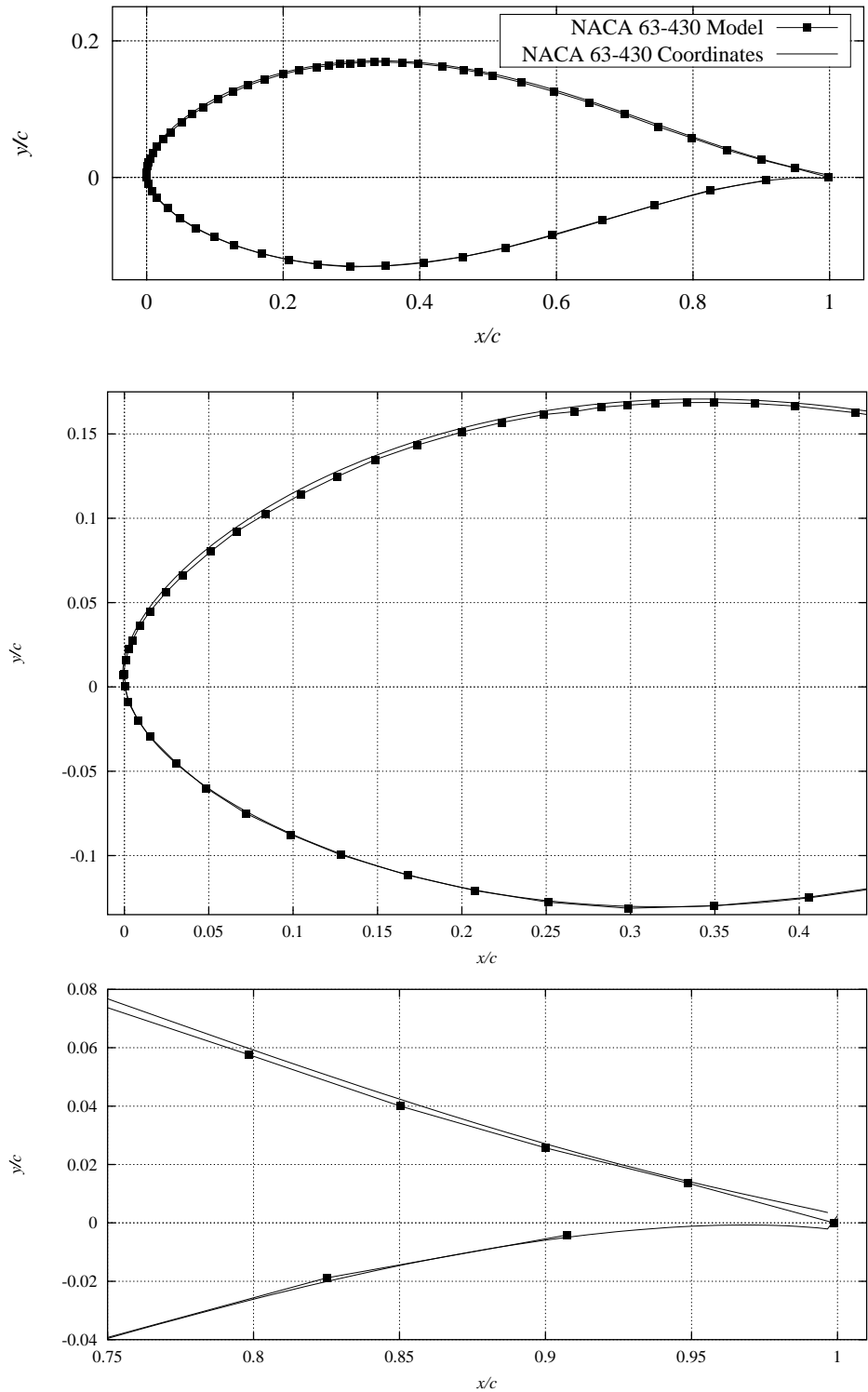
Figure 3-3 The actual NACA 63-430 model coordinates compared with the theoretical coordinates from [7]. Each symbol corresponds to a pressure tap. The leading edge and the trailing edge regions are shown enlarged.

3.2   Vortex generators

Vortex generators (VGs) are often used at the inner part of wind turbine blades between 10% to 30% chord length from the leading edge on the blade suction side. They increase the maximum lift coefficient by delaying separation on the airfoil suction side to higher incidences. At the same time, they increase the drag coefficient.

A parametric study was conducted where two VGs with heights 4 mm and 6 mm were used at three chordwise locations, $x/c = 10\%$, $x/c = 20\%$ and $x/c = 30\%$. However not all the combinations were tried for all the airfoils. The design of the VGs was similar to those used for numerous airfoil tests by Timmer, 1992 [8], at Delft University.

Figure 3-4 and Figure 3-5 show the shapes and dimensions of the used VGs. They have the shape of orthogonal triangles and they are placed with their right-angle perpendicular to the airfoil surface. They are placed so that their height increases towards the trailing edge. The presence of the VGs results in the formation of vortices, which transfer high momentum fluid down to the airfoil surface and thus delay separation. To achieve this the VGs are arranged in pairs at equal and opposite angles relative to the chord of the blade.

The VGs were constructed from a narrow band that was cut in 0.2 mm thick stainless steel. Each VG was cut out in the band, raised from the surface and bend perpendicular to the surface. The band with cut out vortex generators was then glued onto the airfoil model surface. Because of the thickness of the part of the band that was glued to the surface, the measurements will be slightly disturbed. The flow has to enforce the edge of the band and in particular the drag coefficient at low angles of attack will be increased. However, the benefits of the band are a precise location of vortex generators and limited mounting time.

Figure 3-4 shows the Delft, h = 4 mm, configuration with a height of 4 mm and a length of 12 mm. The angles from the chordwise direction are ±19.5°. The leading edge spacing between two VGs is 8 mm and the distance between two consecutive pairs is 20 mm.

Figure 3-5 shows the Delft, h = 6 mm, configuration with a height of 6 mm and a length of 18 mm. The angles from the chordwise direction are ±19.5°. The leading edge spacing between two VGs is 10 mm and the distance between two consecutive pairs is 25 mm.
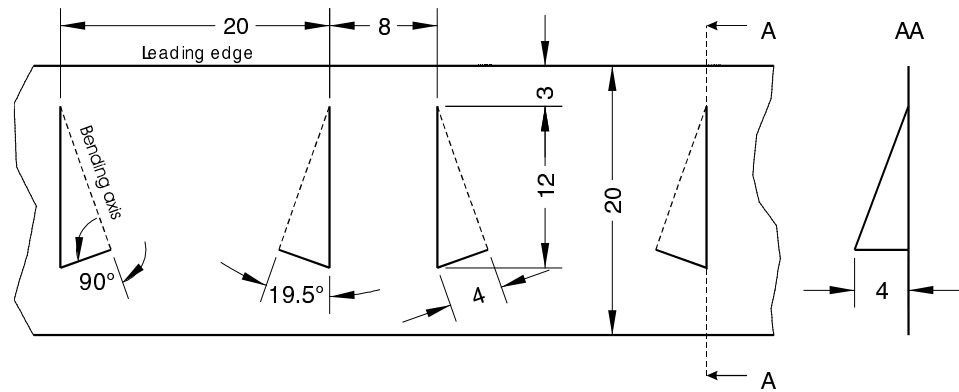
Figure 3-4 Delft vortex generators of height 4 mm, length 12 mm, bend perpendicular from a 0.2 mm thick band of 20 mm width.
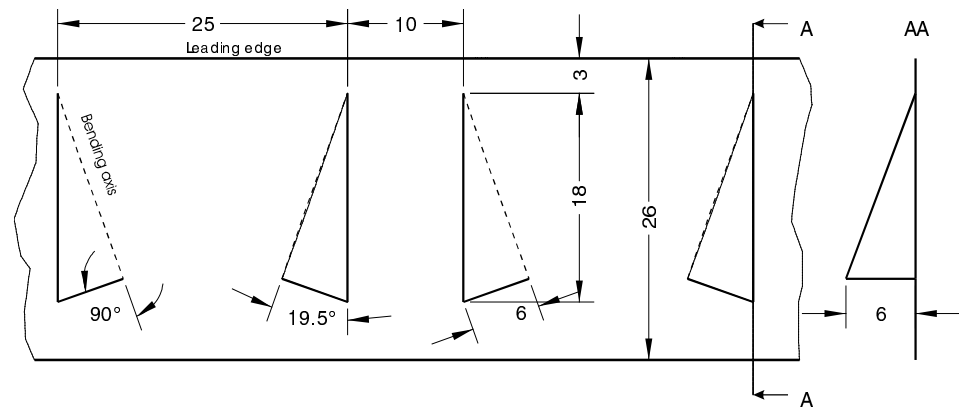

Figure 3-5 Delft vortex generators of height 6 mm, length 18 mm, bend perpendicular from a 0.2 mm thick band of 26 mm width.

3.3 Leading edge roughness

Trip tape was mounted to the airfoil model surface to simulate the effects from leading edge roughness. Leading edge roughness appears when dirt, bugs or soil are accumulated on the wind turbine blades in dirty environments.

Three different types of trip tape were used. In all measurements the trip tape was mounted at $x/c = 0.05$ on the suction side and at $x/c = 0.10$ on the pressure side.

Figure 3-6 to Figure 3-8 show the different trip tapes used. All trip tapes were intended for use on gliders and were manufactured as a plastic tape that was glued to the airfoil model surface.

Figure 3-6 shows the 90° zigzag trip tape with a 90° angle, a width of 3 mm and a thickness of 0.35 mm.

Figure 3-7 shows the 60° zigzag trip tape with a 60° angle, a width of 3 mm and a thickness of 0.5 mm.

Figure 3-8 shows the bulge trip tape with bulges of around 0.5 mm including the tape thickness.
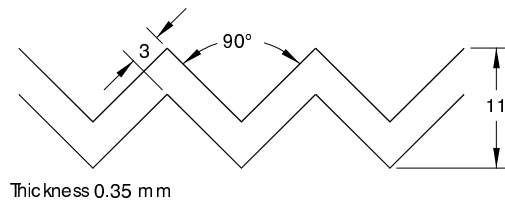
Figure 3-6 Trip tape with 90° zigzag of 3 mm width and 0.35 mm thickness.
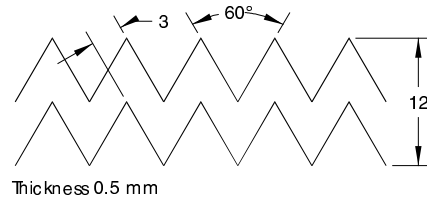
Figure 3-7 Trip tape with 60° zigzag of 3 mm width and 0.35 mm thickness.
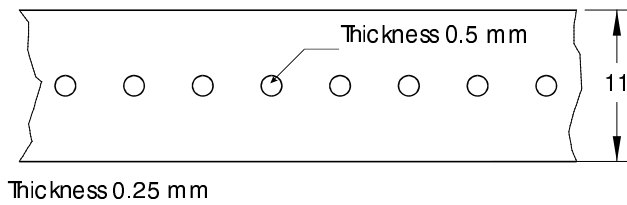
Figure 3-8 Bulge tape of 11 mm width and 0.25 mm thickness. Bulges have a total of 0.5 mm height (the tape thickness is included).

4 FFA-W3-241 Smooth leading edge

This chapter reports steady inflow measurements for the FFA-W3-241 airfoil with smooth leading edge. The Reynolds number was in all measurements $Re = 1.6 \times 10^6$. All shown results were corrected for wind tunnel effects and the aerodynamic forces were referenced to the wind tunnel free stream flow by use of Pitot 1 taking into account corrections for speed-up and pressure loss.

The measurements were compared with numerical calculations. The XFOIL code based on a panel method with a viscous boundary layer formulation was used, following Madsen and Fillipone, 1995 [6]. Free transition was modelled with the e^n method, Drela, 1989 [7]. The Ellipsys2D Navier-Stokes code, Sørensen, 1995 [9], with the k-ω turbulence model, Menter, 1993 [8], was used for turbulent flow calculations. Free transition was modelled using the Michel transition criteria, Michel, 1952 [10].

The different types of conducted measurements are described in Appendix A.

Figure 4-1 shows C_P distributions at different angles of attack. At low angles of attack the flow is attached and the suction side minimum C_P gradually approaches -3 at 10.2°. After this, separation occurs from the trailing edge. The separation point moves gradually towards the leading edge and at 27.5° almost the entire suction side is separated. The minimum C_P in post stall is -3.6.

Figure 4-2 and Figure 4-3 show the C_P distribution at 4.0° and 10.2° respectively compared with XFOIL and EllipSys2D calculations.

At 4.0° the agreement between the measurement and both calculations is in general good. The suction side minimum C_P's compare well and the pressure recovery region is calculated equal to the measurement. Both calculations show the transition point at $x/c = 0.36$, however the transition point is not clearly seen in the measurement. There is a kink in C_P at 0.14 that could be caused by transition. The pressure side C_P is also in good agreement with the calculations. At the trailing edge the measurement resolution is too poor to show the shape of the C_P curve and the transition point at $x/c = 0.50$ is not seen in the measurement.

At 10.2° the agreement is very good on the pressure side except for the transition point, which is not seen in the measurement. On the suction side, C_P is measured irregular near minimum C_P at -2.8. This is not seen in the calculations, where the suction side C_P is lower and the transition point is seen at $x/c = 0.24$. The pressure recovery is smooth in both the measurement and in both calculations.

Figure 4-4 shows the C_P distribution at 12.6° compared with calculations and Figure 4-5 shows the C_P distribution at 16.4°.

At 12.6° the pressure side results of the measurement and the calculations are in good agreement except for C_P at the stagnation point, where the measured C_P is marginally lower than in the calculations. On the suction side the minimum C_P is lower than the calculations. Furthermore the measured C_P on the suction side shows that the flow is separated, whereas the calculations show attached flow.

At 16.4° the agreement between measurements and the calculations is not good. The suction side minimum C_P is measured to -3.2 whereas the calculations show around -5.0 and there is a significant difference in the location of the separation point.

Figure 4-6 to Figure 4-9 show the measured C_L, C_D and C_M curves compared with XFOIL and EllipSys2D calculations.

C_L for the measurement and EllipSys2D are in very good agreement until 5° whereas XFOIL slightly overestimates C_L. The measured maximum C_L is 1.37 and occurs around 11° whereas both calculations overestimates maximum C_L significantly. Until maximum C_L, measured C_D is in very good agreement with the EllipSys2D calculation whereas XFOIL underestimates minimum C_D. The minimum C_D of 0.010 is equal for the measurement and the EllipSys2D calculation and the shape of the C_D curve is similar. In general, C_M is not in good agreement. At low angles of attack there is a difference in the slope of the C_M curve and after 11°, which corresponds to maximum measured C_L, the measured C_M deviates from the calculation.

In summary the measurements show that the agreement between measurements and EllipSys2D calculations is good for low angles of attack where the overall shape of the C_P distribution is similar. At higher angles of attack in stall and in the post stall region the calculations overestimate maximum C_L that is measured to 1.37. Minimum C_D is measured to 0.010, which is in good agreement with EllipSys2D that calculates the shape of the C_D curve well.
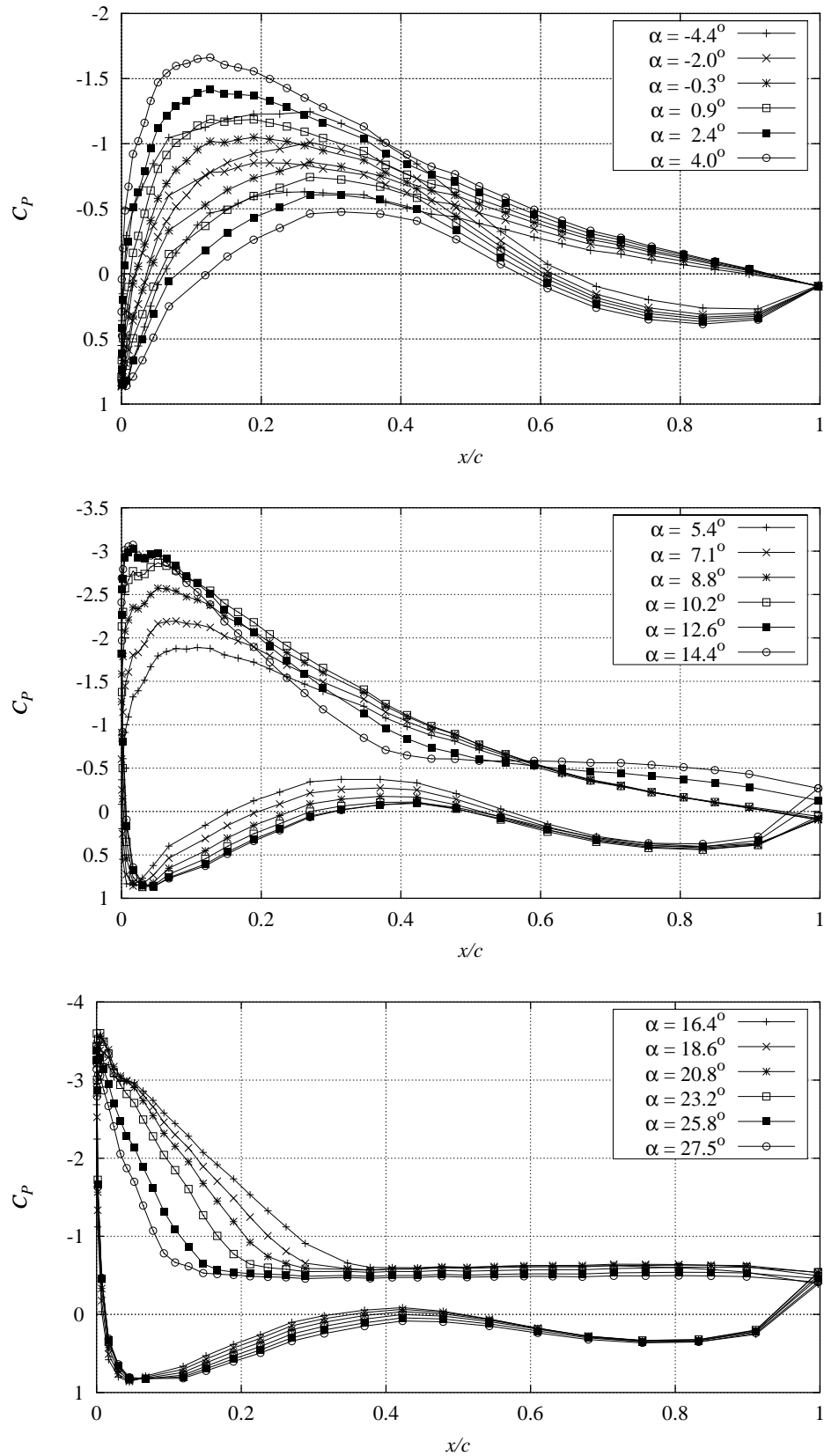
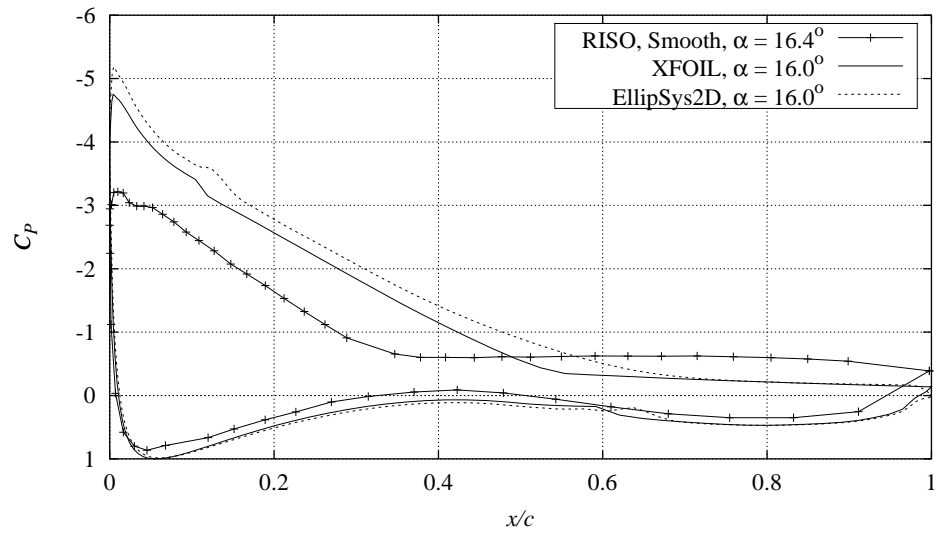*Figure 4-1 Measured C_P distributions at different angles of attack, Re = 1.6×10^6 (FFAW3241STEP091297V1).*
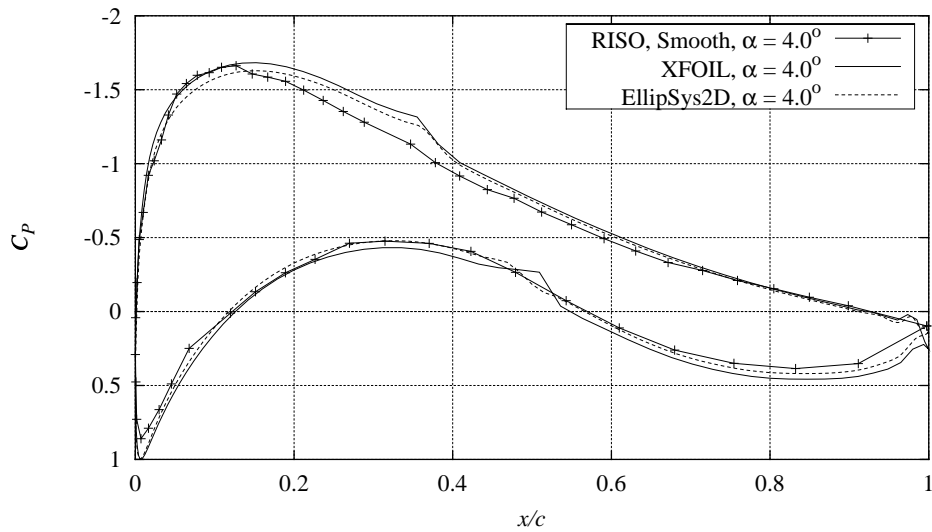
Figure 4-2 Measured C_P distribution compared with XFOIL and Ellipsys2D calculations, Re = 1.6×10⁶, α = 4.0°(FFAW3241STEP091297V1).
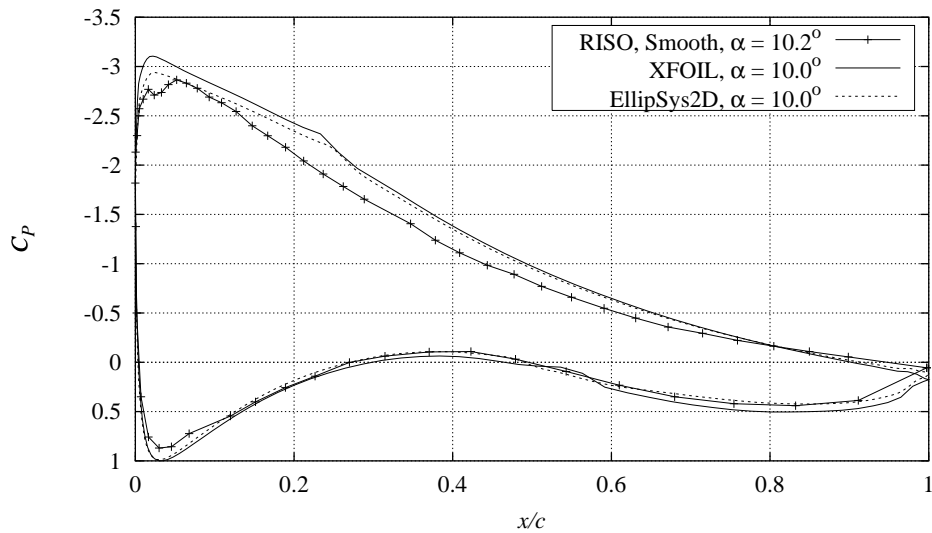

Figure 4-3 Measured C_P distribution compared with XFOIL and Ellipsys2D calculations, Re = 1.6×10⁶, α = 10.2°(FFAW3241STEP091297V1).
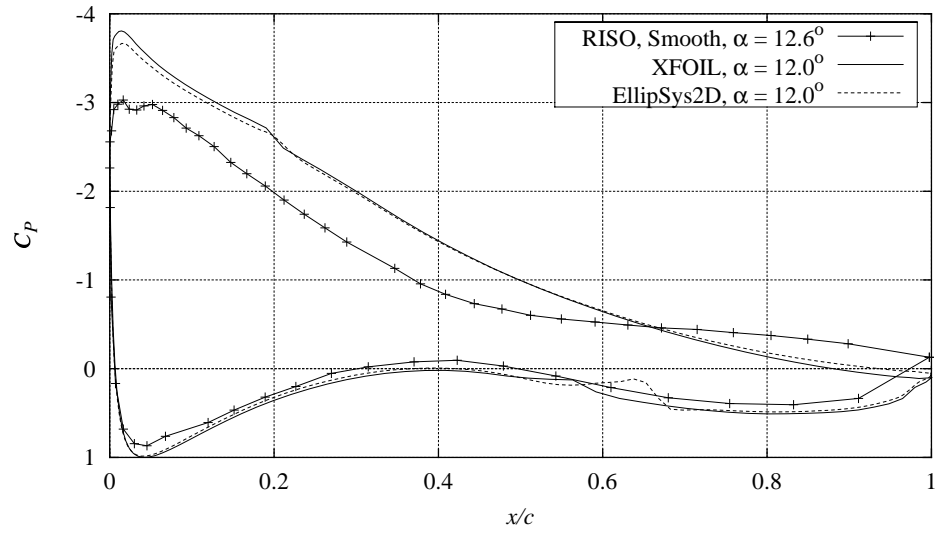
Figure 4-4 Measured C_P distribution compared with XFOIL and Ellipsys2D calculations, Re = 1.6×10^6, α = 12.6° (FFAW3241STEP091297V1).

Figure 4-5 Measured C_P distribution compared with XFOIL and Ellipsys2D calculations, Re = 1.6×10^6, α = 16.4° (FFAW3241STEP091297V1).
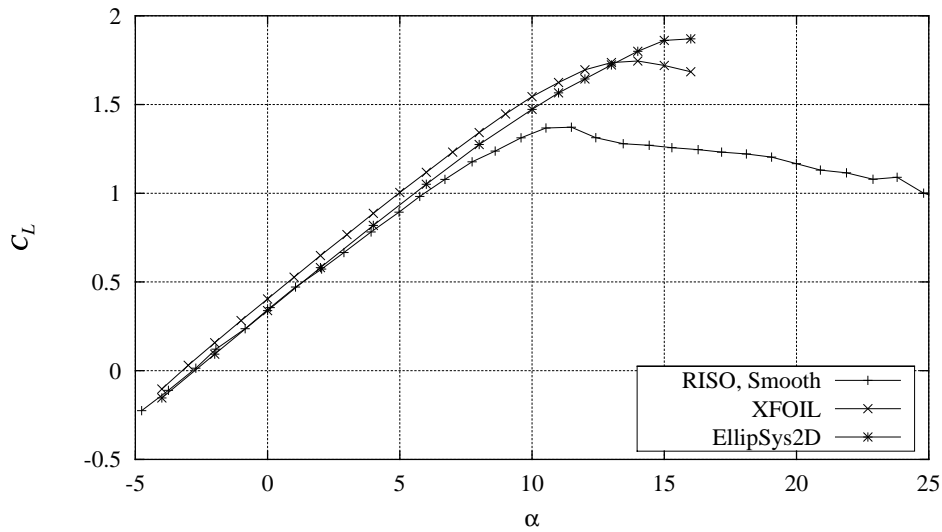
Figure 4-6 Measured C_L curve compared with XFOIL calculations with free transition and EllipSys2D calculations with free transition, Re = 1.6×10^6, (FFAW3241CONT091297V7).
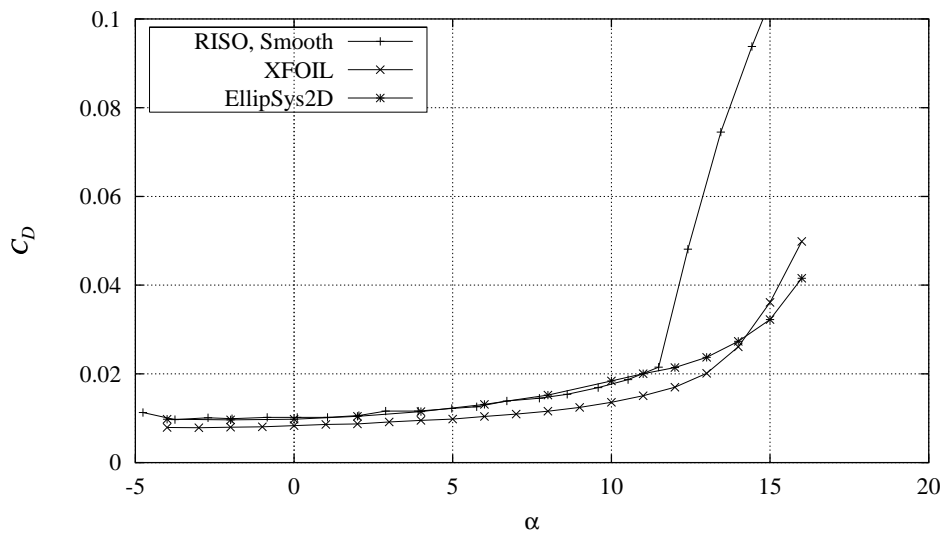
Figure 4-7 Measured C_D curve compared with XFOIL calculations with free transition and EllipSys2D calculations with free transition, Re = 1.6×10^6, (FFAW3241CONT091297V7).
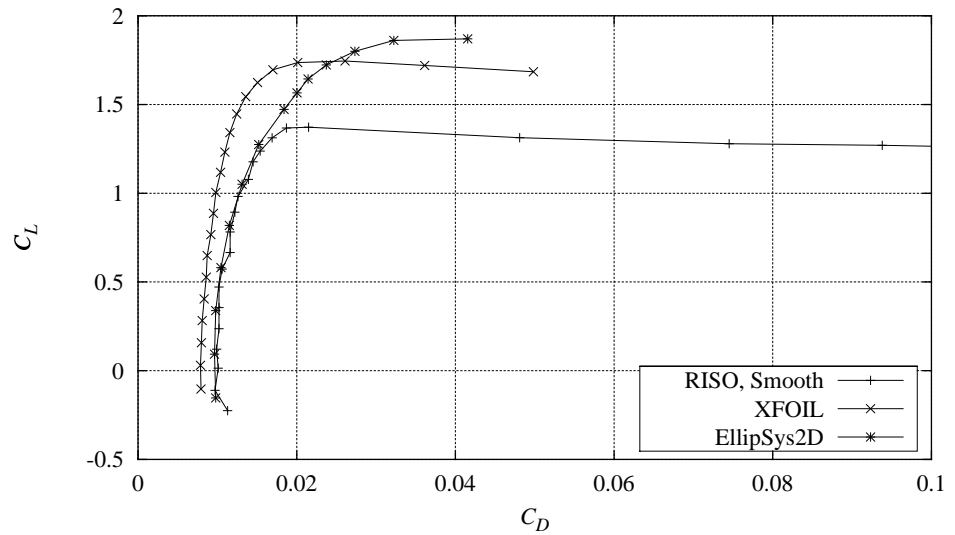
Figure 4-8 Measured C_L-C_D curve compared with XFOIL calculations with free transition and EllipSys2D calculations with free transition, Re = 1.6×10⁶, (FFAW3241CONT091297V7).
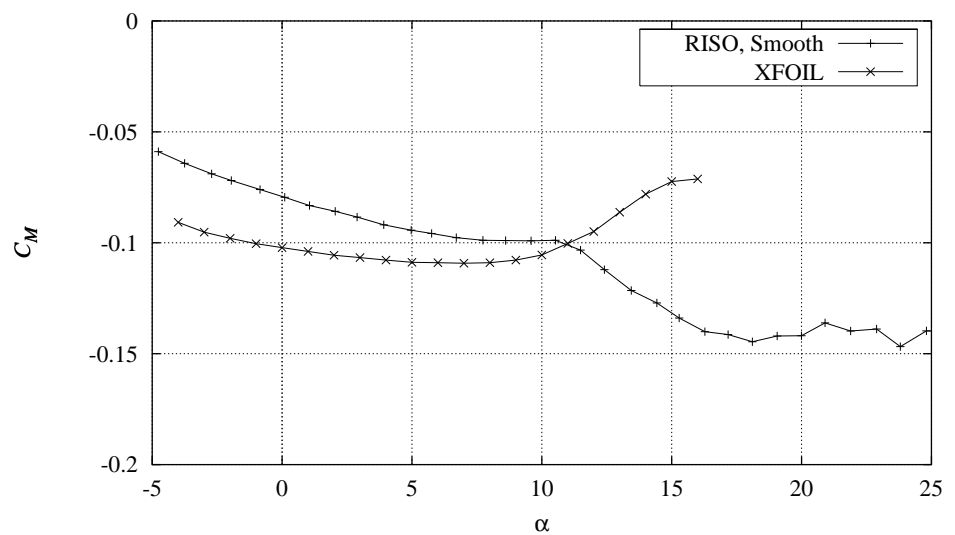
Figure 4-9 Measured C_M curve compared with XFOIL calculations with free transition, Re = 1.6×10⁶, (FFAW3241CONT091297V7).

5 FFA-W3-241 Vortex generators

This chapter presents steady inflow measurements for the FFA-W3-241 airfoil with the following different configurations of vortex generators (VGs):

- Delft vortex generators, $h = 6$ mm at $x/c = 0.2$.
- Delft vortex generators, $h = 6$ mm at $x/c = 0.3$.
- Delft vortex generators, $h = 4$ mm at $x/c = 0.1$.
- Delft vortex generators, $h = 4$ mm at $x/c = 0.2$.

The x/c location corresponds to the leading edge location of the VGs. The VGs are described in Section 3.2 and the different measurements are shown in more detail in Appendix B. The different types of available measurements are described in Appendix A.

The measurements were not compared with numerical calculations since the influence from VGs could not be modelled in the numerical codes. The measurements were instead compared to the smooth flow measurements.

We have investigated that the aerodynamic coefficients derived from the pressure distribution with VGs agree well with the aerodynamic coefficients derived from the strain gauge measurements. This means that the pressure distribution measured at the mid span of the airfoil section is representative even though vortex generators are mounted to the surface in a pattern that varies in the spanwise direction.

Figure 5-1 shows the C_P distributions for the different VG configurations compared with the smooth flow measurement at angles of attack around 10° and Figure 5-2 shows the C_P distributions corresponding to maximum C_L for each configuration.

At 10° the differences in C_P are in general very small and limited to the front part of the suction side, where minimum C_P is slightly different. C_P is minimum for smooth flow and for the $h = 6$ mm, $x/c = 0.30$ VG configuration where the leading edge flow is less disturbed. The pressure recovery part of the suction side and the pressure side C_P are very similar.

At maximum C_L the VG configurations lower the suction side C_P on the front part of the airfoil whereas the pressure side C_P distributions look similar, still with difference in level. Minimum C_P is achieved by the $h = 6$ mm, $x/c = 0.2$ and $h = 4$ mm, $x/c = 0.1$ VG configurations. None of the VG configurations have separated flow at the trailing edge at maximum C_L except for $h = 4$ mm, $x/c = 0.1$, where the angle of attack at maximum C_L is greatest.

Figure 5-3 to Figure 5-6 show the C_L, C_D and C_M curves for the VG configurations compared with smooth flow.

The earliest maximum C_L occurs for smooth flow at 10.2°. Maximum C_L for the VG configurations occur between 14.0° and 19.1° depending on the height and location of the VGs. Minimum C_D is lowest for the $h = 4$ mm, $x/c = 0.1$

configuration and C_D at angles of attack above 5° are higher for both of the $h = 4$ mm configurations so that in conclusion the C_L/C_D ratios are highest for the $h = 6$ mm configurations. C_M is similar at low angles of attack whereas C_M is different in the maximum C_L region depending on the flow separation for each VG configuration.

In summary the measurements showed that VGs have a negligible influence on the C_P distributions at low angles of attack before maximum C_L for smooth flow where the flow is attached. Minimum suction side C_P is achieved for the VG configurations that are located close to the leading edge. Higher angles of attack for maximum C_L are achieved for the VG configurations closest to the leading edge whereas the remaining VG configurations showed higher C_L curve slopes but earlier separation. Maximum C_L is higher for the VG configurations compared with smooth flow and maximum C_L is higher for the configurations with large VGs compared with configurations with smaller VGs and the best VG configuration is $h = 6$ mm, $x/c = 0.2$. Minimum C_D is in general increased for the VG configurations compared to smooth flow. However, because the flow is attached at higher angles of attack, C_D is smaller for the VG configurations at angles of attack close to maximum C_L resulting in higher C_L/C_D ratio at angles of attack just below maximum C_L.
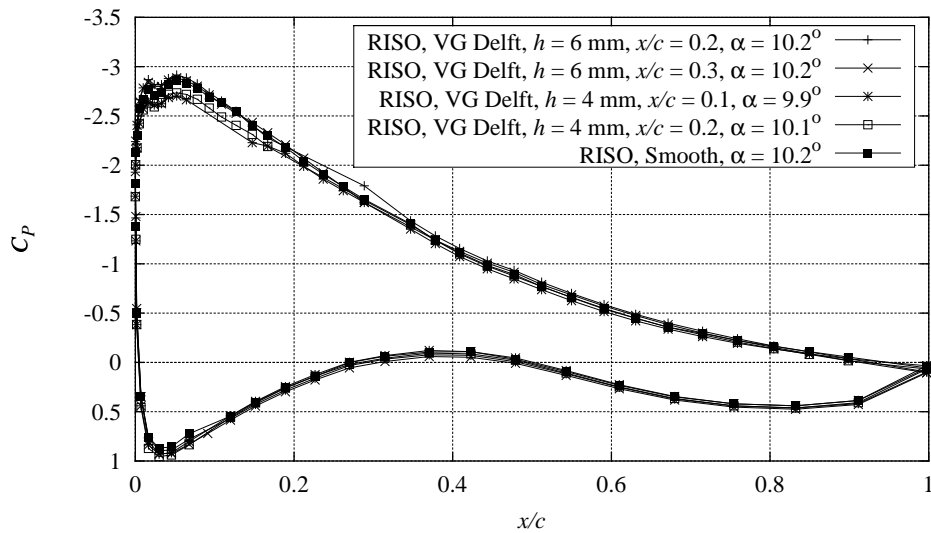
Figure 5-1 Measured C_P distributions for the different vortex generator configurations compared with smooth measurement, Re = 1.6×10^6. α around 10° corresponding to C_{Lmax} for smooth leading edge flow.
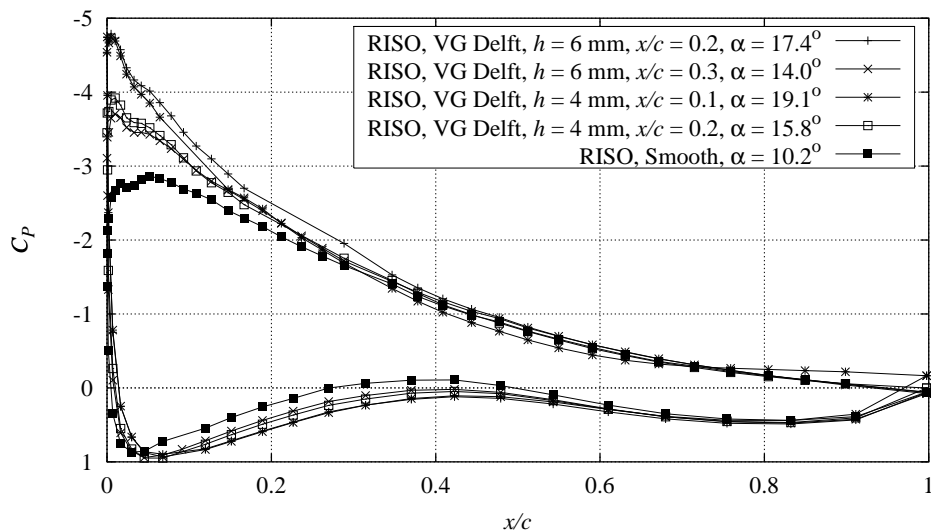
Figure 5-2 Measured C_P distributions for the different vortex generator configurations compared with smooth measurement, Re = 1.6×10^6. Angles of attack corresponding to C_{Lmax}.
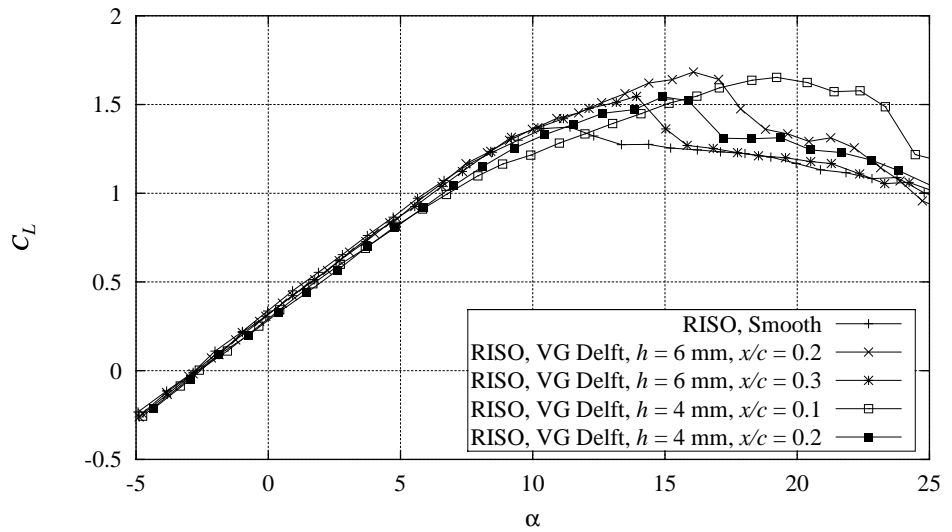
Figure 5-3 Measured C_L curves for the different vortex generator configurations compared with smooth measurement, $Re = 1.6 \times 10^6$.
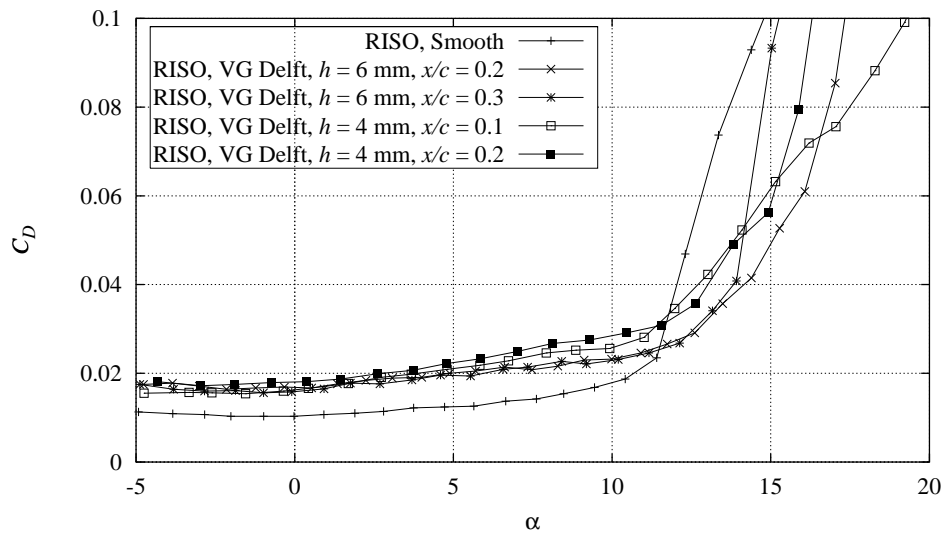
Figure 5-4 Measured C_D curves for the different vortex generator configurations compared with smooth measurement, $Re = 1.6 \times 10^6$.
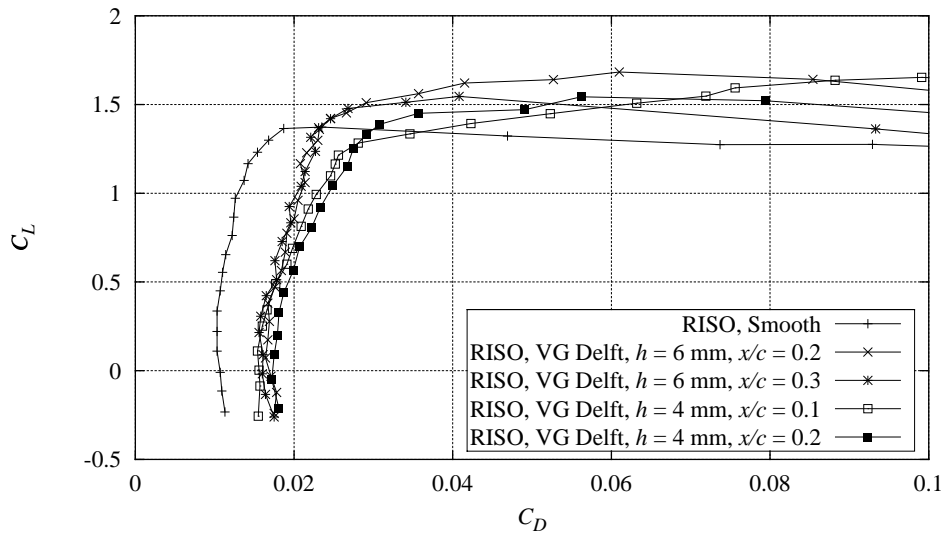
Figure 5-5 Measured C_L-C_D curves for the different vortex generator configurations compared with smooth measurement, Re = 1.6×10⁶.
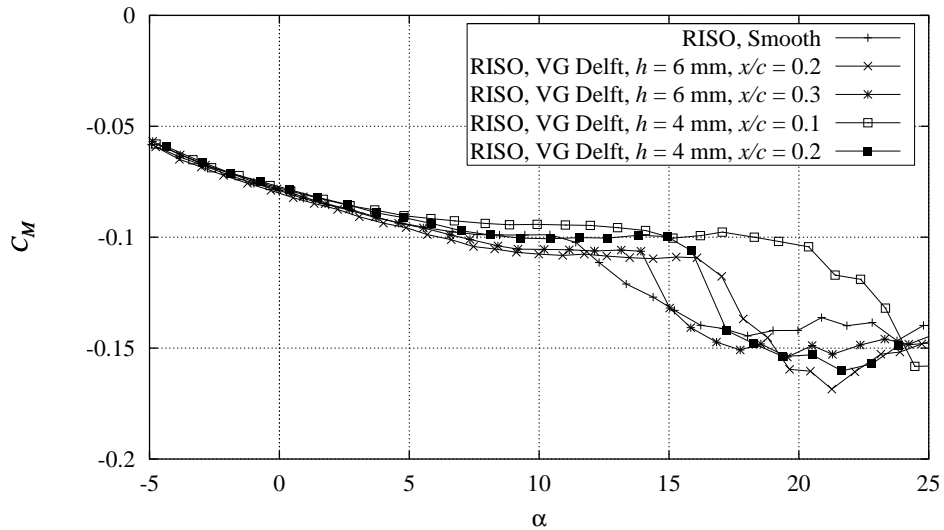
Figure 5-6 Measured C_M curves for the different vortex generator configurations compared with smooth measurement, Re = 1.6×10⁶.

6 FFA-W3-241 Leading edge roughness

This chapter presents steady inflow measurements for the FFA-W3-241 airfoil with the following different configurations of leading edge roughness (LER):

- 90° zigzag trip tape
- 60° zigzag trip tape
- Bulge tape

The LER configurations are described in Section 3.3 and the different measurements are shown in more detail in Appendix C. The different types of available measurements are described in Appendix A.

The measurements were compared with numerical calculations. The XFOIL code was used and prescribing the transition location to be at the leading edge: $x/c = 0.01$ on the suction side and $x/c = 0.10$ on the pressure side simulated LER. The Ellipsys2D Navier-Stokes code was used and having turbulent flow on the entire airfoil simulated leading edge roughness. The measurements were also compared with the smooth flow measurement.

Figure 6-1 shows the C_P distributions for the different LER configurations compared with the smooth flow measurement and XFOIL and EllipSys2D calculations at angles of attack around 10° and Figure 6-2 shows the C_P distributions around 14°.

The C_P curves for the LER configurations are similar except for small differences caused by different angles of attack. Compared to smooth flow, the LER configuration flows have higher C_P on the suction side. For 10° separation occurs around $x/c = 0.8$ for the LER configurations whereas the smooth flow measurement has attached flow. The calculation results look similar and the agreement between measurements and calculations is good on the pressure side, but not so good at the suction side, where the calculations overestimate minimum C_P and C_P on the front part of the suction side. At 14° the calculations agree well with the measurements on the pressure side but the calculations have too low minimum C_P on the front part of the suction side and too high C_P on the trailing part of the suction side.

Figure 6-3 to Figure 6-6 show the C_L, C_D and C_M curves for the LER configurations compared with smooth flow and XFOIL and EllipSys2D calculations.

The C_L curves for the LER configurations are similar. It appears that the 90° configuration has slightly higher C_L compared with the other configurations. Maximum C_L is in general lower and the angle of attack for zero C_L is slightly higher for the LER configurations compared with smooth flow. The lower maximum C_L is caused by earlier separation on the suction side. The EllipSys2D calculation agrees well with the measurements at low angles of attack whereas XFOIL overestimates C_L. Both calculations overestimate

maximum C_L. It appears that the calculation of maximum C_L agrees well with the smooth flow measurement.

The C_D curve is equal for all LER configurations. Minimum C_D is higher for the LER configurations compared with smooth flow and the rise in drag associated with separation occurs at a lower angle of attack. XFOIL underestimates minimum C_D but EllipSys2D calculates minimum C_D to be equal to the LER configuration measurements between 0° and 9°. C_M is similar for all LER configurations and higher than C_M for smooth flow. The agreement with the XFOIL calculation is not good.

In summary the measurements showed that the different LER configurations were measured to have similar C_P curve distributions and equal C_L, C_D and C_M curves. LER reduces maximum C_L and increases minimum C_D so that the C_L/C_D ratio is reduced for all angles of attack compared with smooth flow. The EllipSys2D calculation agrees well with measurements of minimum C_D and C_L at low angles of attack, but maximum C_L is not in good agreement. However maximum C_L for the EllipSys2D calculation is in good agreement with the smooth flow measurement.
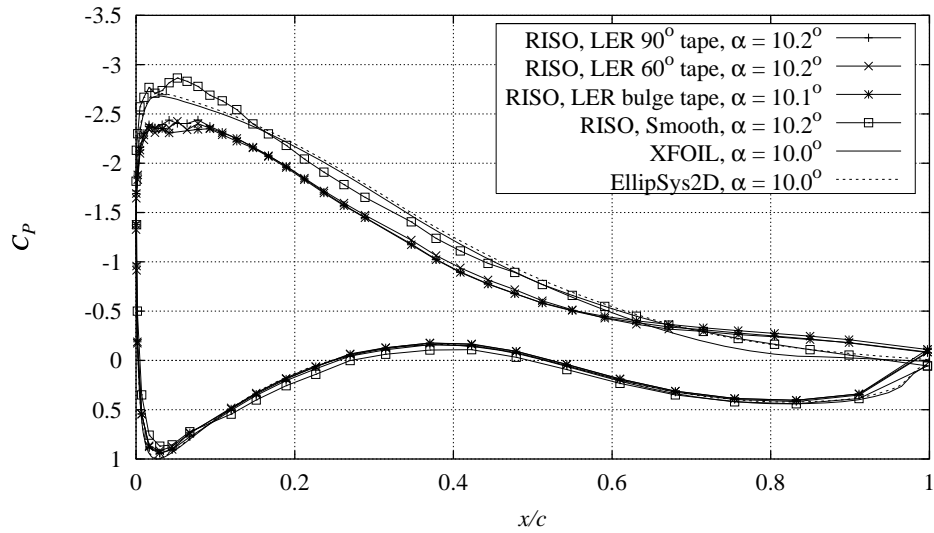
Figure 6-1 Measured C_P distributions for the different leading edge roughness configurations compared with smooth measurement and XFOIL (LE transition) and EllipSys2D (turbulent) calculations, Re = 1.6×10^6, α around 10.2° corresponding to C_{Lmax} for smooth leading edge flow.
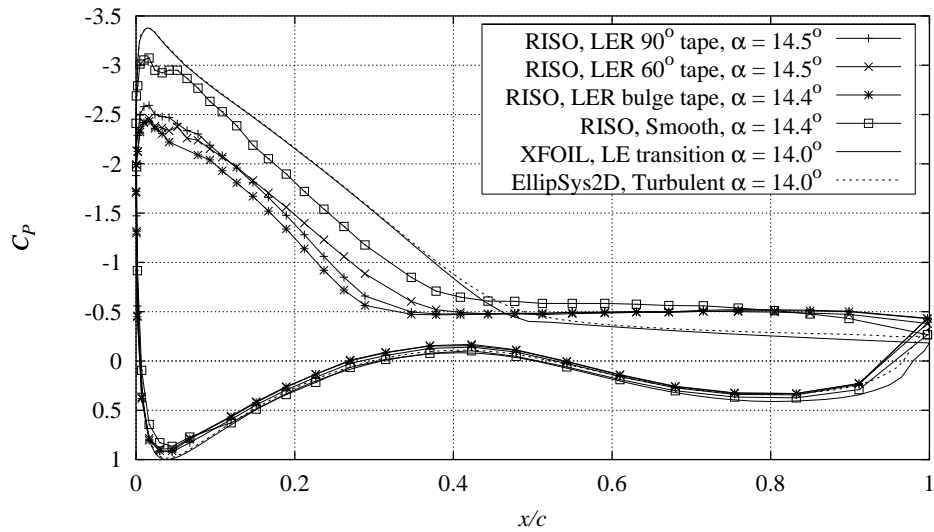
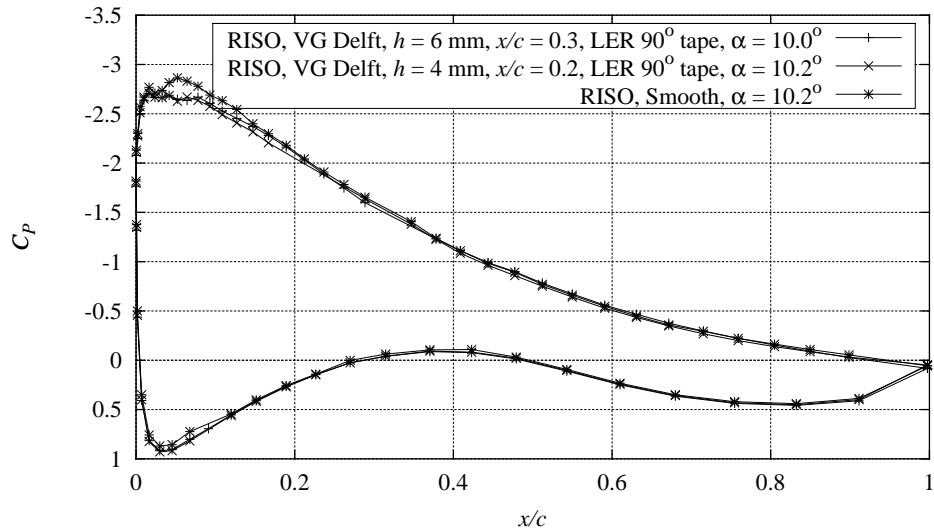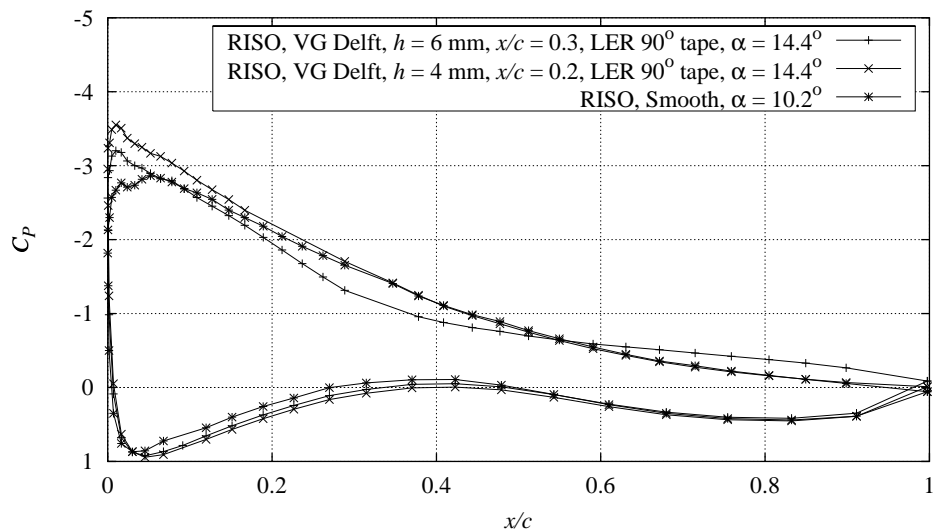*Figure 6-2 Measured C_P distributions for the different leading edge roughness configurations compared with smooth measurement and XFOIL (LE transition) and EllipSys2D (turbulent) calculations, Re = 1.6×10^6, α around 14.4°.*
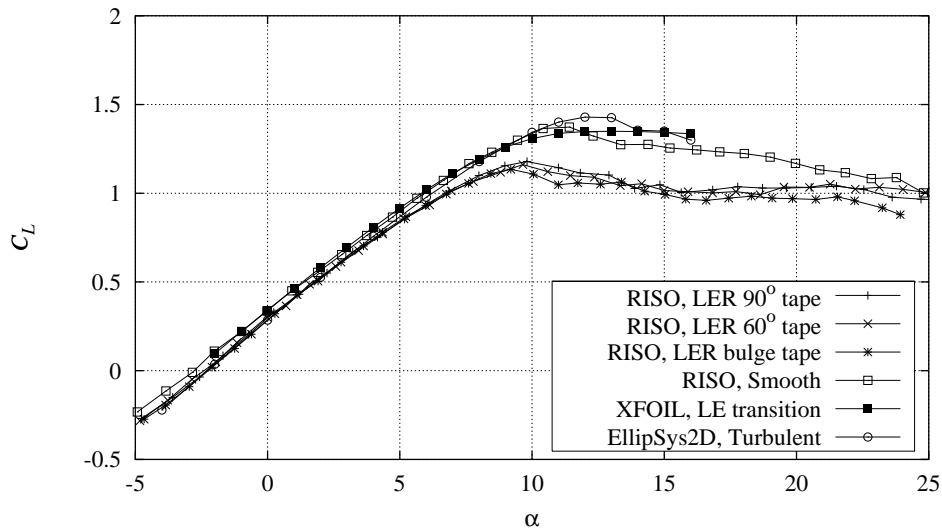
Figure 6-3 Measured C_L curves for the different leading edge roughness configurations compared with smooth measurement and XFOIL (LE transition) and EllipSys2D (turbulent) calculations, Re = 1.6×10^{6}.
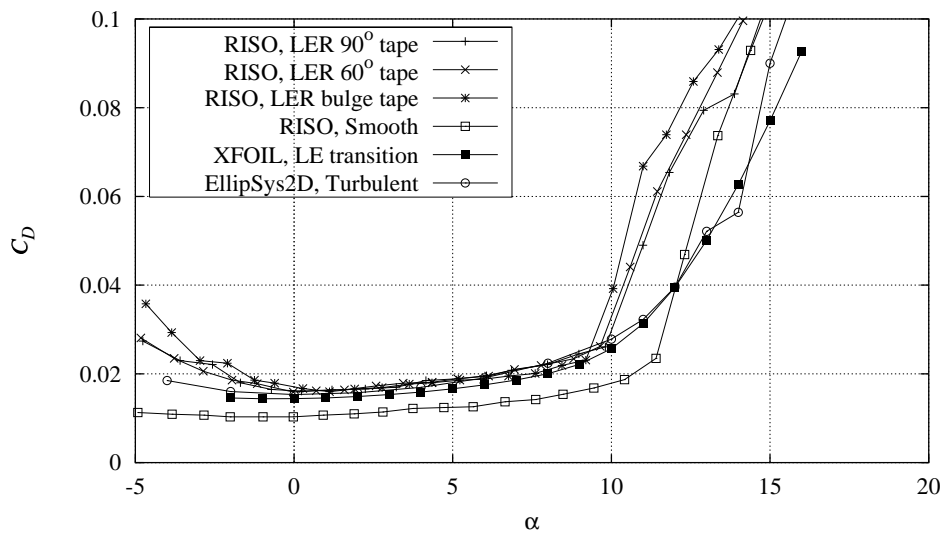
Figure 6-4 Measured C_D curves for the different leading edge roughness configurations compared with smooth measurement and XFOIL (LE transition) and EllipSys2D (turbulent) calculations, Re = 1.6×10^{6}.
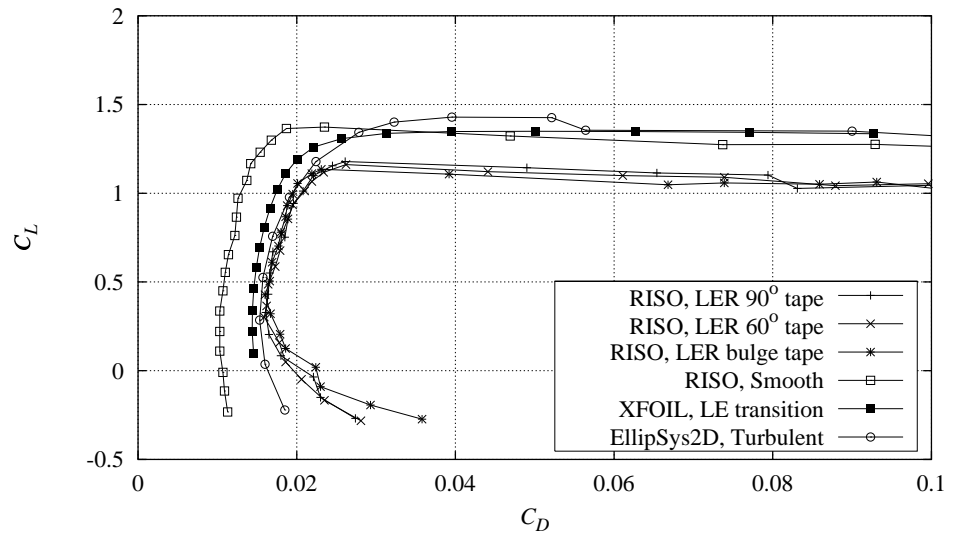
Figure 6-5 Measured C_L-C_D curves for the different leading edge roughness configurations compared with smooth measurement and XFOIL (LE transition) and EllipSys2D (turbulent) calculations, Re = 1.6×10^6.
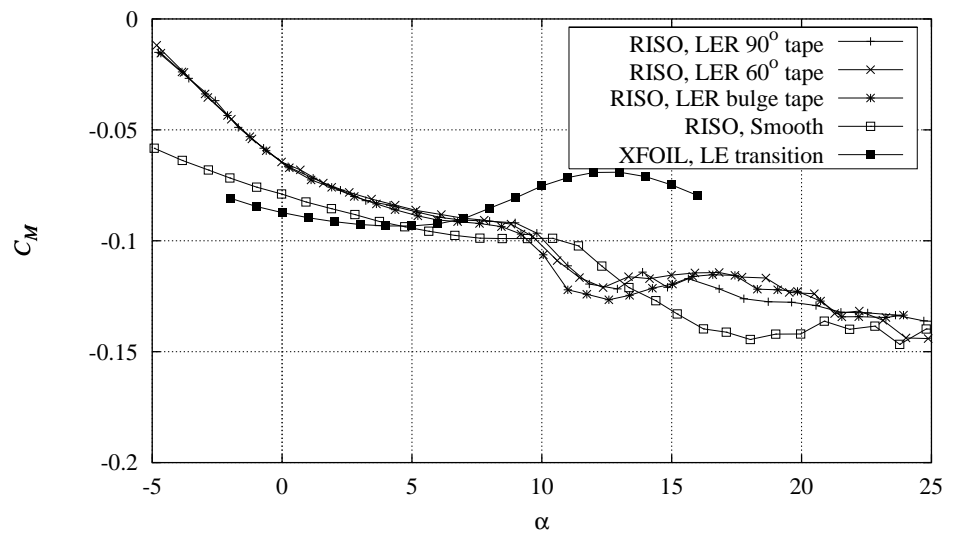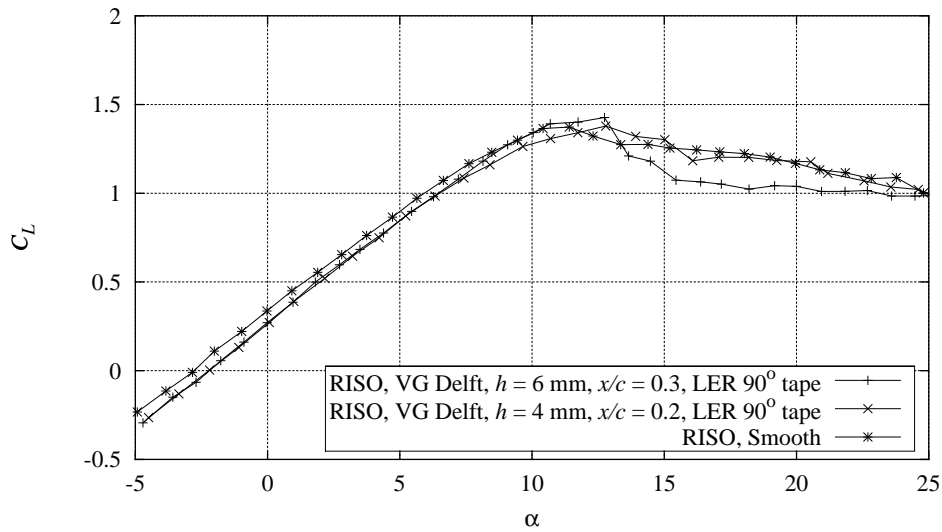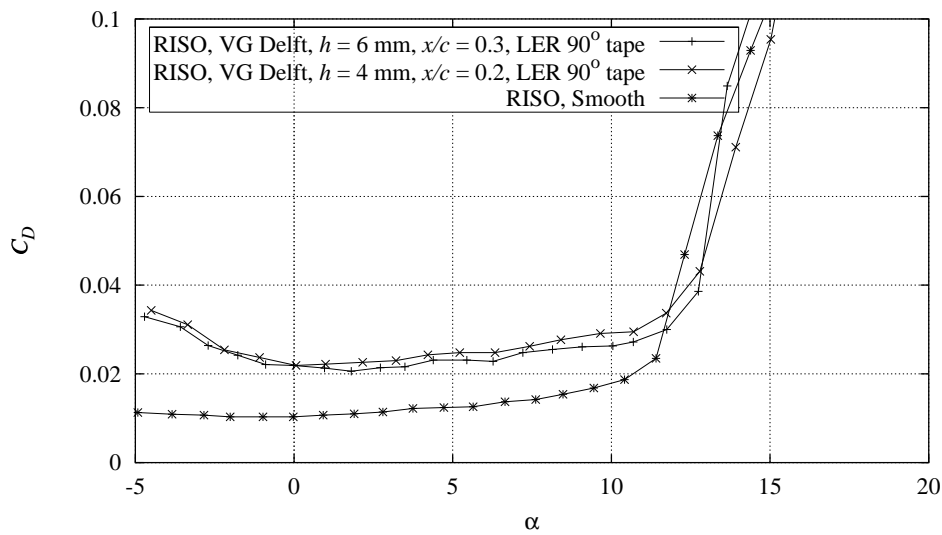

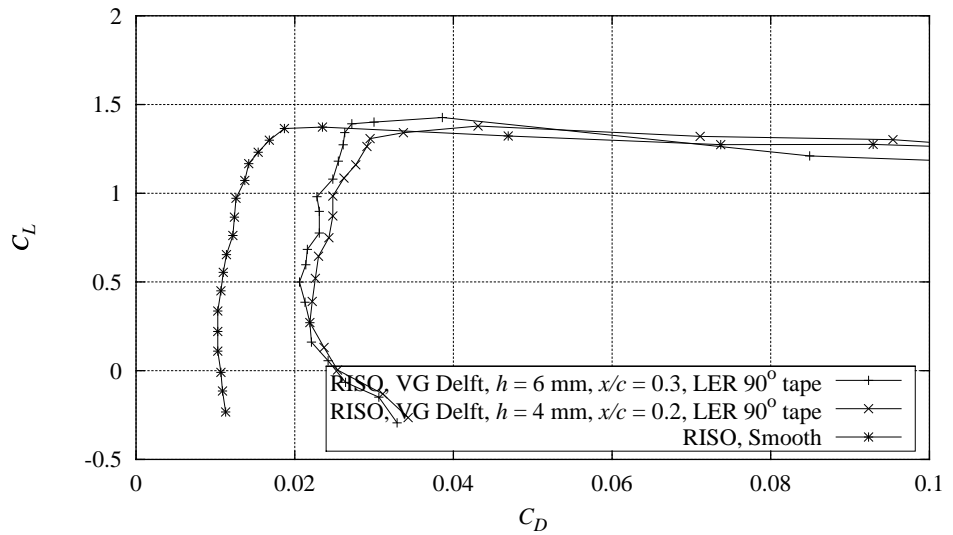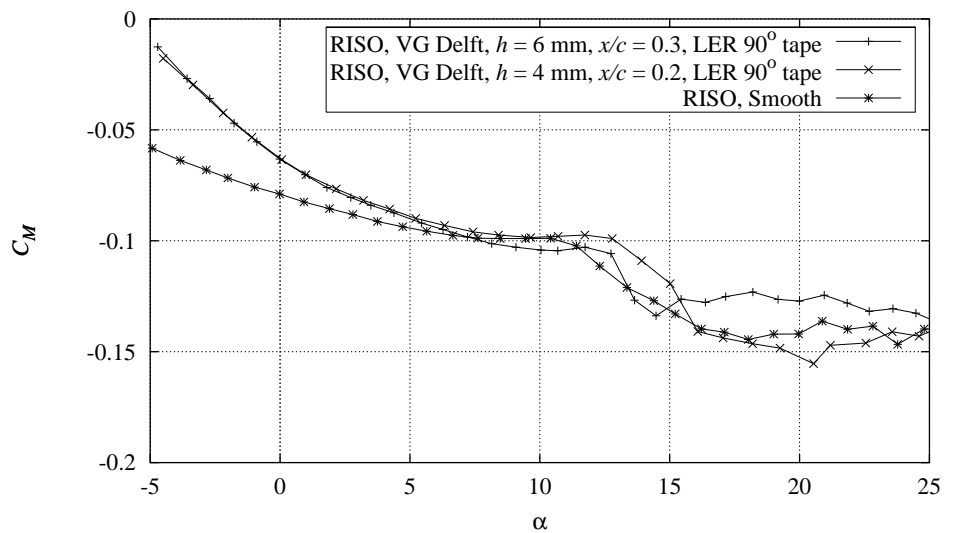*Figure 6-6 Measured C_M curves for the different leading edge roughness configurations compared with smooth measurement and XFOIL (LE transition) and EllipSys2D (turbulent) calculations, Re = 1.6×10^6.*

7 FFA-W3-241 Leading edge roughness and vortex generators

This chapter presents steady inflow measurements for the FFA-W3-241 airfoil with the following combinations of vortex generators and leading edge roughness (VGLER):

- Delft vortex generators, $h = 6$ mm at $x/c = 0.3$ and 90° zigzag trip tape.
- Delft vortex generators, $h = 4$ mm at $x/c = 0.2$ and 90° zigzag trip tape.

The VGs are described in Section 3.2 and the LER configurations are described in Section 3.3. The different measurements are shown in more detail in Appendix D. The different types of available measurements are described in Appendix A.

The measurements were not compared with numerical calculations but they were compared with the smooth flow measurement.

Figure 7-1 shows the C_P curves for the different VGLER configurations compared with smooth flow around 10° and Figure 7-2 shows the C_P curves around 14°:

For 10° the agreement between VGLER configurations and smooth flow is very good except for the suction side C_P peak, where C_P is higher for the measured VGLER configurations compared with smooth flow.

At 14° the pressure side C_P curves are similar for both VGLER configurations and smooth flow. The suction side minimum C_P is higher for the VGLER configurations than for smooth flow but the suction side C_P on the front part is in general lower for the $h = 6$ mm, $x/c = 0.3$ configuration than for the $h = 4$ mm, $x/c = 0.2$ configuration.

Figure 7-3 to Figure 7-6 show the C_L, C_D and C_M curves for the different VGLER configurations compared with smooth flow.

The angle of attack for zero C_L is in general slightly higher for the VGLER configurations than for smooth flow. Maximum C_L is equal for both VGLER configurations and smooth flow, however the slope of the C_L curve toward maximum C_L is steeper for the VGLER configuration. Minimum C_D is increased significantly for the VGLER configurations compared with smooth flow and the VGs do not delay separation significantly. C_M for the VGLER configurations is increased at low angles of attack compared with smooth flow, but at angles of attack above 6°, C_M appears to be similar.

In summary the measurements showed that the different VGLER configurations were measured to have nearly equal C_L and C_D characteristics. VGs increase C_L and C_D and C_D is further increased when LER is applied at the leading edge. The reduction in maximum C_L from LER is counterbalanced by the VGs so that maximum C_L for the VGLER configurations is equal to that for smooth flow.

Figure 7-1 Measured C_P distributions for the different vortex generator and leading edge roughness configurations compared with smooth measurement, $Re = 1.6 \times 10^6$, α around $10°$ corresponding to C_{Lmax} for smooth leading edge flow.

Figure 7-2 Measured C_P distributions for the different vortex generator and leading edge roughness configurations compared with smooth measurement, $Re = 1.6 \times 10^6$, α around $14.4°$ corresponding to C_{Lmax}.

Figure 7-3 Measured C_L curves for the different vortex generator and leading edge roughness configurations compared with smooth measurement, Re = 1.6×10^6.

Figure 7-4 Measured C_D curves for the different vortex generator and leading edge roughness configurations compared with smooth measurement, Re = 1.6×10^6.

Figure 7-5 Measured C_L-C_D curves for the different vortex generator and leading edge roughness configurations compared with smooth measurement, $Re = 1.6\times10^6$.

Figure 7-6 Measured C_M curves for the different vortex generator and leading edge roughness configurations compared with smooth measurement, $Re = 1.6\times10^6$.

8 FFA-W3-241 Dynamic stall

This chapter presents dynamic inflow measurements for the FFA-W3-241 airfoil. The following reduced frequencies and amplitudes were measured:

- Smooth flow, $k = 0.093$, $1.4^o < A < 2.0^o$.
- Smooth flow, $k = 0.070$, $1.4^o < A < 2.0^o$.
- Delft vortex generators, $h = 6$ mm at $x/c = 0.2$, $k = 0.093$, $1.4^o < A < 2.0^o$.

The vortex generators are described in Section 3.2. The different measurements are shown in more detail in Appendix D. The different types of available measurements are shown in Appendix A.

There is a time lag between a change in the angle of attack and a change in the aerodynamic loading on the airfoil because of the travel time of the vortices that are shed from the airfoil surface. In case of a harmonic variation in the pitch angle, the time lag causes hysteresis loops for the aerodynamic coefficients. The shapes and the slopes of the hysteresis loops are important in the development dynamic stall models.

The shape and slope of the hysteresis loops vary with the amplitude and the reduced frequency of the harmonic motion. To obtain an averaged hysteresis loop, the angle of attack is sorted into 30 bins of a phase angle, which runs from 0 to 2π in each loop, as explained in [1].

The directions of the hysteresis loops are determined and in the Figures, arrows indicate whether the loops are clockwise or counter clockwise. An arrow from left to right means clockwise whereas an arrow from right to left means anti clockwise. In case of a crossover point two arrows are shown. Because of the unsteady flow, the wake rake could not be used to obtain C_D and this was in stead based only on the C_P distribution, which means that C_D does not include skin friction and is too low, which is especially important at low angles of attack. The amplitudes of the loops are not similar because they are influenced by the wind tunnel corrections since the angle of attack depends on C_L, Section 2.3.

The measurements were not compared with numerical calculations but the derived hysteresis loops were compared with the static mean curves.

Figure 8-1 shows the measured C_L, C_D and C_M hysterersis loops for $k = 0.093$, $1.4° < A < 2.0$ compared with the static curves. The mean values of the loops compare well with the static curves.

At angles of attack below 8° all C_L loops are counter clockwise whereas they are clockwise above 8°. At low angles of attack, the C_L loops are narrow and their slopes tend to follow the static curve. At maximum C_L, the C_L loops open and their slopes are steeper than the corresponding slope of the static curve. At high angles of attack in post stall, the slopes of the C_L loops become horizontal.

The C_D loops for angles of attack below 10° and angles of attack above 15° are clockwise whereas the remaining C_D loops are counterclockwise. Crossover points are seen at both 10° and 15°. The slopes of the C_D loops at low angles of attack follow the static curve. At maximum C_L, the slope of the static curve is steeper than the slope of the corresponding C_D loop. At high angles of attack in post stall, the slopes of the C_D loops are steeper than the static curve.

The C_M loops are counter clockwise at low and high angles of attack and clockwise between 11° and 15°. At low angles of attack the slope of the C_M loops follow the static curve, but at high angles of attack the C_M loops have steeper slopes compared with the measurements.

Figure 8-2 shows the measured C_L, C_D and C_M hysterersis loops compared with the static curves for $k = 0.070$, $1.4° < A < 2.0$. In general the loops correspond to Figure 8-1 except for the C_D loops that are not in good agreement with the static curve. This is caused by drift in the calibration of the flow free stream total pressure since C_D from the C_P distribution is relatively sensitive to the calibration compared with C_L.

Figure 8-3 shows the measured C_L, C_D and C_M hysteresis loops compared with the static curves for $h = 6$ mm, $x/c = 0.2$ VG configuration, $k = 0.093$, $1.4° < A < 2.0$. The mean values of the loops compare well with the static curves. At angles above 10° the C_L loops are clockwise. Until maximum C_L, the slopes of the loops follow the static curve. All C_D loops are clockwise whereas all C_M loops are anti clockwise.

In summary the measurements showed that hysteresis loops for C_L, C_D and C_M could be derived and the slopes of the loops tend to follow the static curve at low angles of attack, but are steeper than the slope of the static curve at high angles of attack. The directions of the loops for C_L are counter clockwise at low angles of attack and clockwise at maximum C_L and in the post stall area. This corresponds well with the literature. The hysteresis loops for the VG configuration behave similar to the smooth flow configurations except for differences in the direction between 10° and 15°.
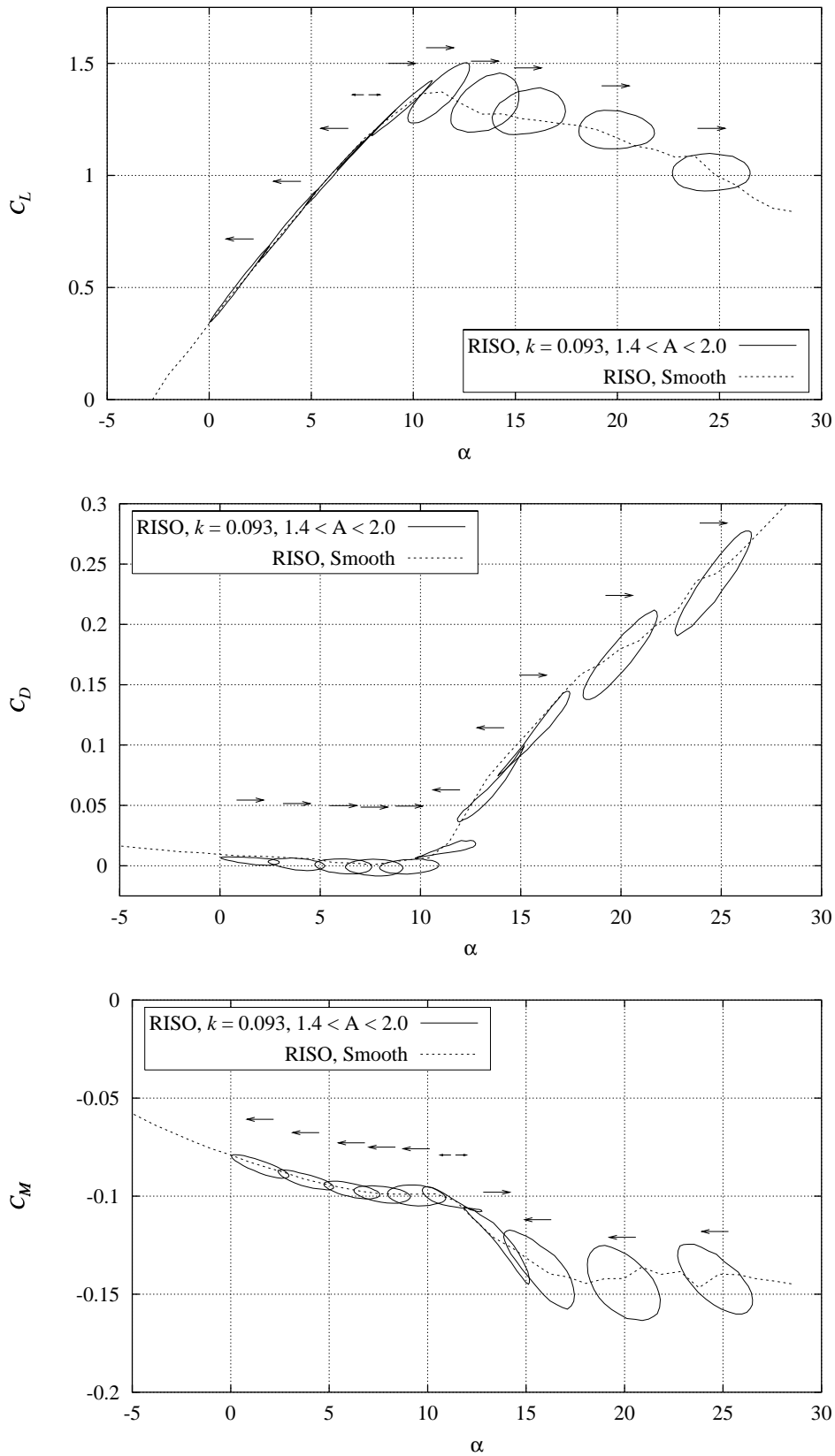
Figure 8-1 Measured C_L, C_D and C_M hysteresis loops compared with mean curves for steady smooth leading edge flow at k = 0.093, A between 1.4° and 2°, Re = 1.6×10^6 (FFAW3241PITCH091297V1).
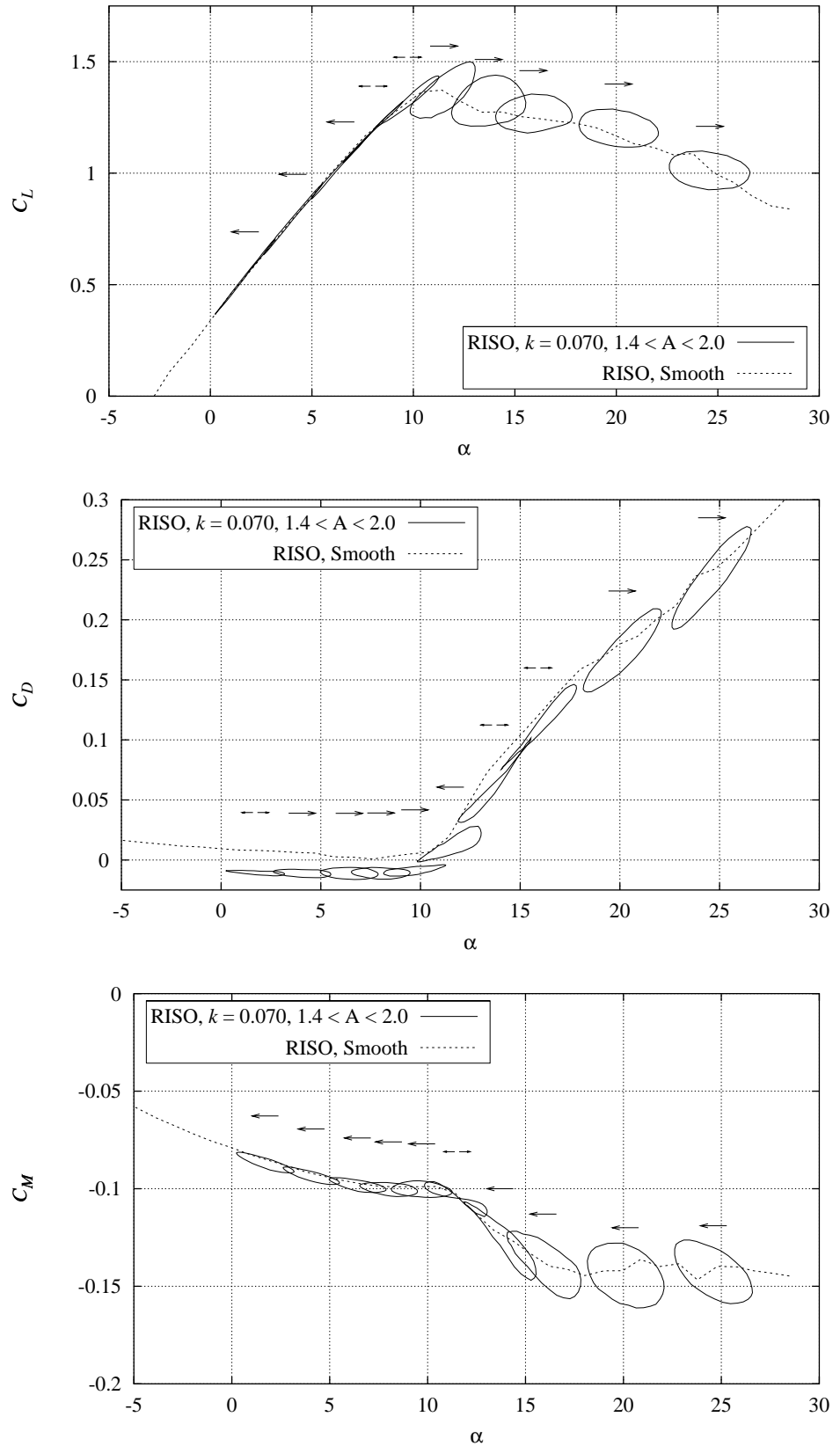
Figure 8-2 Measured C_L, C_D and C_M hysteresis loops compared with mean curves for steady smooth leading edge flow at k = 0.070, A between 1.4° and 2.0°, Re = 1.6×10⁶ (FFAW3241PITCH091297V2).
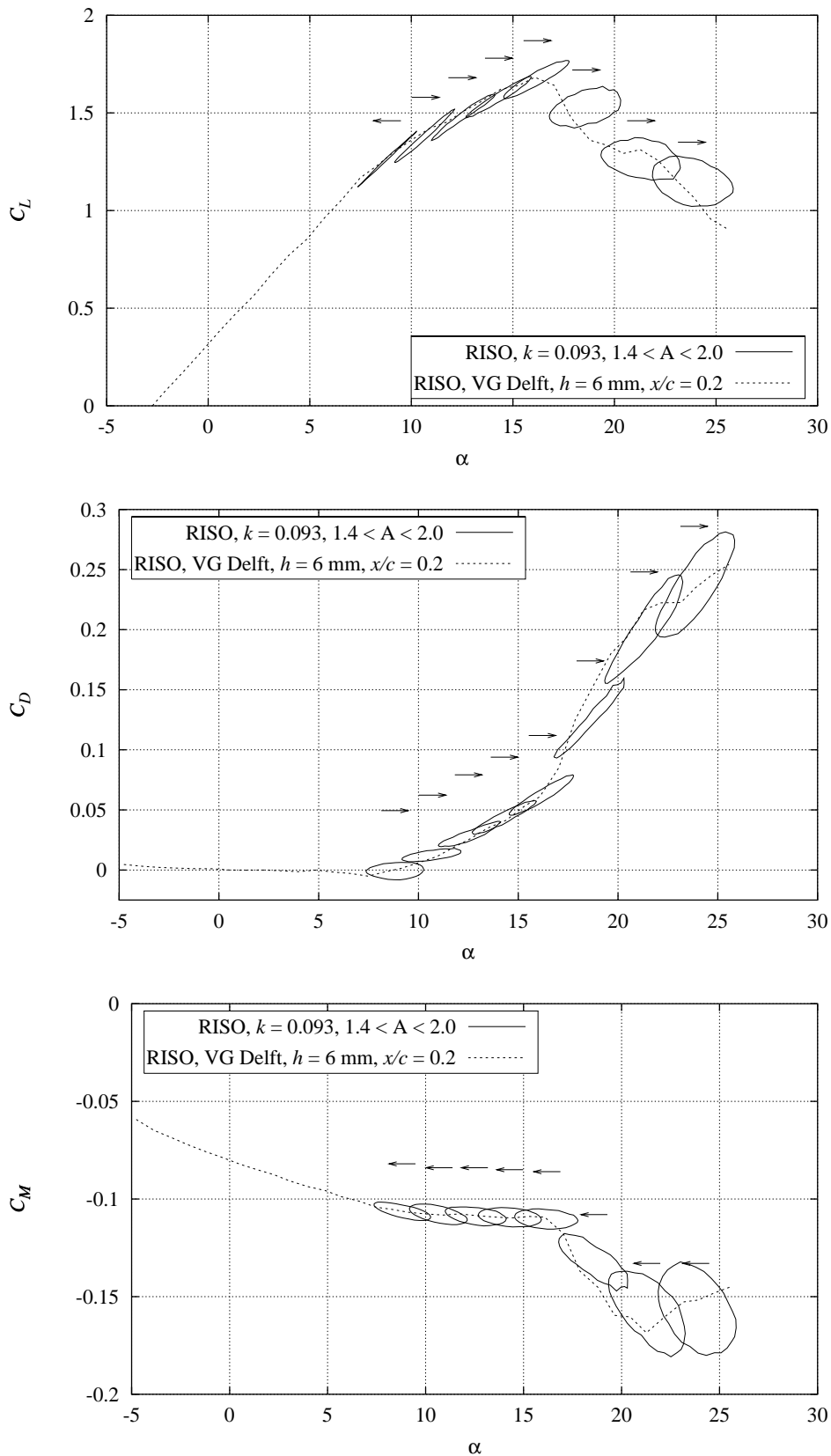
Figure 8-3 Measured C_L, C_D and C_M hysteresis loops compared with mean curve for steady flow with Delft vortex generators, h = 6 mm, x/c = 0.2 at k = 0.093, A between 1.4° and 2.0°, Re = 1.6×10^6 (FFAW3241PITCH091297V3).

9 FFA-W3-301 Smooth leading edge

This chapter reports steady inflow measurements for the FFA-W3-301 airfoil with smooth leading edge.

The measurements were compared with numerical calculations from XFOIL and EllipSys2D as in Chapter 4.

The different types of available measurements are described in Appendix A.

Figure 9-1 shows C_P distributions at different angles of attack. The flow is attached until 11.2° where C_P is reduced at the trailing edge. The minimum C_P is –3 and this is maintained from 14.6° until 27.7°.

Figure 9-2 shows the C_P distribution at 4.2° compared with XFOIL and EllipSys2D calculations and Figure 9-3 shows the C_P distribution at 14.6°.

At 4.2° the agreement is in general good. The shape of the measured C_P curve at the leading edge is not so smooth as in the calculations and the calculations underestimate C_P on the front part of the suction side. Furthermore the transition point can not be found in the measurement.

At 14.6° the agreement is not good. The suction side C_P is lower in the calculations than in the measurement. In the measurements, the suction side flow is separated from the trailing edge, which is not the case in the calculations. The pressure side C_P distributions are in fair agreement.

Figure 9-4 to Figure 9-7 show the measured C_L, C_D and C_M curves compared with XFOIL and EllipSys2D calculations.

The slopes of C_L at low angles of attack for the measurement agree well with the calculations but there is a difference in the zero C_L angle of attack. The measured maximum C_L is 1.30 at 16° and this is significantly overestimated by both calculations. The measured minimum C_D of 0.015 is higher than both calculations and this together with lower maximum C_L results in lower measured C_L/C_D ratios. C_M is not in good agreement since there is a difference in the level of C_M at low angles of attack and a difference in the slope of C_M at angles of attack above 10°.

In summary the agreement between measurements and calculations is fair for the overall shape of the C_P distribution at low angles of attack. However the agreement is not good for C_L, C_D and C_M. The calculations predict the slope of C_L at low angles of attack well but maximum C_L is overestimated and minimum C_D is underestimated.
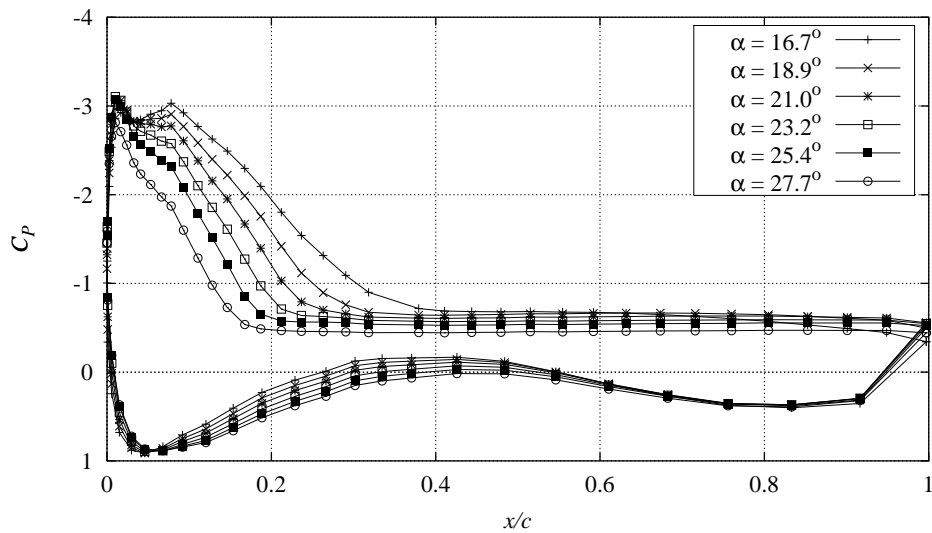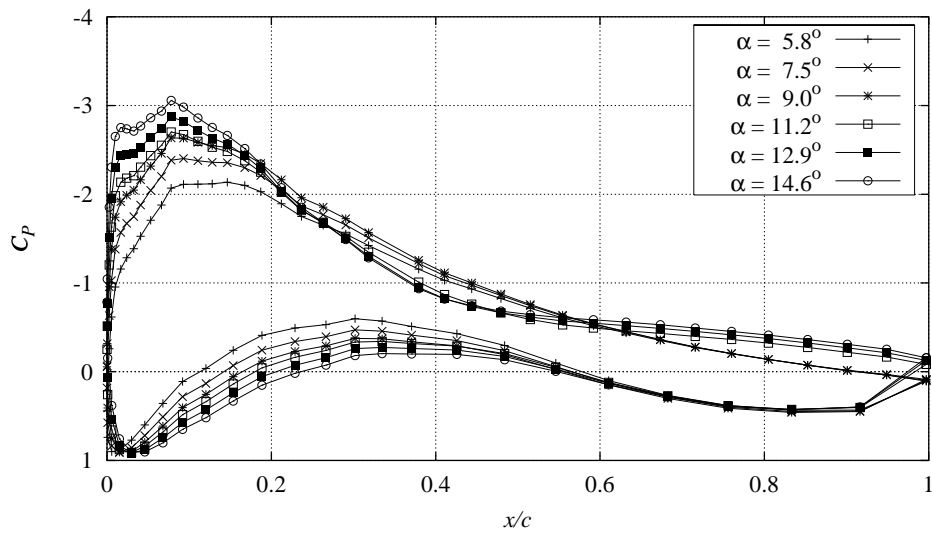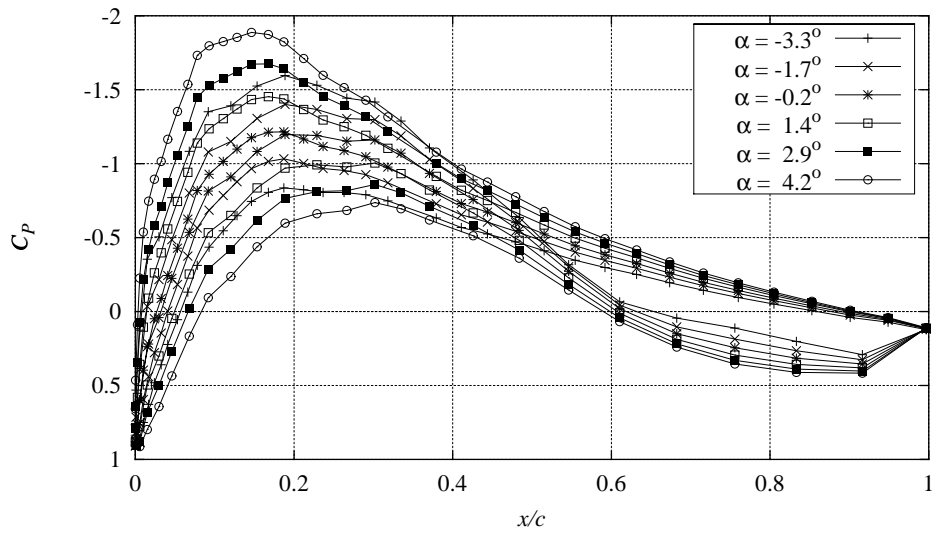
Figure 9-1 Measured C_P distributions at different angles of attack (FFAW3301STEP091297V1).
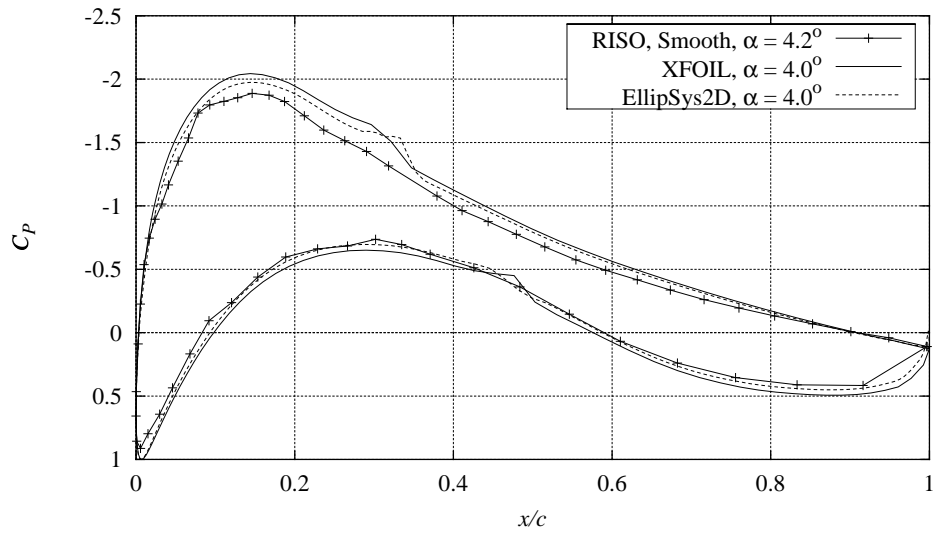
Figure 9-2 Measured C_P distribution compared with XFOIL and Ellipsys2D calculations, $Re = 1.6 \times 10^6$, $\alpha = 4.2°$ (FFAW3301STEP091297V1)
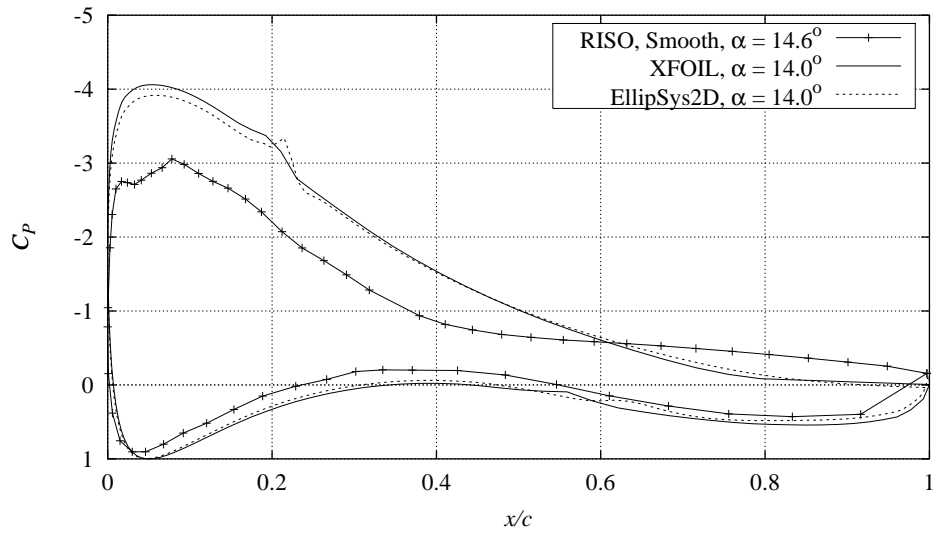
Figure 9-3 Measured C_P distribution compared with XFOIL and Ellipsys2D calculations, $Re = 1.6 \times 10^6$, $\alpha = 14.6°$ (FFAW3301STEP091297V1).
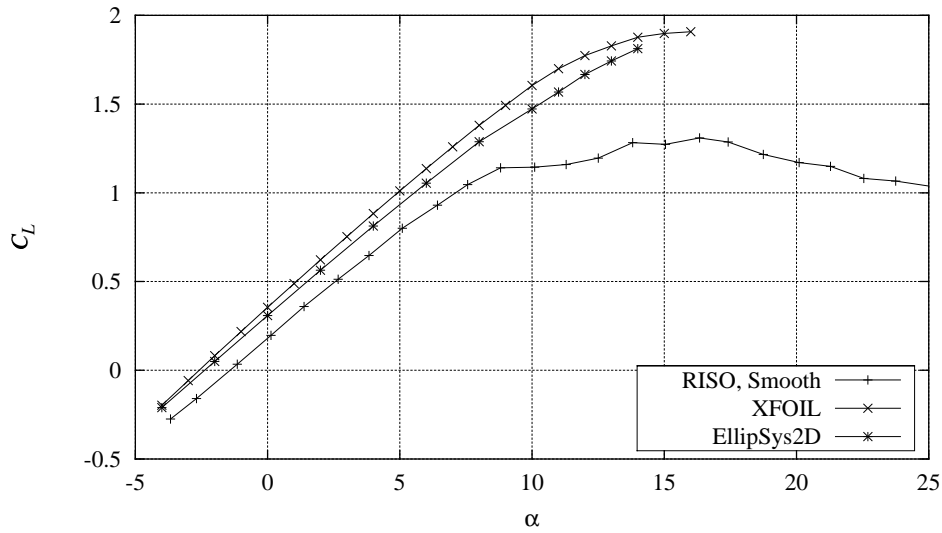
Figure 9-4 Measured C_L curve compared with XFOIL calculations with free transition and EllipSys2D calculations with free transition, Re = 1.6×10^6 (FFAW3301CONT091297V4).
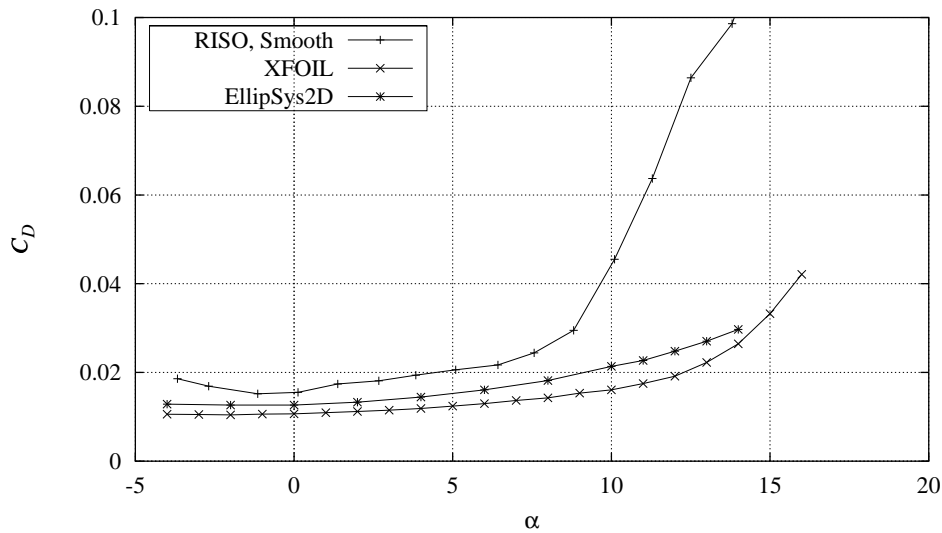
Figure 9-5 Measured C_D curve compared with XFOIL calculations with free transition and EllipSys2D calculations with free transition, Re = 1.6×10^6 (FFAW3301CONT091297V4).
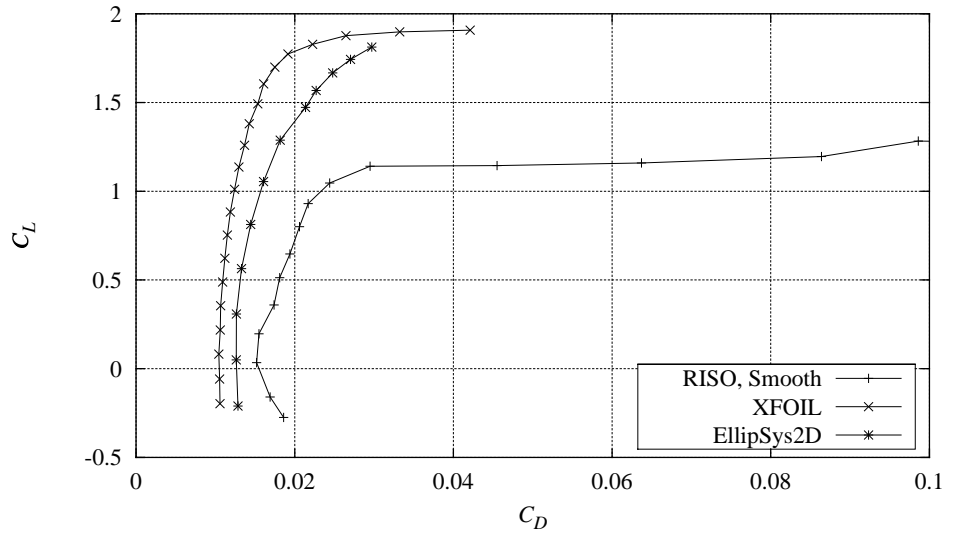
Figure 9-6 Measured C_L-C_D curve compared with XFOIL calculations with free transition and EllipSys2D calculations with free transition, Re = 1.6×10⁶ (FFAW3301CONT091297V4).
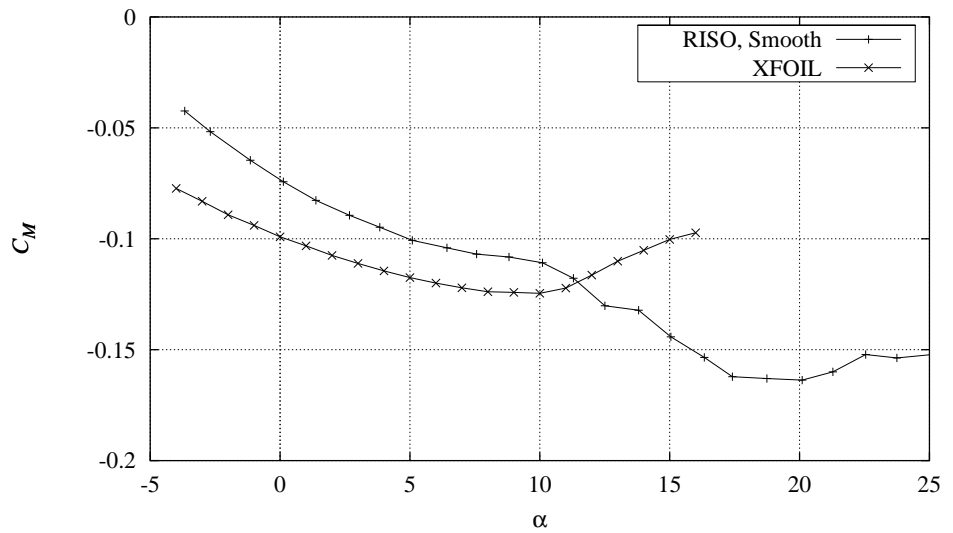
Figure 9-7 Measured C_M curve compared with XFOIL calculations with free transition, Re = 1.6×10⁶ (FFAW3301CONT091297V4).

10 FFA-W3-301 Vortex generators

This chapter presents steady inflow measurements for the FFA-W3-301 airfoil with the following different configurations of vortex generators:

- Delft vortex generators, $h = 6$ mm at $x/c = 0.2$.
- Delft vortex generators, $h = 6$ mm at $x/c = 0.3$.

The vortex generators are described in Section 3.2 and the different measurements are shown in more detail in Appendix F. The different types of available measurements are described in Appendix A.

The measurements were not compared with numerical calculations since the influence from VGs could not be modelled in the numerical codes. The measurements were instead compared to the smooth flow measurements.

Figure 10-1 shows the C_P distributions at 9.4° for the different VG configurations compared with smooth flow and Figure 10-2 shows the C_P distributions corresponding to maximum C_L.

For low angles of attack, the differences in C_P are small, but for the angles of attack corresponding to maximum C_L, the minimum C_P is lower for the VG configurations. Minimum C_P is lower for the $h = 6$ mm, $x/c = 0.2$ configuration compared with the $h = 6$ mm, $x/c = 0.3$ configuration.

Figure 10-3 to Figure 10-6 show the C_L, C_D and C_M curves for the VG configurations compared with smooth flow.

Maximum C_L is increased and delayed to higher angles of attack for both VG configurations compared to smooth flow and the $h = 6$ mm, $x/c = 0.20$ configuration is best, since it results in the highest maximum C_L of 1.64. Both VG configurations have similar C_D, which is higher compared with smooth flow. Because separation is delayed to higher angles of attack, C_D is lower above 9° until the angle of attack for maximum C_L.

In summary the measurements agree with the results from Chapter 5 and showed that the VGs do not influence the C_P distribution at low angles of attack but minimum C_P is reduced at high angles of attack around maximum C_L. For this airfoil the VGs should be located in $x/c = 0.2$ to achieve the highest maximum C_L and the highest C_L/C_D ratio.
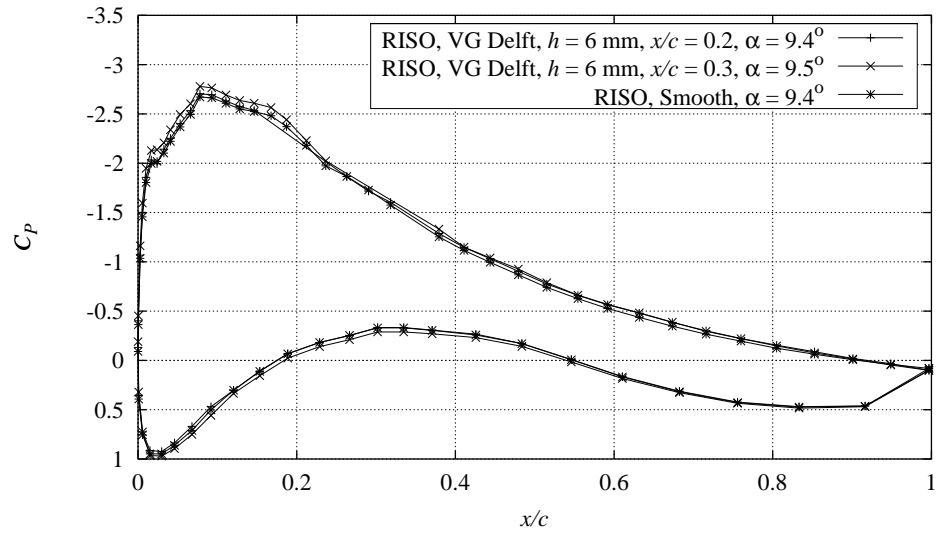
Figure 10-1 Measured C_P distributions for the different vortex generator configurations compared with smooth measurement, Re = 1.6×10^6, α around 9.4° corresponding to C_{Lmax} for smooth leading edge flow.
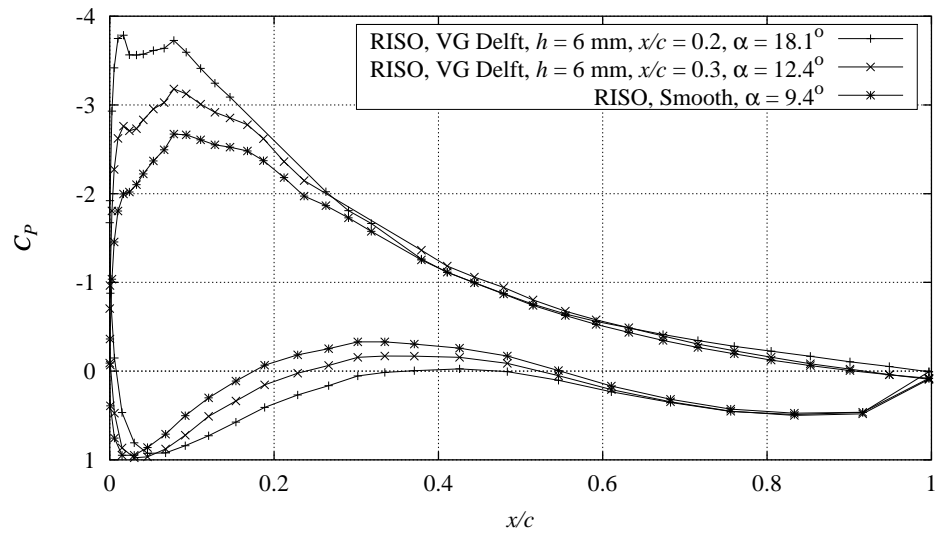
Figure 10-2 Measured C_P distributions for the different vortex generator configurations compared with smooth measurement, Re = 1.6×10^6, α corresponding to C_{Lmax}.
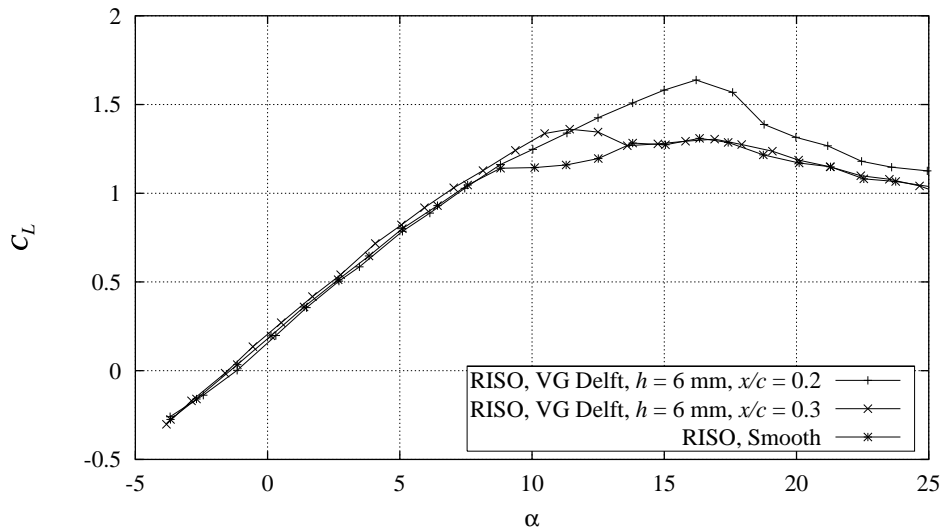
Figure 10-3 Measured C_L curves for the different vortex generator configurations compared with smooth measurement, Re = 1.6×10^6.
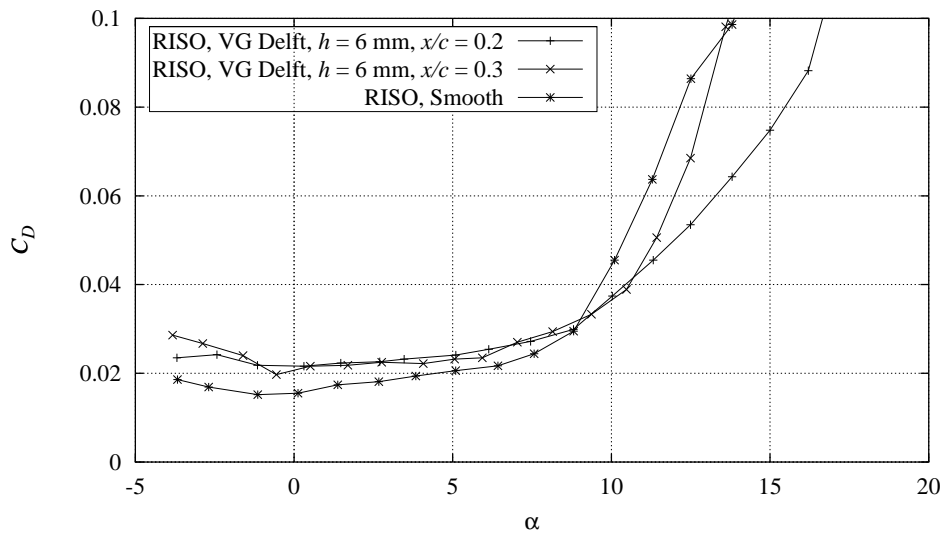
Figure 10-4 Measured C_D curves for the different vortex generator configurations compared with smooth measurement, Re = 1.6×10^6.
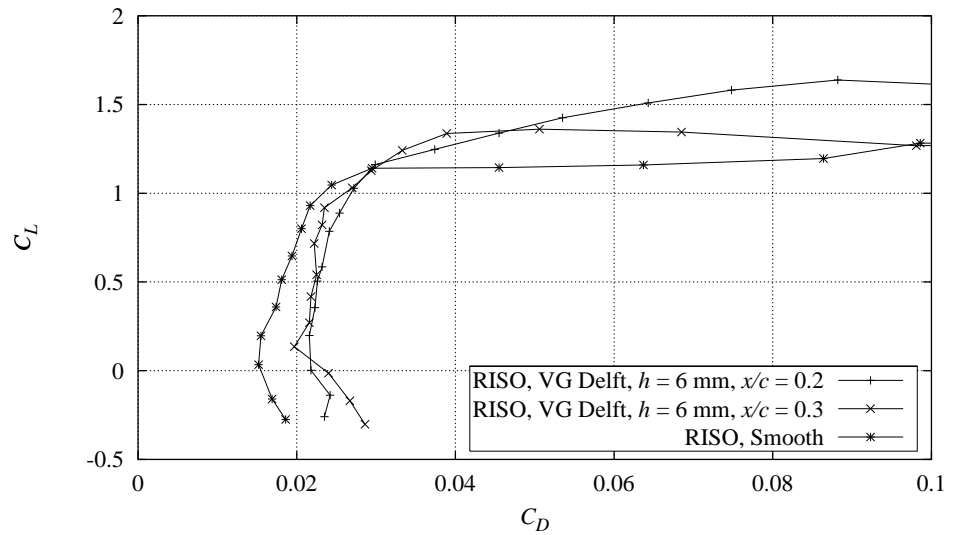
Figure 10-5 Measured C_L-C_D curves for the different vortex generator configurations compared with smooth measurement, Re = 1.6×10⁶.
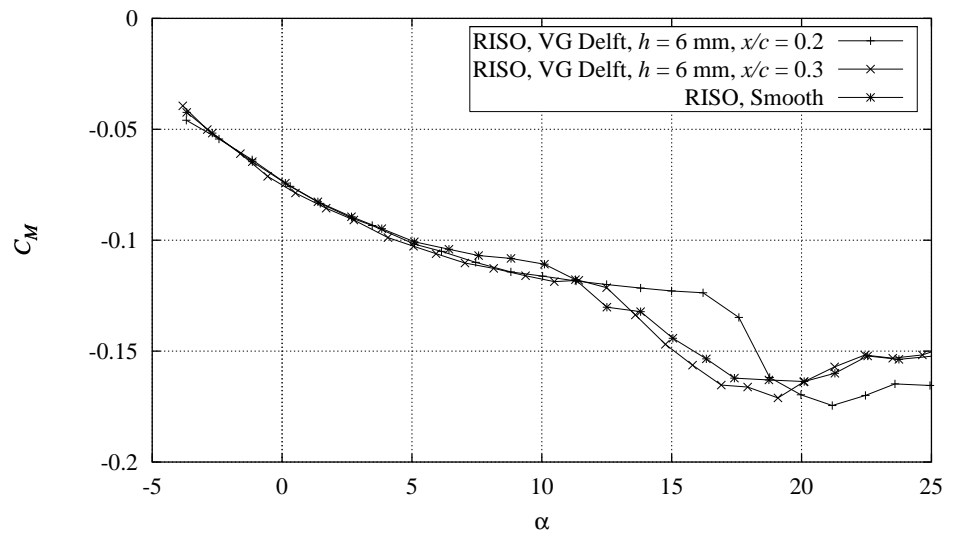
Figure 10-6 Measured C_M curves for the different vortex generator configurations compared with smooth measurement, Re = 1.6×10⁶.

11 FFA-W3-301 Leading edge roughness

This chapter presents steady inflow measurements for the FFA-W3-301 airfoil with the leading edge roughness configuration: 90° zigzag trip tape.

The leading edge roughness configurations are described in Section 3.3. The different types of available measurements are described in Appendix A.

The measurements were compared with numerical calculations. The XFOIL code was used and prescribing the transition location to be at the leading edge: $x/c = 0.01$ on the suction side and $x/c = 0.10$ on the pressure side simulated leading edge roughness. The Ellipsys2D Navier-Stokes code was used and having turbulent flow on the entire airfoil simulated leading edge roughness as in Chapter 6. The measurements were also compared with the smooth flow measurement.

Figure 11-1 shows the C_P distribution at 6° compared with smooth flow and XFOIL and EllipSys2D calculations and Figure 11-2 shows the C_P distribution at 9.9°.

The LER configuration has higher C_P on the suction side compared to smooth flow, whereas the pressure side C_P distributions are in good agreement with both smooth flow and the calculations. At 9.9° the trailing edge flow is separated for the LER configuration, but attached for the smooth flow measurement. Both calculations overestimate minimum C_P to be lower than for both the LER configuration measurement and the smooth flow measurement.

Figure 11-3 to Figure 11-6 show the C_L, C_D and C_M curves for the LER configuration compared with smooth flow and XFOIL and EllipSys2D calculations.

At angles of attack below 0° the C_L curve slopes for the LER configuration and for both calculations are lower than at higher angles of attack. This is caused by separation on the pressure side. Maximum C_L is reduced for the LER configuration compared to smooth flow and appears at 7°. Minimum C_D for the LER configuration is increased compared with smooth flow and separation occurs from 7°. C_D at very low angle of attack is not measured accurately by the wake rake because of the separation of the pressure side. Both calculations overestimate maximum C_L and underestimate minimum C_D.

In summary the measurements agree with the results of Chapter 6 and show that LER reduces maximum C_L and increases minimum C_D. For this airfoil the pressure side flow is separated at very low angles of attack.
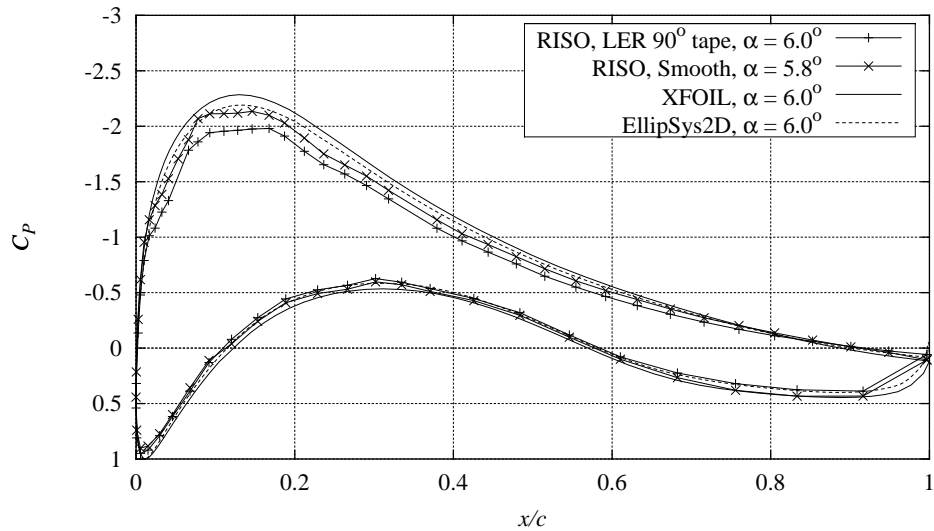
Figure 11-1 Measured C_P distribution for 90° zigzag trip tape compared with smooth measurement and XFOIL (LE transition) and EllipSys2D (turbulent) calculations, Re = 1.6×10^{6}, α = 6.0°(FFAW3301CONT091297V3).
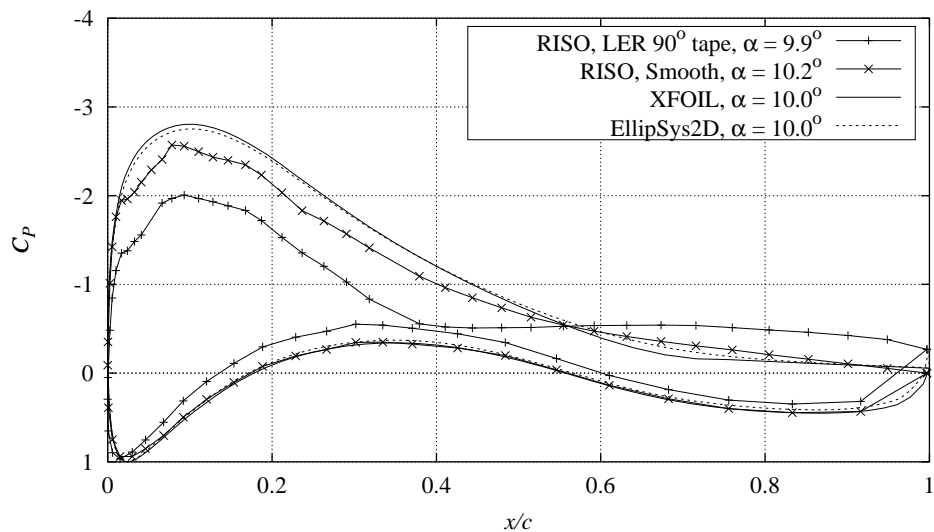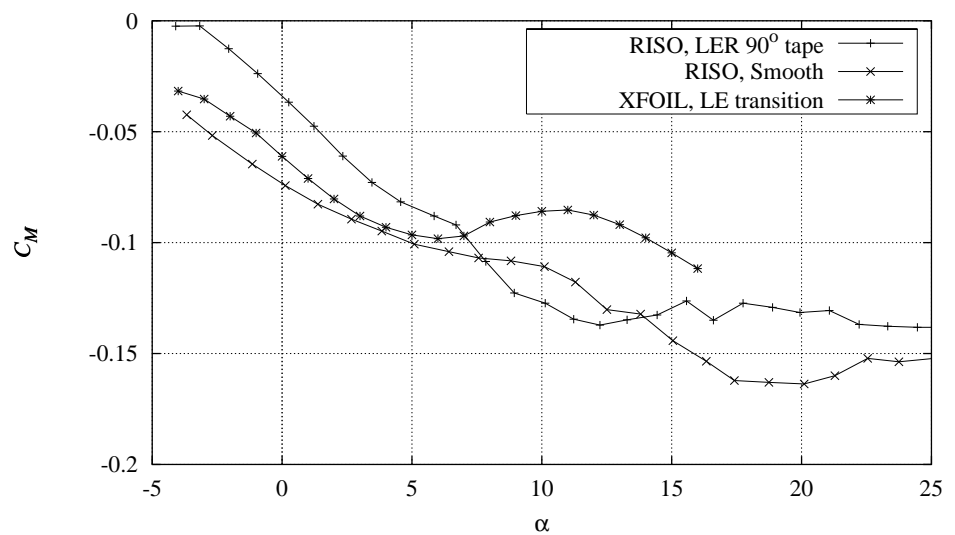

Figure 11-2 Measured C_P distribution for 90° zigzag trip tape compared with smooth measurement and XFOIL (LE transition) and EllipSys2D (turbulent) calculations, Re = 1.6×10^{6}, α = 9.9°(FFAW3301CONT091297V3).
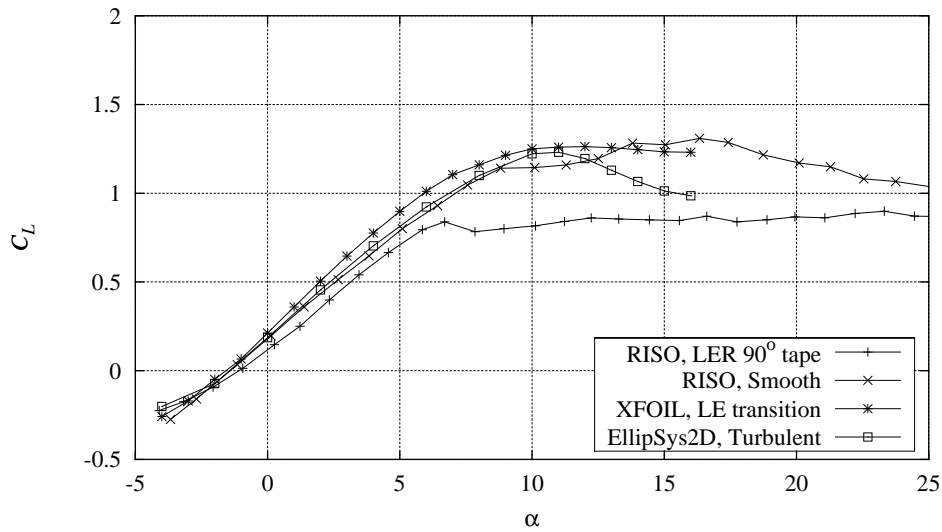
Figure 11-3 Measured C_L curve for 90° zigzag trip tape compared with smooth measurement and XFOIL (LE transition) and EllipSys2D (turbulent) calculations, Re = 1.6×10⁶ (FFAW3301CONT091297V3).
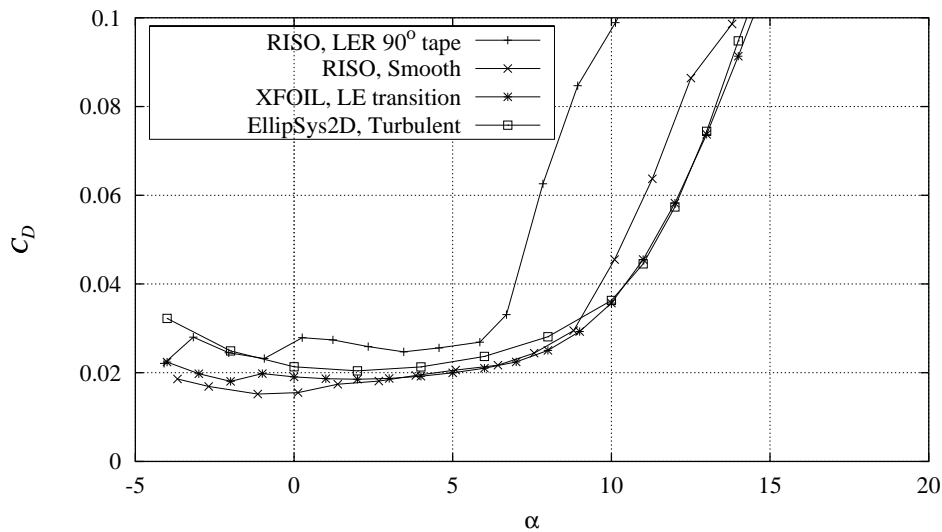
Figure 11-4 Measured C_D curve for 90° zigzag trip tape compared with smooth measurement and XFOIL (LE transition) and EllipSys2D (turbulent) calculations, Re = 1.6×10⁶ (FFAW3301CONT091297V3).
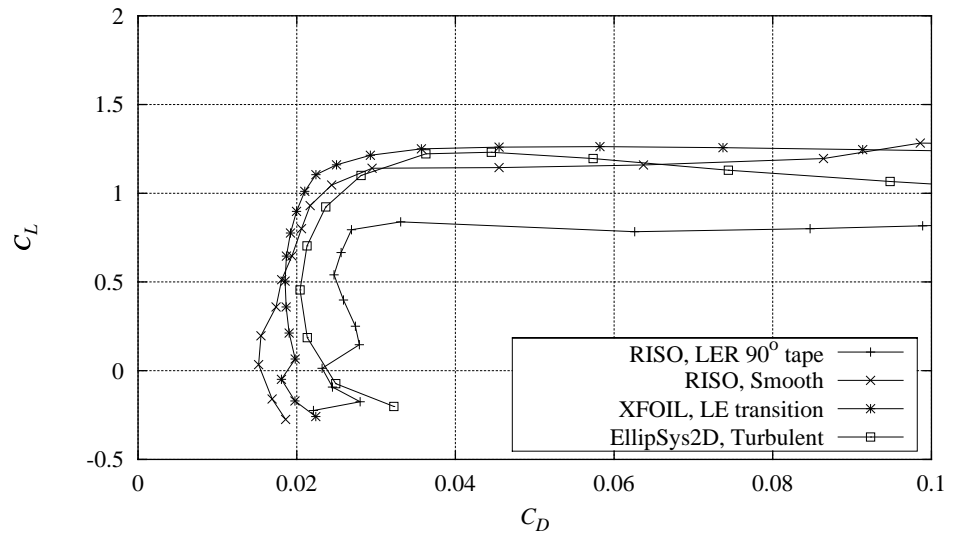
Figure 11-5 Measured C_L-C_D curve for 90° zigzag trip tape compared with smooth measurement and XFOIL (LE transition) and EllipSys2D (turbulent) calculations, Re = 1.6×10^{6} (FFAW3301CONT091297V3).

Figure 11-6 Measured C_M curve for 90° zigzag trip tape compared with smooth measurement and XFOIL (LE transition) calculations, Re = 1.6×10^{6} (FFAW3301CONT091297V3).

12 FFA-W3-301 Vortex generators and leading edge roughness

This chapter presents steady inflow measurements for the FFA-W3-301 airfoil with vortex generators and leading edge roughness configuration: Delft vortex generators, $h = 6$ mm at $x/c = 0.3$ and 90° zigzag trip tape.

The vortex generators are described in Section 3.2 and the leading edge roughness configurations are described in Section 3.3. The different types of available measurements are described in Appendix A.

The measurements were not compared with numerical calculations but to measurements of the corresponding VG configuration, measurements of the corresponding LER configuration and smooth flow measurements.

Figure 12-1 shows the C_P curve for the VGLER configuration compared with the VG configuration, the LER configuration and smooth flow around 6° and Figure 12-2 shows the C_P curves around 10°.

For 6° the agreement between the VGLER configuration and the LER configuration is good. The VG configuration and the smooth flow measurement have slightly lower minimum C_P compared with the LER and VGLER configurations. At 10° the LER configuration has higher suction C_P and a larger extent of separated flow compared with the other configurations.

Figure 12-3 to 12 6 show the C_L, C_D and C_M curves for the VGLER configuration compared with the VG configuration, the LER configuration and smooth flow.

The C_L curve slope at very low angles of attack is reduced for the VGLER and LER configurations because of pressure side separation. Maximum C_L of 1 appears at 9° for the VGLER configuration, which is higher than the LER configuration but below smooth flow and the VG configuration. Minimum C_D is increased for the VGLER configuration compared with the other configurations and the rise in C_D from separation occurs already at 6.5°.

In summary the measurement showed that the VGLER configuration had lower maximum C_L and higher minimum C_D compared with smooth flow. The increase in maximum C_L from VGs could not counterbalance the reduction from LER.
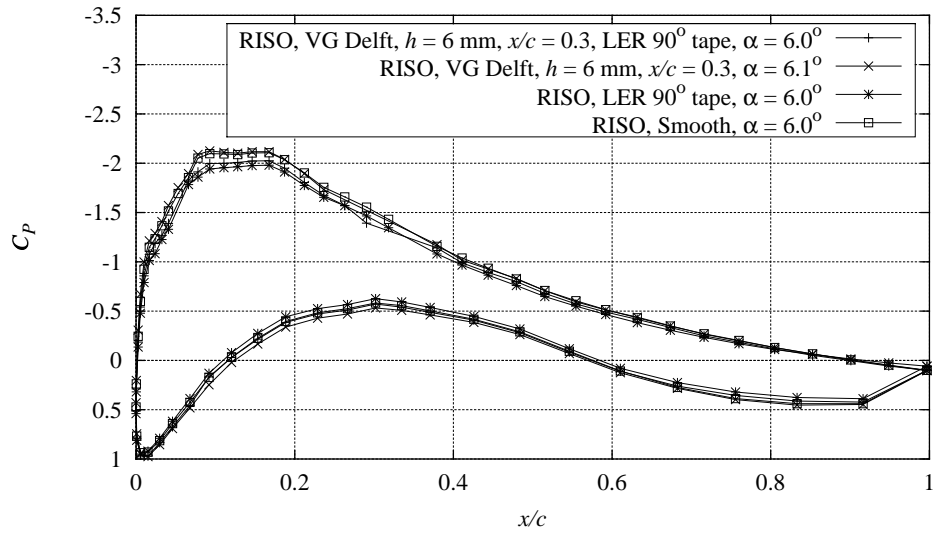
Figure 12-1 Measured C_P distributions with combinations of Delft vortex generators, h = 6 mm, x/c = 0.3, and 90° zigzag trip tape compared with smooth measurement, Re = 1.6×10^6, α = 6.0°(FFAW3301CONT091297V2).
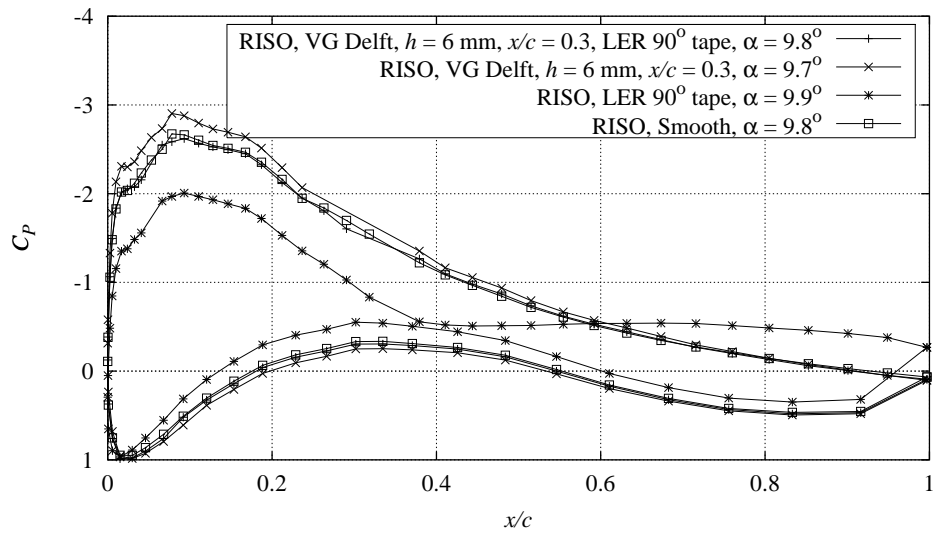
Figure 12-2 Measured C_P distributions with combinations of Delft vortex generators, h = 6 mm, x/c = 0.3, and 90° zigzag trip tape compared with smooth measurement, Re = 1.6×10^6, α = 9.8°(FFAW3301CONT091297V2).
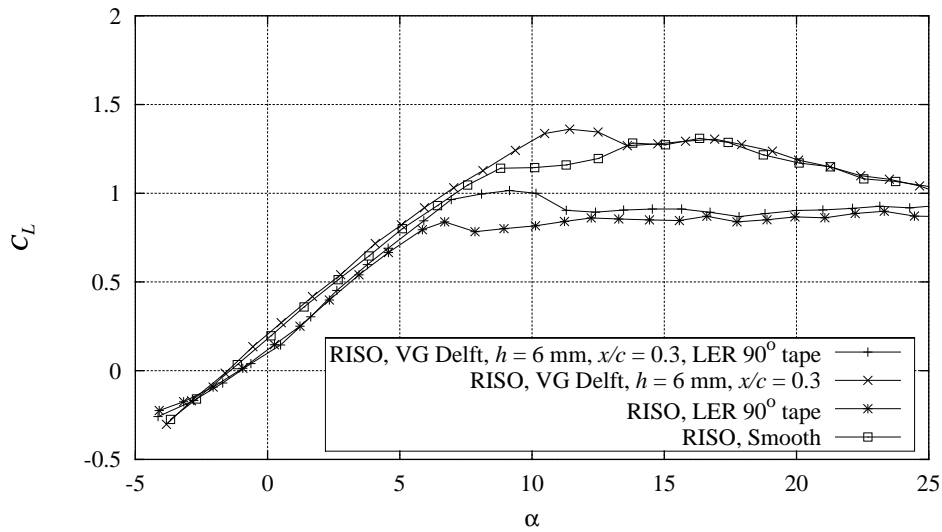
Figure 12-3 Measured C_L curves with combinations of Delft vortex generators, h = 6 mm, x/c = 0.3, and 90° zigzag trip tape compared with smooth measurement, Re = 1.6×10⁶ (FFAW3301CONT091297V2).
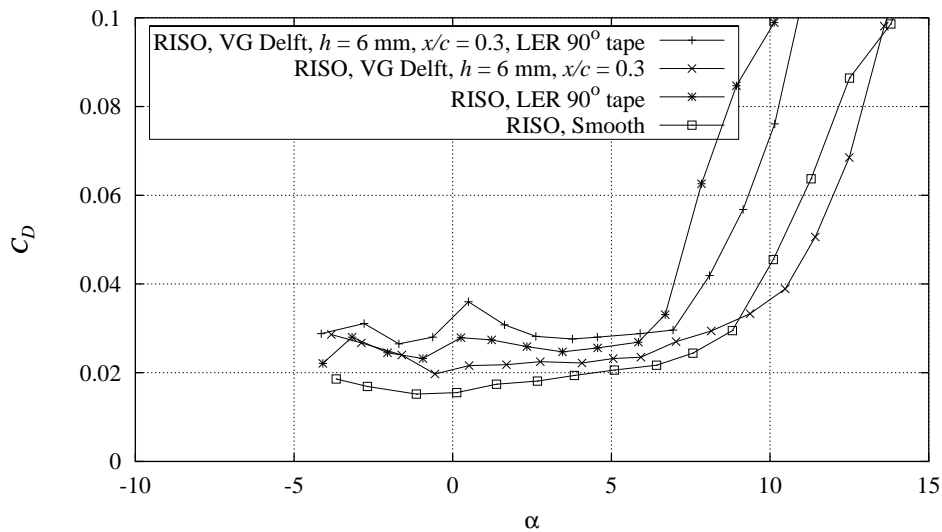
Figure 12-4 Measured C_D curves with combinations of Delft vortex generators, h = 6 mm, x/c = 0.3, and 90° zigzag trip tape compared with smooth measurement, Re = 1.6×10⁶ (FFAW3301CONT091297V2).
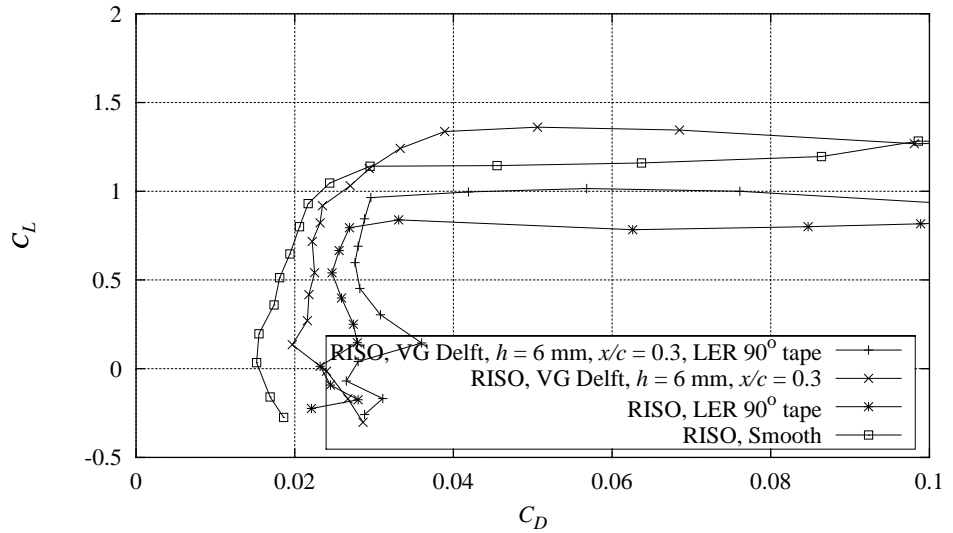
Figure 12-5 Measured C_L-C_D curves with combinations of Delft vortex generators, $h = 6$ mm, $x/c = 0.3$, and $90°$ zigzag trip tape compared with smooth measurement, Re = $1.6×10^6$ (FFAW3301CONT091297V2).
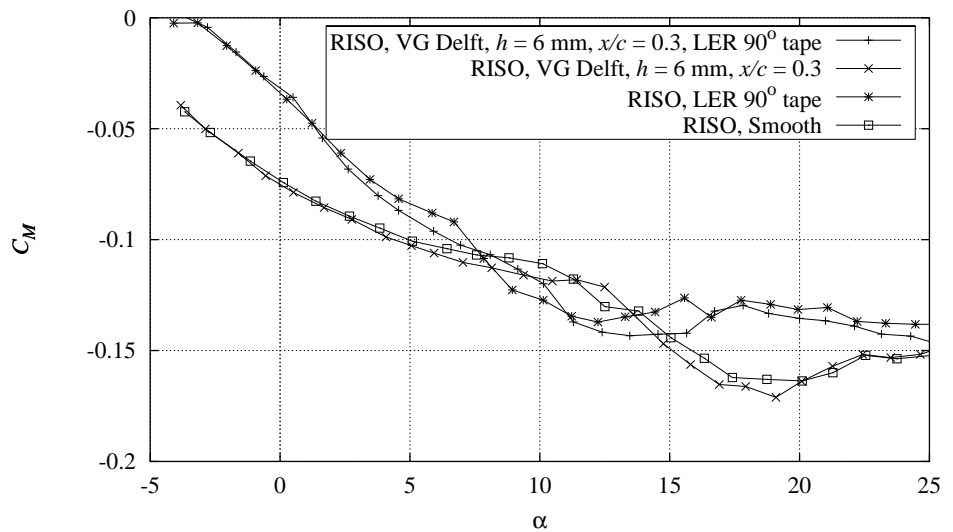
Figure 12-6 Measured C_M curves with combinations of Delft vortex generators, $h = 6$ mm, $x/c = 0.3$, and $90°$ zigzag trip tape compared with smooth measurement, Re = $1.6×10^6$ (FFAW3301CONT091297V2).

13 FFA-W3-301 Dynamic stall

This chapter presents dynamic inflow measurements for the FFA-W3-301 airfoil. The following reduced frequencies and amplitudes were measured:

- Smooth flow, $k = 0.093$, $1.4^o < A < 2.0^o$.
- Smooth flow, $k = 0.070$, $1.4^o < A < 2.0^o$.

The different measurements are shown in more detail in Appendix G. The different types of available measurements are shown in Appendix A.

The derivation of the hysteresis loops is explained in Chapter 8 and in [1].

The measurements were not compared with numerical calculations but the derived hysteresis loops were compared with the static mean curves.

Figure 13-1 shows the measured C_L, C_D and C_M hysteresis loops for $k = 0.093$, $1.4° < A < 2.0°$ compared with the static curves.

The mean values of the C_D and C_M loops are not in good agreement with the static curves. This is caused by drift of the calibration and will not influence the shape of the hysteresis loops. For C_L the loops are counter clockwise below 8° and clockwise above 8°. The C_D loops are all clockwise and the C_M loops are all counter clockwise. At low angles of attack, the slopes of the loops tend to follow the slope of the static curves. At higher angles of attack the slopes of the loops are steeper compared with the slope of the static curve.

Figure 13-2 shows the measured C_L, C_D and C_M hysteresis loops compared with the static curves for $k = 0.070$, $1.4° < A < 2.0°$. In general the loops correspond to Figure 13-1.

In summary the measurements showed the derived hysteresis loops for C_L, C_D and C_M. The behavior of the hysteresis loops was found similar to Chapter 8 and is in good agreement with the literature.
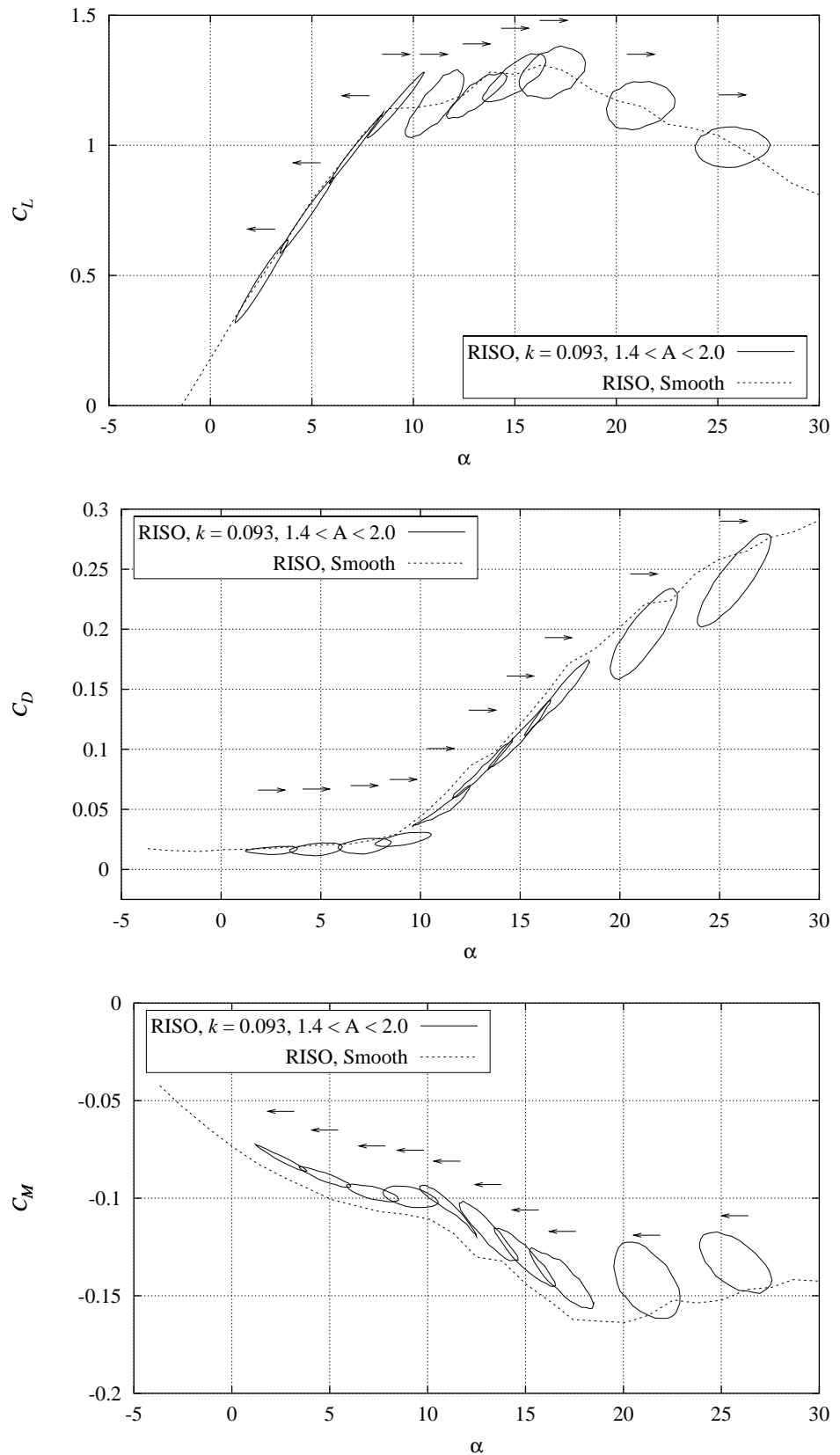
Figure 13-1 Measured C_L, C_D and C_M hysteresis loops compared with mean curves for steady smooth leading edge flow at k = 0.093, A between 1.3° and 1.9°, Re = 1.6×10⁶ (FFAW3301PITCH091297V1).
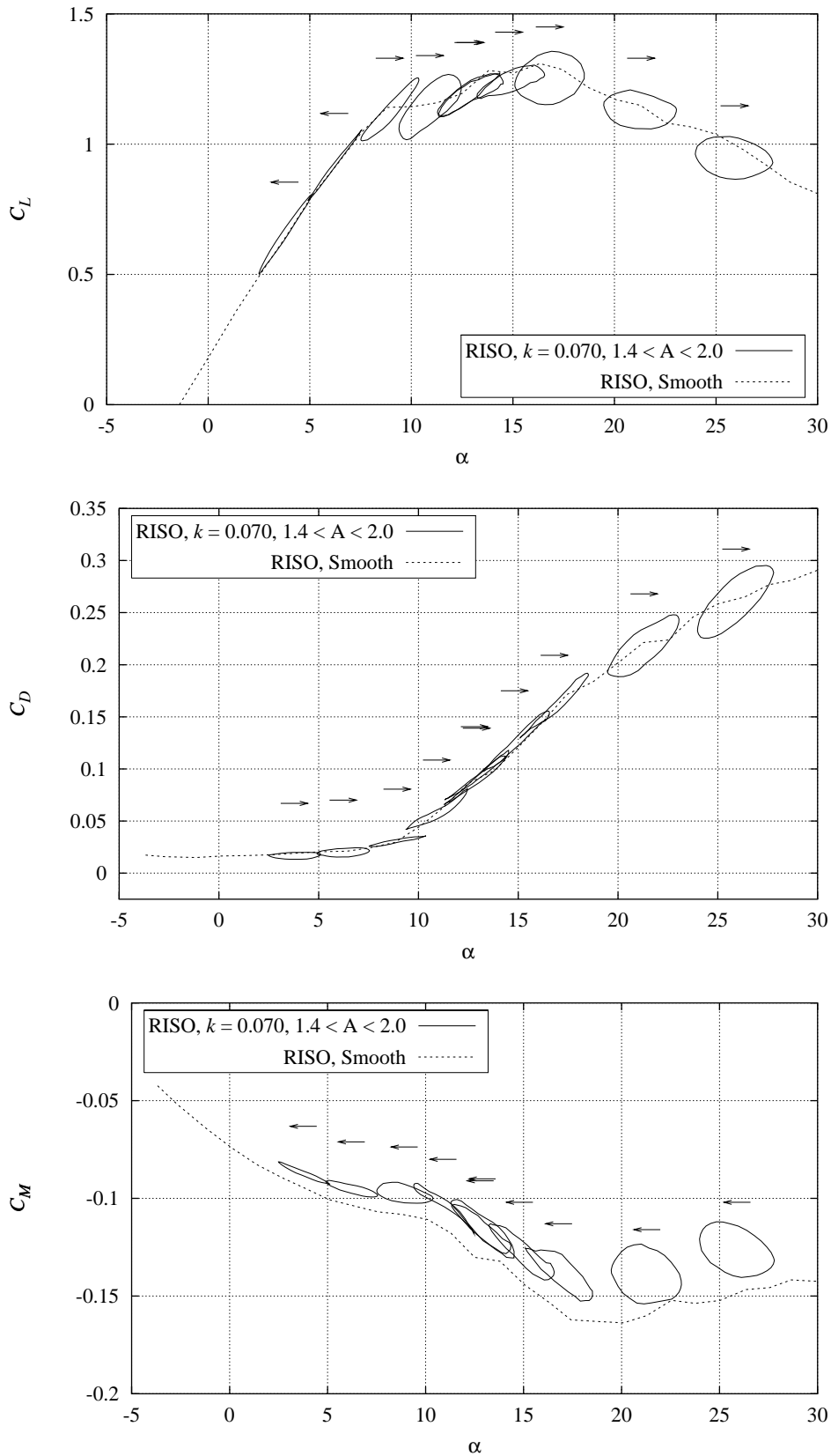
Figure 13-2 Measured C_L, C_D and C_M hysteresis loops compared with mean curves for steady smooth leading edge flow at k = 0.070, A between 1.3° and 1.9°, Re = 1.6×10⁶ (FFAW3301PITCH091297V2).

14 NACA 63-430 Smooth leading edge

This chapter reports steady inflow measurements for the NACA 63-430 airfoil with smooth leading edge.

The measurements were compared with numerical calculations from XFOIL and EllipSys2D as explained in Chapter 4.

The different types of available measurements are described in Appendix A.

Figure 14-1 shows C_P distributions at different angles of attack. The flow is attached until 9.2° where C_P is reduced at the trailing edge. C_P is gradually reduced from -2.2 to -3.3 when the angle of attack is increased from 15.1° to 27.7°.

Figure 14-2 shows the C_P distribution at 4.4° compared with XFOIL and EllipSys2D calculations and Figure 14-3 shows the C_P distribution at 15.1°.

At 4.4° the agreement is in general good for the pressure side C_P. On the suction side, the agreement is good at the leading edge, but around $x/c = 0.05$ the measured C_P curve starts to deviate from the calculations and minimum C_P is calculated too low. The transition point can not be seen in the measurement.

At 15.1° the agreement is not good. The shape of the pressure side C_P and the overall shape of the suction side C_P agree but the minimum C_P is significantly too high in the measurement. The measurement shows separation on the suction side from $x/c = 0.40$ whereas the flow remains attached until $x/c = 0.6$ for the calculations.

Figure 14-4 to Figure 14-7 show the measured C_L, C_D and C_M curves compared with XFOIL and EllipSys2D calculations.

The slope of the C_L curve is lower for the measurement compared with the calculations and maximum C_L is measured to 1.1 which is significantly lower than the calculated values since the calculations do not predict separation as early as in the measurement. There is a small deviation in the angle of attack for zero C_L between the measurement and the calculations. The measured minimum C_D of 0.011 is in good agreement with the EllipSys2D calculation and the shapes of the C_D curve at low angles of attack are in good agreement. The XFOIL calculation predicts too low minimum C_D. C_M is not in good agreement since there is an offset of the C_M level at low angles of attack and a difference in slope at higher angles of attack.

In summary the measurements of C_P at low angles of attack are in fair agreement with the EllipSys2D calculations. The C_L curve slope and the maximum C_L are however not in good agreement whereas minimum C_D and the shape of the C_D curve are in good agreement.
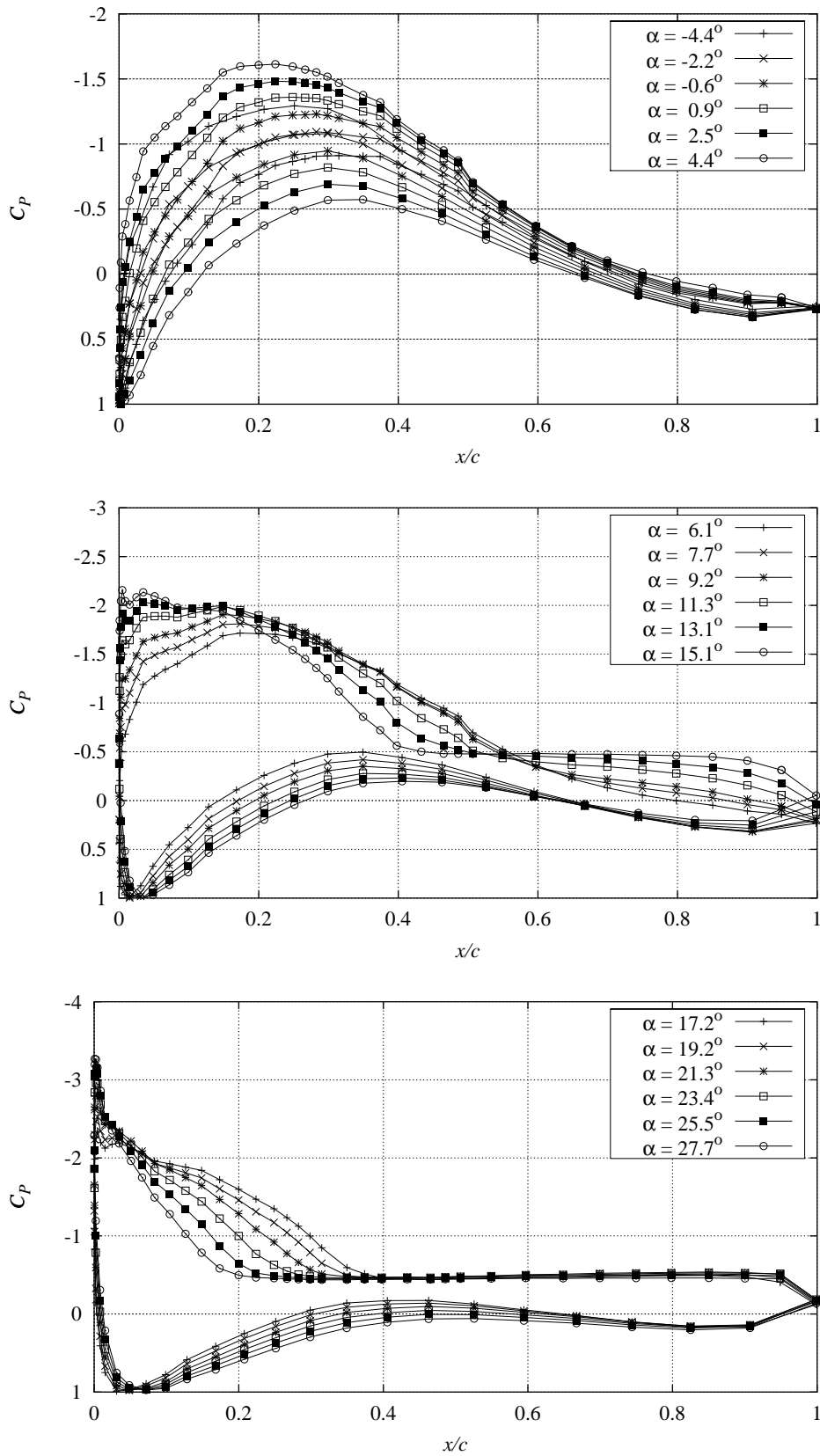
Figure 14-1 Measured C_P distributions at different angles of attack
(NACA63430STEP091297V1).
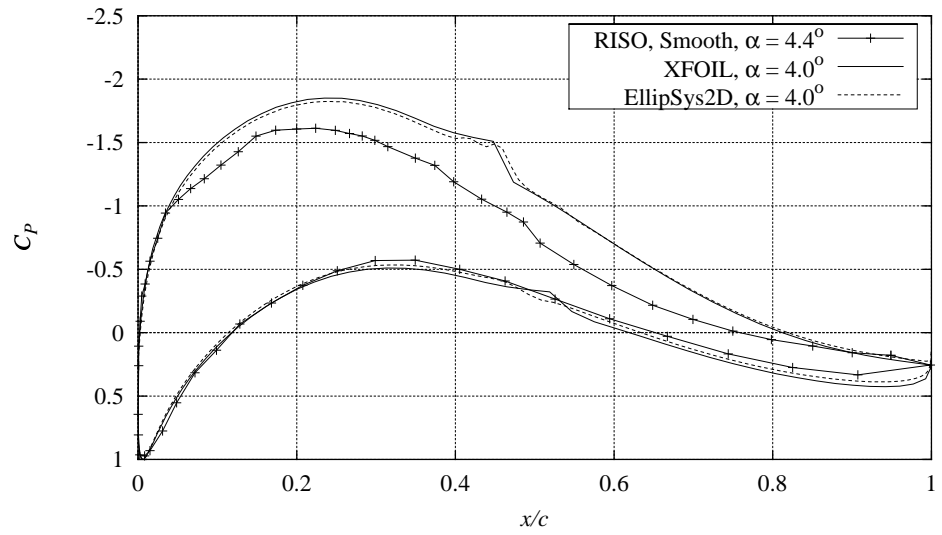
Figure 14-2 Measured C_P distribution compared with XFOIL and Ellipsys2D calculations, Re = 1.6×10⁶, α = 4.4°(NACA63430STEP091297V1).
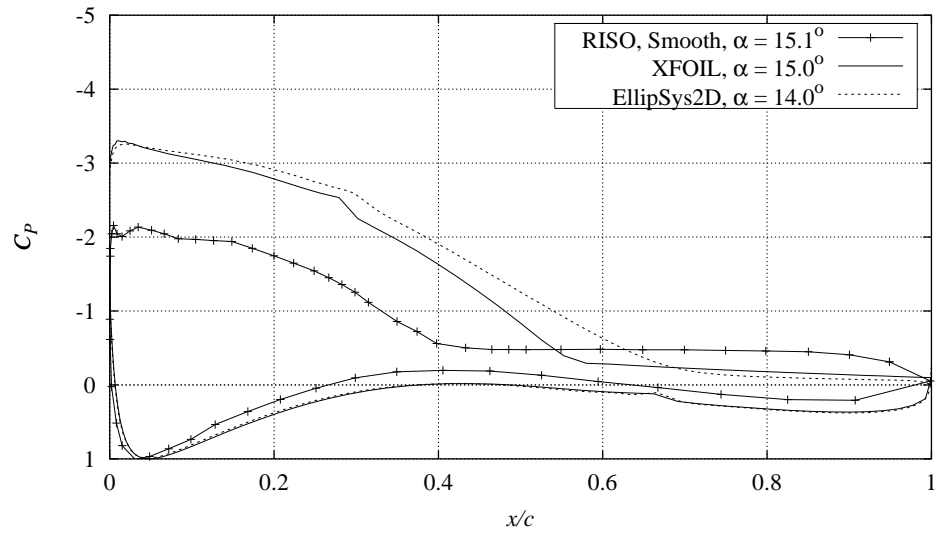
Figure 14-3 Measured C_P distribution compared with XFOIL and Ellipsys2D calculations, Re = 1.6×10⁶, α = 15.1°(NACA63430STEP091297V1).
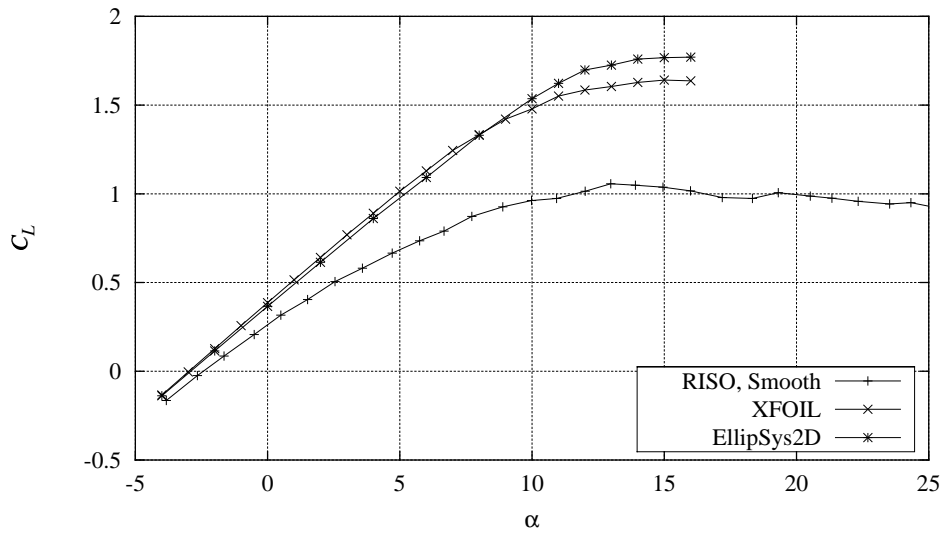
Figure 14-4 Measured C_L curve compared with XFOIL calculations with free transition and EllipSys2D calculations with free transition, Re = 1.6×10⁶ (NACA63430CONT091297V4).
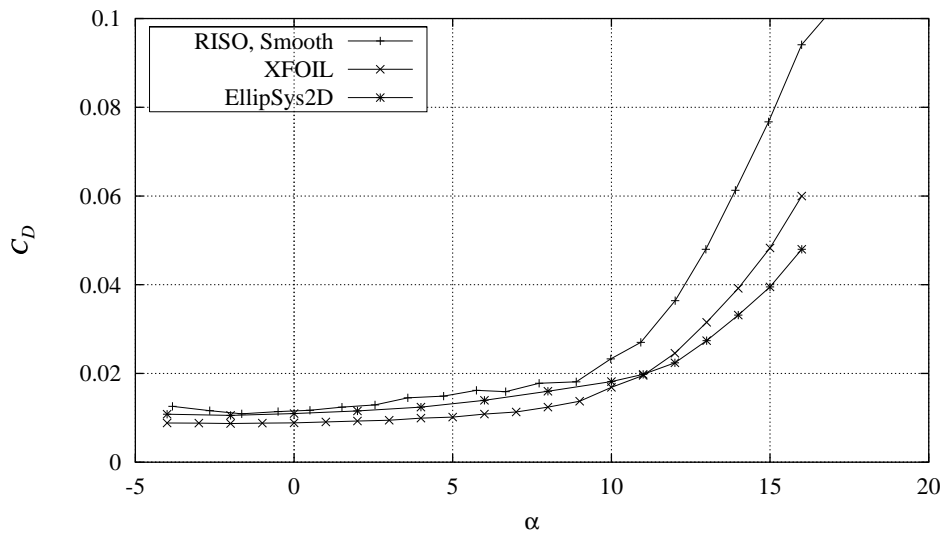
Figure 14-5 Measured C_D curve compared with XFOIL calculations with free transition and EllipSys2D calculations with free transition, Re = 1.6×10⁶ (NACA63430CONT091297V4).
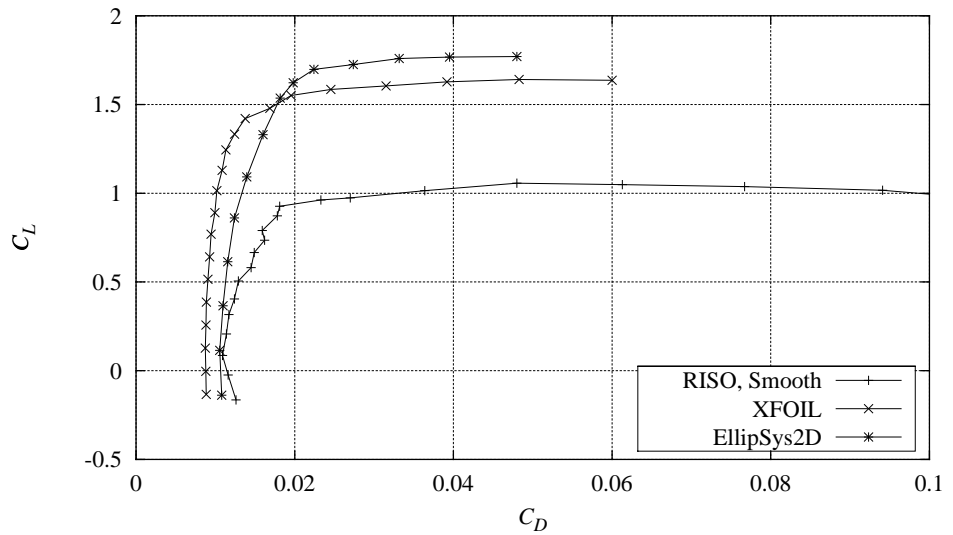
Figure 14-6 Measured C_L-C_D curve compared with XFOIL calculations with free transition and EllipSys2D calculations with free transition, Re = 1.6×10⁶ (NACA63430CONT091297V4).
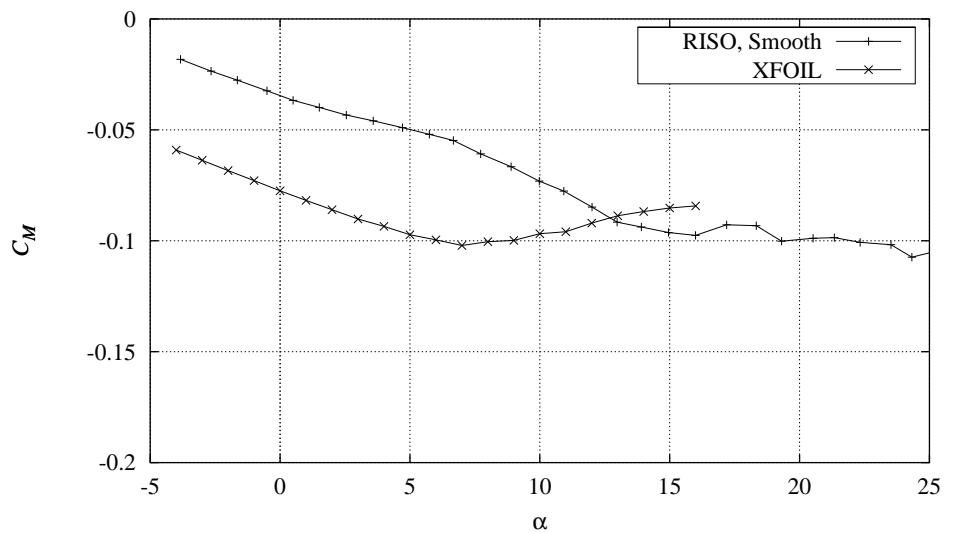
Figure 14-7 Measured C_M curve compared with XFOIL calculations with free transition, Re = 1.6×10⁶ (NACA63430CONT091297V4).

15 NACA 63-430 Vortex generators

This chapter presents steady inflow measurements for the NACA 63-430 airfoil with the following different configurations of vortex generators:

- Delft vortex generators, h = 6 mm at x/c = 0.2.
- Delft vortex generators, h = 6 mm at x/c = 0.3.

The VGs are described in Section 3.2 and the different measurements are shown in more detail in Appendix H. The different types of available measurements are described in Appendix A.

The measurements were not compared with numerical calculations since the influence from VGs could not be modelled in the numerical codes. The measurements were instead compared to the smooth flow measurements.

Figure 15-1 shows the C_P distribution at 10.0° for the different VG configurations compared with smooth flow and Figure 15-2 shows the C_P distributions corresponding to maximum C_L.

At 10° there is a clear difference in the minimum C_P, which is lower for the VG configurations compared with smooth flow. Lowest C_P is achieved for the h = 6 mm, x/c = 0.3 configuration where C_P is lower on the entire leading edge part of the suction side. At the angles of attack corresponding to maximum C_L the suction peak is also higher for the VG configurations. Whereas the flow is separated from the trailing edge for smooth flow and for the h = 6 mm, x/c = 0.2 configuration, the h = 6 mm, x/c = 0.3 VG configuration has attached flow.

Figure 15-3 to 15-6 show C_L, C_D and C_M curves for the VG configurations compared with smooth flow.

For both VG configurations, maximum C_L is increased together with the angle of attack at maximum C_L. For the h = 6 mm, x/c = 0.3 configuration maximum C_L is increased to 1.4. Furthermore the slope of the C_L curve is steeper compared with smooth flow and the h = 6 mm, x/c = 0.2 VG configuration. Minimum C_D is increased for both VG configurations and minimum C_D is slightly higher for the h = 6 mm, x/c = 0.2 configuration because of the forwarded location of the VGs compared to the h = 6 mm, x/c = 0.3 configuration. Separation is delayed resulting in reduced C_D at angles of attack close to maximum C_L.

In summary the measurements agree with Chapter 5 and showed that minimum C_P is reduced at high angles of attack around maximum C_L. However opposite to Chapter 5 and Chapter 10, the VGs should for this airfoil be located in x/c = 0.3 to achieve the highest maximum C_L, the steepest C_L curve slope and the highest C_L/C_D ratio.
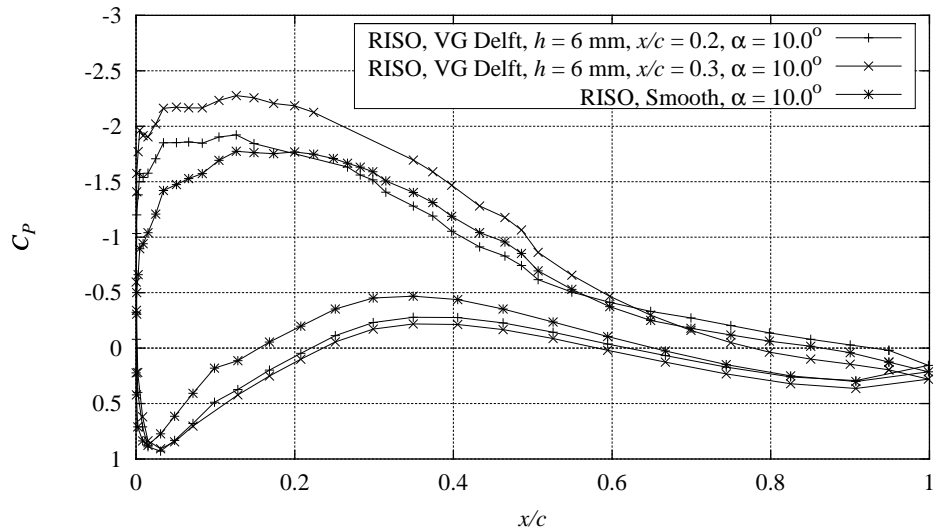
Figure 15-1 Measured C_P distributions for the different vortex generator configurations compared with smooth measurement, Re = 1.6×10⁶, α around 10° corresponding to C_{Lmax} for smooth leading edge flow.
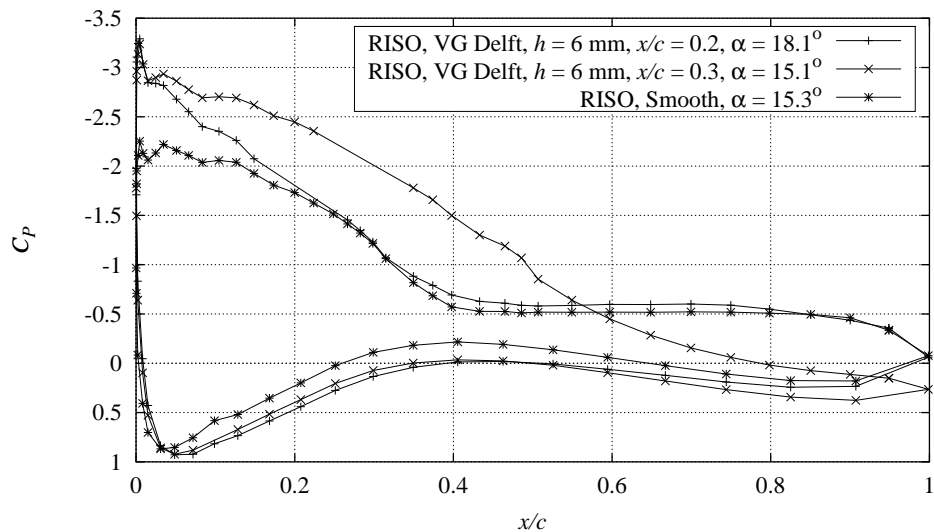
Figure 15-2 Measured C_P distributions for the different vortex generator configurations compared with smooth measurement, Re = 1.6×10⁶, α corresponding to C_{Lmax}.
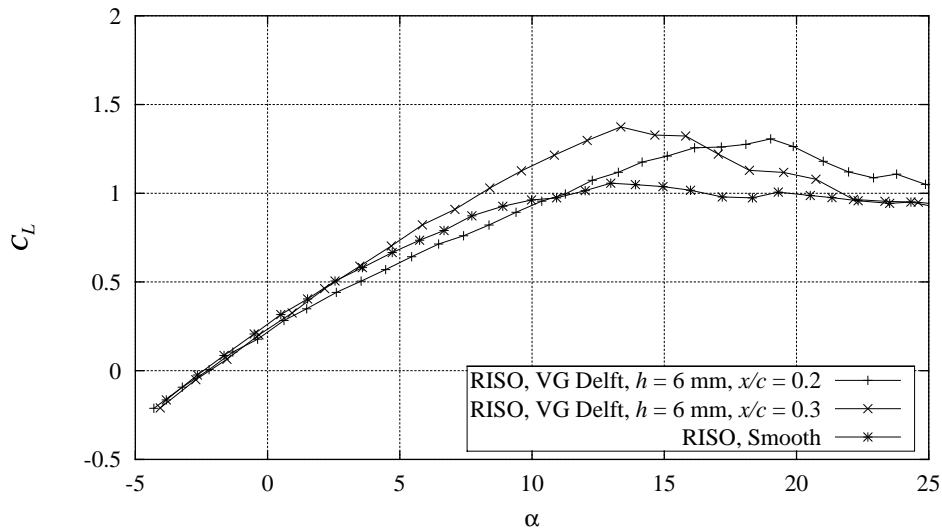
Figure 15-3 Measured C_L curves for the different vortex generator configurations compared with smooth measurement, Re = 1.6×10⁶.
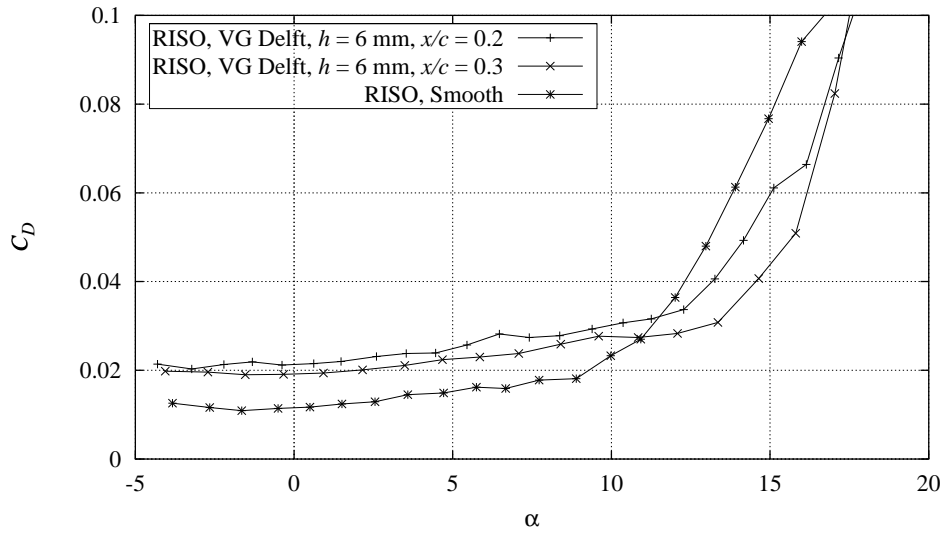
Figure 15-4 Measured C_D curves for the different vortex generator configurations compared with smooth measurement, Re = 1.6×10⁶.
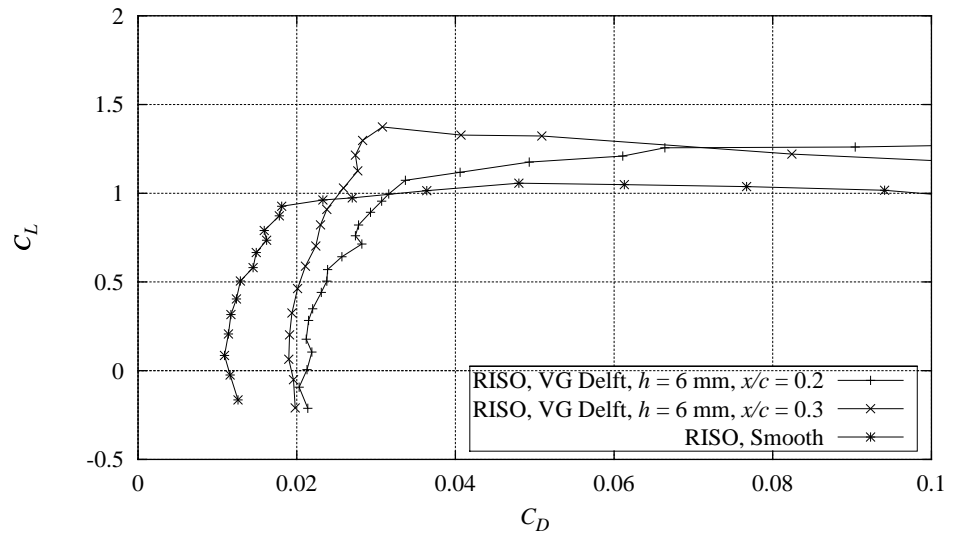
Figure 15-5 Measured C_L-C_D curves for the different vortex generator configurations compared with smooth measurement, $Re = 1.6 \times 10^6$.
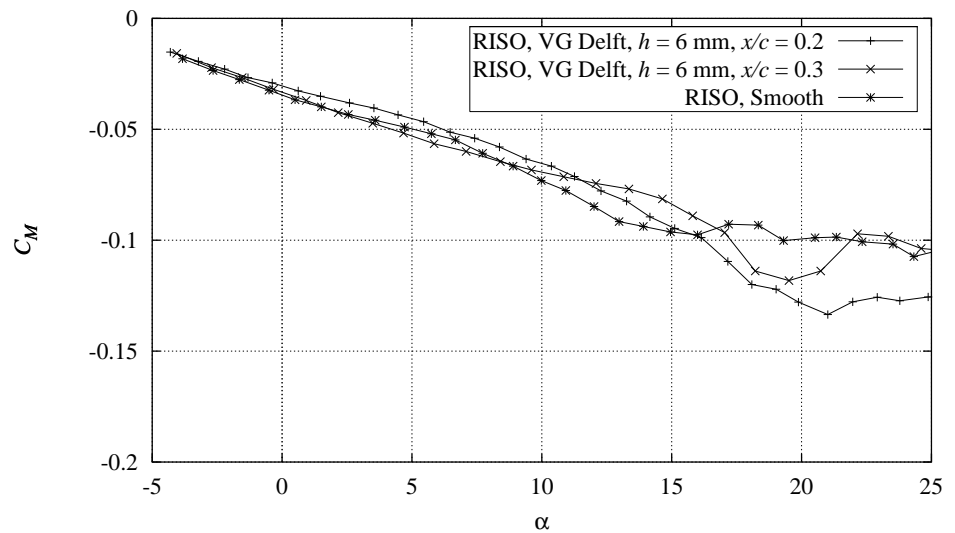
Figure 15-6 Measured C_M curves for the different vortex generator configurations compared with smooth measurement, $Re = 1.6 \times 10^6$.

16 NACA 63-430 Leading edge roughness

This chapter presents steady inflow measurements for the NACA 63-430 airfoil with the leading edge roughness configuration: 90° zigzag trip tape.

The LER configurations are described in Section 3.3. The different types of available measurements are described in Appendix A.

The measurements were compared with numerical calculations. The XFOIL code was used and prescribing the transition location to be at the leading edge: $x/c = 0.01$ on the suction side and $x/c = 0.10$ on the pressure side simulated leading edge roughness. The Ellipsys2D Navier-Stokes code was used and having turbulent flow on the entire airfoil simulated leading edge roughness. The measurements were also compared with smooth flow measurements.

Figure 16-1 shows the C_P distribution at 5.8° compared with smooth flow and XFOIL and EllipSys2D calculations and Figure 16-2 shows the C_P distribution at 9.9°.

The LER configuration has higher C_P on the suction side compared to smooth flow and the flow on the trailing part of the suction side is separated. The calculations predict too low C_P on the front part of the suction side, but they also predict separation. The C_P distributions on the pressure side are in fair agreement. At 9.9° the shape of the C_P curve for the LER measurements is in fair agreement with the calculations but the level of C_P is higher on the suction side. The smooth flow measurement is in good agreement with the calculations.

Figure 16-3 to 16-6 show the C_L, C_D and C_M curves for the LER configuration compared with smooth flow and XFOIL and EllipSys2D calculations.

Maximum C_L is reduced for the LER configuration compared with smooth flow. The calculations overestimate the C_L curve slope and maximum C_L compared with the LER configuration and it appears that the calculations agree well with the smooth flow measurement. The C_D curve for the LER configuration is irregular because of the very early transition that influences the wake rake measurement. The minimum C_D for the LER configuration is increased compared to smooth flow. Both calculations agree well with the LER configuration.

In summary the measurements agree with Chapter 6 and show that LER reduces maximum C_L and increases minimum C_D. The EllipSys2D calculation agrees well with measurements of minimum C_D, but maximum C_L is too high in the calculation and not in good agreement with the LER configuration measurement.
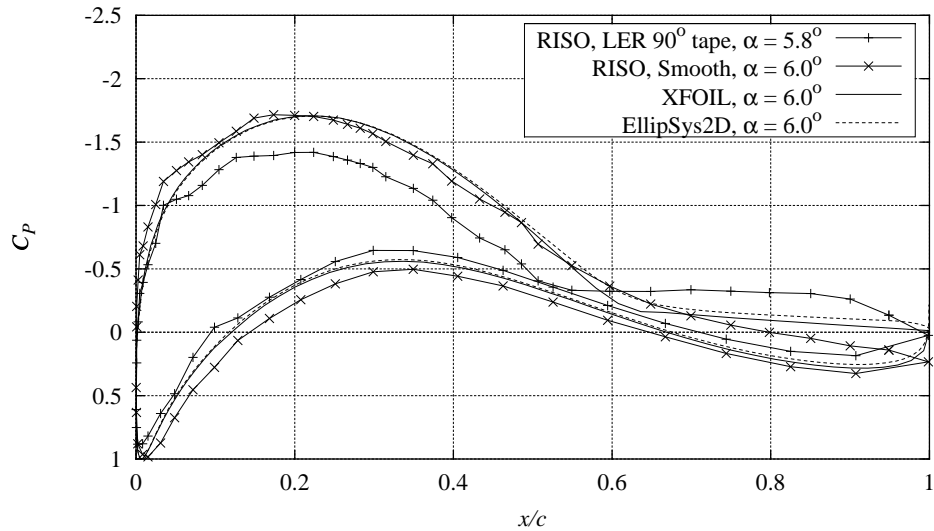
Figure 16-1 Measured C_P distribution for 90° zigzag trip tape compared with smooth measurement and XFOIL (LE transition) and EllipSys2D (turbulent) calculations, Re = 1.6×10⁶, α = 6°(NACA63430CONT091297V3).
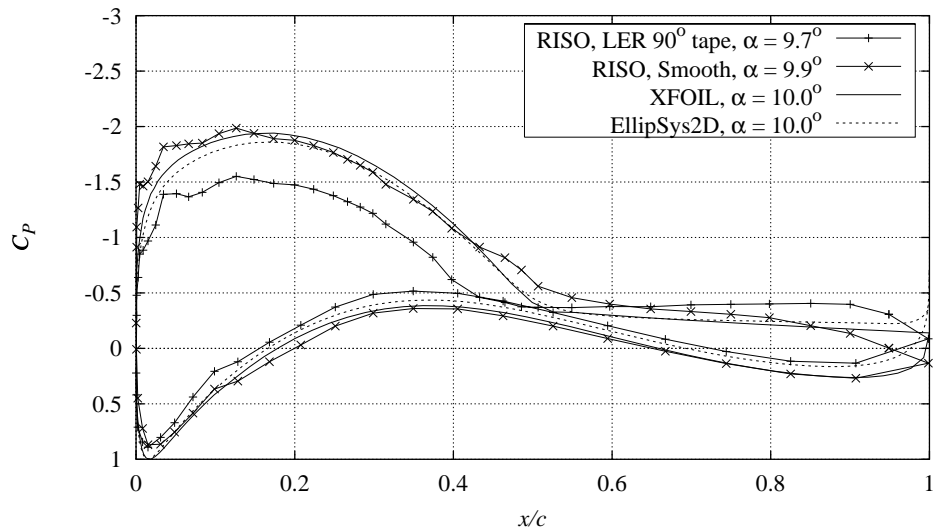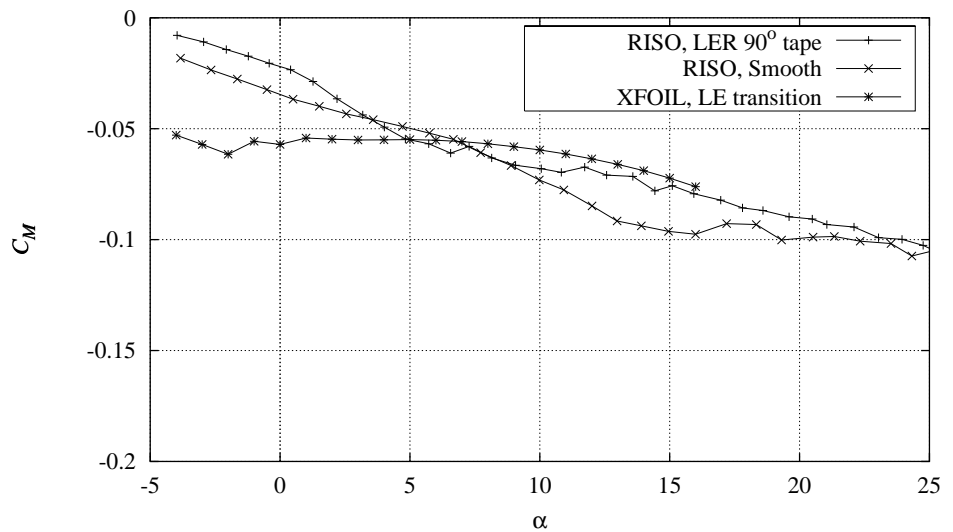

Figure 16-2 Measured C_P distribution for 90° zigzag trip tape compared with smooth measurement and XFOIL (LE transition) and EllipSys2D (turbulent) calculations, Re = 1.6×10⁶, α = 10°(NACA63430CONT091297V3).
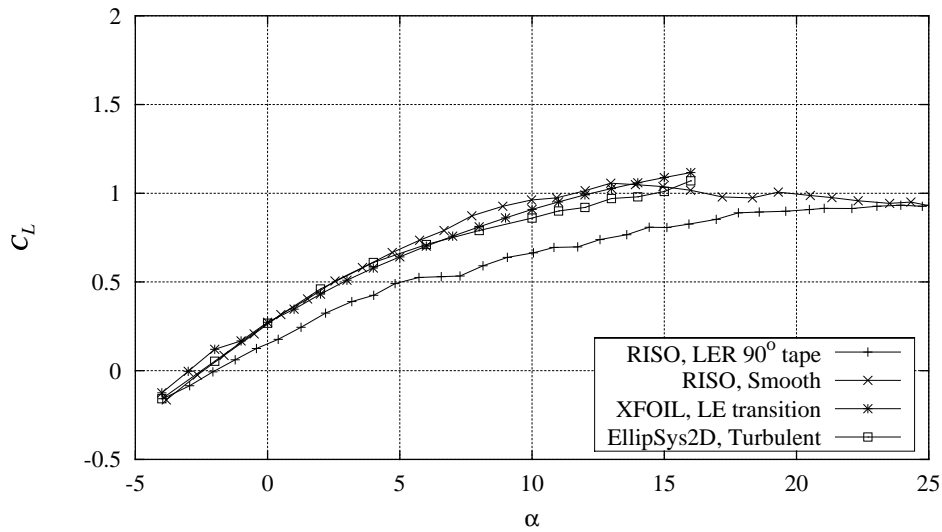
Figure 16-3 Measured C_L curve for 90° zigzag trip tape compared with smooth measurement and XFOIL (LE transition) and EllipSys2D (turbulent) calculations, Re = 1.6×10^{6} (NACA63430CONT091297V3).
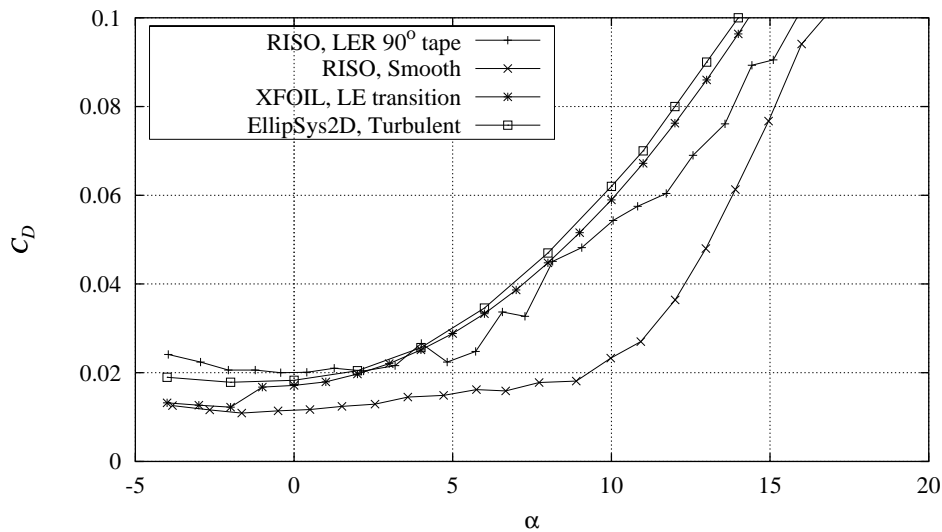
Figure 16-4 Measured C_D curve for 90° zigzag trip tape compared with smooth measurement and XFOIL (LE transition) and EllipSys2D (turbulent) calculations, Re = 1.6×10^{6} (NACA63430CONT091297V3).
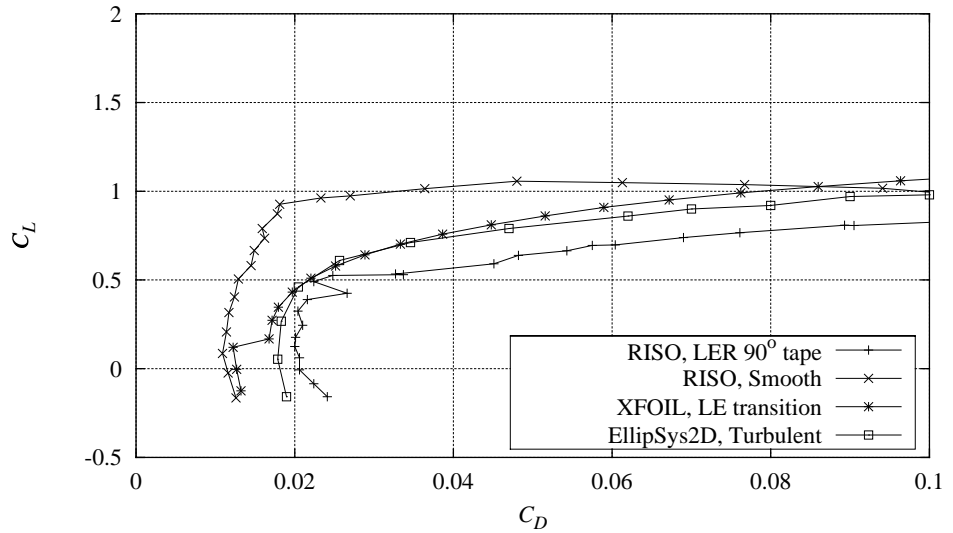
Figure 16-5 Measured C_L-C_D curve for 90° zigzag trip tape compared with smooth measurement and XFOIL (LE transition) and EllipSys2D (turbulent) calculations, Re = 1.6×10^6 (NACA63430CONT091297V3).

Figure 16-6 Measured C_M curve for 90° zigzag trip tape compared with smooth measurement and XFOIL (LE transition) calculations, Re = 1.6×10^6 (NACA63430CONT091297V3).

17 NACA 63-430 Vortex generators and leading edge roughness

This chapter presents steady inflow measurements for the NACA 63-430 airfoil with vortex generators and leading edge roughness configuration: Delft vortex generators, $h = 6$ mm at $x/c = 0.3$ and 90° zigzag trip tape.

The vortex generators are described in Section 3.2 and the leading edge roughness configurations are described in Section 3.3. The different types of available measurements are described in Appendix A.

The measurements were not compared with numerical calculations but to measurements of the corresponding VG configuration, measurements of the corresponding LER configuration and smooth flow measurements.

Figure 17-1 shows the C_P curve for the VGLER configuration compared with the VG configuration, the LER configuration and smooth flow around 6° and Figure 17-2 shows the C_P curves around 10°.

For 6° the agreement between the VGLER configuration and the smooth flow configuration is good on both the pressure and the suction sides. The LER configuration has higher minimum C_P whereas the VG configuration has lower minimum C_P. The flow is separated for the LER configuration but not for the remaining configurations. At 10° the flow for the VGLER and the VG configurations is different on the suction side where a large region of low pressure is maintained and no separation occurs towards the trailing edge. Both smooth flow and LER the configuration are separated on a large part of the suction side.

Figure 17-3 to Figure 17-6 show the C_L, C_D and C_M curves for the VGLER configuration compared with the VG configuration, the LER alone configuration and smooth flow.

The C_L curve slope is equal for the VGLER, VG and smooth flow configurations whereas the C_L curve slope is reduced for the LER configuration. Maximum C_L is increased for the VGLER configuration compared with smooth flow and better defined at 11° whereas maximum C_L for smooth flow appears at 14°. Minimum C_D is higher for the VGLER configuration than for the remaining configurations but a low C_D is maintained until 11° where maximum C_L appears in contrast to the early rise in C_D for the LER configuration.

In summary the measurement showed that the VGLER configuration had higher maximum C_L but also higher minimum C_D than smooth flow. The increase in C_L from VGs counterbalanced the reduction from LER and maximum C_L was better defined compared with smooth flow.
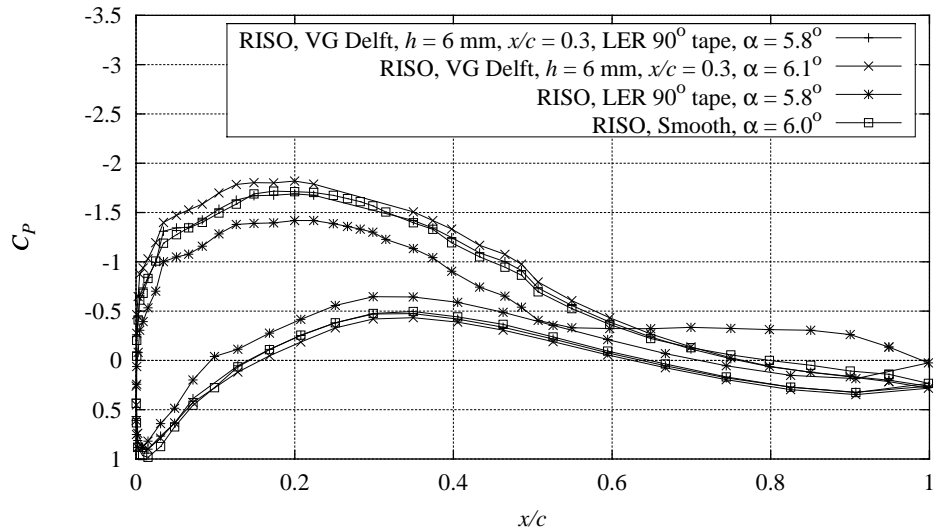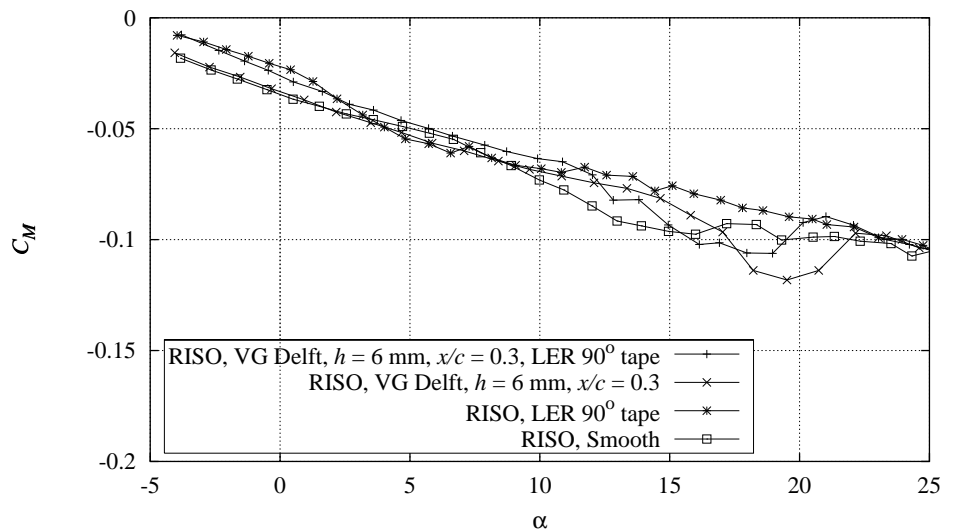
Figure 17-1 Measured C_P distributions with combinations of Delft vortex generators, h = 6 mm, x/c = 0.3, and 90° zigzag trip tape compared with smooth measurement, Re = 1.6×10^6, α = 5.8°(NACA63430CONT091297V2).
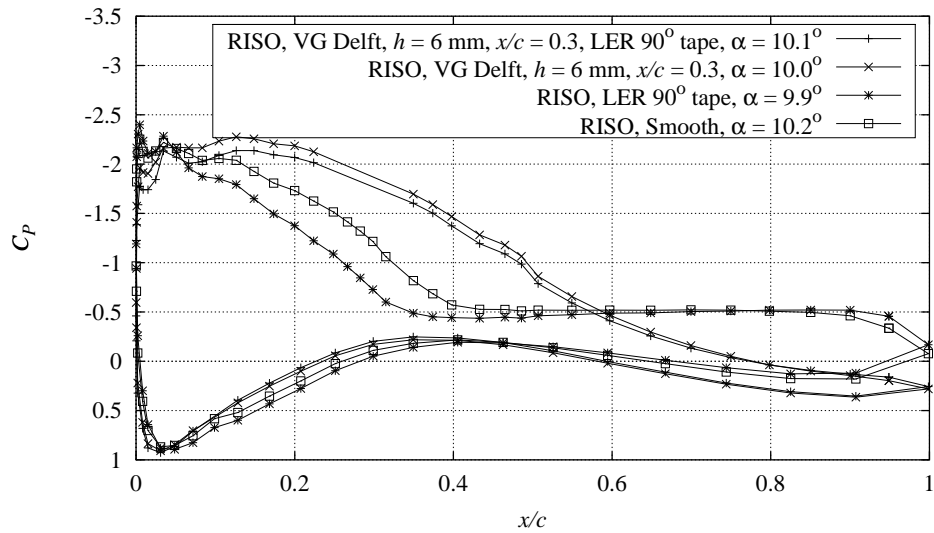
Figure 17-2 Measured C_P distributions with combinations of Delft vortex generators, h = 6 mm, x/c = 0.3, and 90° zigzag trip tape compared with smooth measurement, Re = 1.6×10^6, α = 10.1°(NACA63430CONT091297V2).
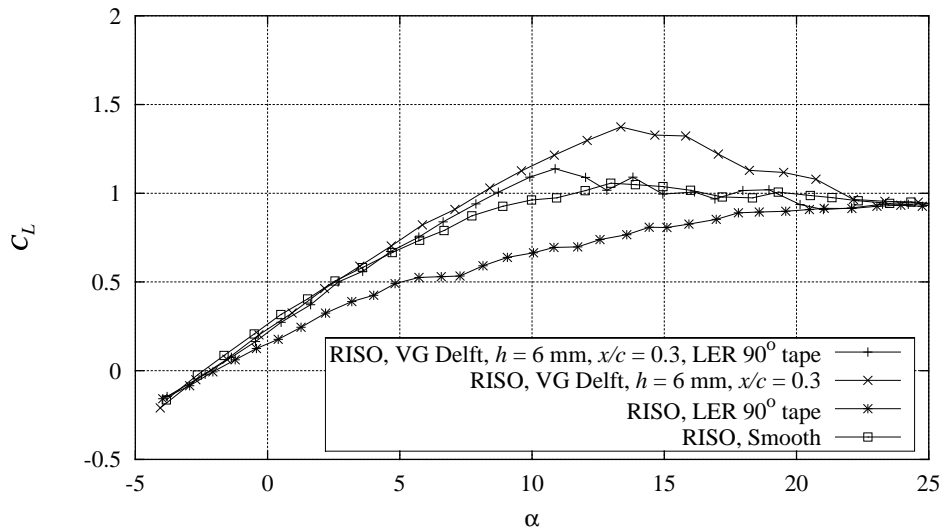
Figure 17-3 Measured C_L curves with combinations of Delft vortex generators, h = 6 mm, x/c = 0.3, and 90° zigzag trip tape compared with smooth measurement, Re = 1.6×10⁶ (NACA63430CONT091297V2).
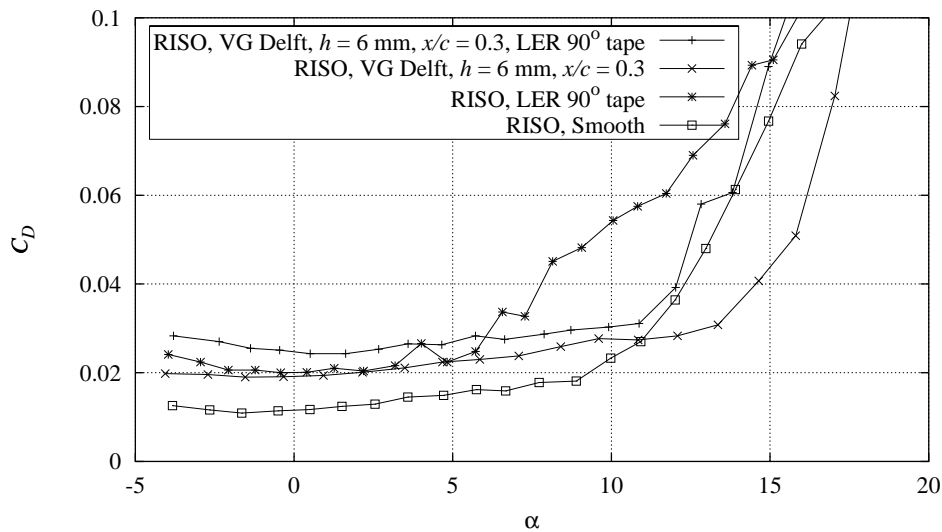
Figure 17-4 Measured C_D curves with combinations of Delft vortex generators, h = 6 mm, x/c = 0.3, and 90° zigzag trip tape compared with smooth measurement, Re = 1.6×10⁶ (NACA63430CONT091297V2).
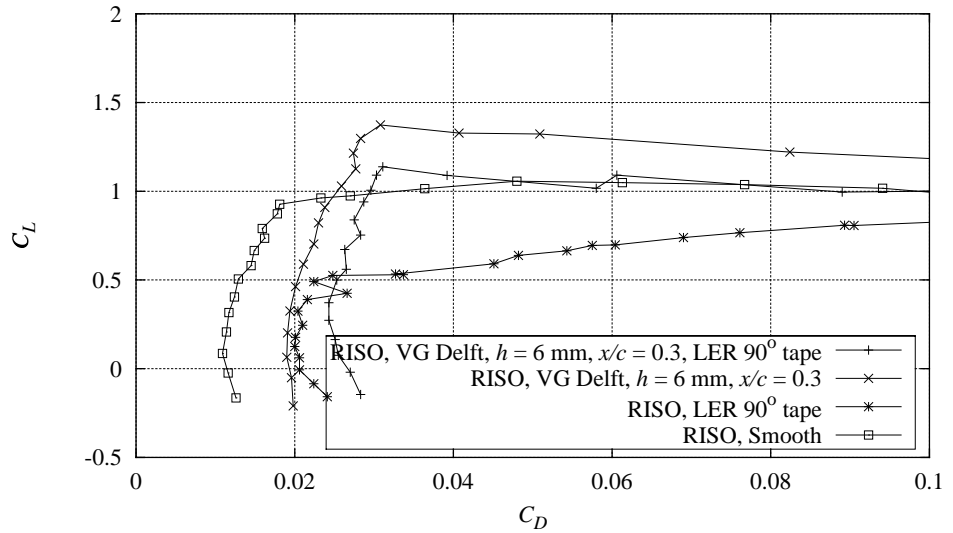
Figure 17-5 Measured C_L-C_D curves with combinations of Delft vortex generators, $h = 6$ mm, $x/c = 0.3$, and 90° zigzag trip tape compared with smooth measurement, Re = 1.6×10⁶ (NACA63430CONT091297V2).

Figure 17-6 Measured C_M curves with combinations of Delft vortex generators, $h = 6$ mm, $x/c = 0.3$, and 90° zigzag trip tape compared with smooth measurement, Re = 1.6×10⁶ (NACA63430CONT091297V2).

18 NACA 63-430 Dynamic stall

This chapter presents dynamic inflow measurements for the NACA 63-430 airfoil. The following reduced frequencies and amplitudes were measured:

- Smooth flow, $k = 0.093$, $1.4^o < A < 2.0^o$.
- Smooth flow, $k = 0.070$, $1.4^o < A < 2.0^o$.

The different measurements are shown in more detail in Appendix I. The different types of available measurements are shown in Appendix A.

The derivation of the hysteresis loops is explained in Chapter 8 and in [1].

The measurements were not compared with numerical calculations but the derived hysteresis loops were compared with the static mean curves.

Figure 18-1 shows the measured C_L, C_D and C_M hysteresis loops for $k = 0.093$ and $1.4° < A < 2.0°$ compared with the static curves.

The mean values of the hysteresis loops agree well with the static curves. The directions of the C_L loops are clockwise already from 3°. They become more open from 5° until maximum C_L where they are very open. The slopes of the loops tend to follow the slope of the static curve at the entire C_L curve. The C_D loops are very narrow at low angles of attack so that the direction is not well determined. However at angles of attack above 13° they are clockwise. The slopes of the C_D loops at high angles of attack are more steep compared with the static curve. The C_M loops are all counter clockwise and the slopes of the loops at high angles of attack are steeper than the static curve.

Figure 18-2 shows the measured C_L, C_D and C_M hysteresis loops for $k = 0.070$ and $1.4° < A < 2.0°$ compared with the static curves. In general the loops correspond to Figure 18-1.

In summary the measurements showed the derived hysteresis loops for C_L, C_D and C_M. The behavior of the hysteresis loops was found similar to Chapter 8 and Chapter 13 and in good agreement with the literature.
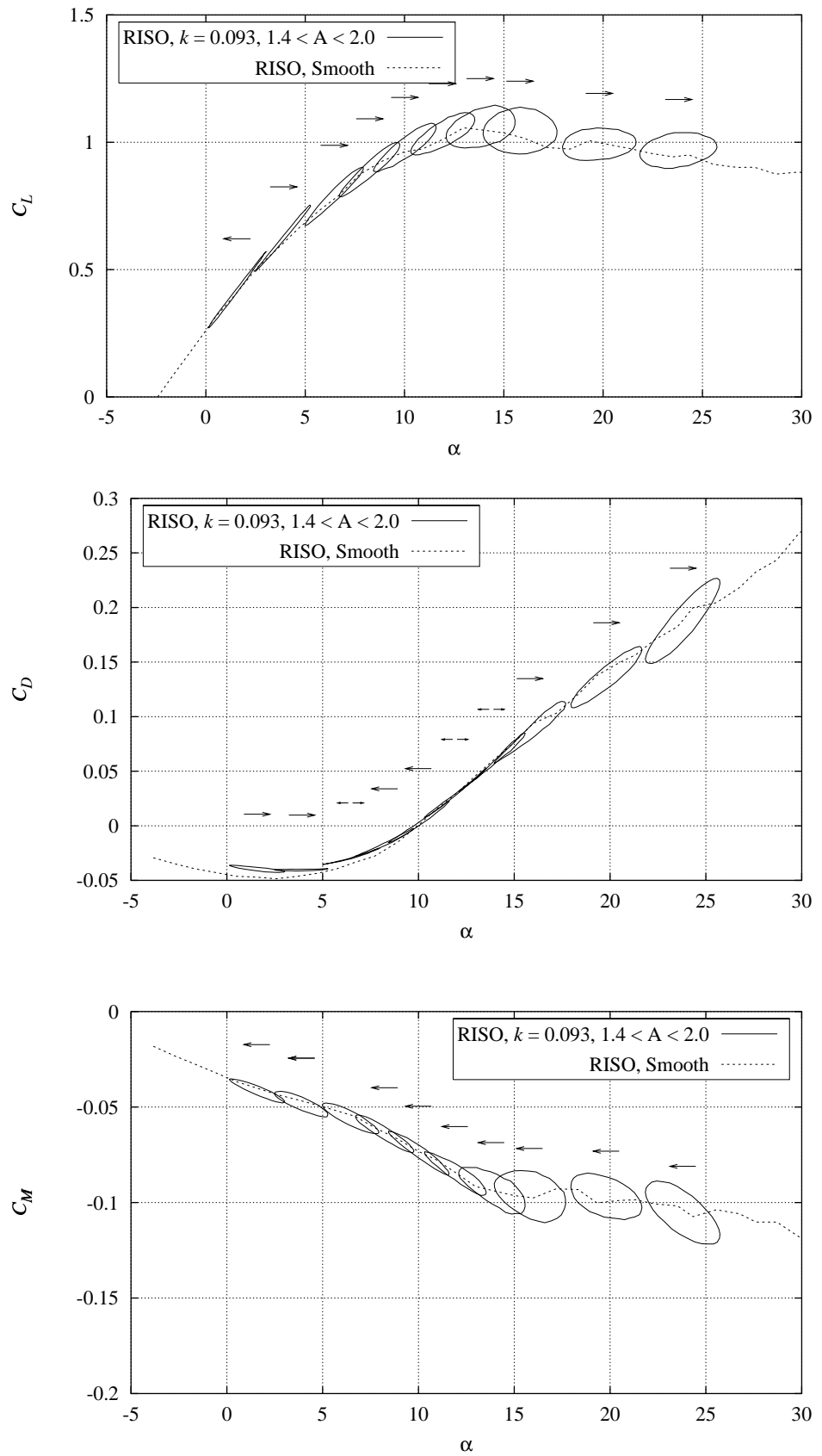
Figure 18-1 Measured C_L, C_D and C_M hysteresis loops compared with mean curves for steady smooth leading edge flow at k = 0.093, A between 1.4° and 2.0°, Re = 1.6×10^{6} (NACA63430PITCH091297V1).
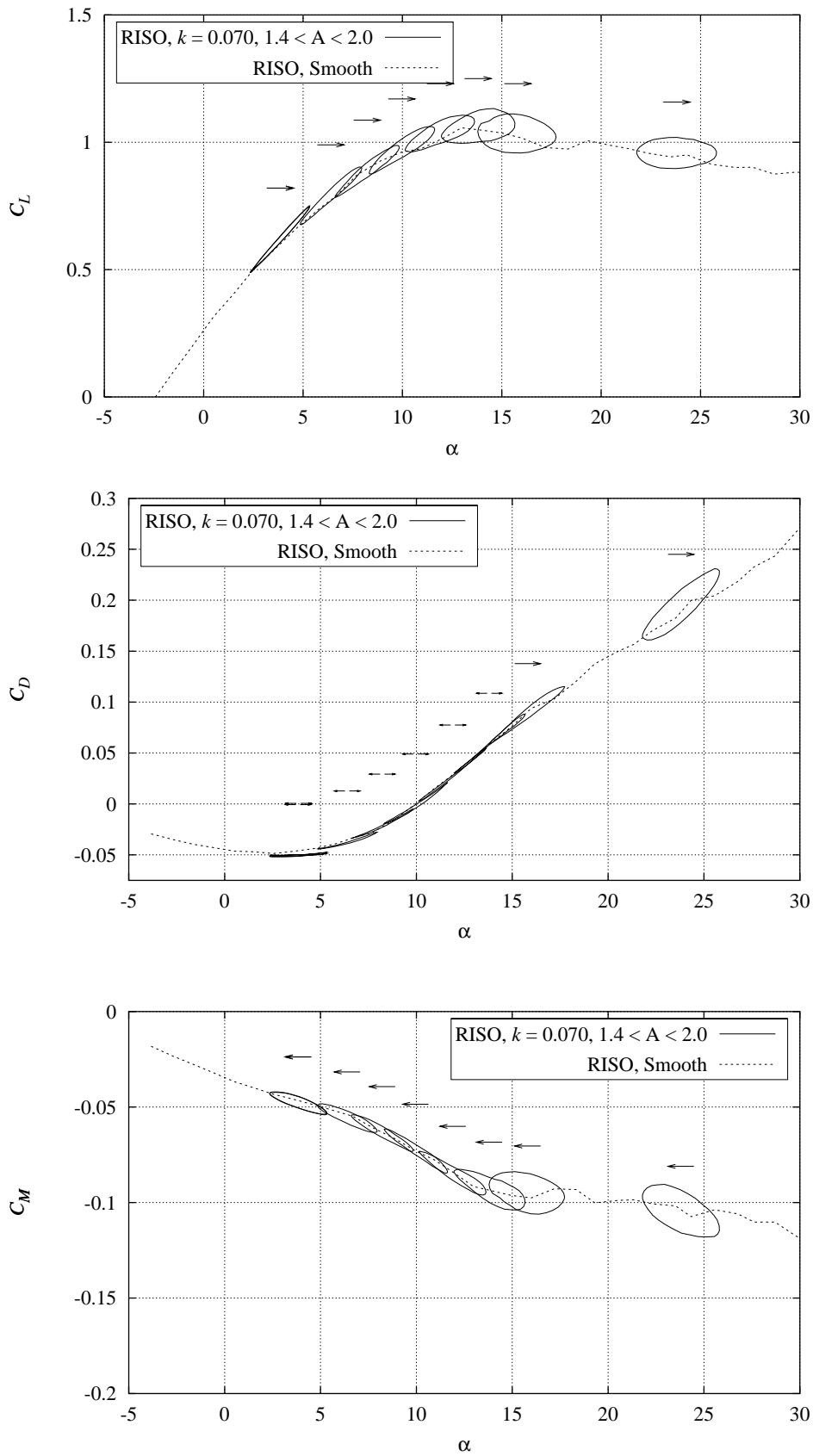
Figure 18-2 Measured C_L, C_D and C_M hysteresis loops compared with mean curves for steady smooth leading edge flow at k = 0.070, A between 1.4° and 2.0°, Re = 1.6×10⁶ (NACA63430PITCH091297V2).

19 Conclusions

This report deals with 2D measurements of the FFA-W3-241, FFA-W3-301 and NACA 63-430 airfoils. The aerodynamic properties were measured at $Re = 1.6 \times 10^6$. The VELUX open jet wind tunnel was used with a background turbulence intensity of 1%. The airfoil sections had a chord of 0.60 m and a span of 1.9 m and end plates were used to minimize 3D flow effects. The measurements comprised both static and dynamic inflow where the dynamic inflow was obtained by pitching the airfoil in a harmonic motion around the $x/c = 0.4$ axis. We tested the influence from vortex generators (VGs) and leading edge roughness (LER) both individually and in combination.

Smooth flow

Smooth flow measurements were carried out for all airfoils. All airfoils had a relative low C_L curve slope compared with thinner airfoils and separation occurred from the trailing edge. The value of minimum suction side C_P did not come below –3 from angles of attack at maximum C_L until deep stall and the shapes of the C_P curves were slightly irregular at the leading edge at high angles of attack. The transition points were in general not clearly seen in the measurements. C_D was derived from wake rake measurements until separation and after that C_D was based on pressure drag.

For the FFA-W3-241 airfoil maximum C_L was 1.37 and minimum C_D was 0.010 at -4°. The flow remained attached until maximum C_L at 11°. A large area of low C_D was found at low angles of attack.

For the FFA-W3-301 airfoil maximum C_L was 1.30 and minimum C_D was 0.015 at 0° and C_D was gradually increased until the flow separated at 8°. The C_L curve slope at very low angles of attack was reduced due to separation of the pressure side flow.

For the NACA 63-430 airfoil maximum C_L was 1.10 and minimum C_D was 0.011 at –2° and C_D was slightly increased until the flow separated at 9°. The C_L curve started to bend off already at 0°. This resulted in a very smooth progress of C_L toward maximum C_L and constant low C_L in the post stall area.

Vortex generators

A parametric study was conducted where vortex generators (VGs) of different height were used at different locations. We compared measurements of the aerodynamic coefficients from pressure measurements and strain gauge measurements and found that the pressure measurements were representative for the VG flow. Hence it made sense to derive aerodynamic coefficients from the C_P distributions for the different VG configurations.

The presence of the VGs did not affect the C_P distribution at angles of attack where the smooth flow measurement had attached flow. However, at higher angles of attack the suction minimum C_P was reduced for all airfoils, maximum

C_L was increased and minimum C_D was increased. The VGs delayed separation to higher angles of attack and this reduced C_D close to maximum C_L and hence increased the C_L/C_D ratio at angles of attack in this area.

The maximum C_L and minimum C_D depended on the height and the location of the VGs. C_L was highest for the $h = 6$ mm configurations and C_D was lowest for the $h = 4$ mm configurations but the C_L/C_D ratios were higher for the $h = 6$ mm configurations. The C_L curve slope was steepest for the VG configurations closest to the leading edge, but these locations did not necessarily result in maximum C_L.

For the FFA-W3-241 airfoil the $h = 6$ mm, $x/c = 0.2$ VG configuration was best. The suction peak C_P was –4.8 at 17.4° and this led to a maximum C_L of 1.68 compared with 1.37 for smooth flow. Minimum C_D was increased to 0.016 compared with 0.010 for smooth flow.

For the FFA-W3-301 airfoil the $h = 6$ mm, $x/c = 0.2$ VG configuration was best. The suction peak C_P was –3.8 at 18.1° and this led to a maximum C_L of 1.64 compared with 1.30 for smooth flow. Minimum C_D was increased to 0.022 compared with 0.015 for smooth flow.

For the NACA 63-430 airfoil the $h = 6$ mm, $x/c = 0.3$ VG configuration was best. The suction peak C_P was –3.3 resulting in a maximum C_L of 1.37 compared with 1.1 for smooth flow. Minimum C_D was increased to 0.019 compared with 0.011 for smooth flow.

Leading edge roughness

Measurements were carried out with leading edge roughness (LER) at the leading edge. This simulated the accumulation of dirt and bugs under operation in natural conditions. Different types of trip tape were used but the differences in the aerodynamic characteristics between these were negligible.

LER did in general reduce the suction peak. Separation occurred earlier than for smooth flow and maximum C_L was reduced whereas minimum C_D was increased so that C_L/C_D was reduced for all angles of attack compared with smooth flow. The slope of C_L was in general reduced at angles of attack close to maximum C_L.

For the FFA-W3-241 airfoil the maximum C_L was reduced to 1.18 and minimum C_D was increased to 0.018. For the FFA-W3-301 airfoil the maximum C_L was reduced to 0.86 and minimum C_D was increased to 0.023. For the NACA 63-430 airfoil the maximum C_L was not clearly defined since C_L increases until very high angles of attack. However C_L was 0.5 at 5° and minimum C_D was 0.020.

Vortex generators and leading edge roughness

Measurements were carried out with a combination of leading edge roughness and vortex generators. For all airfoils minimum C_D was increased from both LER and VG. For the FFA-W3-241 and NACA 63-430 airfoils we found that the VGs counterbalanced the reduction in maximum CL from LER. For the FFA-W3-301 airfoil the VGs could not counterbalance the reduction in C_L from LER.

Dynamic measurements

Measurements were carried out with dynamic inflow from forcing the airfoil in a harmonic pitch motion around the 40% chordwise location. The reduced frequencies were 0.070 and 0.093 respectively and the amplitude varied between 1.4° and 2.0°.

The measurements showed that for all airfoils hysteresis loops could be derived for C_L, C_D and C_M at different mean angles of attack. The slopes of the loops tended to follow the static curve at low angles of attack, but were often steeper than the static curve at high angles of attack. The C_L loops at low angles of attack were counter clockwise whereas the C_L loops at high angles of attack were clockwise. The hysteresis loops for a VG configuration behaved similar to smooth flow except for the higher maximum C_L and small differences in the directions of the loops.

Comparison of measurements and calculations

The measurements were compared with XFOIL and EllipSys2D calculations. For smooth flow, transition was modeled whereas turbulent flow was assumed on the entire airfoil in the calculation when leading edge roughness was applied in the measurement.

For smooth flow at low angles of attack, the agreement between measurements and calculations was in general good for the overall shape of the C_P distribution and for the level of the suction peak. At higher angles of attack at stall and in the post stall region, both calculations overestimate the suction peak resulting in too high maximum C_L because the flow does not separate as it appears in the measurements. Calculated and measured C_M is in general not in good agreement. Both calculation codes predict C_L too high. XFOIL predicts C_D too low and a steeper C_L curve slope compared with EllipSys2D and this code is in general in better agreement with the measurements compared with XFOIL.

For the FFA-W3-241 airfoil EllipSys2D was in very good agreement with measurements of minimum C_D and the C_D and C_L curves at low angles of attack until measured maximum C_L. The angle of attack for zero C_L was well predicted.

For the FFA-W3-301 airfoil EllipSys2D predicts the slope of C_L at low angles of attack well but the angle of attack for zero C_L was calculated too negative and minimum C_D is predicted too low.

For the NACA 63-430 airfoil EllipSys2D predicts the slope of the C_L curve too high and the angle of attack for zero C_L too negative. Minimum C_D and the shape of the C_D curve were in good agreement.

For leading edge transition the calculations in general overestimated maximum C_L and the slope of the C_L curve compared with the measurements with LER. For the FFA-W3-241 airfoil EllipSys2D was in good agreement with measurements of minimum C_D and the shape of the C_D curve but C_D was calculated too low for the other airfoils. For all airfoils it appeared that maximum C_L for the calculations with leading edge transition were in good agreement with the smooth flow measurements.

Comparison of FFA-W3 and NACA 63-4xx airfoils

Table 19-1 shows a comparison of the FFA-W3 airfoils and the NACA 63-4xx airfoils. FFA-W3 airfoils have higher maximum C_L for smooth flow as well as for VG flow at the expense of higher minimum C_D. However, for equal airfoil thickness the FFA-W3 airfoils have better aerodynamic properties than the NACA 63-4xx airfoils for inboard stations of a wind turbine blade.

Table 19-1 Comparison of C_{Dmin} and C_{Lmax} for FFA-W3 and NACA 63-4xx airfoils. NACA 63-425 measurements were obtained from [3].

	Smooth flow $C_{D\mathrm{min}}$	Smooth flow $C_{L\mathrm{max}}$	VG flow $C_{L\mathrm{max}}$
FFA-W3-241	0.010	1.37	1.68
FFA-W3-301	0.015	1.30	1.64
NACA 63-425	0.007	1.30	N/A
NACA 63-430	0.011	1.10	1.37

In conclusion

- We now know the aerodynamic characteristics of the thick FFA-W3 and NACA 63-4xx airfoils.
- The agreement between Ellipsys2D and measurements is fair for FFA-W3-241 but not good for FFA-W3-301 and NACA 63-430. In general calculations overestimate maximum C_L and sometimes underestimate minimum C_D.
- Maximum C_L for smooth flow is in good agreement with calculated maximum C_L for leading edge transition flow and this could serve as a worst case calculation.
- We determined the influence from vortex generators and they should always be applied on thick airfoils to increase the maximum C_L.
- We determined the influence from leading edge roughness, which reduced maximum C_L and increased minimum C_D.
- The FFA-W3 airfoils were found better than the NACA 63-4xx airfoils for the inboard part of a wind turbine blade both with and without vortex generators.

References

[1]   Fuglsang, P., Antoniou, I., Sørensen, N.N., Madsen, H. Aa., 1998, 'Validation of a Wind Tunnel Testing Facility for Blade Surface Pressure Measurements.' Risø-R-981(EN), Risø National Laboratory, Denmark.

[2]   Timmer, W.A., van Rooy, R.P.J.O.M., 1992, Thick airfoils for HAWTs, J. of Wind Engineering and Industrial Aerodynamics, vol. 39 pp. 151-160.

[3]   Timmer, W.A., van Rooy, R.P.J.O.M., 1993, Wind Tunnel Results for a 25% Thick Wind Turbine Blade Airfoil. Proc. EUWEC'93, Lübeck-Travemünde, Germany, pp. 416 - 419.

[4]   Rae Jr., W.H., Pope, A., 1984, Low-Speed Wind Tunnel Testing, SE, John Wiley & Sons, ISBN 0-471-87402-7.

[5]   Brooks, T.F. and Marcolini, M.A., 1984, Airfoil Trailing Edge Flow Measurements and Comparison with Theory Incorporating Open Wind Tunnel Corrections, AIAA-84-2266, AIAA/NASA 9th Aeroacoustic Conference.

[6]   Björck, A., 1990, Coordinates and Calculations for the FFA-W1-xxx, FFA-W2-xxx and FFA-W3-xxx Series of Airfoils for Horizontal Axis Wind Turbines. FFA TN 1990-15. The Aeronautical Research Institute of Sweden.

[7]   Abbot, I.H., von Doenhoff, A.E., 1959, Theory of wing sections. Dower Publications, Inc. New York.

[8]   Timmer, W.A., 1992, The design and testing of airfoil DU 91-W2-250. Proc. IEA Joint Action. Aerodynamics of Wind Turbines. 6th Symposium.

[9]   Madsen, H.A., Filippone, A, 1995, Implementation and Test of the XFOIL Code for Airfoil Analysis and Design, Risø-R-644(EN), Risø National Laboratory, Denmark.

[10]   Drela, M., 1989, XFOIL: An Analysis and Design system for Low Reynolds Number Airfoils, In: Low Reynolds Number Aerodynamics, Springer-Verlag Lec. Notes in Eng. 54.

[11]   Sørensen, N.N., 1995, General Purpose Flow Solver Applied to Flow over Hills, Risø-R-827(EN), Risø National Laboratory, Denmark.

[12]   Menter, F.R., 1993, Zonal Two Equation k-ω Turbulence Models for Aerodynamic Flows. AIAA Paper 93-2906.

[13]   Michel, R., 1952, Etude de la transition sur les profiles d'aile. ONERA Report 1/1578-A. See White F.M., Viscous fluid flow, p. 442.

A Measurement survey

This appendix describes the performed measurements in detail to make the measurements stored on CD available for subsequent exploitation. The different measurement types are described and the naming convention for the data files is explained. The format of the data files is given and each performed measurement is listed and described.

A.1 List of symbols

H	[cm]	Wake rake vertical position, positive toward floor, origin at wake rake top
K		Reduced frequency
P	[Pa]	Static pressure
p_o	[Pa]	Total pressure head
p_{atm}	[Pa]	Atmospheric pressure
Q	[Pa]	Dynamic pressure
X		Airfoil chordwise coordinate relative to chord, positive toward trailing edge, origin at leading edge
Y		Airfoil vertical coordinate relative to chord, positive toward ceiling, origin at leading edge
A	[°]	Pitch motion amplitude
C_D		Drag coefficient
C_L		Lift coefficient
C_M		Moment coefficient
C_P		Airfoil pressure coefficient
Re		Reynolds number
T	[°C]	Air temperature
α	[°]	Angle of attack
ρ	[kg/m^3]	Air density

Subscripts

C	Corrected value
P	Pressure measurement (opposite to wake rake measurement)
W	Wake rake measurement
∞	Reference for normalisation of airfoil forces

A.2 Measurement types

There are four different basic types of measurements of the airfoil flow as shown in Table A-1:
- STEP
- CONT
- STAT
- PITCH

Table A-1 Overview of the different types of measurements that have been performed.

Name	Short description	Purpose
STEP	• Discrete measurements at different angles of attack. • Angle of attack range: -6° to 30°. • Interval between different angles: 1° to 4°. • Time series length: 20 s. • Sampling frequency: 5 Hz.	The lift, drag and moment polar versus angle of attack.
CONT	• Continuos measurements at different angles of attack. • Angle of attack range: -6° to 30°. • Rate of change of angle of attack: 0.1°/s to 0.5°/s (manually changed). • Time series length app: 250 s. • Sampling frequency: 50 Hz.	The lift, drag and moment polar versus angle of attack. (shorter measurement time compared to 'STEP')
STAT	• Stationary measurements at different angles of attack. • Time series length: 20s to 180s. • Sampling frequency: 100 Hz.	Time series of airfoil flow at different angles of attack, usually in stall.
PITCH	• Dynamic measurements at different mean angles of attack with the airfoil in pitching motion. • Pitching amplitude: 3° to 6° • Reduced frequency: to 0.12 • Time series length: 30s to 40s. • Sampling frequency: 100 Hz.	Time series of unsteady airfoil flow from pitching motion for determination of hysteresis loops for lift, drag and moment at different pitching frequencies and amplitudes.

A.3 Data file naming convention

The different data files are stored in the following directory structure:
• The name of the airfoil.
• The measurement type keyword from Table A-1.

Each data file is named by:
• The date of measurement, data, DD, month, MM, year, YY, 'DDMMYY'.
• A version number, VNN, where NN is the version number.
• The filename extension. For time averaged data, '.DAT', and for time series, 'NNN', where NNN is a time series run number.

As an example, the measurement of FFA-W3-241 airfoil of type *STEP* version *V1* performed on the 101297 is named, '101297*V1.DAT*' and stored in: '*ffaw3241\STEP*'.

A.4 Data file formats

The different data files are shown in Table A-2.

Table A-2 Available data files.

'data file name'.nnn	General data file with each measurement frame/average formatted in rows. The first two rows contain the column number and the sensor name. The format of the data files is described in Table A-3
'data file name'-10hz.nnn	For 'CONT', 'STAT' and 'PITCH' measurements the same as the general data file but the frames are averaged to 10 Hz scan rate.
'data file name'-pol.nnn	The same as the general data file but only column 1 to 15.
'data file name'-bin.nnn	For 'CONT' measurements where the measurement frames are sorted in bins of α_c. The angle of attack range is divided into 30 bins. The files contain 4 columns: 1. Corrected angle of attack 2. Lift coefficient 3. Drag coefficient 4. Moment coefficient
'data file name'-loop.nnn	For 'PITCH' measurements where the measured frames are sorted in bins of the phase in the hysteresis loop. The phase range is divided into 30 bins. The files contain 4 columns: 1. Corrected angle of attack 2. Lift coefficient 3. Drag coefficient 4. Moment coefficient

Table A-3 The content of the columns in the general data file.

Col.	Symbol	Sensor	Unit	Description
1	α_c	αc	°	Corrected angle of attack
2	C_L	cl	-	Lift coefficient (pressure)
3	C_{Dc}	cdc	-	Corrected drag coefficient (wake rake + pressure)
4	C_{Mc}	cmc	-	Corrected moment coefficient (pressure)
5	C_{Dpc}	cdpc	-	Corrected drag coefficient (pressure)
6[*]	C_{Dw}	cdw		Drag coefficient (wake rake)
7	α	α	°	Raw angle of attack
8	C_D	cd	-	Raw drag coefficient (wake rake + pressure)
9	C_{Dp}	cdp		Raw drag coefficient (pressure)
10	C_M	cm	-	Raw moment coefficient (pressure)
11	Re	re		Free stream Reynolds Number
12	q_∞	qref	Pa	Free stream dynamic pressure
13	p_∞	ps,ref	Pa	Free stream static pressure
14	T	t	°	Tunnel temperature
15	p_{atm}	patm	Mbar	Atmospheric pressure
16-71[**]	C_P	cp(x)		Pressure coefficients corresponding to the coordinates in top row
72-74	p_{1-3}	ps,Pitot()	Pa	Pitot tube static pressures
75-77	p_{o1-3}	pt,Pitot()	Pa	Pitot tube total pressures
78-82[*]	p_w	ps,wake	Pa	Wake rake static pressures corresponding to the coordinates in top row
83-136[*]	p_{ow}	pt,wake	Pa	Wake rake total pressures corresponding to the coordinates in top row

*) At the 'PITCH' type measurements, the wake rake was not used. C_{DW} was set to C_{DP} and p_w and p_{ow} were not written in the data files

**) In some measurements one or more of the airfoil pressure sensors were excluded because of unstable calibration or because the pressure hole was blocked by vortex generators or roughness elements. The corresponding column in the file was then removed and the number of subsequent sensors changed.

A.5 Additional files

For correct interpretation of C_P, p_w and p_{ow} at different sensors, the sensor locations for each measurement were listed in the files listed in Table A-4. These files were written for each of the measurement runs, since the number of used sensor was changed.

Table A-4 Additional data files that describe the sensor locations.

'data file name'.cor	Airfoil section pressure sensor file Three columns with: 1. Sensor number corresponding to C_P in the data file. 2. x-coordinate 3. y-coordinate
'data file name'.ws[*]	Wake rake static pressure sensor file Two columns with: 1. Sensor number corresponding to p_w in the data file 2. h-coordinate
'data file name'.wt[*]	Wake rake total pressure sensor file Two collumns with: 1. Sensor number corresponding to p_{ow} in the data file 2. h-coordinate

*) For the 'PITCH' type measurements these files were not written, since the wake rake was not used.

A.6 Performed measurements

Table A-5 to Table A-7 contain a list of the performed measurements for the different airfoil sections.

Table A-5 Performed measurements for FFA-W3-241

Data file	Extension	Description and remarks
\FFAW3241\ STEP\ 091297V1	000-018	• Smooth leading edge • 20s time series at 5 Hz for each α
	DAT	• 20s average values
\FFAW3241\ CONT\ 091297V1	003	• Vortex generators, Delft 6 mm, at x/c = 0.2 • 50 Hz time series at different α
\FFAW3241\ CONT\ 091297V2	000, 001	• Vortex generators, Delft 4 mm, at x/c = 0.2 • 50 Hz time series at different α
\FFAW3241\ CONT\ 091297V3	002, 003	• Vortex generators, Delft 6 mm, at x/c = 0.3 • 50 Hz time series at different α
\FFAW3241\ CONT\ 091297V4	000, 001	• Vortex generators, Delft 6 mm, at x/c = 0.3 • Leading edge roughness, 90° zigzag tape • 50 Hz time series at different α
\FFAW3241\ CONT\ 091297V5	000, 001	• Leading edge roughness, 90° zigzag tape • 50 Hz time series at different α
\FFAW3241\ CONT\ 091297V6	000, 001	• Leading edge roughness, 60° zigzag tape • 50 Hz time series at different α
\FFAW3241\ CONT\ 091297V7	000, 001	• Smooth leading edge • 50 Hz time series at different α
\FFAW3241\ CONT\ 091297V8	001, 002	• Vortex generators, Delft 4 mm, at x/c = 0.2 • Leading edge roughness, 90° zigzag tape • 50 Hz time series at different α
\FFAW3241\ CONT\ 091297V9	001, 002	• Leading edge roughness, bulge tape • 50 Hz time series at different α
\FFAW3241\ CONT\ 091297V10	001, 002	• Vortex generators, Delft 4 mm, at x/c = 0.1 • 50 Hz time series at different α

\FFAW3241\ PITCH\ 091297V1	000-009	• Smooth leading edge • Amplitude between 1.4° to 2.0° • Reduced frequency, k = 0.093 • 30 s time series at 100 Hz for each α
\FFAW3241\ PITCH\ 091297V2	000-009	• Smooth leading edge • Amplitude between 1.4° to 2.0° • Reduced frequency, k = 0.070 • 30 s time series at 100 Hz for each α
\FFAW3241\ PITCH\ 091297V3	000-009	• Vortex generators, Delft 6 mm, at x/c = 0.2 • Amplitude between 1.4° to 2.0° • Reduced frequency, k = 0.093 • 30 s time series at 100 Hz for each α

Table A-6 Performed measurements for FFA-W3-301

Data file	Extension	Description and remarks
\FFAW3301\ STEP\ 091297V1	001-018, 020-038	• Smooth leading edge • 20s time series at 5 Hz for each α
	DAT	• 20s average values
\FFAW3301\ CONT\ 091297V1	000	• Vortex generators, Delft 6 mm, at x/c = 0.3 • 50 Hz time series at different α
\FFAW3301\ CONT\ 091297V2	000, 001	• Vortex generators, Delft 6 mm, at x/c = 0.3 • Leading edge roughness, 90° zigzag tape • 50 Hz time series at different α
\FFAW3301\ CONT\ 091297V3	000, 001	• Leading edge roughness, 90° zigzag tape • 50 Hz time series at different α
\FFAW3301\ CONT\ 091297V4	000, 001	• Smooth leading edge • 50 Hz time series at different α
\FFAW3301\ CONT\ 091297V5	001, 002	• Vortex generators, Delft 6 mm, at x/c = 0.2 • 50 Hz time series at different α
\FFAW3301\ PITCH\ 091297V1	000-009	• Smooth leading edge • Amplitude between 1.4° to 2.0° • Reduced frequency, k = 0.093 • 30 s time series at 100 Hz for each α
\FFAW3301\ PITCH\ 091297V2	000-009	• Smooth leading edge • Amplitude between 1.4° to 2.0° • Reduced frequency, k = 0.070 • 30 s time series at 100 Hz for each α

Table A-7 Performed measurements for NACA 63-430

Data file	Extension	Description and remarks
\NA63430\ STEP\ 091297V1	001-018	• Smooth leading edge • 20s time series at 5 Hz for each α
	DAT	• 20s average values
\NA63430\ CONT\ 091297V1	000, 001	• Vortex generators, Delft 6 mm, at x/c = 0.3 • 50 Hz time series at different α
\NA63430\ CONT\ 091297V2	001, 002	• Vortex generators, Delft 6 mm, at x/c = 0.3 • Leading edge roughness, 90° zigzag tape • 50 Hz time series at different α
\NA63430\ CONT\ 091297V3	001, 002	• Leading edge roughness, 90° zigzag tape • 50 Hz time series at different α
\NA63430\ CONT\ 091297V4	000, 001	• Smooth leading edge • 50 Hz time series at different α
\NA63430\ CONT\ 091297V5	001, 001, 002	• Vortex generators, Delft 6 mm, at x/c = 0.2 • 50 Hz time series at different α
\NA63430\ PITCH\ 091297V1	000-009	• Smooth leading edge • Amplitude between 1.4° to 2.0° • Reduced frequency, k = 0.093 • 30 s time series at 100 Hz for each α
\NA63430\ PITCH\ 091297V2	000, 002-009	• Smooth leading edge • Amplitude between 1.4° to 2.0° • Reduced frequency, k = 0.070 • 30 s time series at 100 Hz for each α

B FFA-W3-241 Vortex generators

B.1 Delft Vortex generators, *h* = 6 mm at *x/c* = 0.2
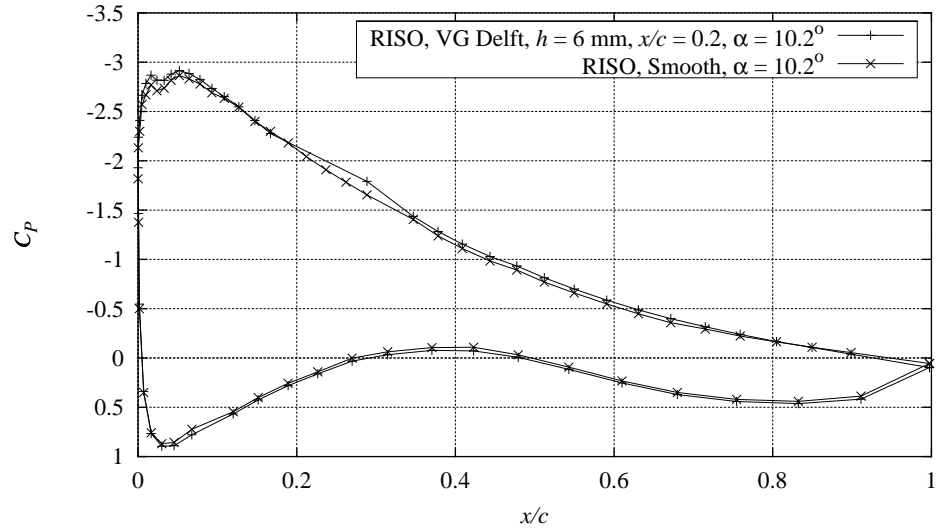
Figure B-1 Measured C_P distribution with Delft vortex generators, h = 6 mm, x/c = 0.2, compared with smooth measurement, Re = 1.6×10^{6}, α = 10.2° (FFAW3241CONT091297V1).
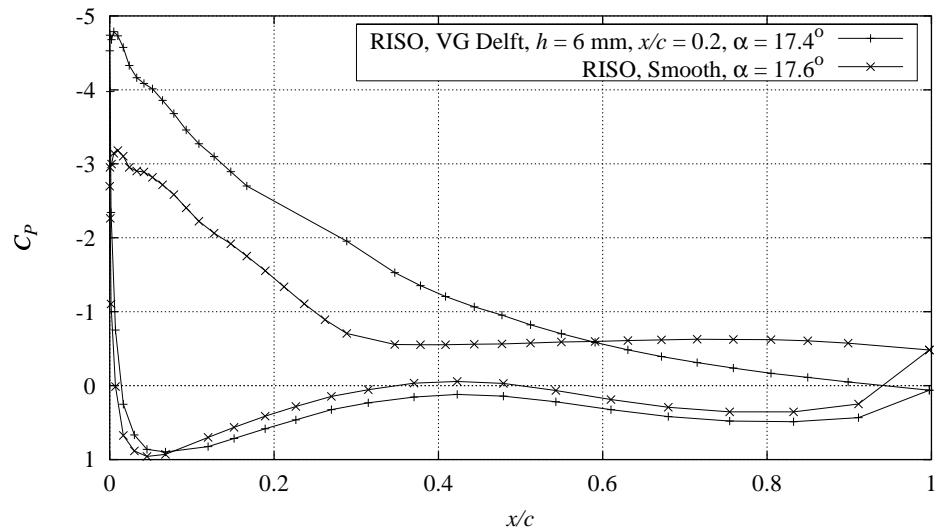
Figure B-2 Measured C_P distribution with Delft vortex generators, h = 6 mm, x/c = 0.2, compared with smooth measurement, Re = 1.6×10^{6}, α = 17.4° (FFAW3241CONT091297V1).
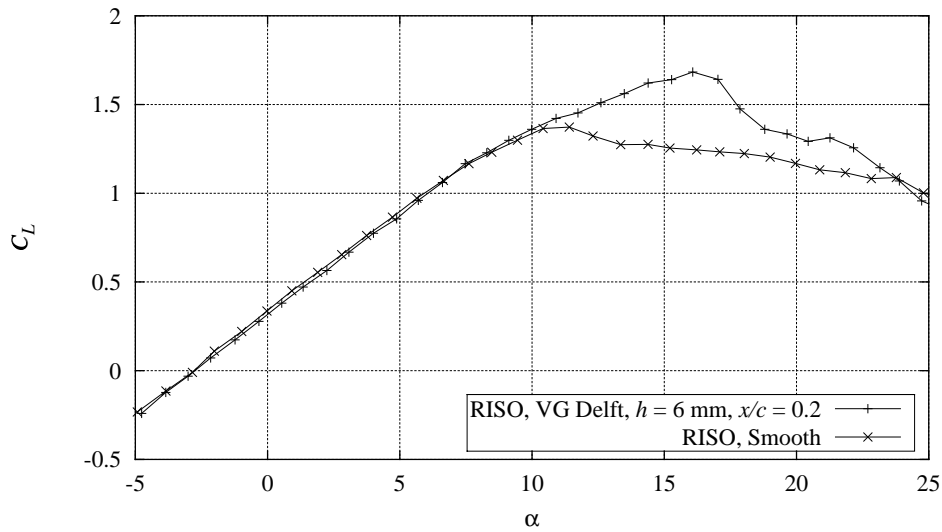
Figure B-3 Measured C_L curve with Delft vortex generators, h = 6 mm, x/c = 0.2, compared with smooth measurement, Re = 1.6×10^6, (FFAW3241CONT091297V1).
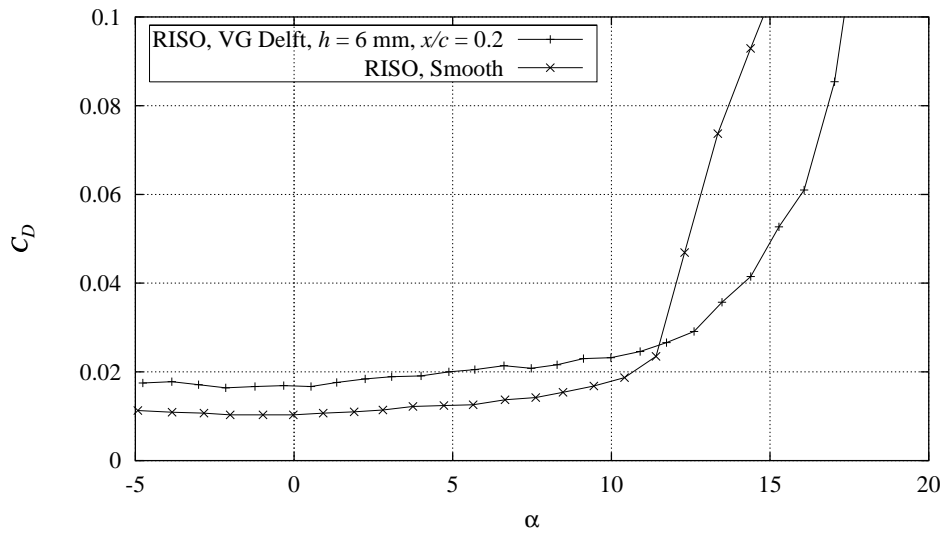
Figure B-4 Measured C_D curve with Delft vortex generators, h = 6 mm, x/c = 0.2, compared with smooth measurement, Re = 1.6×10^6, (FFAW3241CONT091297V1).
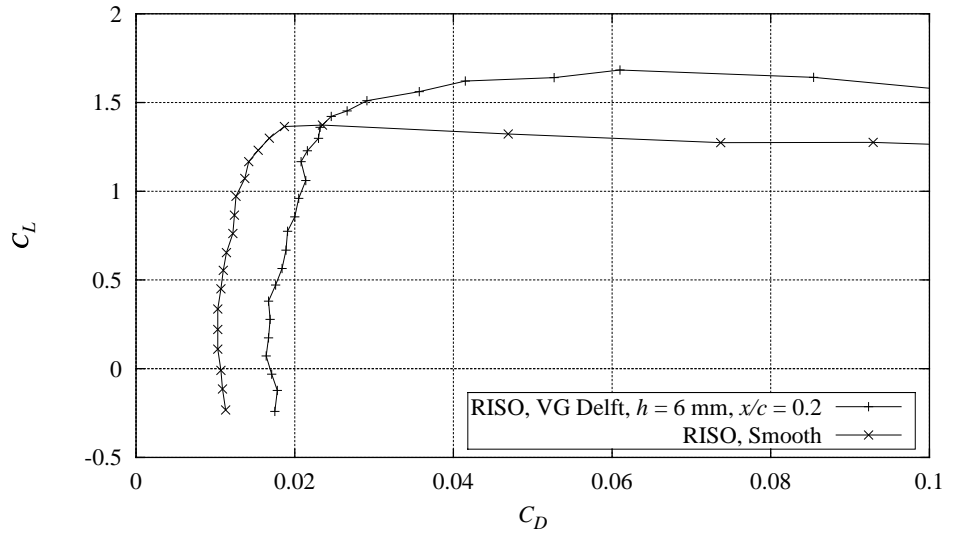
Figure B-5 Measured C_L-C_D curve with Delft vortex generators, h = 6 mm, x/c = 0.2, compared with smooth measurement, Re = 1.6×10^6, (FFAW3241CONT091297V1).
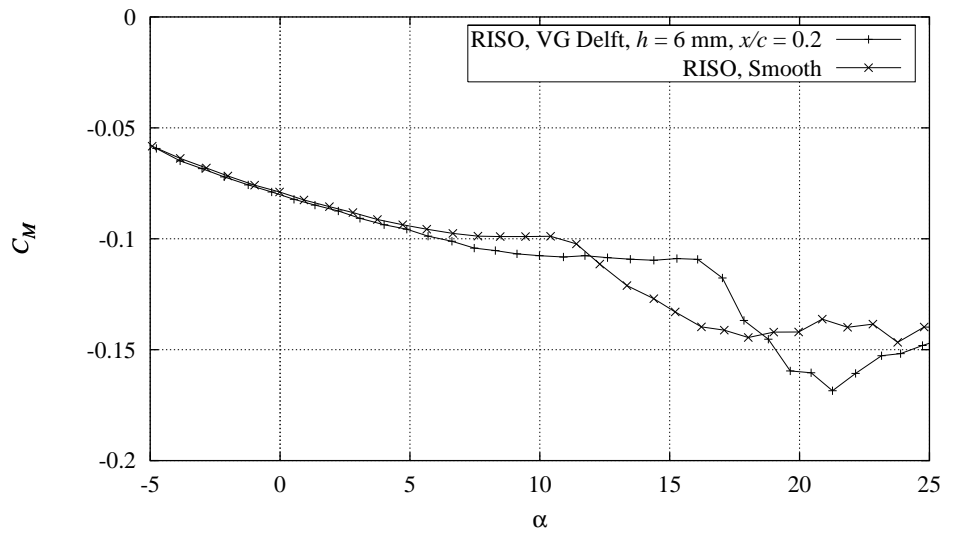
Figure B-6 Measured C_M curve with Delft vortex generators, h = 6 mm, x/c = 0.2, compared with smooth measurement, Re = 1.6×10^6, (FFAW3241CONT091297V1).

B.2 Delft Vortex generators, h = 6 mm at x/c = 0.3
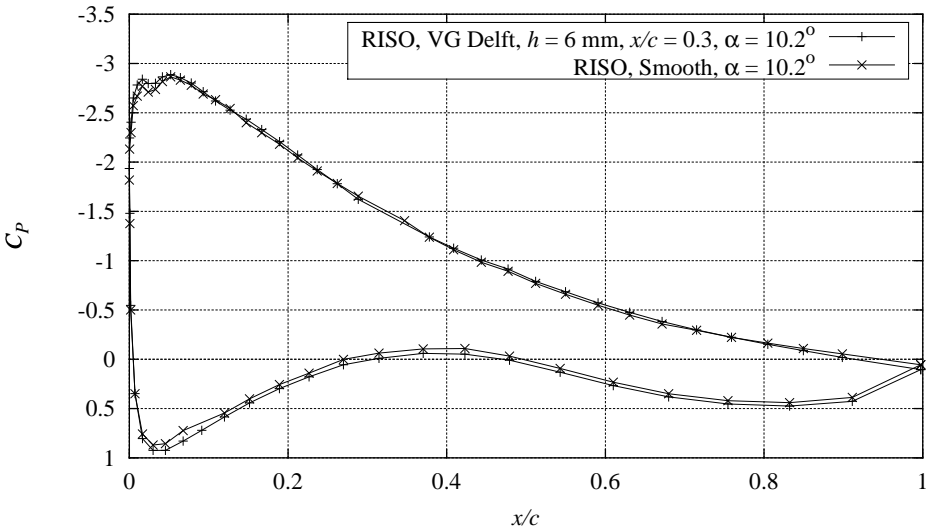
Figure B-7 Measured C_P distribution with Delft vortex generators, h = 6 mm, x/c = 0.3, compared with smooth measurement, Re = 1.6×10⁶, α = 10.2° (FFAW3241CONT091297V3).
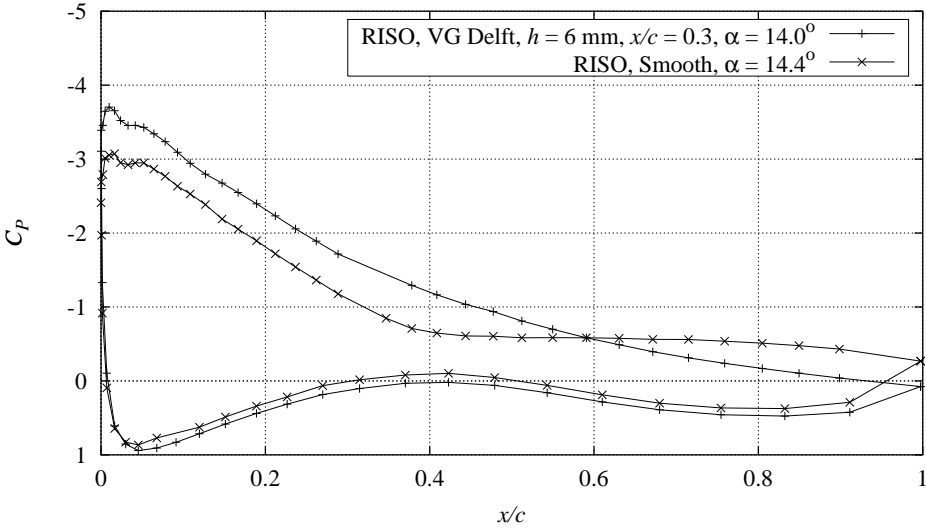
Figure B-8 Measured C_P distribution with Delft vortex generators, h = 6 mm, x/c = 0.3, compared with smooth measurement, Re = 1.6×10⁶, α = 14.0° (FFAW3241CONT091297V3).
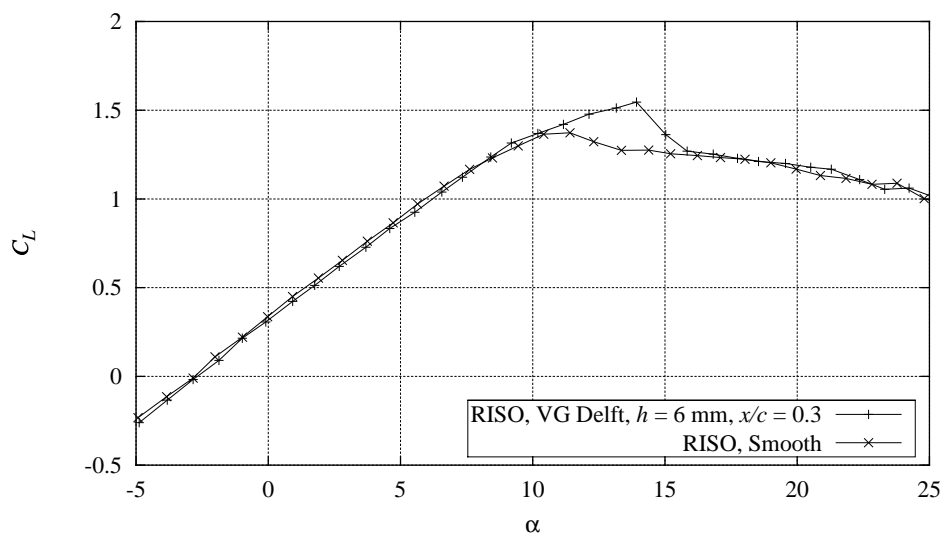
Figure B-9 Measured C_L curve with Delft vortex generators, h = 6 mm, x/c = 0.3, compared with smooth measurement, Re = 1.6×10^{6} (FFAW3241CONT091297V3).
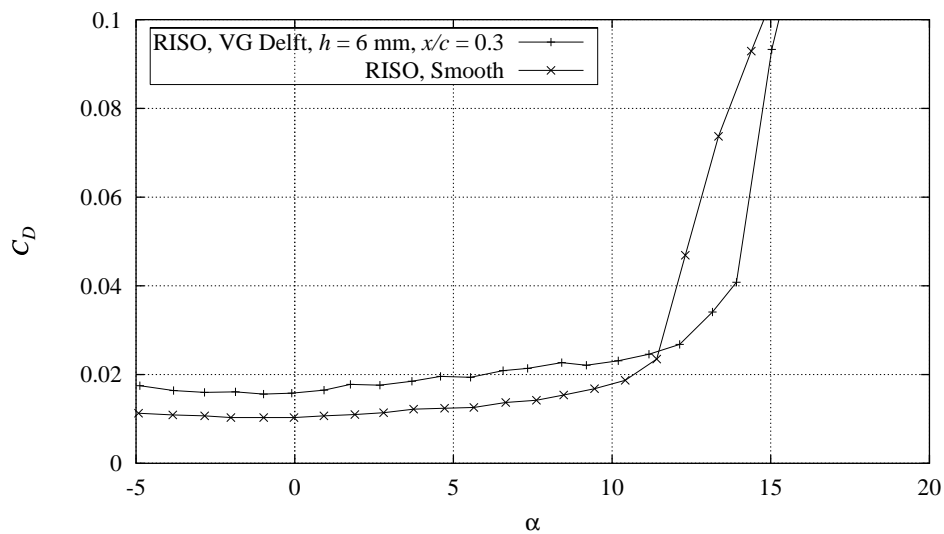
Figure B-10 Measured C_D curve with Delft vortex generators, h = 6 mm, x/c = 0.3, compared with smooth measurement, Re = 1.6×10^{6} (FFAW3241CONT091297V3).
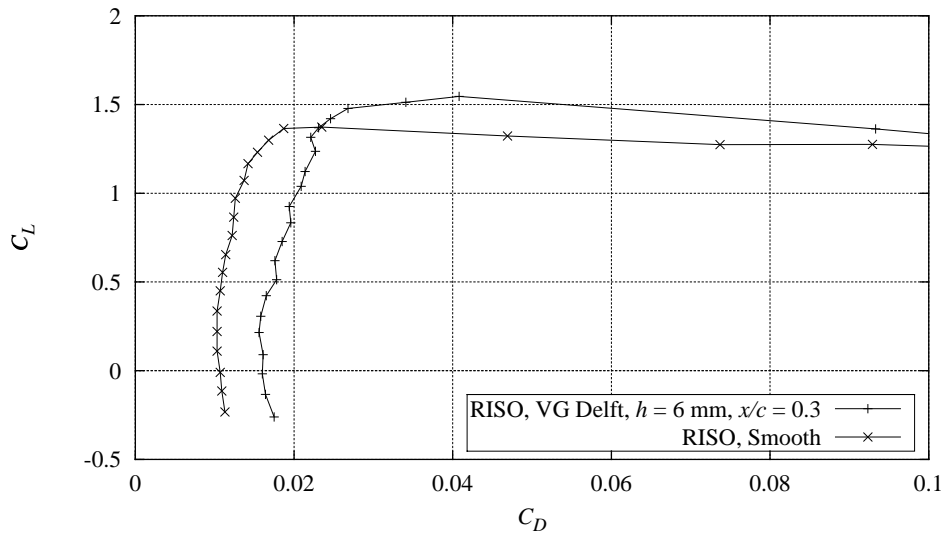
Figure B-11 Measured C_L-C_D curve with Delft vortex generators, h = 6 mm, x/c = 0.3, compared with smooth measurement, Re = 1.6×10⁶ (FFAW3241CONT091297V3).
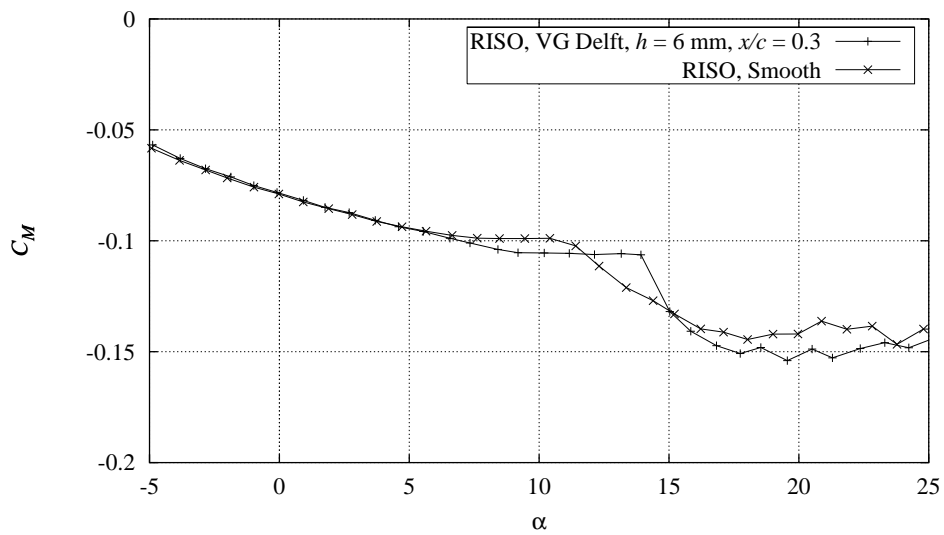
Figure B-12 Measured C_M curve with Delft vortex generators, h = 6 mm, x/c = 0.3, compared with smooth measurement, Re = 1.6×10⁶ (FFAW3241CONT091297V3).

B.3 Delft Vortex generators, *h* = 4 mm at *x/c* = 0.1
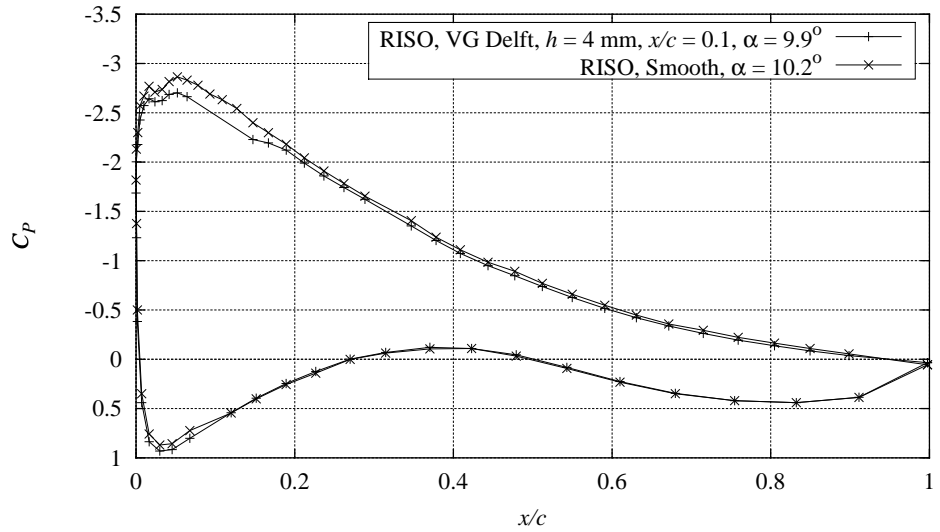
Figure B-13 Measured C_P distribution with Delft vortex generators, h = 4 mm, x/c = 0.1, compared with smooth measurement, Re = 1.6×10⁶, α = 9.9° (FFAW3241CONT091297V10).
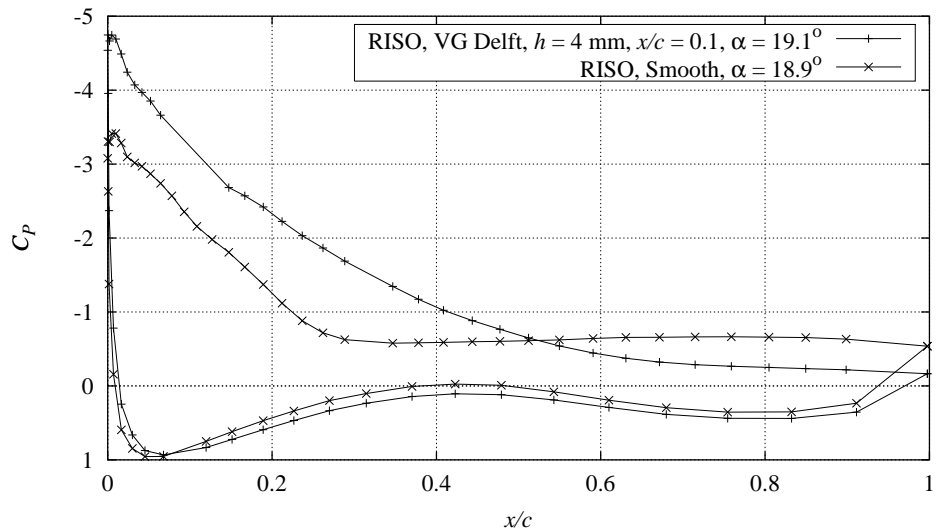
Figure B-14 Measured C_P distribution with Delft vortex generators, h = 4 mm, x/c = 0.1, compared with smooth measurement, Re = 1.6×10⁶, α = 19.1° (FFAW3241CONT091297V10).
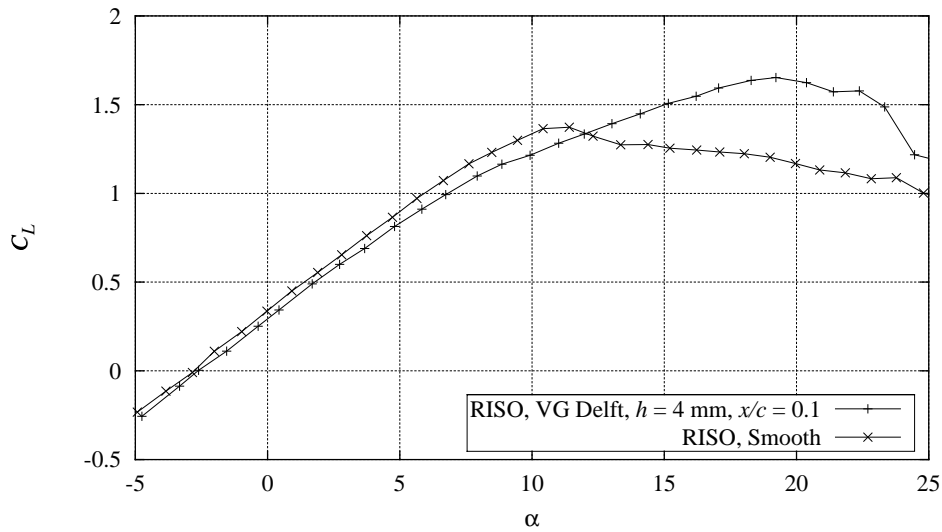
Figure B-15 Measured C_L curve with Delft vortex generators, h = 4 mm, x/c = 0.1, compared with smooth measurement, Re = 1.6×10^6 (FFAW3241CONT091297V10).
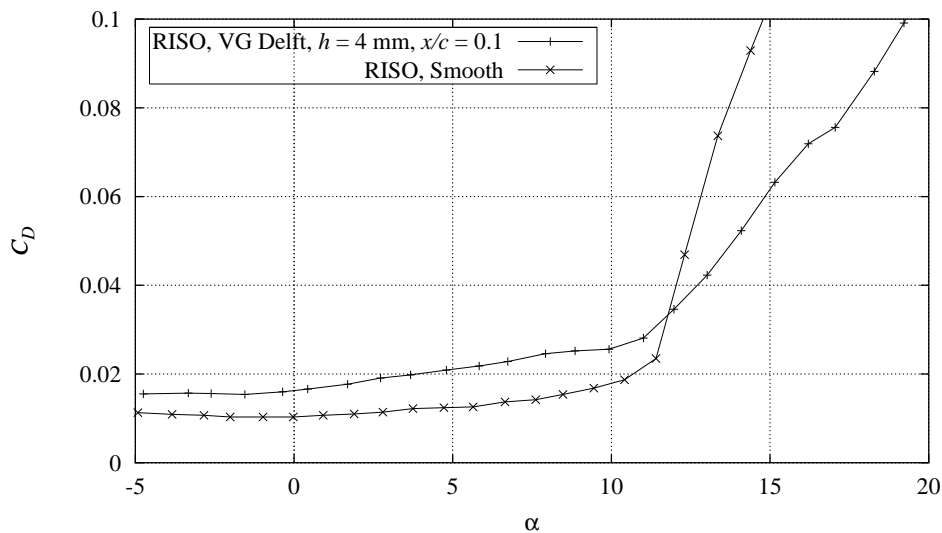
Figure B-16 Measured C_D curve with Delft vortex generators, h = 4 mm, x/c = 0.1, compared with smooth measurement, Re = 1.6×10^6 (FFAW3241CONT091297V10).
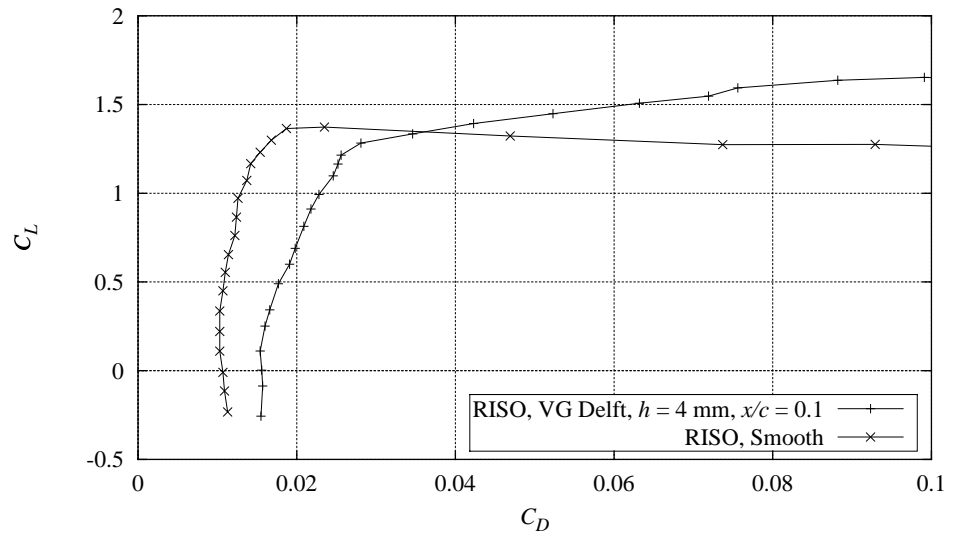
Figure B-17 Measured C_L-C_D curve with Delft vortex generators, h = 4 mm, x/c = 0.1, compared with smooth measurement, Re = 1.6×10^6 (FFAW3241CONT091297V10).
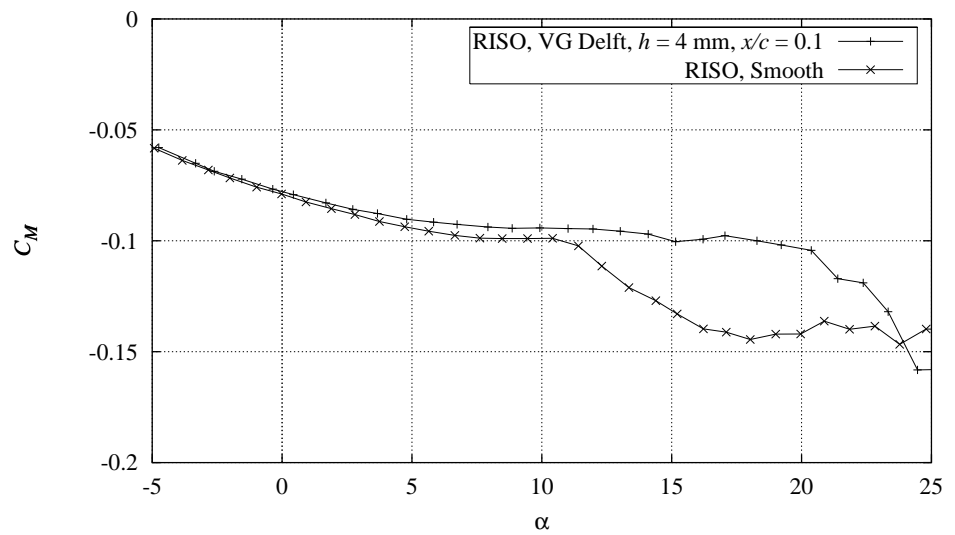
Figure B-18 Measured C_M curve with Delft vortex generators, h = 4 mm, x/c = 0.1, compared with smooth measurement, Re = 1.6×10^6 (FFAW3241CONT091297V10).

B.4 Delft Vortex generators, *h* = 4 mm at *x/c* = 0.2
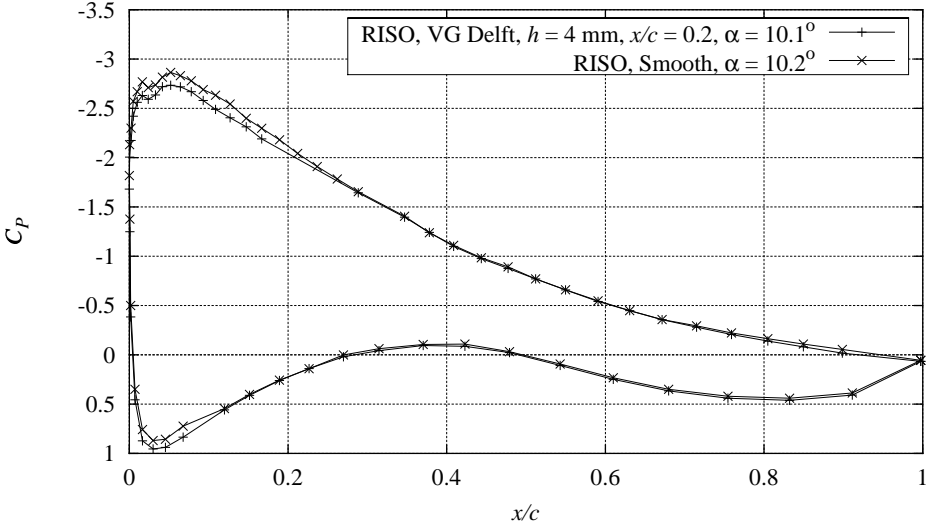
Figure B-19 Measured C_P distribution with Delft vortex generators, h = 4 mm, x/c = 0.2, compared with smooth measurement, Re = 1.6×10^6, α = 10.1° (FFAW3241CONT091297V2).
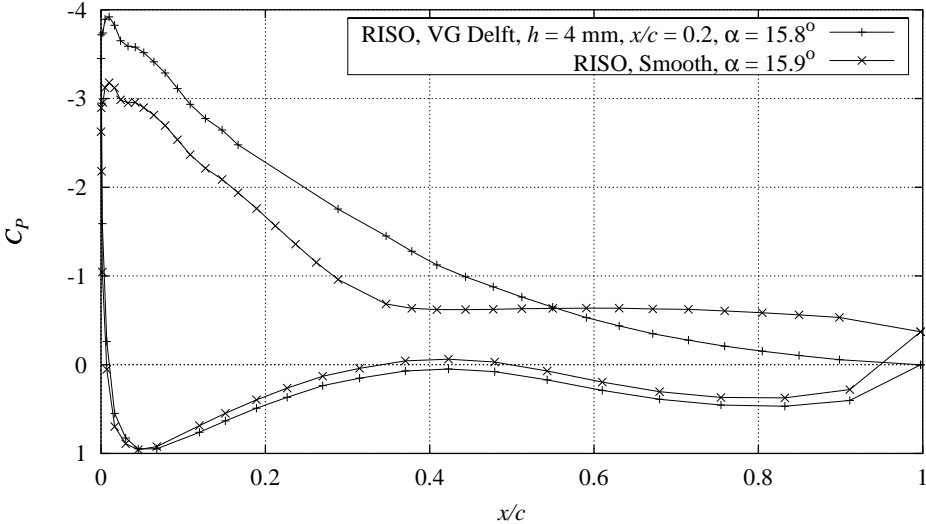
Figure B-20 Measured C_P distribution with Delft vortex generators, h = 4 mm, x/c = 0.2, compared with smooth measurement, Re = 1.6×10^6, α = 15.8° (FFAW3241CONT091297V2).
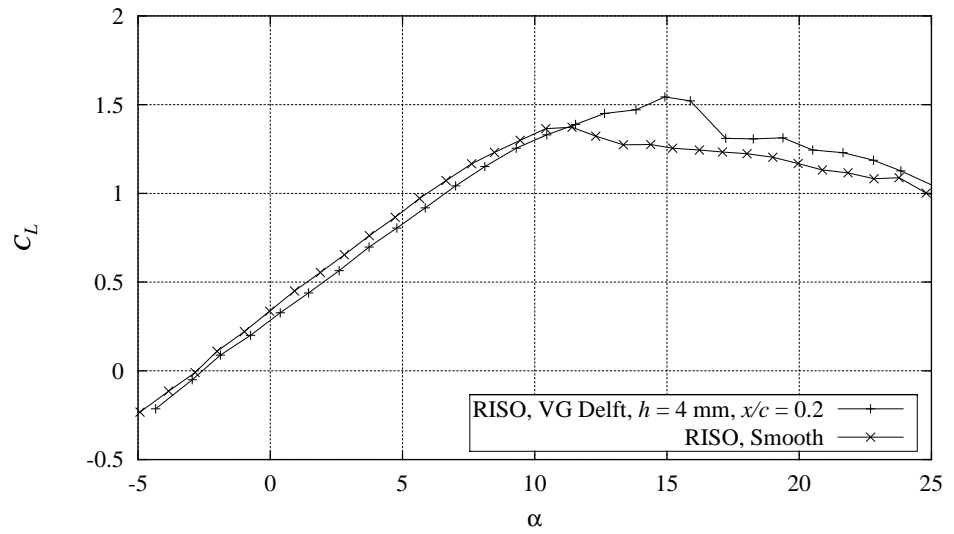
Figure B-21 Measured C_L curve with Delft vortex generators, h = 4 mm, x/c = 0.2, compared with smooth measurement, Re = 1.6×10⁶ (FFAW3241CONT091297V2).
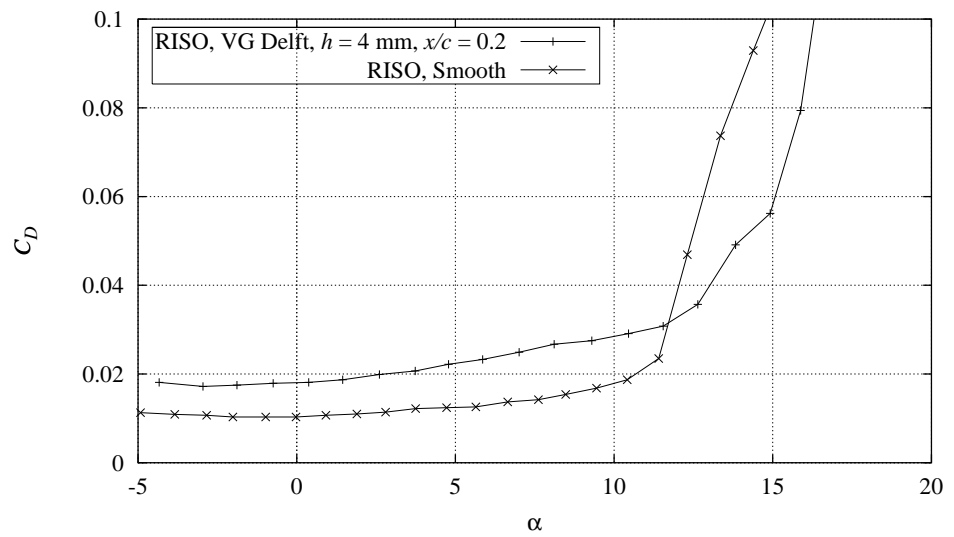
Figure B-22 Measured C_D curve with Delft vortex generators, h = 4 mm, x/c = 0.2, compared with smooth measurement, Re = 1.6×10⁶ (FFAW3241CONT091297V2).

Risø-R-1041(EN)
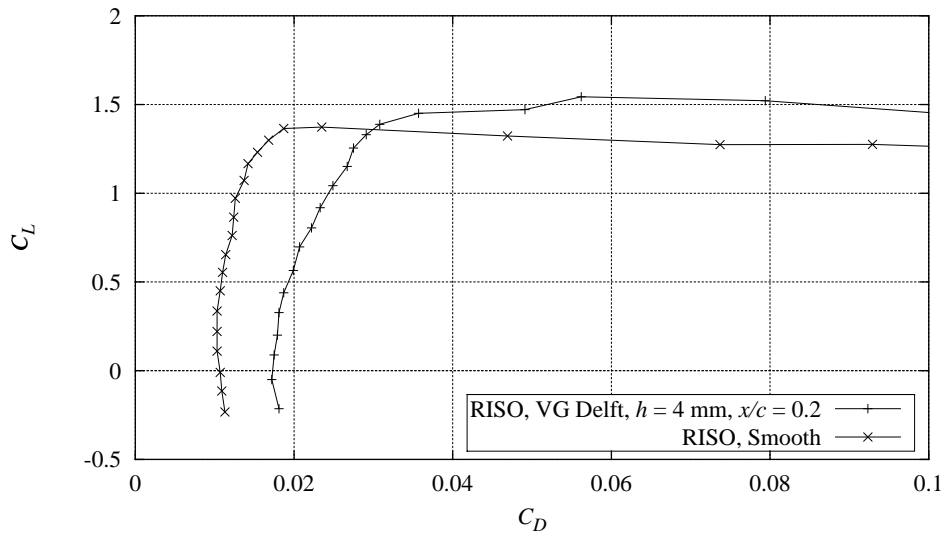
Figure B-23 Measured C_L-C_D curve with Delft vortex generators, h = 4 mm, x/c = 0.2, compared with smooth measurement, Re = 1.6×10^6 (FFAW3241CONT091297V2).
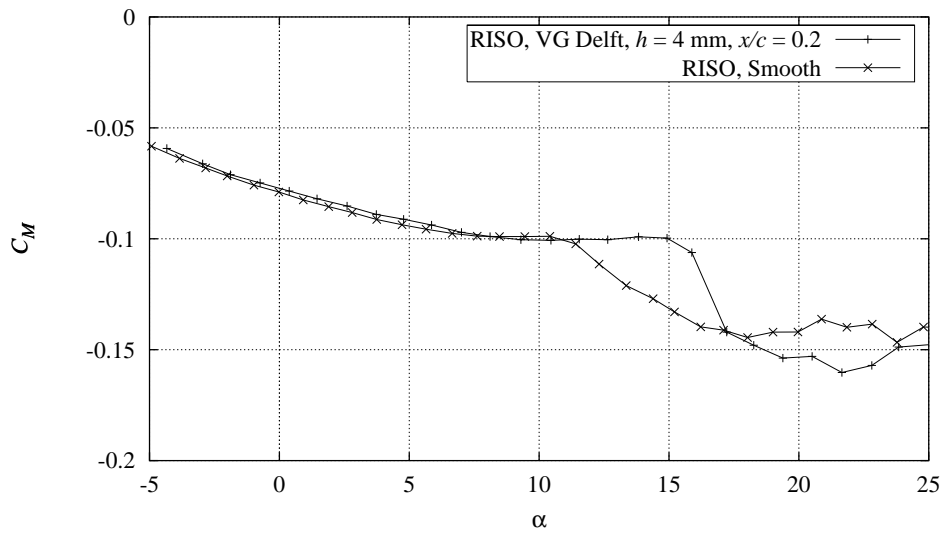
Figure B-24 Measured C_M curve with Delft vortex generators, h = 4 mm, x/c = 0.2, compared with smooth measurement, Re = 1.6×10^6 (FFAW3241CONT091297V2).
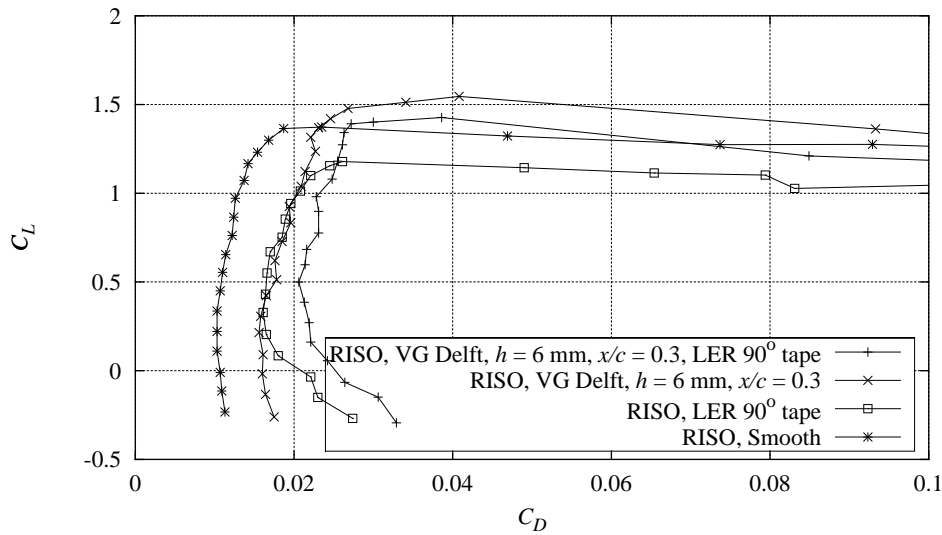
C FFA-W3-241 Leading edge roughness

C.1 90° zigzag trip tape
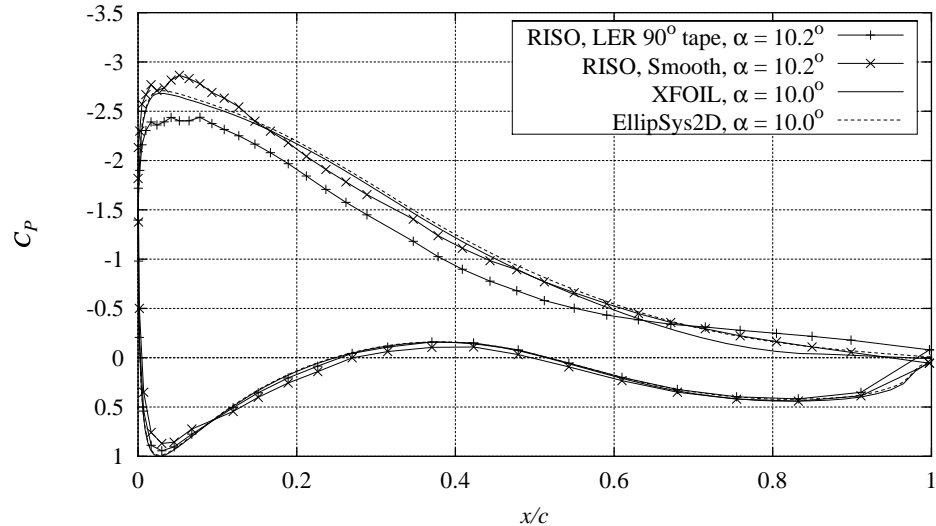
Figure C-1 Measured C_P distribution for 90° zigzag trip tape compared with smooth measurement and XFOIL (LE transition) and EllipSys2D (turbulent) calculations, Re = 1.6×10⁶, α = 10.2°(FFAW3241CONT091297V5).
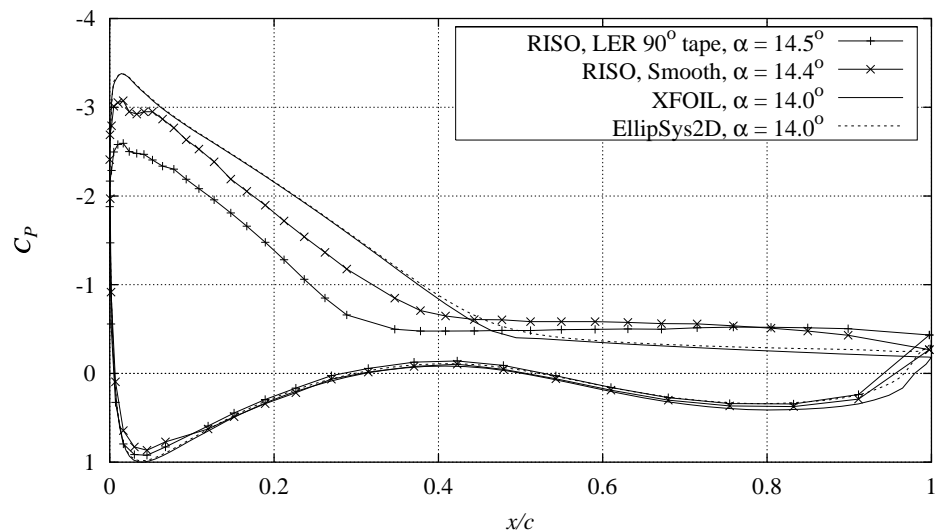
Figure C-2 Measured C_P distribution for 90° zigzag trip tape compared with smooth measurement and XFOIL (LE transition) and EllipSys2D (turbulent) calculations, Re = 1.6×10⁶, α = 14.5°(FFAW3241CONT091297V5).
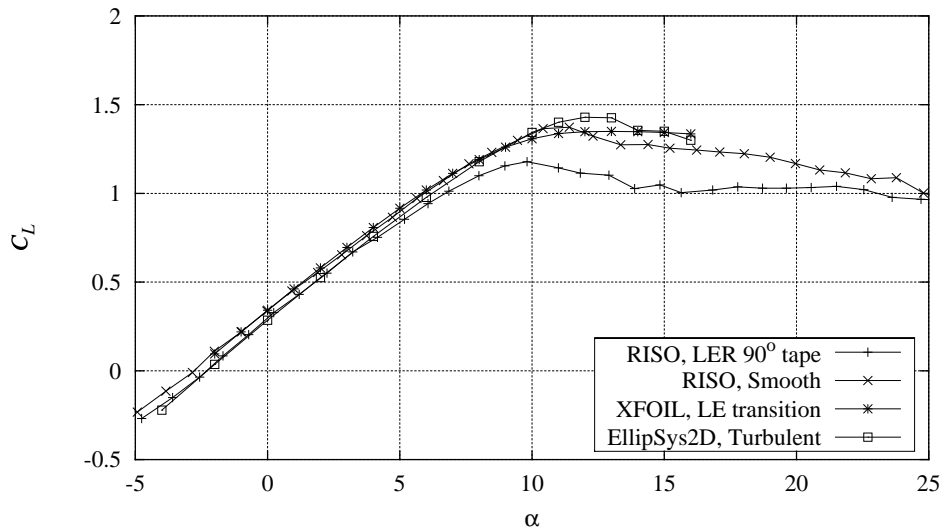
Figure C-3 Measured C_L curve for 90° zigzag trip tape compared with smooth measurement and XFOIL (LE transition) and EllipSys2D (turbulent) calculations, Re = 1.6×10^6 (FFAW3241CONT091297V5).
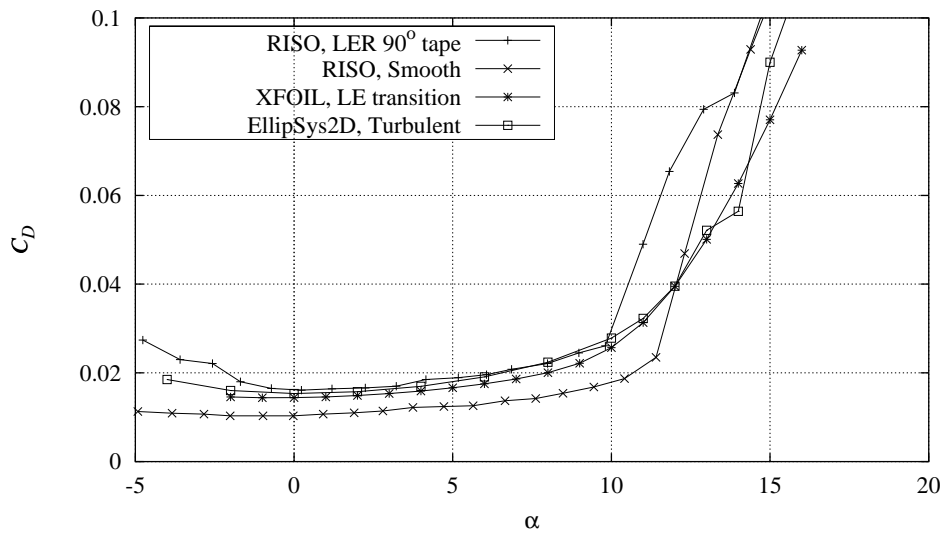
Figure C-4 Measured C_D curve for 90° zigzag trip tape compared with smooth measurement and XFOIL (LE transition) and EllipSys2D (turbulent) calculations, Re = 1.6×10^6 (FFAW3241CONT091297V5).
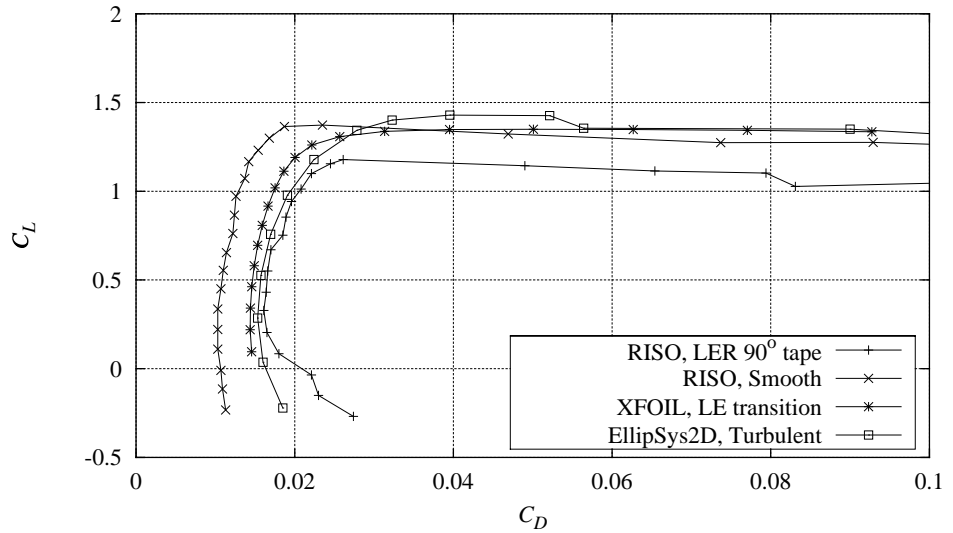
Figure C-5 Measured C_L-C_D curve for 90° zigzag trip tape compared with smooth measurement and XFOIL (LE transition) and EllipSys2D (turbulent) calculations, Re = 1.6×10^6 (FFAW3241CONT091297V5).
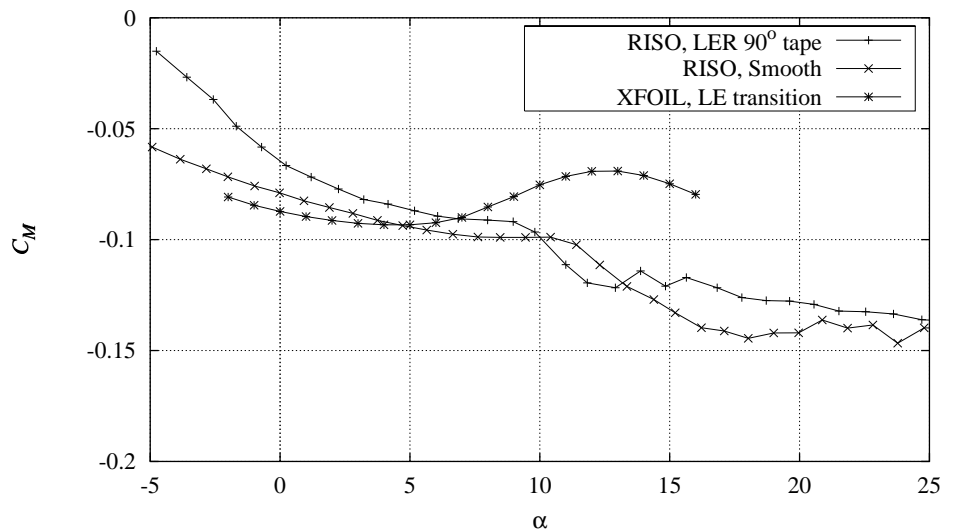
Figure C-6 Measured C_M curve for 90° zigzag trip tape compared with smooth measurement and XFOIL (LE transition) calculations, Re = 1.6×10^6 (FFAW3241CONT091297V5).

C.2 60° zigzag trip tape
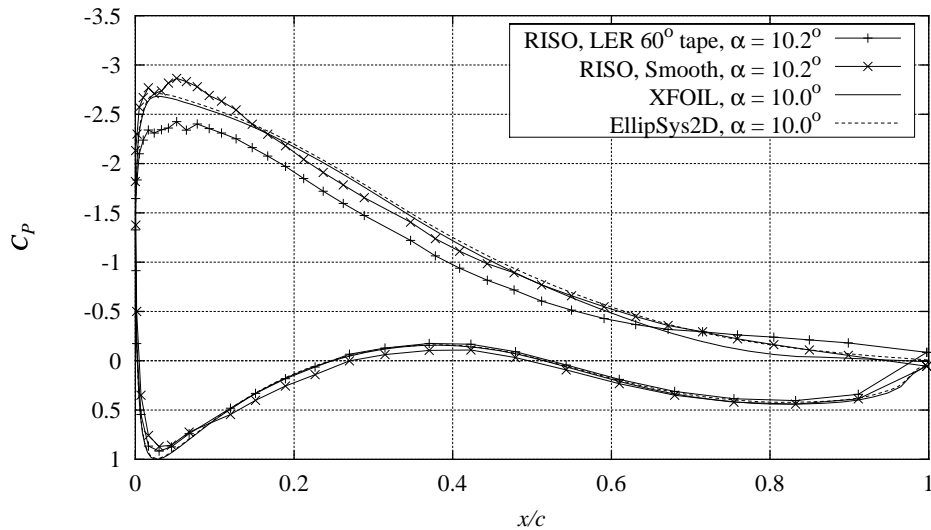
Figure C-7 Measured C_P distribution for 60° zigzag trip tape compared with smooth measurement and XFOIL (LE transition) and EllipSys2D (turbulent) calculations, Re = 1.6×10^6, α = 10.2°(FFAW3241CONT091297V6).
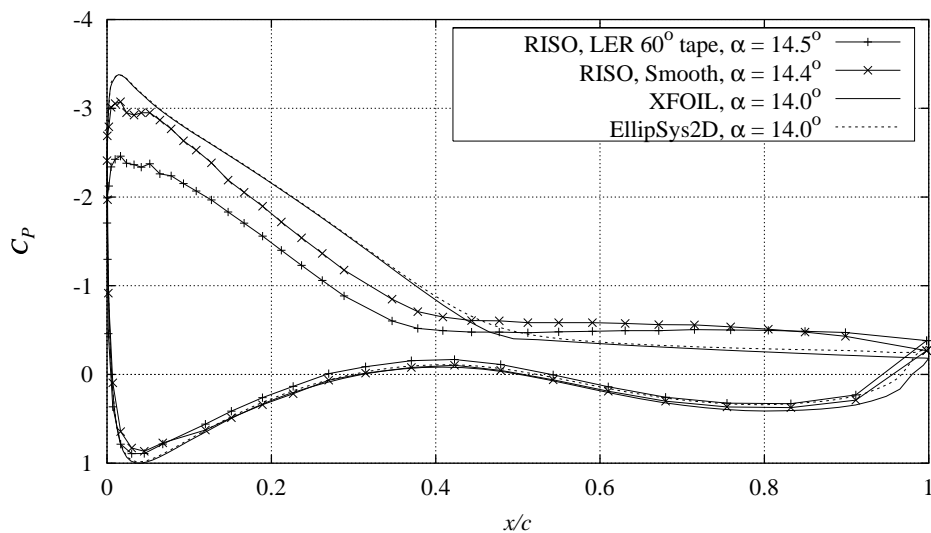
Figure C-8 Measured C_P distribution for 60° zigzag trip tape compared with smooth measurement and XFOIL (LE transition) and EllipSys2D (turbulent) calculations, Re = 1.6×10^6, α = 14.5°(FFAW3241CONT091297V6).
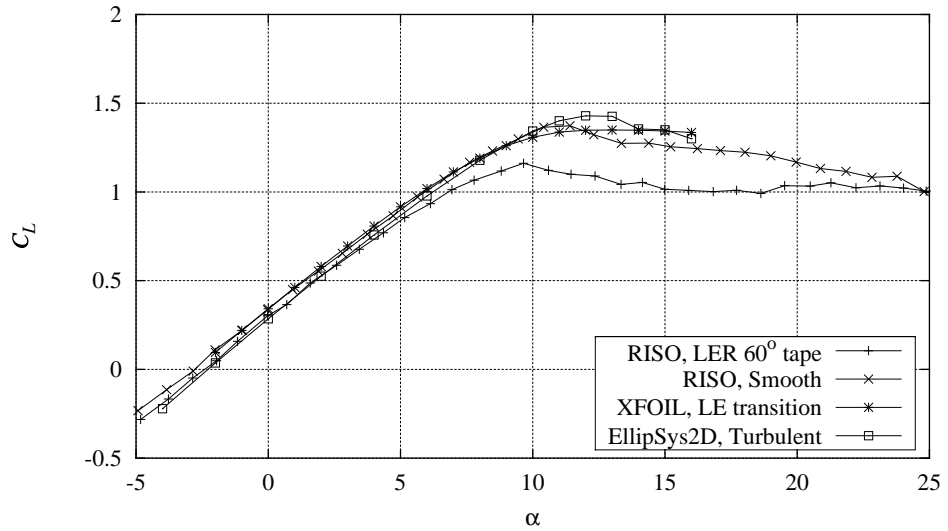
Figure C-9 Measured C_L curve for 60° zigzag trip tape compared with smooth measurement and XFOIL (LE transition) and EllipSys2D (turbulent) calculations, Re = 1.6×10^6 (FFAW3241CONT091297V6).
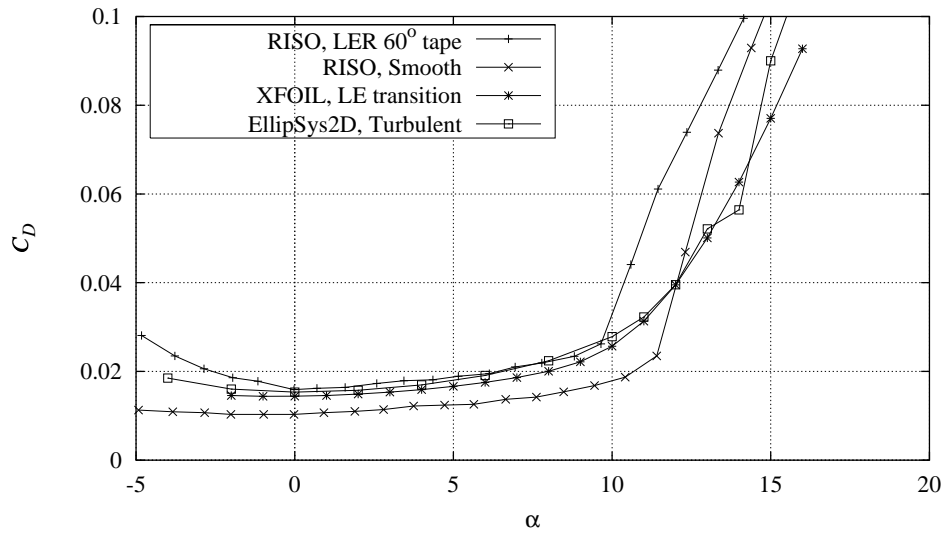
Figure C-10 Measured C_D curve for 60° zigzag trip tape compared with smooth measurement and XFOIL (LE transition) and EllipSys2D (turbulent) calculations, Re = 1.6×10^6 (FFAW3241CONT091297V6).
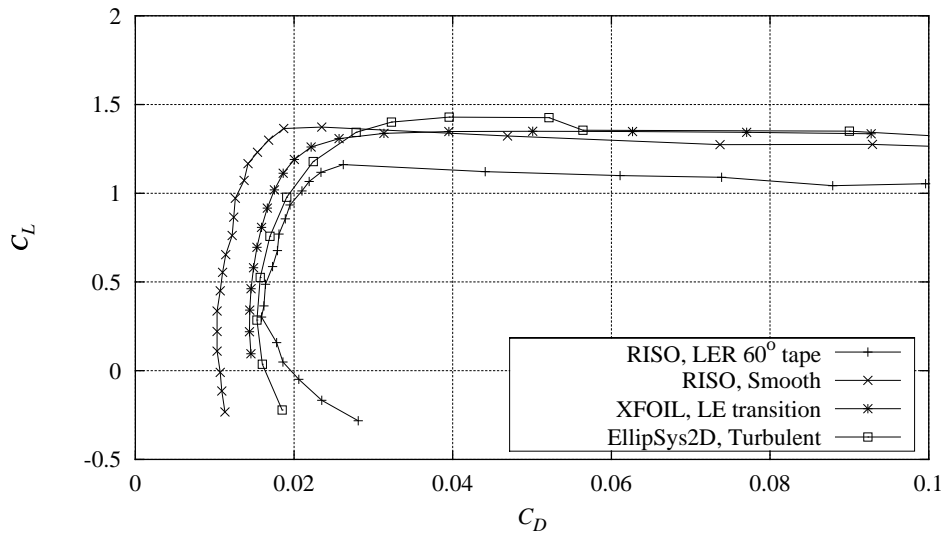
Figure C-11 Measured C_L-C_D curve for 60° zigzag trip tape compared with smooth measurement and XFOIL (LE transition) and EllipSys2D (turbulent) calculations, Re = 1.6×10^6 (FFAW3241CONT091297V6).
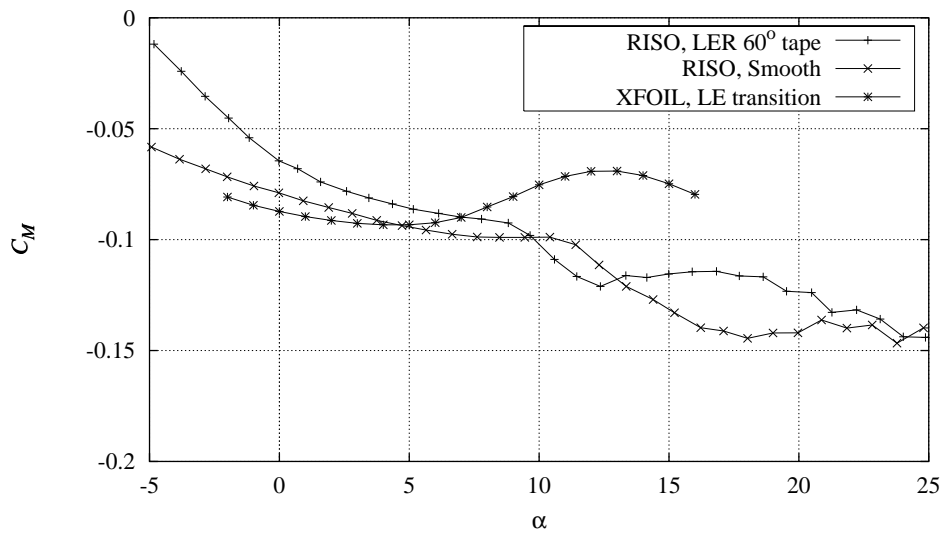
Figure C-12 Measured C_M curve for 60° zigzag trip tape compared with smooth measurement and XFOIL (LE transition) calculations, Re = 1.6×10^6 (FFAW3241CONT091297V6).

C.3 Bulge tape
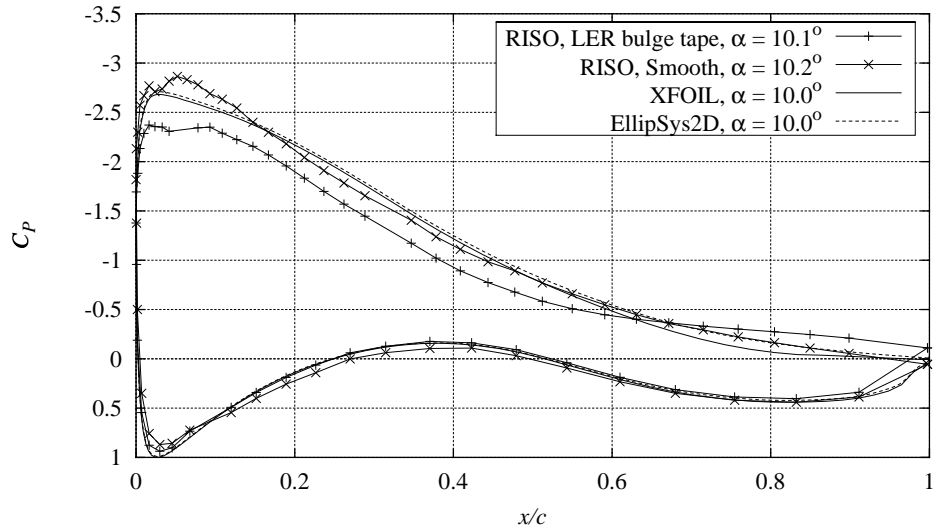
Figure C-13 Measured C_P distribution for bulge tape compared with smooth measurement and XFOIL (LE transition) and EllipSys2D (turbulent) calculations, Re = 1.6×10⁶, α = 10.1°(FFAW3241CONT091297V9).
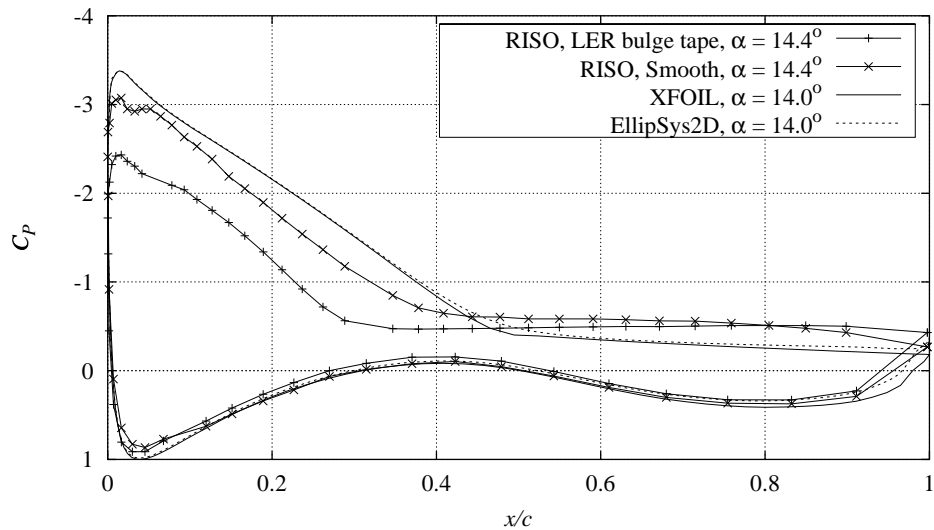
Figure C-14 Measured C_P distribution for bulge tape compared with smooth measurement and XFOIL (LE transition) and EllipSys2D (turbulent) calculations, Re = 1.6×10⁶, α = 14.4°(FFAW3241CONT091297V9).
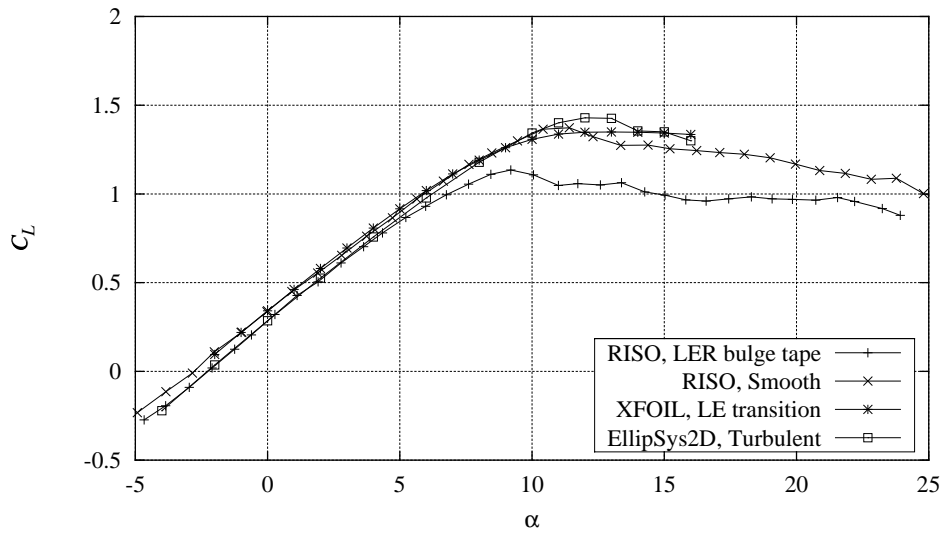
Figure C-15 Measured C_L curve for bulge tape compared with smooth measurement and XFOIL (LE transition) and EllipSys2D (turbulent) calculations, Re = 1.6×10^6 (FFAW3241CONT091297V9).
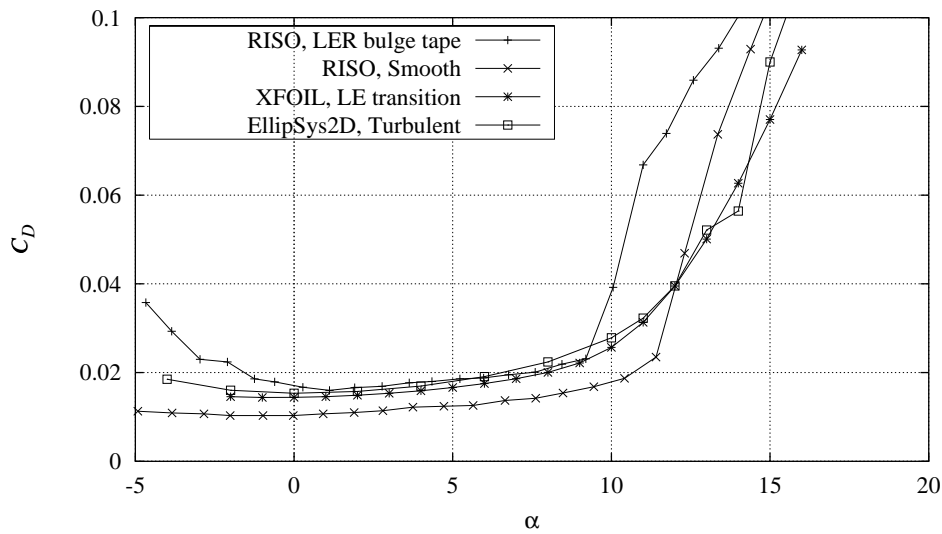
Figure C-16 Measured C_D curve for bulge tape compared with smooth measurement and XFOIL (LE transition) and EllipSys2D (turbulent) calculations, Re = 1.6×10^6 (FFAW3241CONT091297V9).
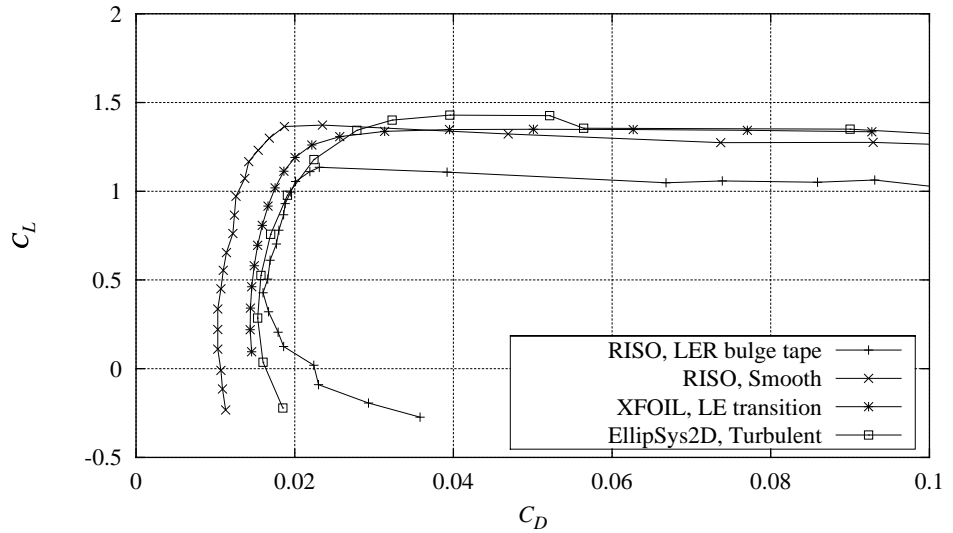
Figure C-17 Measured C_L-C_D curve for bulge tape compared with smooth measurement and XFOIL (LE transition) and EllipSys2D (turbulent) calculations, Re = 1.6×10⁶ (FFAW3241CONT091297V9).
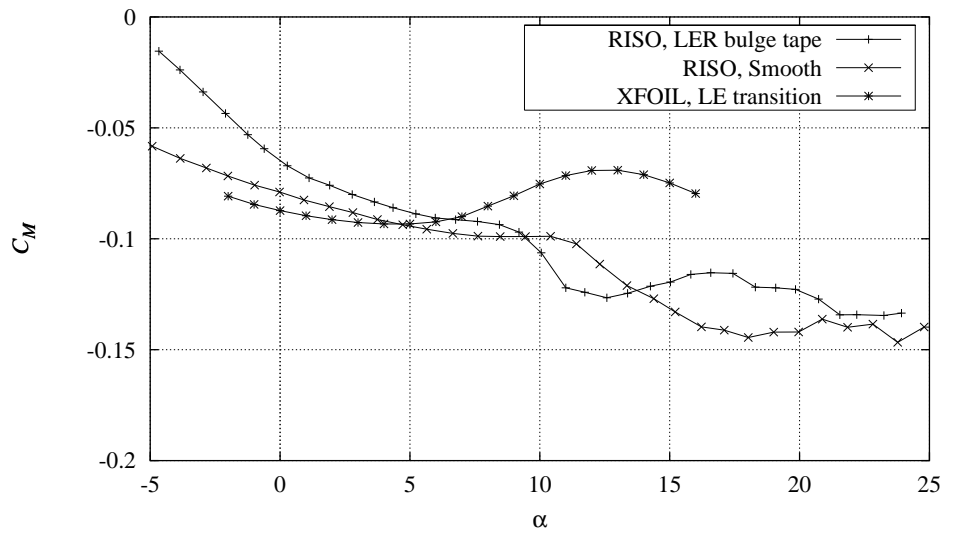
Figure C-18 Measured C_M curve for bulge tape compared with smooth measurement and XFOIL (LE transition) calculations, Re = 1.6×10⁶ (FFAW3241CONT091297V9).

D FFA-W3-241 Leading edge roughness and vortex generators

D.1 Delft vortex generators, h = 6 mm at x/c = 0.3, 90° zigzag trip tape
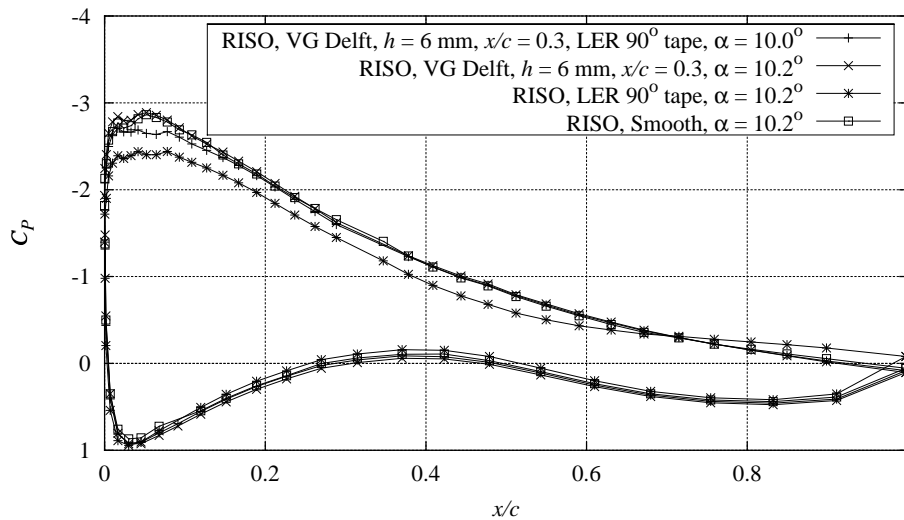
Figure D-1 Measured C_P distributions with combinations of Delft vortex generators, h = 6 mm, x/c = 0.3, and 90° zigzag trip tape compared with smooth measurement, Re = 1.6×10⁶, α = 10.0°(FFAW3241CONT091297V4).
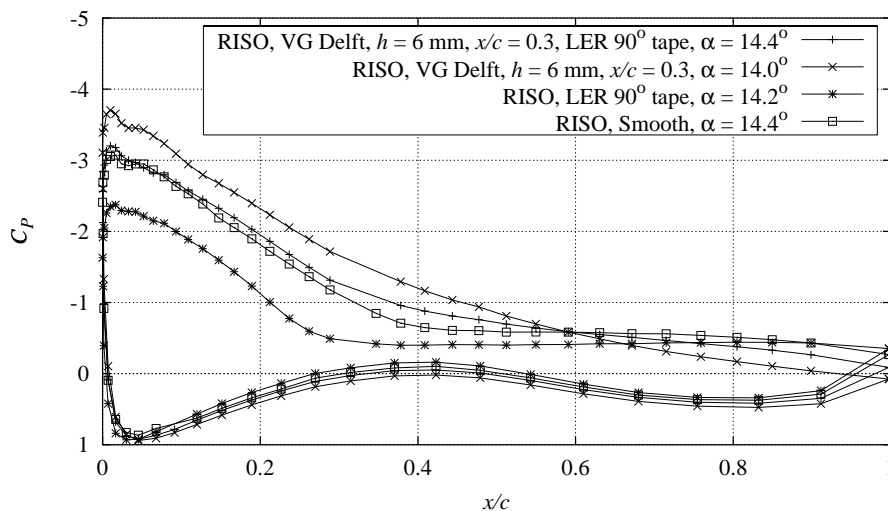
Figure D-2 Measured C_P distributions with combinations of Delft vortex generators, h = 6 mm, x/c = 0.3, and 90° zigzag trip tape compared with smooth measurement, Re = 1.6×10⁶, α = 14.4°(FFAW3241CONT091297V4).
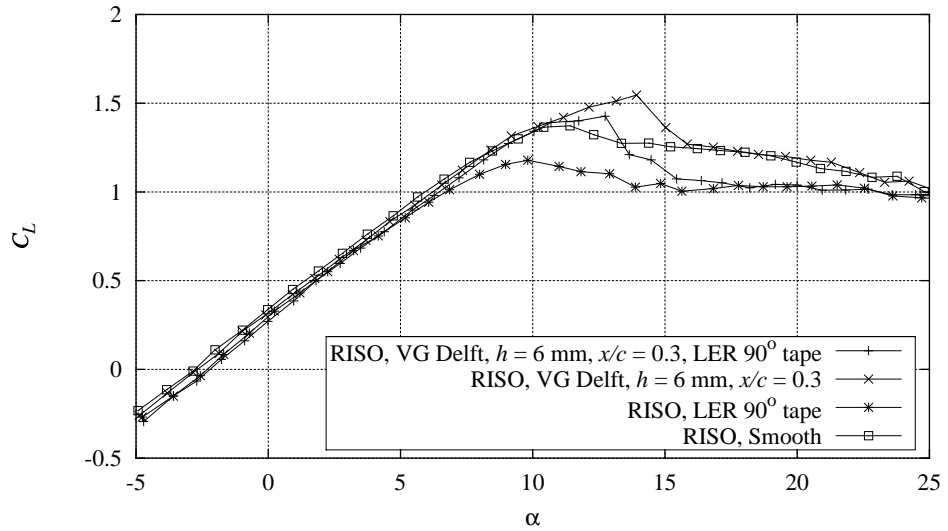
Figure D-3 Measured C_L curves with combinations of Delft vortex generators, $h = 6$ mm, $x/c = 0.3$, and $90°$ zigzag trip tape compared with smooth measurement, Re = 1.6×10^6 (FFAW3241CONT091297V4).
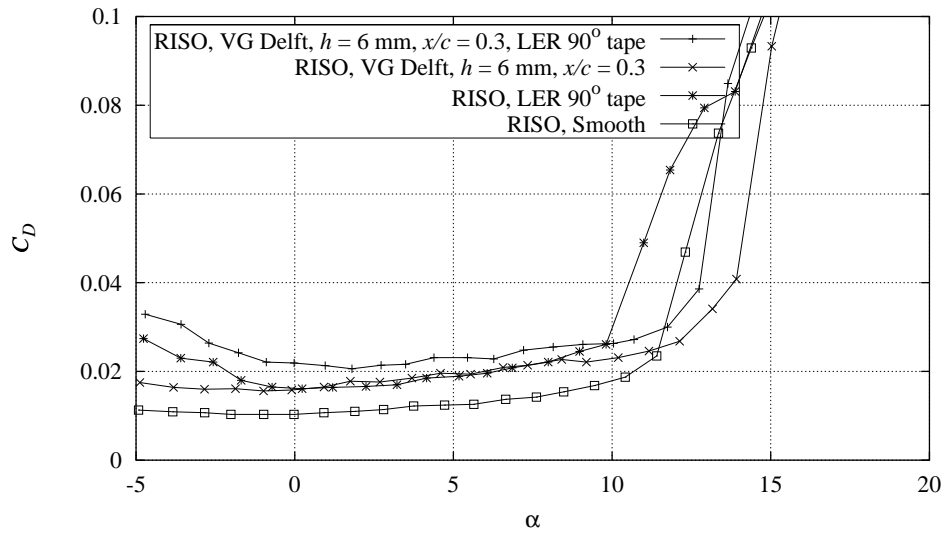
Figure D-4 Measured C_D curves with combinations of Delft vortex generators, $h = 6$ mm, $x/c = 0.3$, and $90°$ zigzag trip tape compared with smooth measurement, Re = 1.6×10^6 (FFAW3241CONT091297V4).

2

1.5

C_L

1

0.5

0

-0.5

| RISO, VG Delft, h = 6 mm, x/c = 0.3, LER 90° tape ——+—— |
| RISO, VG Delft, h = 6 mm, x/c = 0.3 ——×—— |
| RISO, LER 90° tape ——□—— |
| RISO, Smooth ——*—— |

0   0.02   0.04   0.06   0.08   0.1

C_D

Figure D-5 Measured C_L-C_D curves with combinations of Delft vortex generators, h = 6 mm, x/c = 0.3, and 90° zigzag trip tape compared with smooth measurement, Re = 1.6×10^6 (FFAW3241CONT091297V4).

0

-0.05

C_M

-0.1

-0.15

-0.2

| RISO, VG Delft, h = 6 mm, x/c = 0.3, LER 90° tape ——+—— |
| RISO, VG Delft, h = 6 mm, x/c = 0.3 ——×—— |
| RISO, LER 90° tape ——*—— |
| RISO, Smooth ——□—— |

-5   0   5   10   15   20   25

α
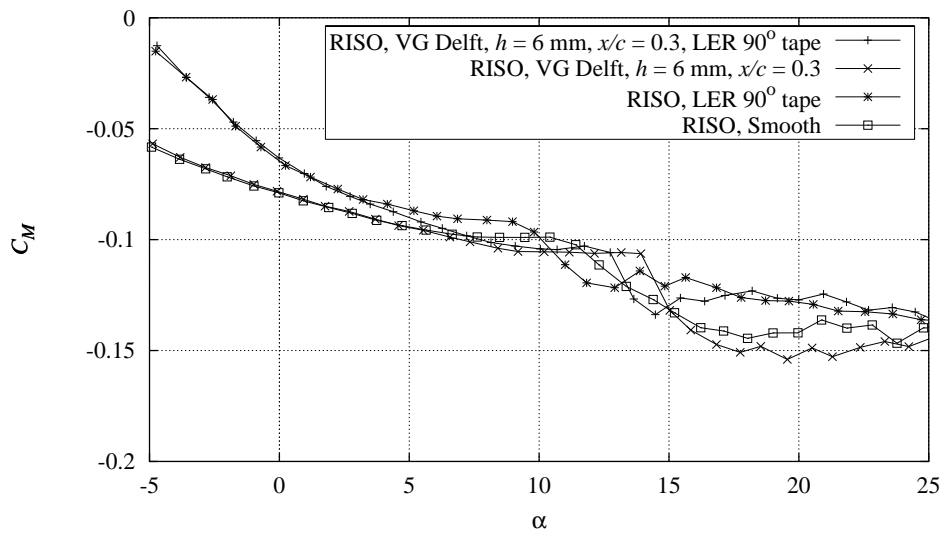
Figure D-6 Measured C_M curves with combinations of Delft vortex generators, h = 6 mm, x/c = 0.3, and 90° zigzag trip tape compared with smooth measurement, Re = 1.6×10^6 (FFAW3241CONT091297V4).

D.2 Delft vortex generators, h = 4 mm at x/c = 0.2, 90° zigzag trip tape
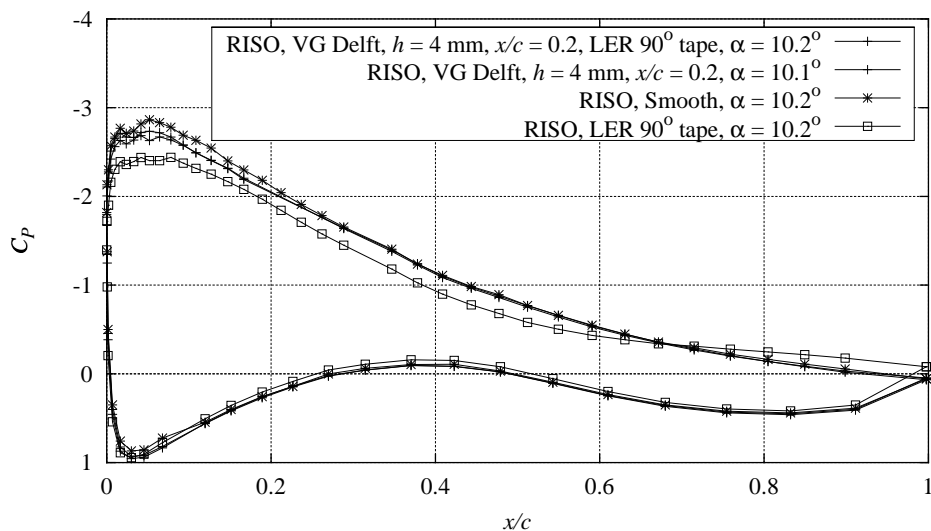
Figure D-7 Measured C_P distributions with combinations of Delft vortex generators, h = 4 mm, x/c = 0.2, and 90° zigzag trip tape compared with smooth measurement, Re = 1.6×10⁶, α around 10° (FFAW3241CONT091297V8).
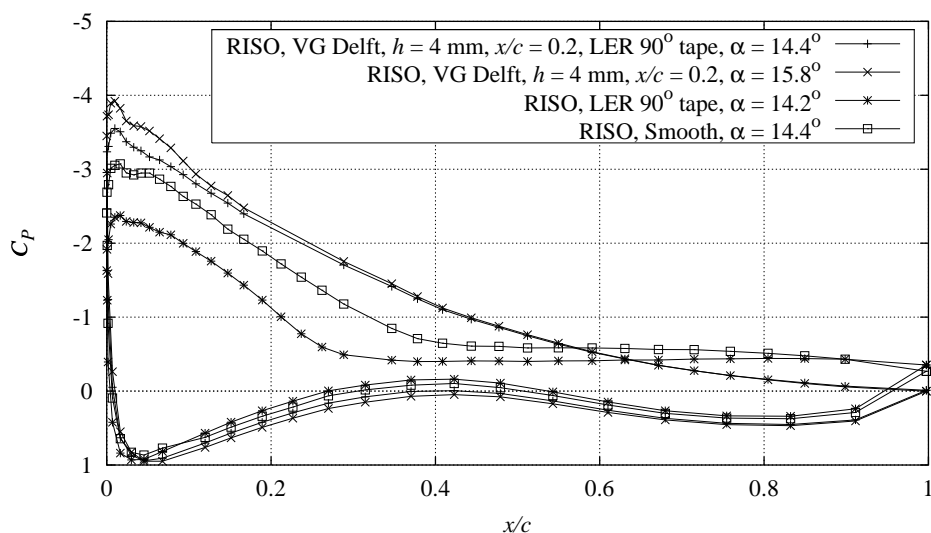
Figure D-8 Measured C_P distributions with combinations of Delft vortex generators, h = 4 mm, x/c = 0.2, and 90° zigzag trip tape compared with smooth measurement, Re = 1.6×10⁶, α around 14.4° (FFAW3241CONT091297V8).
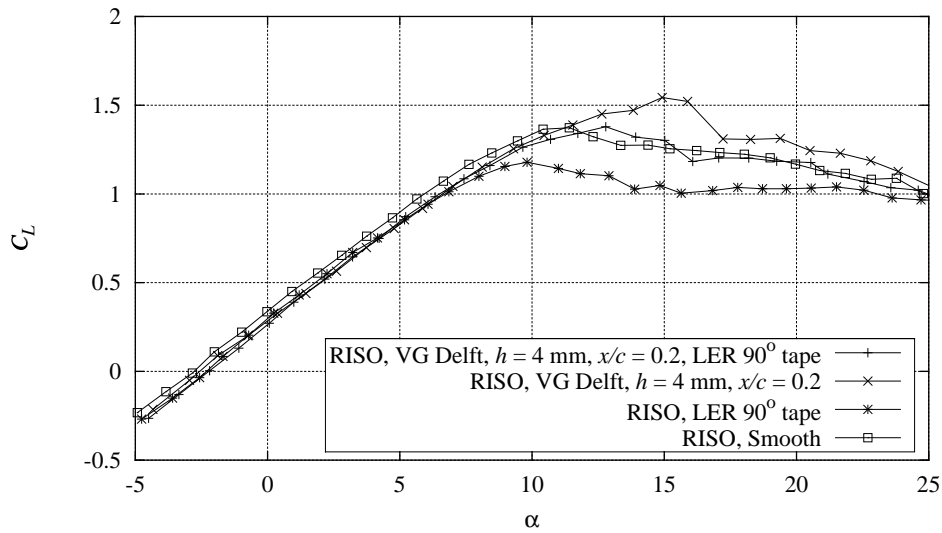
Figure D-9 Measured C_L curves with combinations of Delft vortex generators, h = 4 mm, x/c = 0.2, and 90° zigzag trip tape compared with smooth measurement, Re = 1.6×10^6 (FFAW3241CONT091297V8).
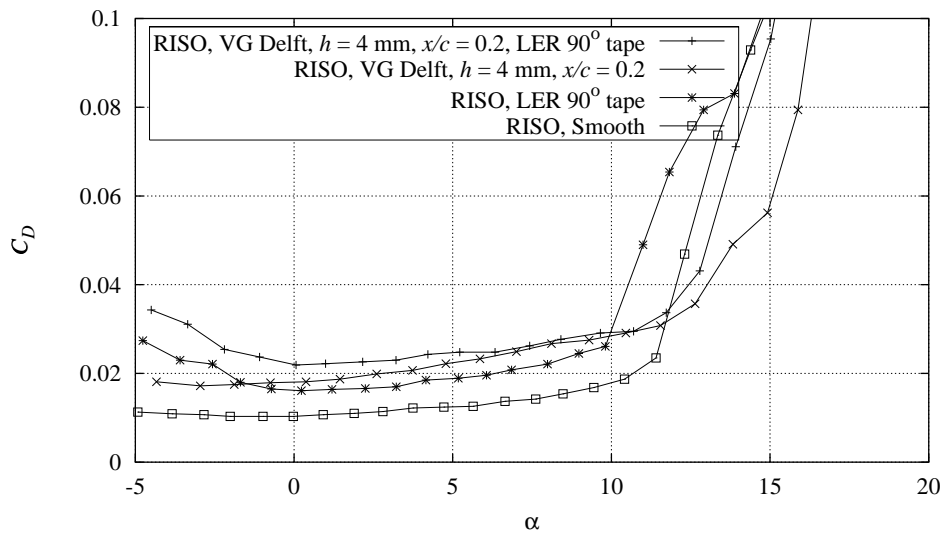
Figure D-10 Measured C_D curves with combinations of Delft vortex generators, h = 4 mm, x/c = 0.2, and 90° zigzag trip tape compared with smooth measurement, Re = 1.6×10^6 (FFAW3241CONT091297V8).
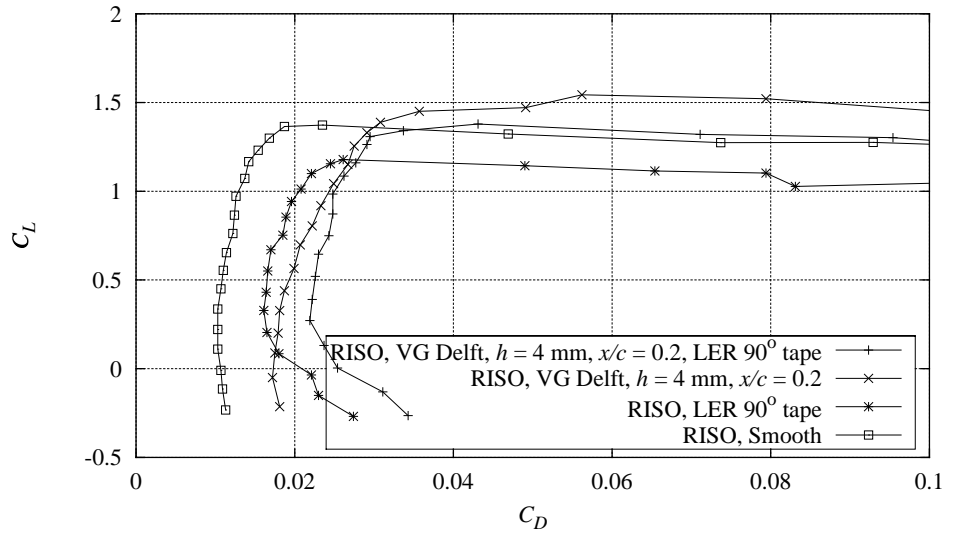
Figure D-11 Measured C_L-C_D curves with combinations of Delft vortex generators, h = 4 mm, x/c = 0.2, and 90° zigzag trip tape compared with smooth measurement, Re = 1.6×10⁶ (FFAW3241CONT091297V8).
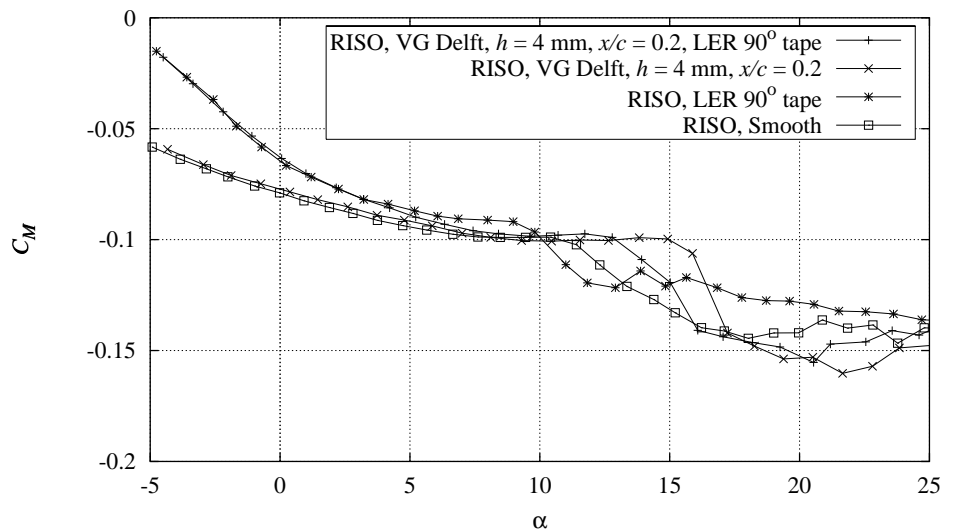
Figure D-12 Measured C_M curves with combinations of Delft vortex generators, h = 4 mm, x/c = 0.2, and 90° zigzag trip tape compared with smooth measurement, Re = 1.6×10⁶ (FFAW3241CONT091297V8).

E FFA-W3-241 Dynamic stall

E.1 $k = 0.093$
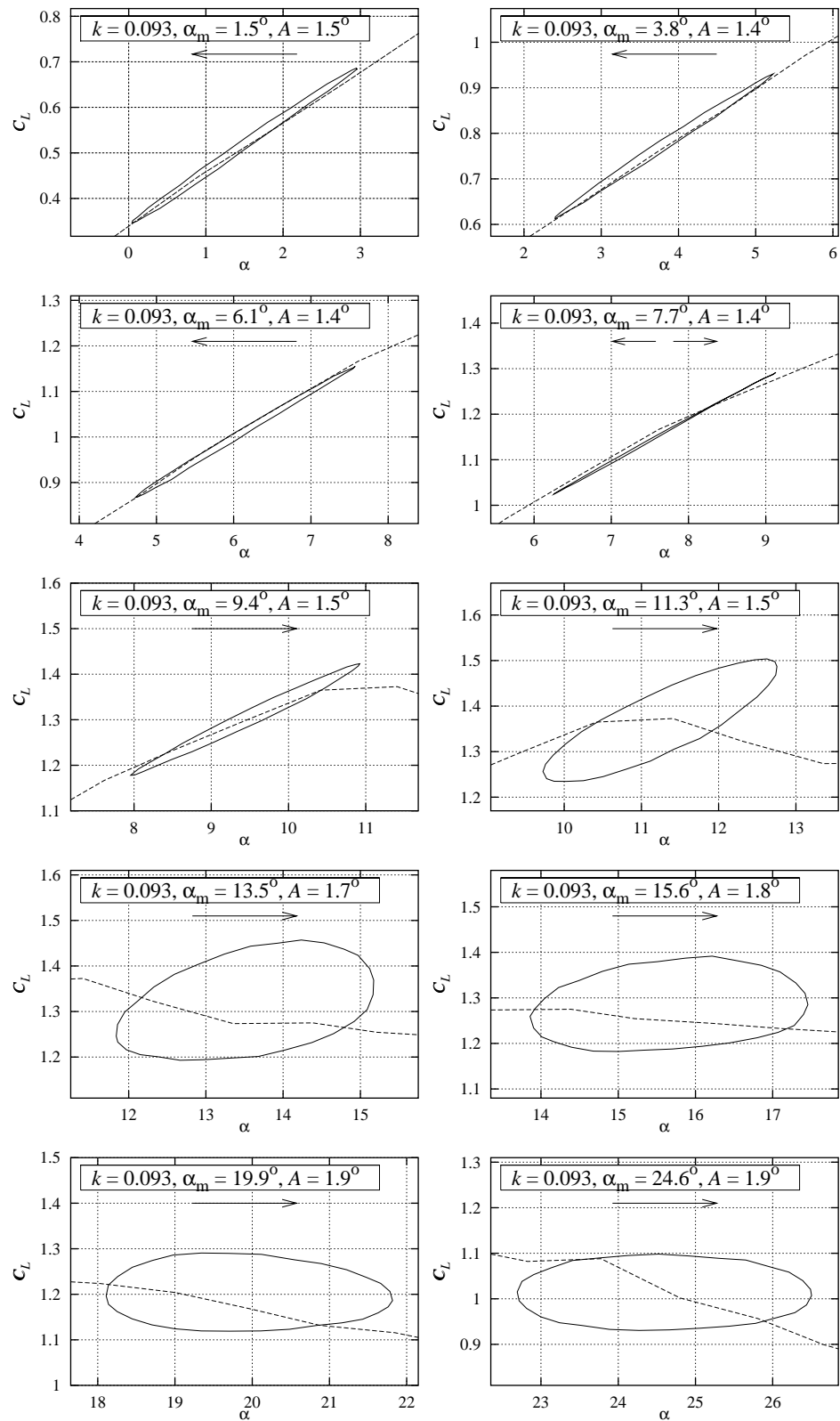
Figure E-1 Measured C_L hysteresis loops for smooth leading edge flow at $k = 0.093$, A between 1.4° and 2°, $Re = 1.6 \times 10^6$ (FFAW3241PITCH091297V1).
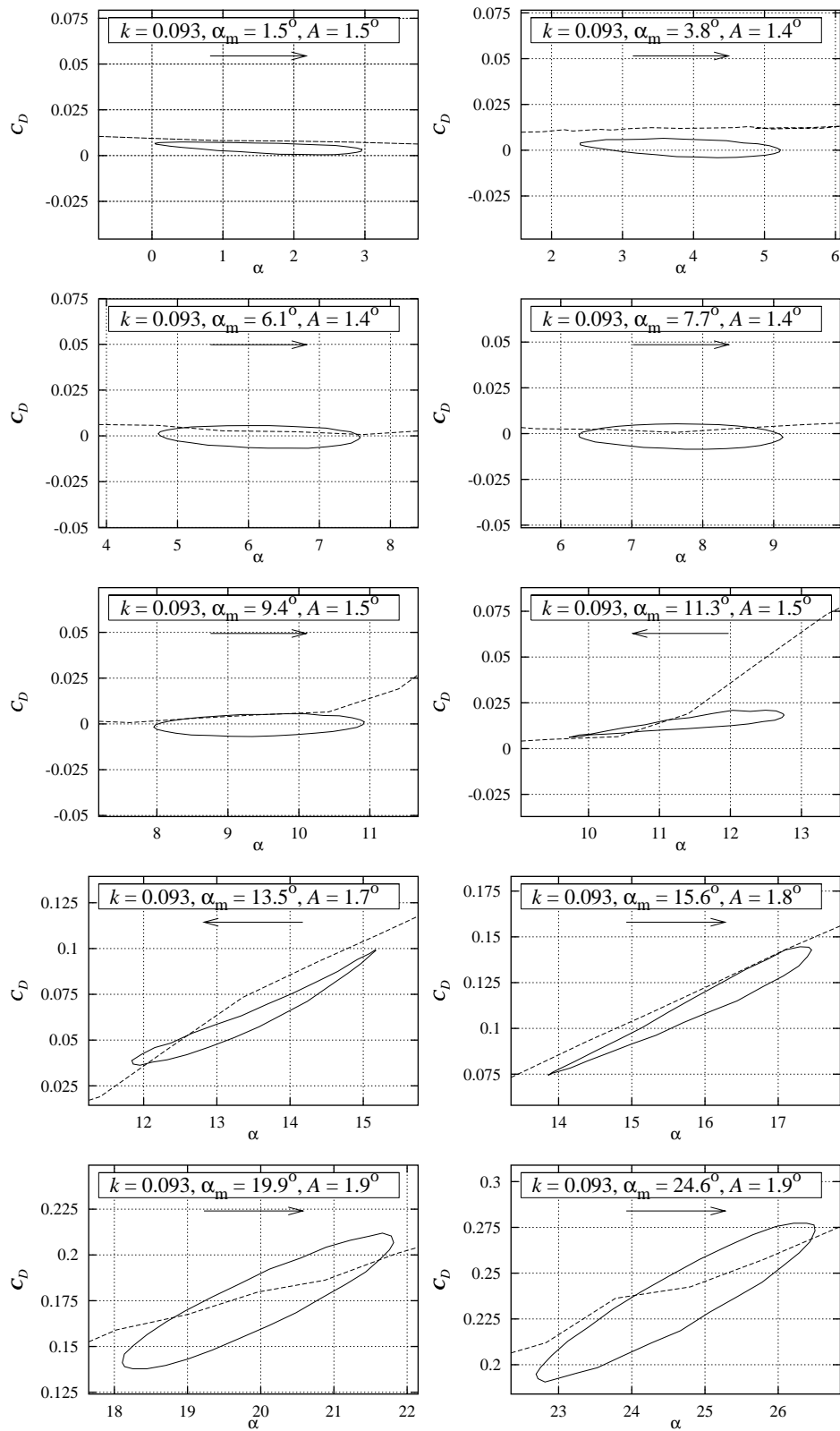
Figure E-2 Measured C_D hysteresis loops for smooth leading edge flow at k = 0.093, A between 1.4° and 2°, Re = 1.6×10⁶ (FFAW3241PITCH091297V1).
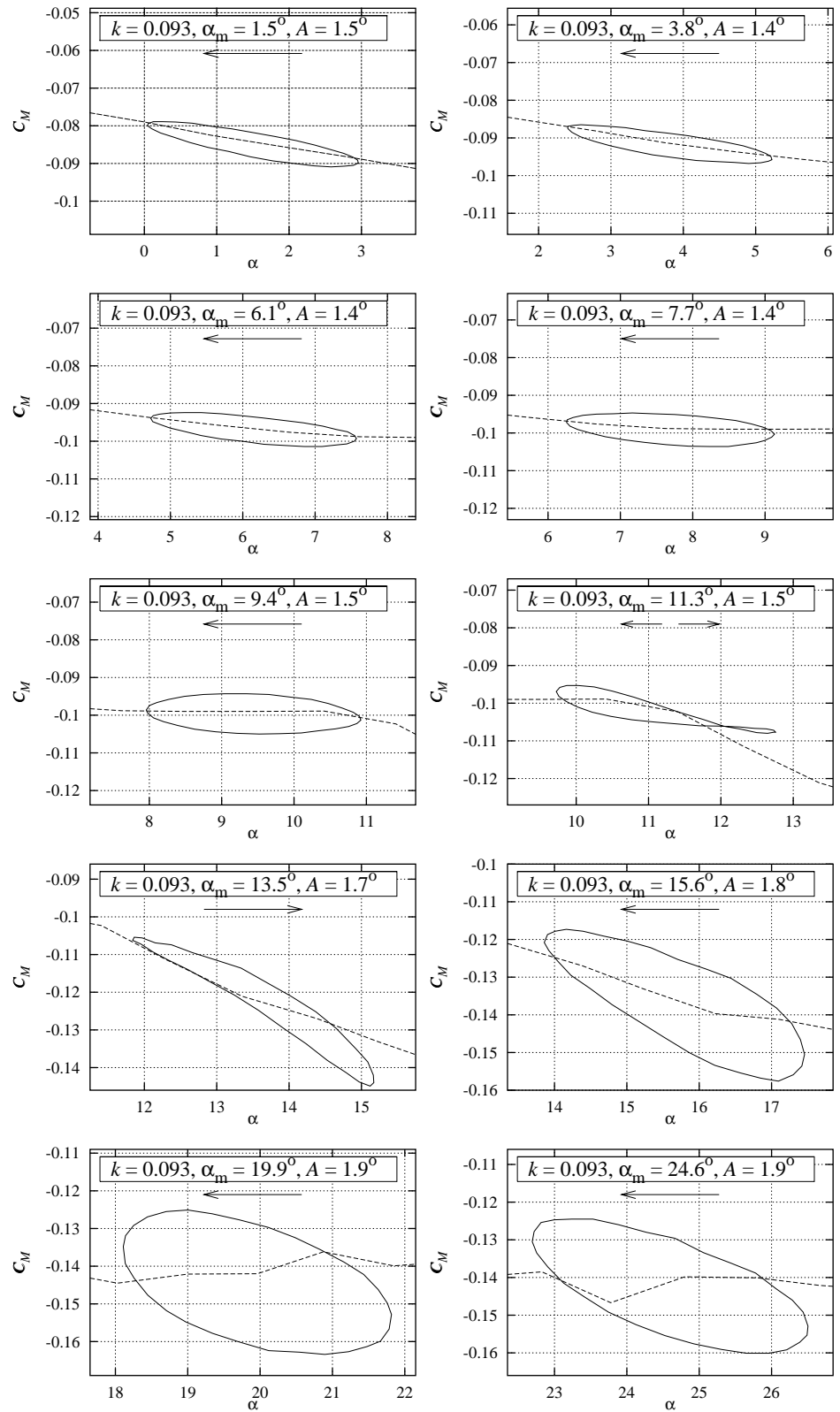
Figure E-3 Measured C_M hysteresis loops for smooth leading edge flow at $k = 0.093$, A between 1.4° and 2°, Re = 1.6×10⁶ (FFAW3241PITCH091297V1).

E.2 $k = 0.070$
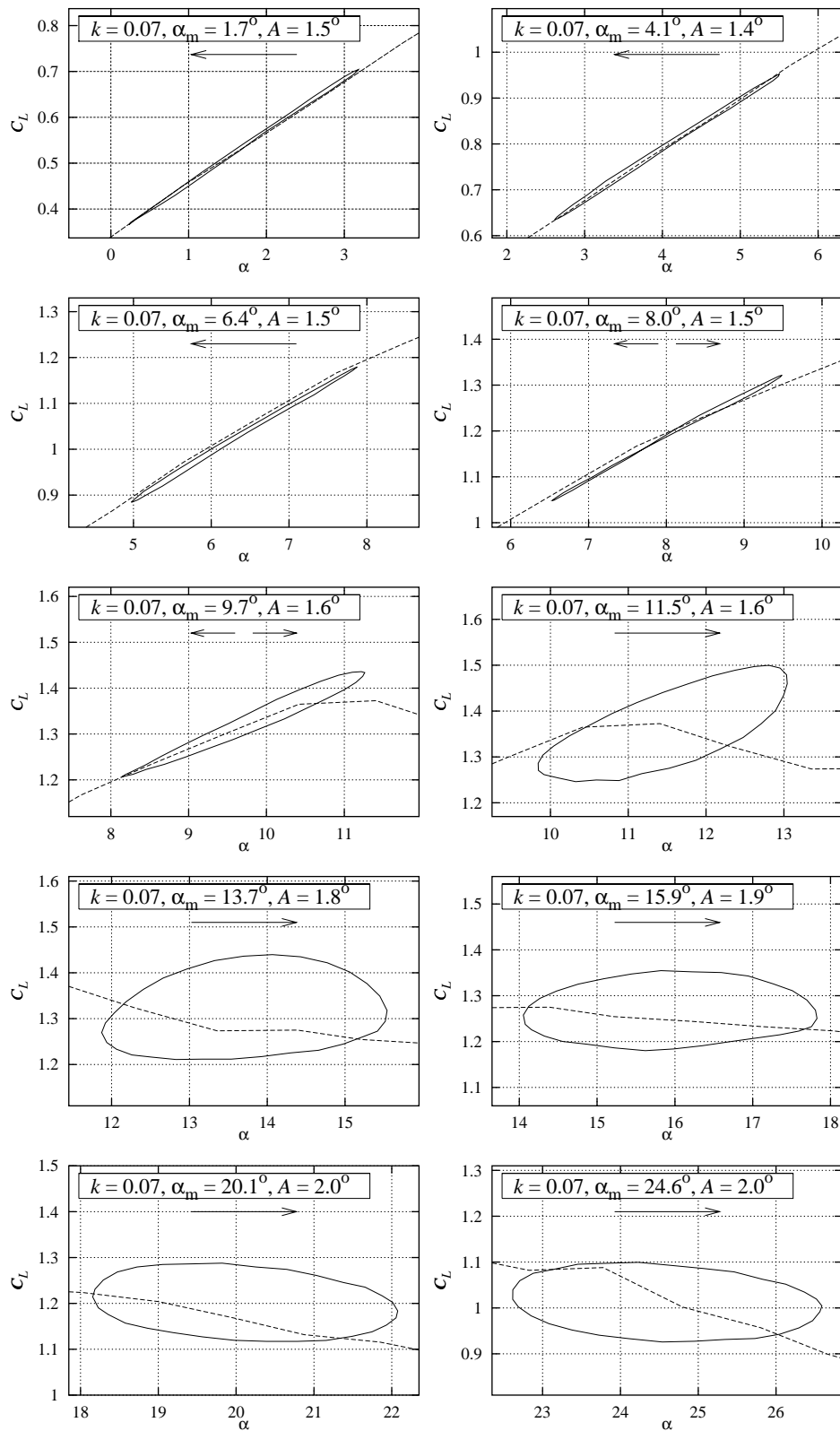
Figure E-4 Measured C_L hysteresis loops for smooth leading edge flow at $k = 0.070$, A between $1.4°$ and $2.0°$, Re = $1.6×10^6$ (FFAW3241PITCH091297V2).
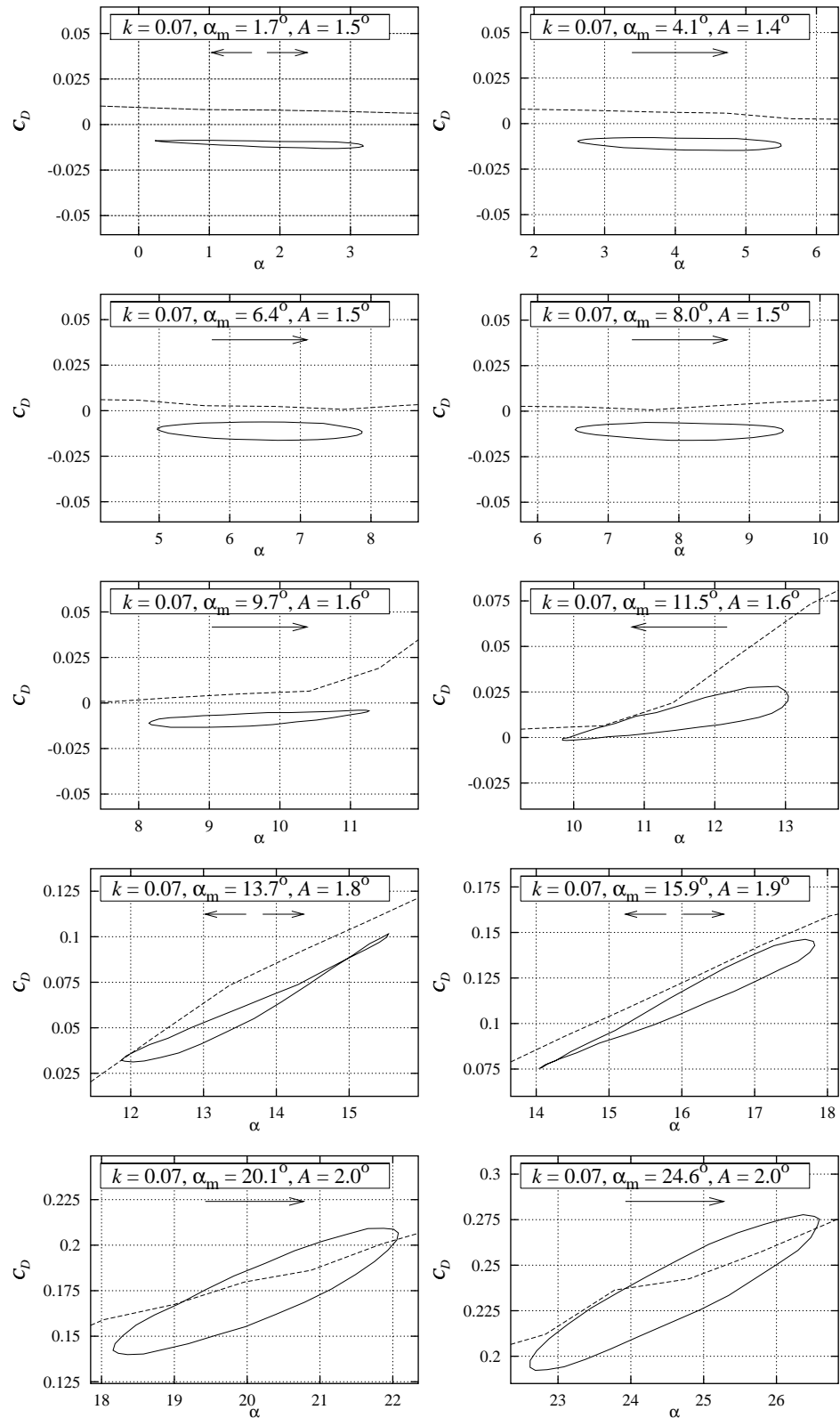
Figure E-5 Measured C_D hysteresis loops for smooth leading edge flow at k = 0.070, A between 1.4° and 2.0°, Re = 1.6×10^6 (FFAW3241PITCH091297V2).
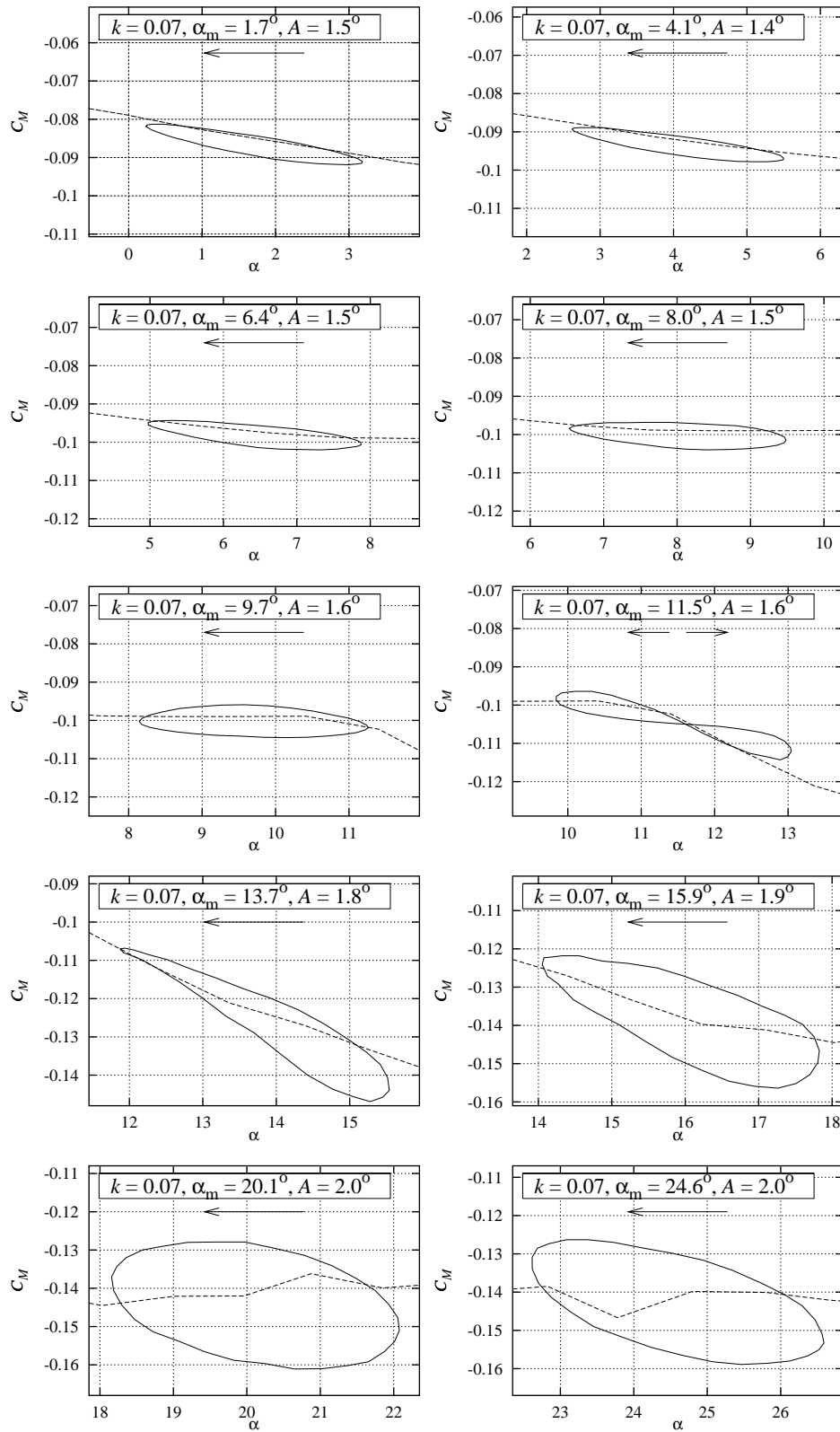
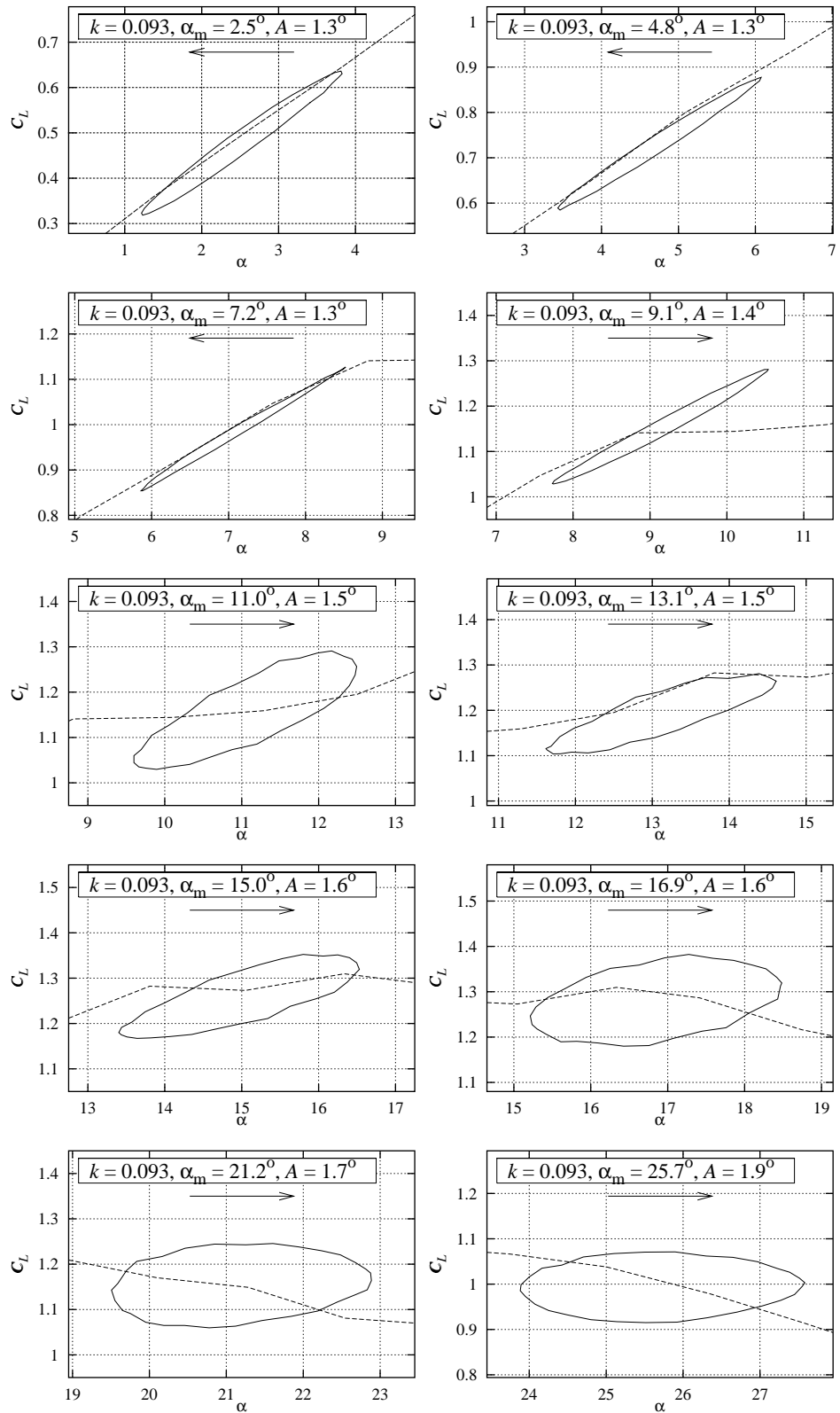*Figure E-6 Measured C_M hysteresis loops for smooth leading edge flow at k = 0.070, A between 1.4° and 2.0°, Re = 1.6×10⁶ (FFAW3241PITCH091297V2).*

E.3 $k = 0.093$, $1.4 < A < 2.0$, Delft vortex generators, $h = 6$ mm, $x/c = 0.2$
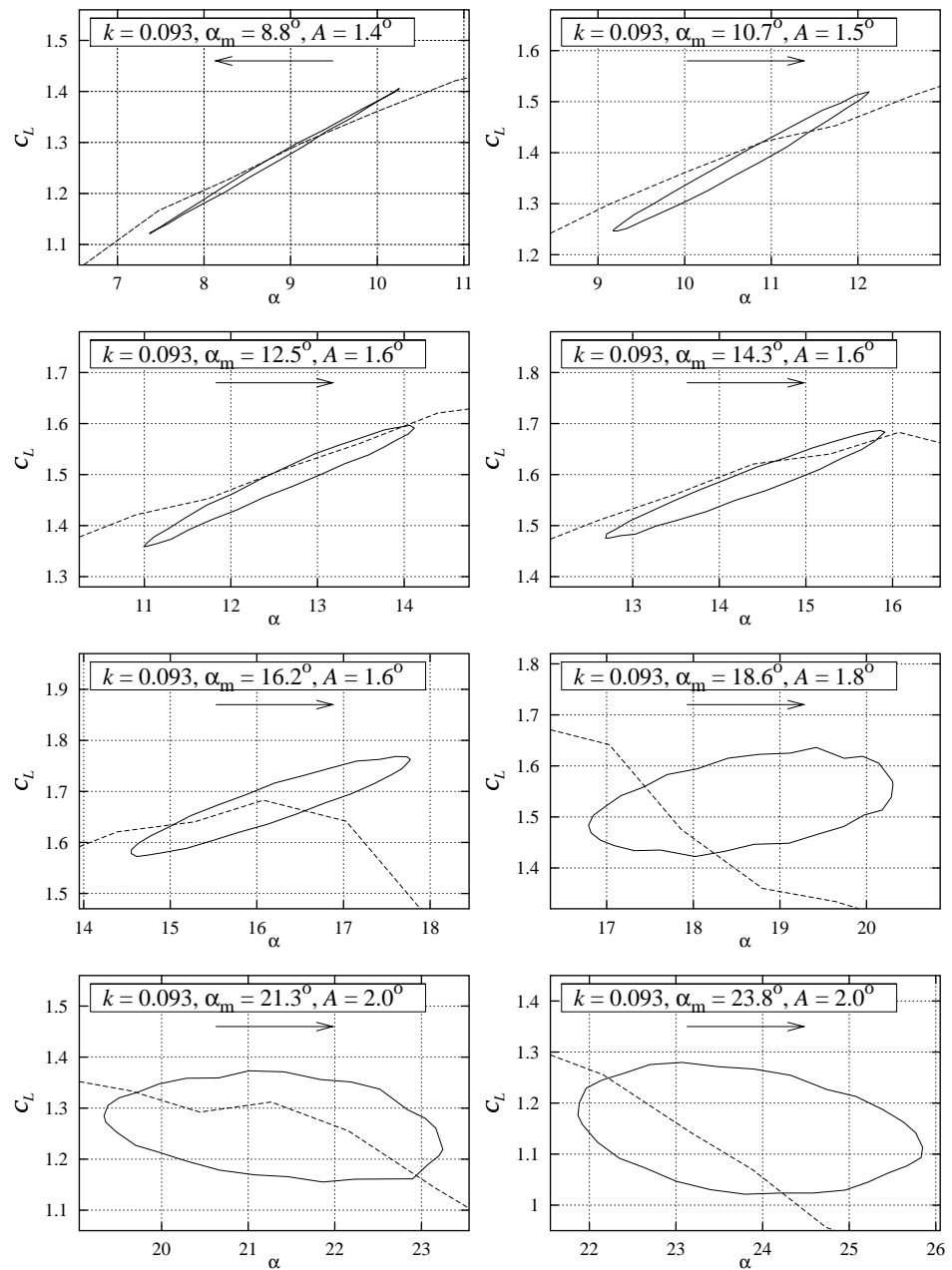
Figure E-7 Measured C_L hysteresis loops with Delft vortex generators, $h = 6$ mm, $x/c = 0.2$ at $k = 0.093$, A between 1.4° and 2.0°, Re = 1.6×10^{6} (FFAW3241PITCH091297V3).
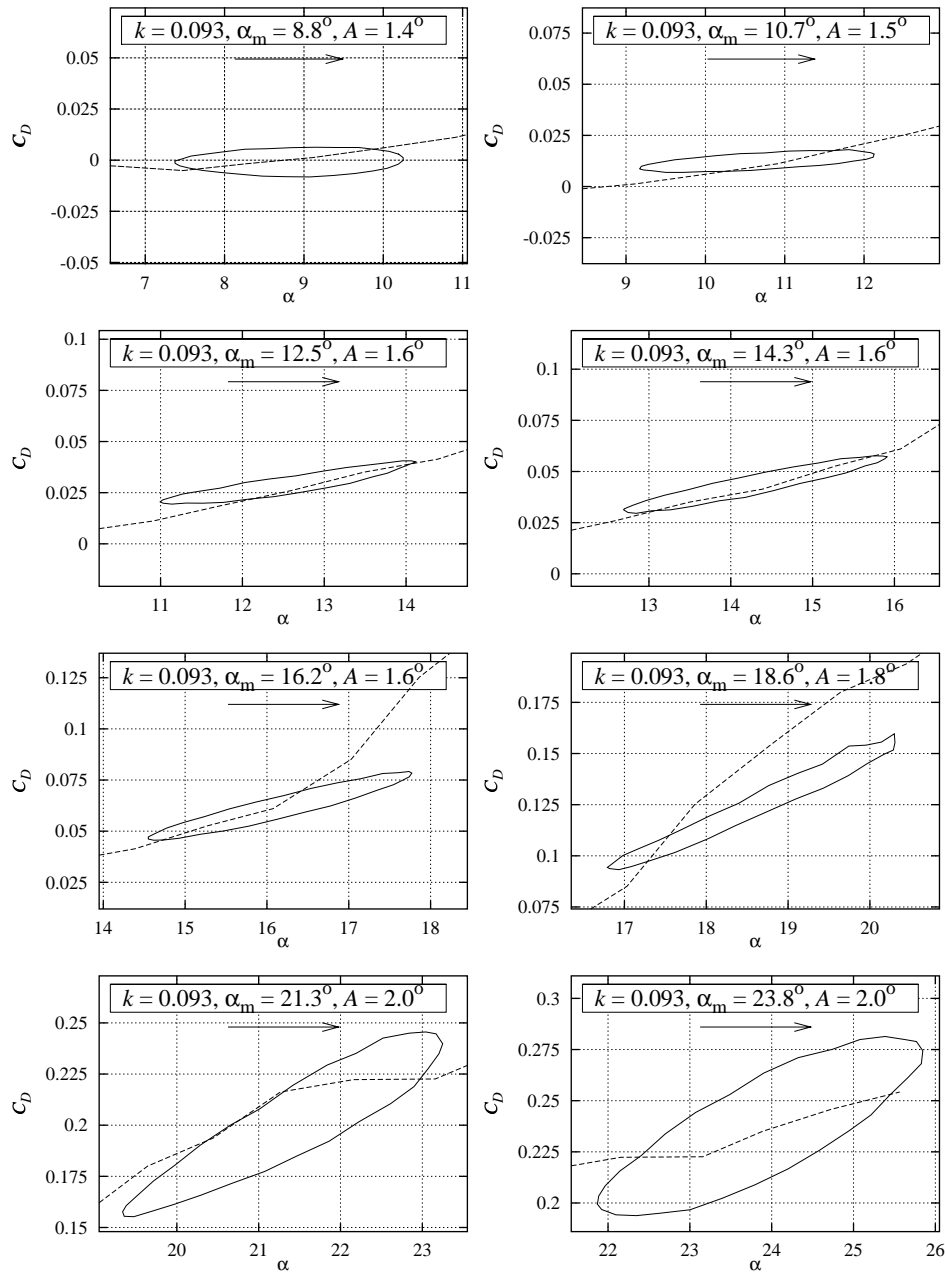
Figure E-8 Measured C_D hysteresis loops with Delft vortex generators, h = 6 mm, x/c = 0.2 at k = 0.093, A between 1.4° and 2.0°, Re = 1.6×10⁶ (FFAW3241PITCH091297V3).
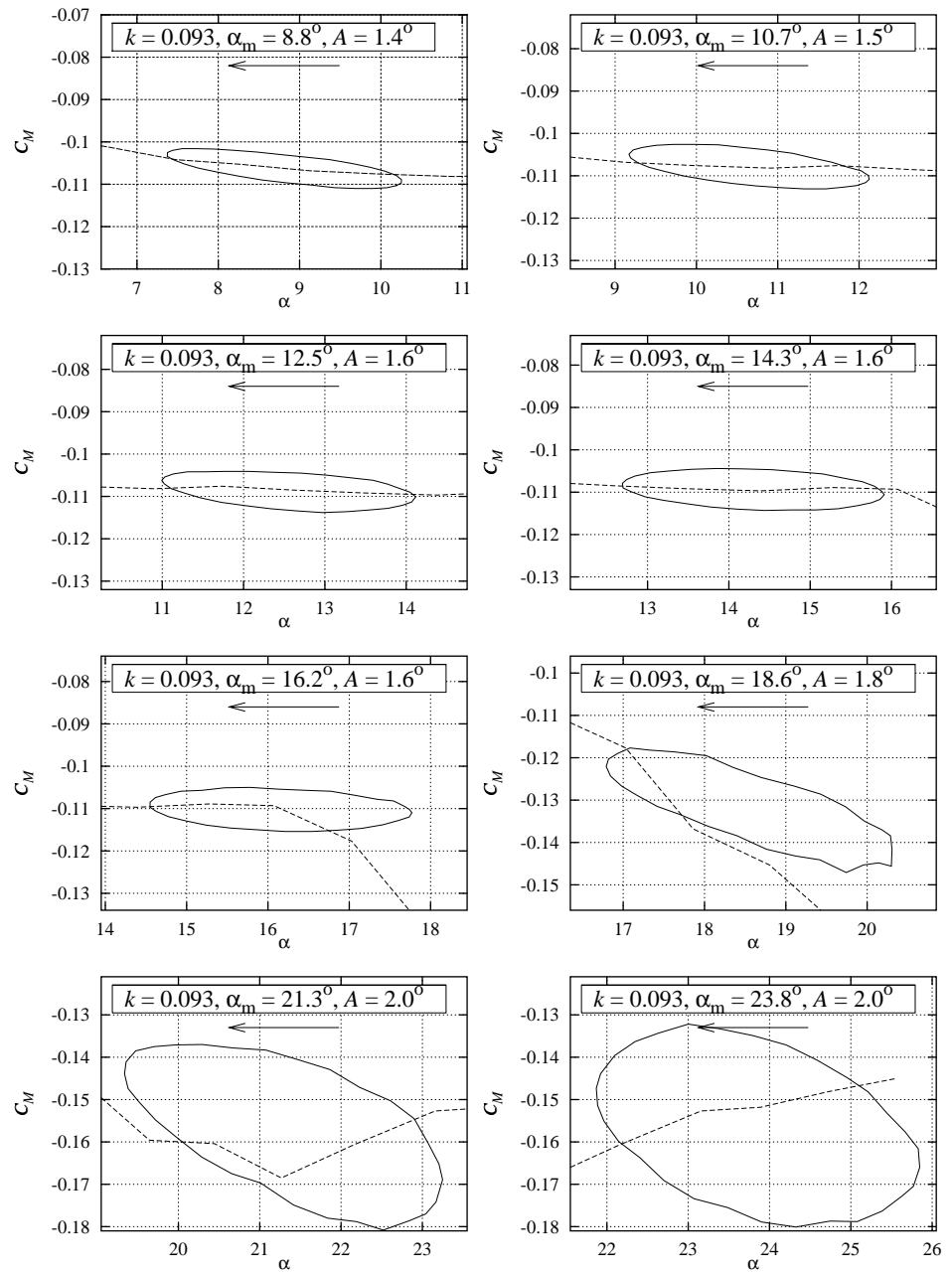
Figure E-9 Measured C_M hysteresis loops with Delft vortex generators, h = 6 mm, x/c = 0.2 at k = 0.093, A between 1.4° and 2.0°, Re = 1.6×10^{6} (FFAW3241PITCH091297V3).

F FFA-W3-301 Vortex generators

F.1 Delft vortex generators, *h* = 6 mm at *x/c* = 0.2
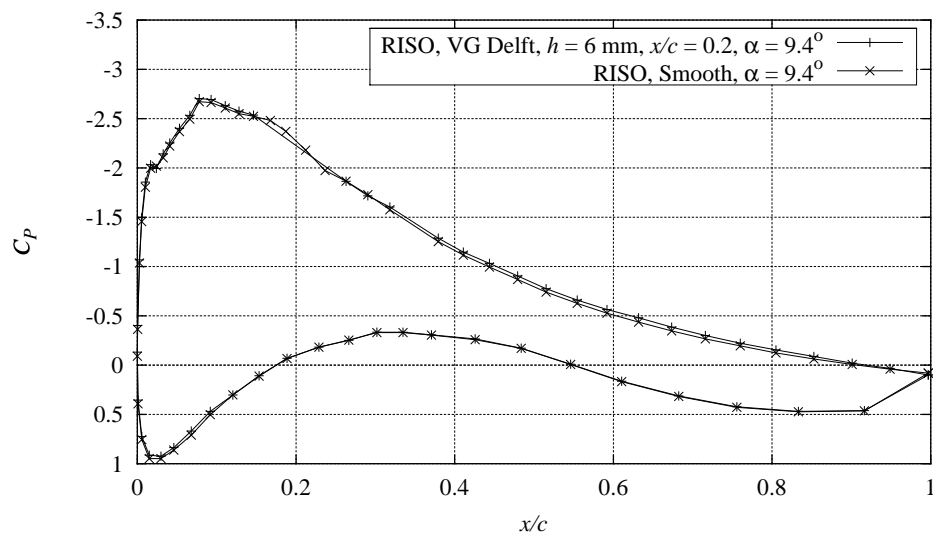
Figure F-1 Measured C_P distribution with Delft vortex generators, h = 6 mm, x/c = 0.2, compared with smooth measurement, Re = 1.6×10^{6}, α = 9.4° (FFAW3301CONT091297V5).
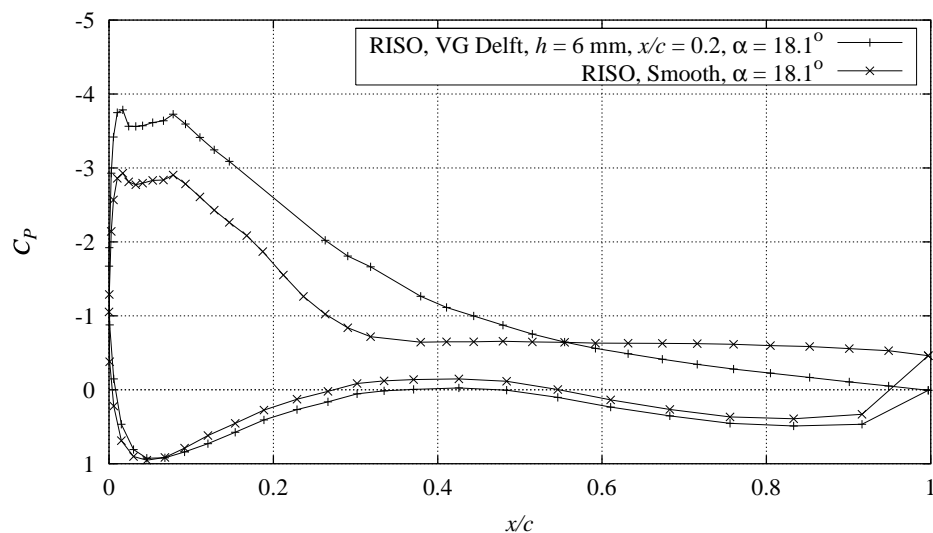
Figure F-2 Measured C_P distribution with Delft vortex generators, h = 6 mm, x/c = 0.2, compared with smooth measurement, Re = 1.6×10^{6}, α = 18.1° (FFAW3301CONT091297V5).
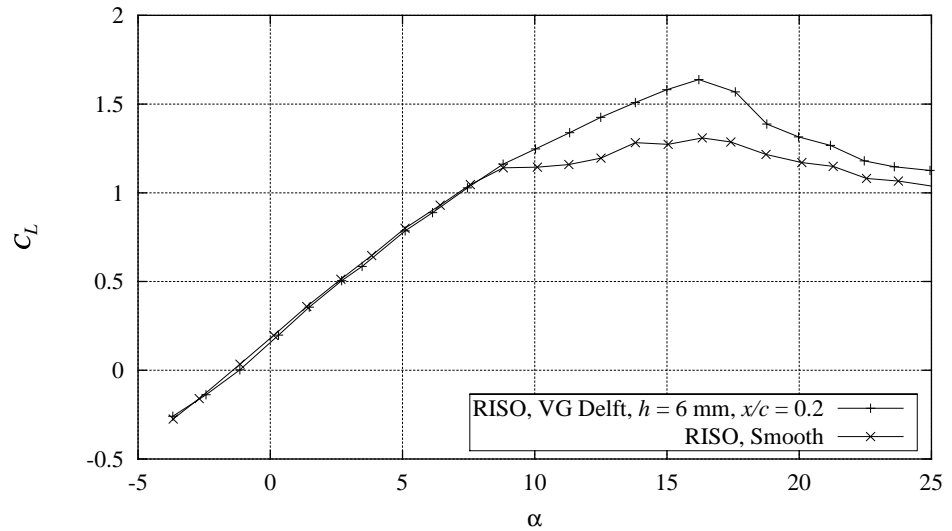
Figure F-3 Measured C_L curve with Delft vortex generators, h = 6 mm, x/c = 0.2, compared with smooth measurement, Re = 1.6×10⁶, (FFAW3301CONT091297V5).
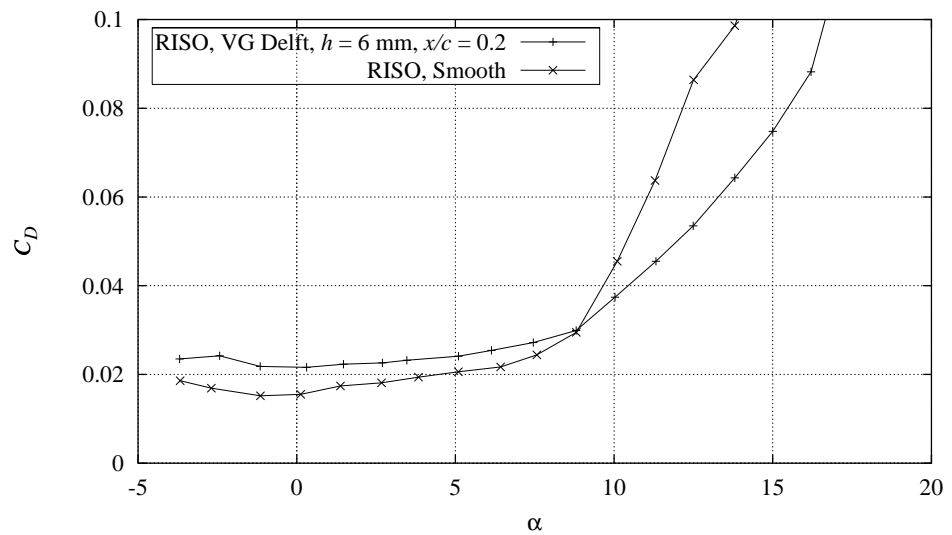
Figure F-4 Measured C_D curve with Delft vortex generators, h = 6 mm, x/c = 0.2, compared with smooth measurement, Re = 1.6×10⁶, (FFAW3301CONT091297V5).
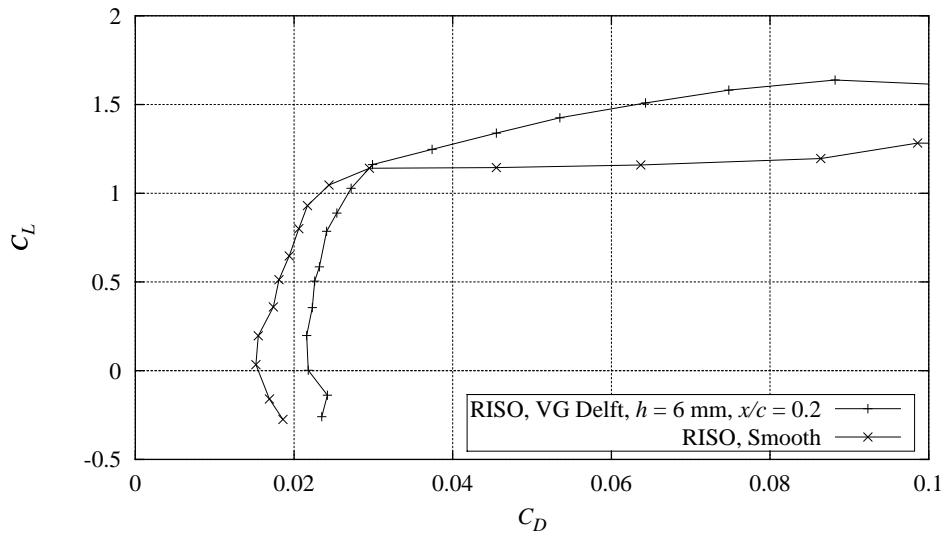
Figure F-5 Measured C_L-C_D curve with Delft vortex generators, h = 6 mm, x/c = 0.2, compared with smooth measurement, Re = 1.6×10^6, (FFAW3301CONT091297V5).
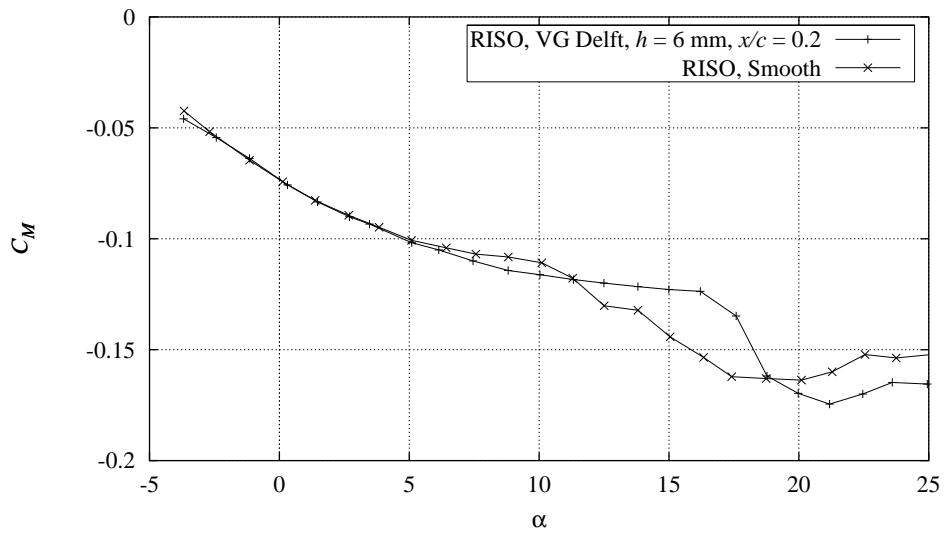
Figure F-6 Measured C_M curve with Delft vortex generators, h = 6 mm, x/c = 0.2, compared with smooth measurement, Re = 1.6×10^6, (FFAW3301CONT091297V5).

F.2 Delft vortex generators, *h* = 6 mm, at *x/c* = 0.3
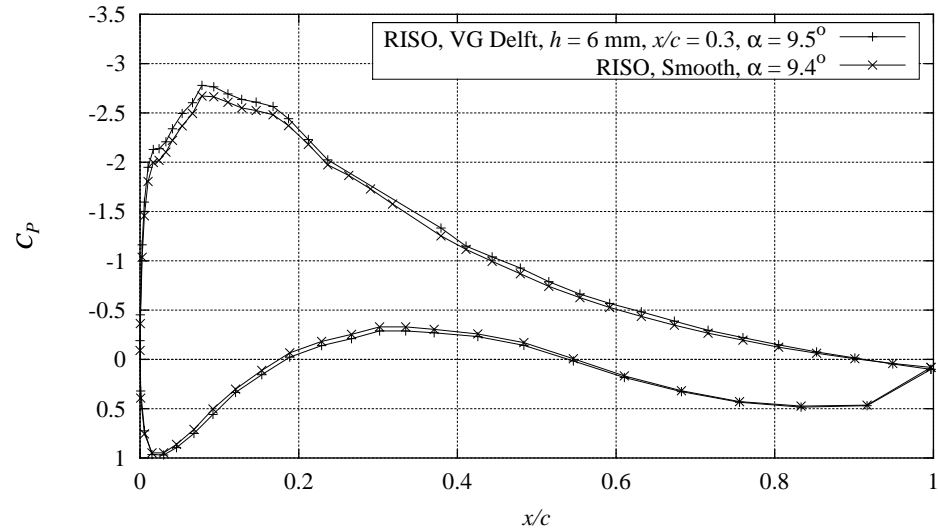
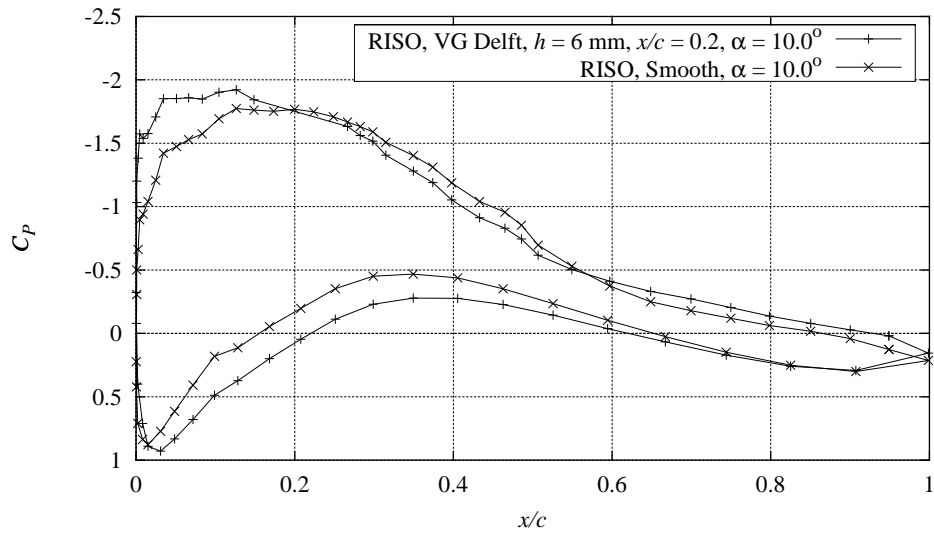*Figure F-7 Measured C_P distribution with Delft vortex generators, h = 6 mm, x/c = 0.3, compared with smooth measurement, Re = 1.6×10⁶, α = 9.5° (FFAW3301CONT091297V1).*
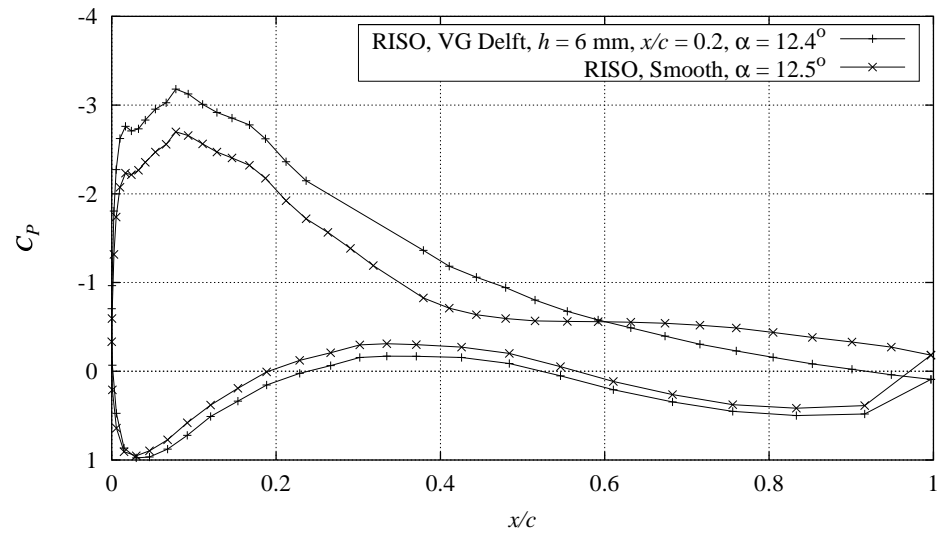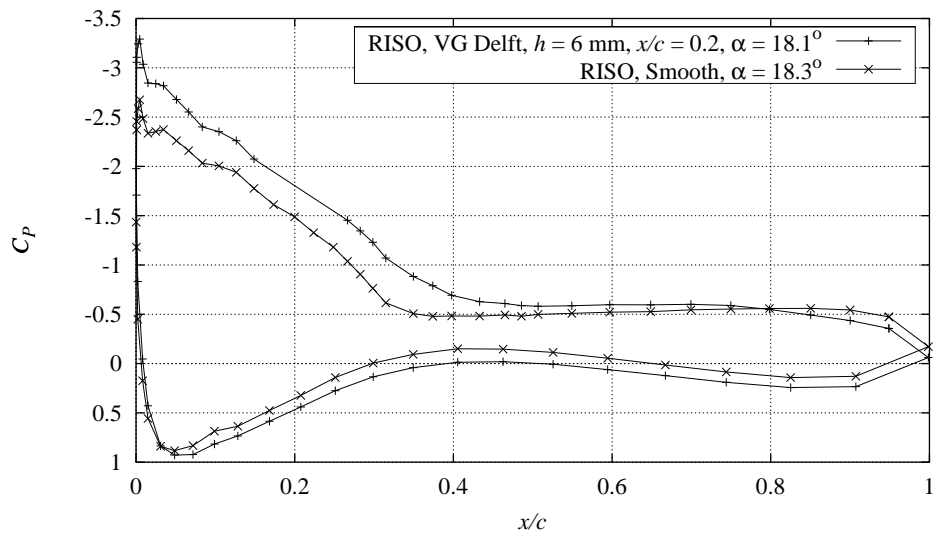

Figure F-8 Measured C_P distribution with Delft vortex generators, h = 6 mm, x/c = 0.3, compared with smooth measurement, Re = 1.6×10⁶, α = 12.4° (FFAW3301CONT091297V1).

Risø-R-1041(EN)
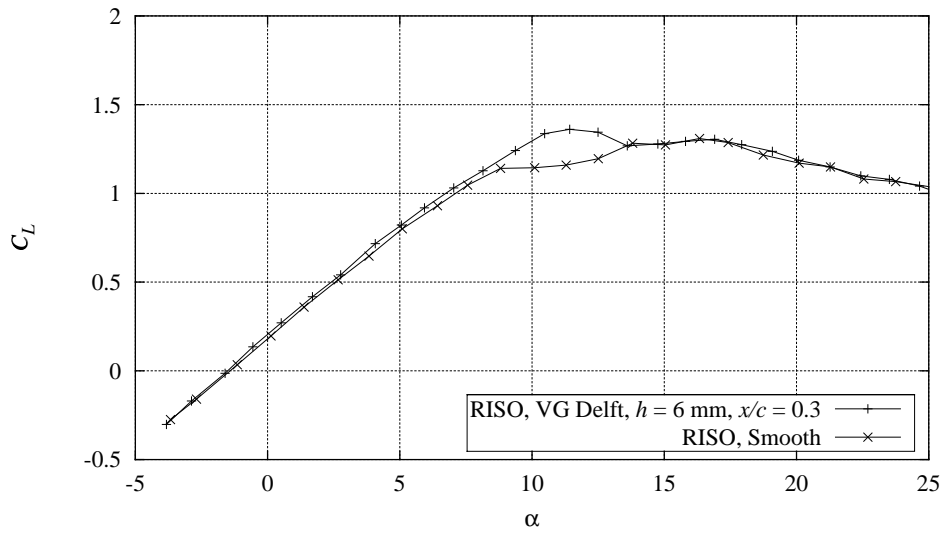
Figure F-9 Measured C_L curve with Delft vortex generators, h = 6 mm, x/c = 0.3, compared with smooth measurement, Re = 1.6×10⁶, (FFAW3301CONT091297V1).
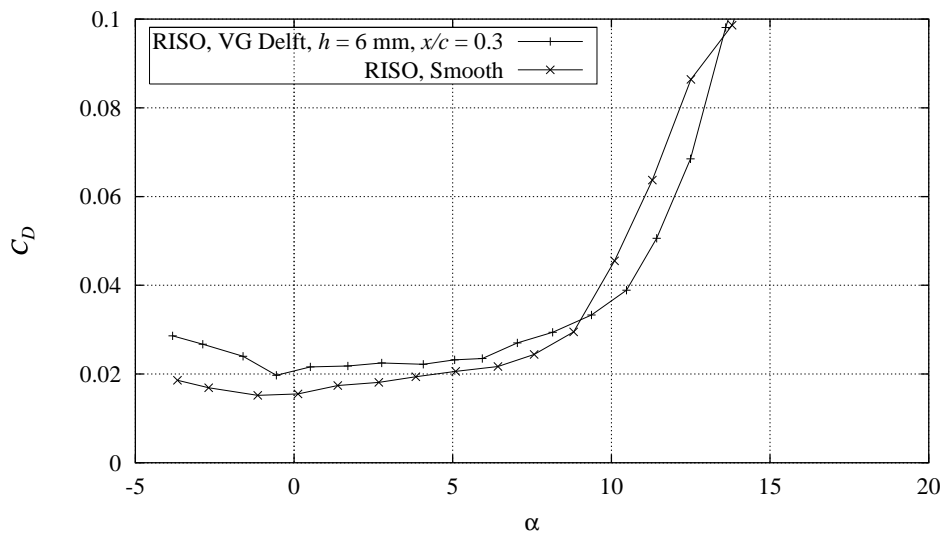
Figure F-10 Measured C_D curve with Delft vortex generators, h = 6 mm, x/c = 0.3, compared with smooth measurement, Re = 1.6×10⁶, (FFAW3301CONT091297V1).
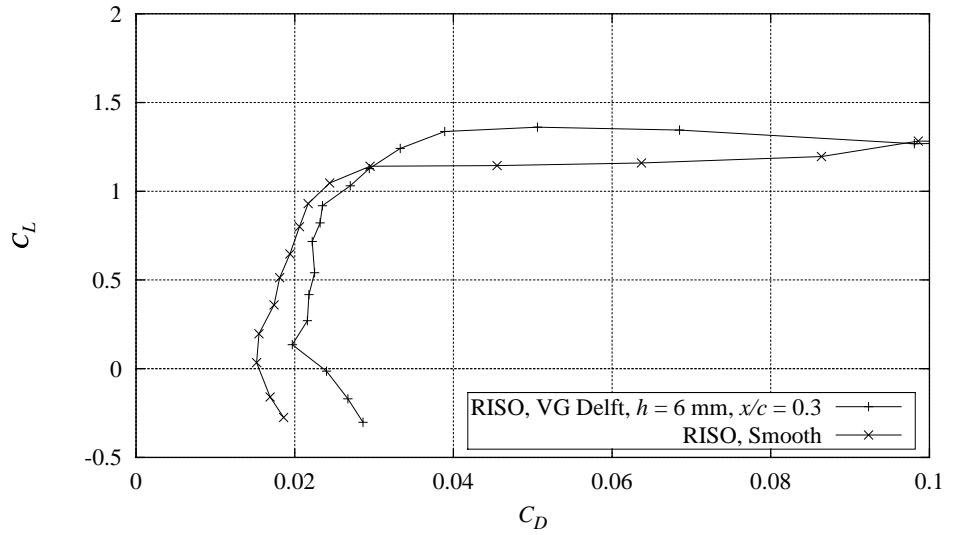
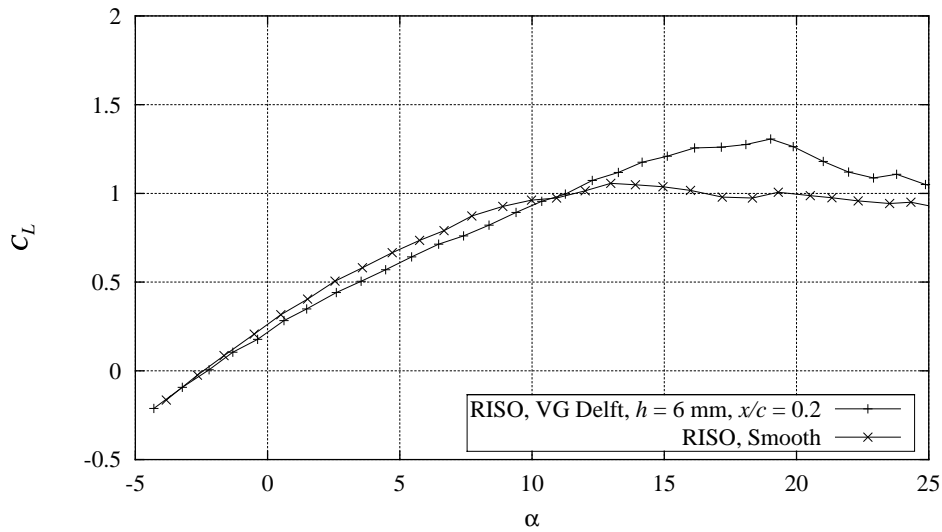*Figure F-11 Measured C_L-C_D curve with Delft vortex generators, h = 6 mm, x/c = 0.3, compared with smooth measurement, Re = 1.6×10^6, (FFAW3301CONT091297V1).*
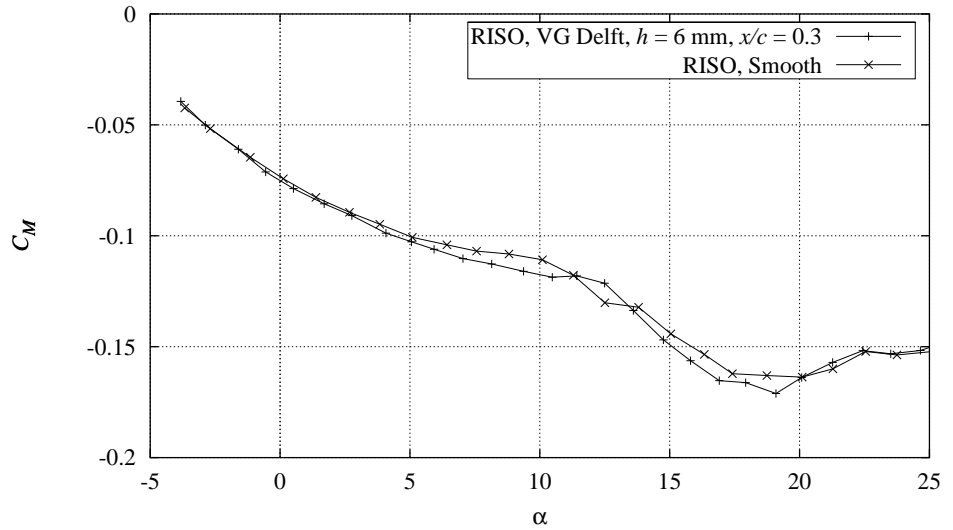
Figure F-12 Measured C_M curve with Delft vortex generators, h = 6 mm, x/c = 0.3, compared with smooth measurement, Re = 1.6×10^6, (FFAW3301CONT091297V1).

# G FFA-W3-301 Dynamic stall

G.1 $k = 0.093$

Figure G-1 Measured C_L hysteresis loops for smooth leading edge flow at $k = 0.093$, A between 1.3° and 1.9°, Re = 1.6×10⁶ (FFAW3301PITCH091297V1).
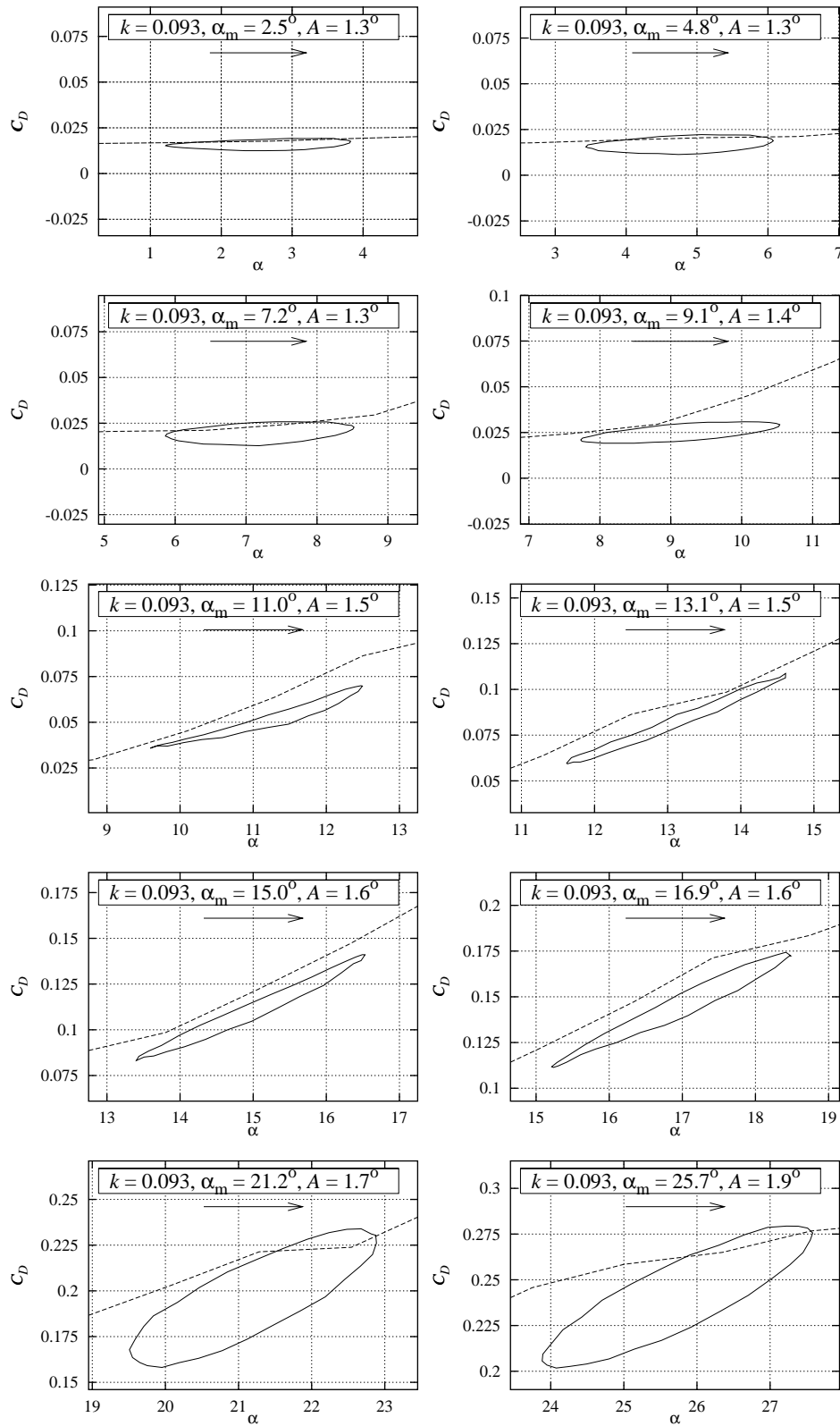
Figure G-2 Measured C_D hysteresis loops for smooth leading edge flow at k = 0.093, A between 1.3° and 1.9°, Re = 1.6×10^6 (FFAW3301PITCH091297V1).
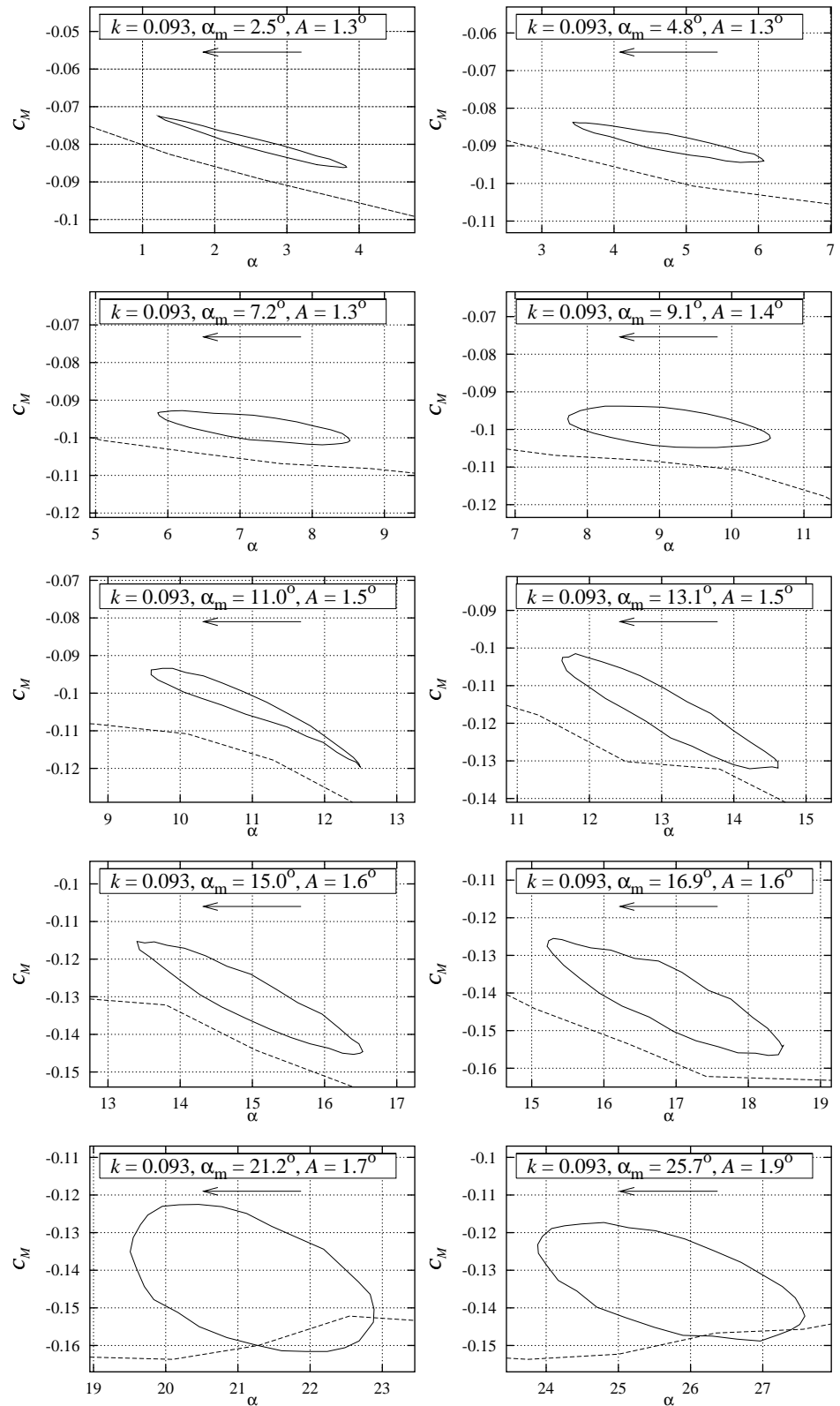
Figure G-3 Measured C_M hysteresis loops for smooth leading edge flow at k = 0.093, A between 1.3° and 1.9°, Re = 1.6×10⁶ (FFAW3301PITCH091297V1).

G.2 $k = 0.070$
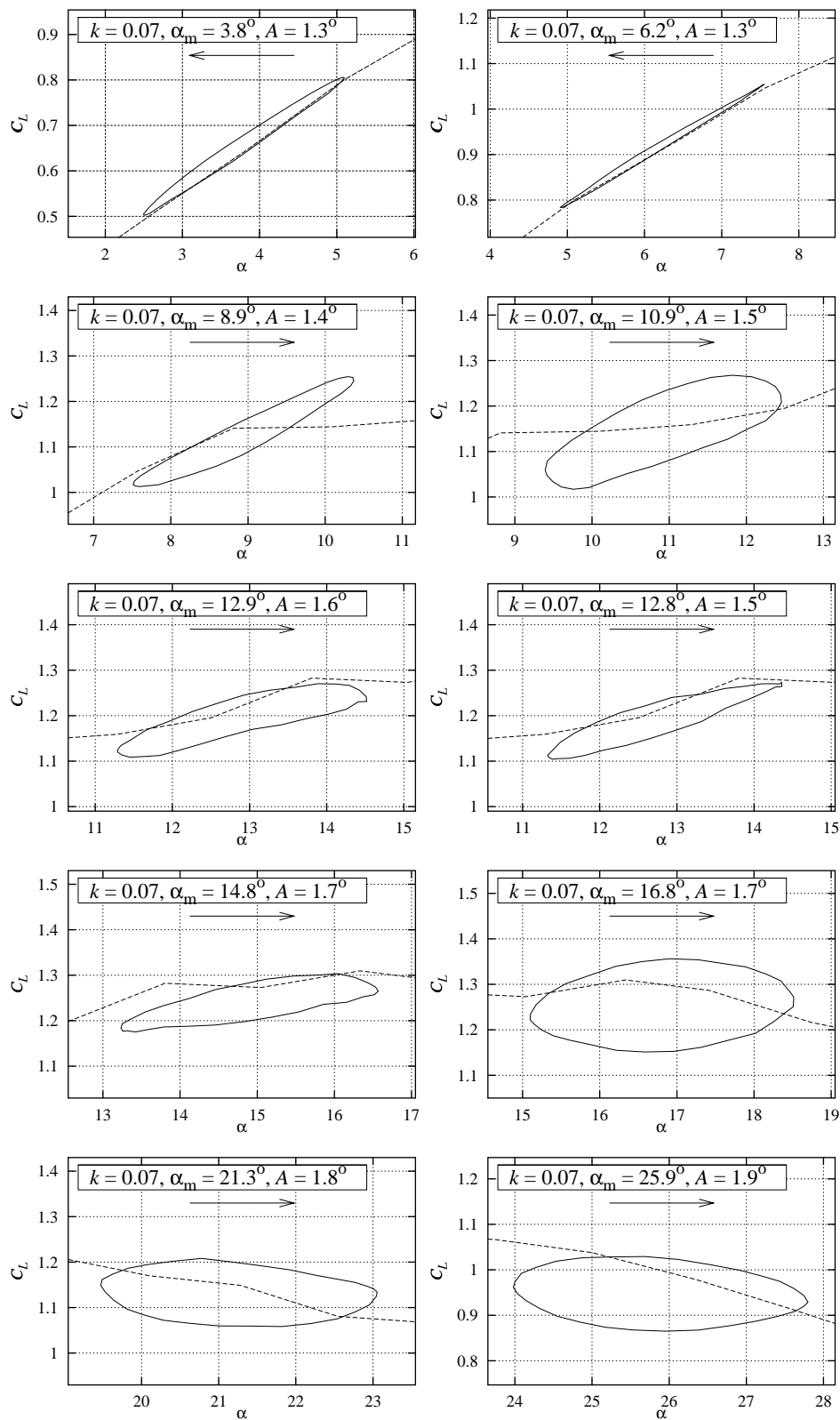
Figure G-4 Measured C_L hysteresis loops for smooth leading edge flow at $k = 0.070$, A between 1.3° and 1.9°, Re = 1.6×10⁶ (FFAW3301PITCH091297V2).
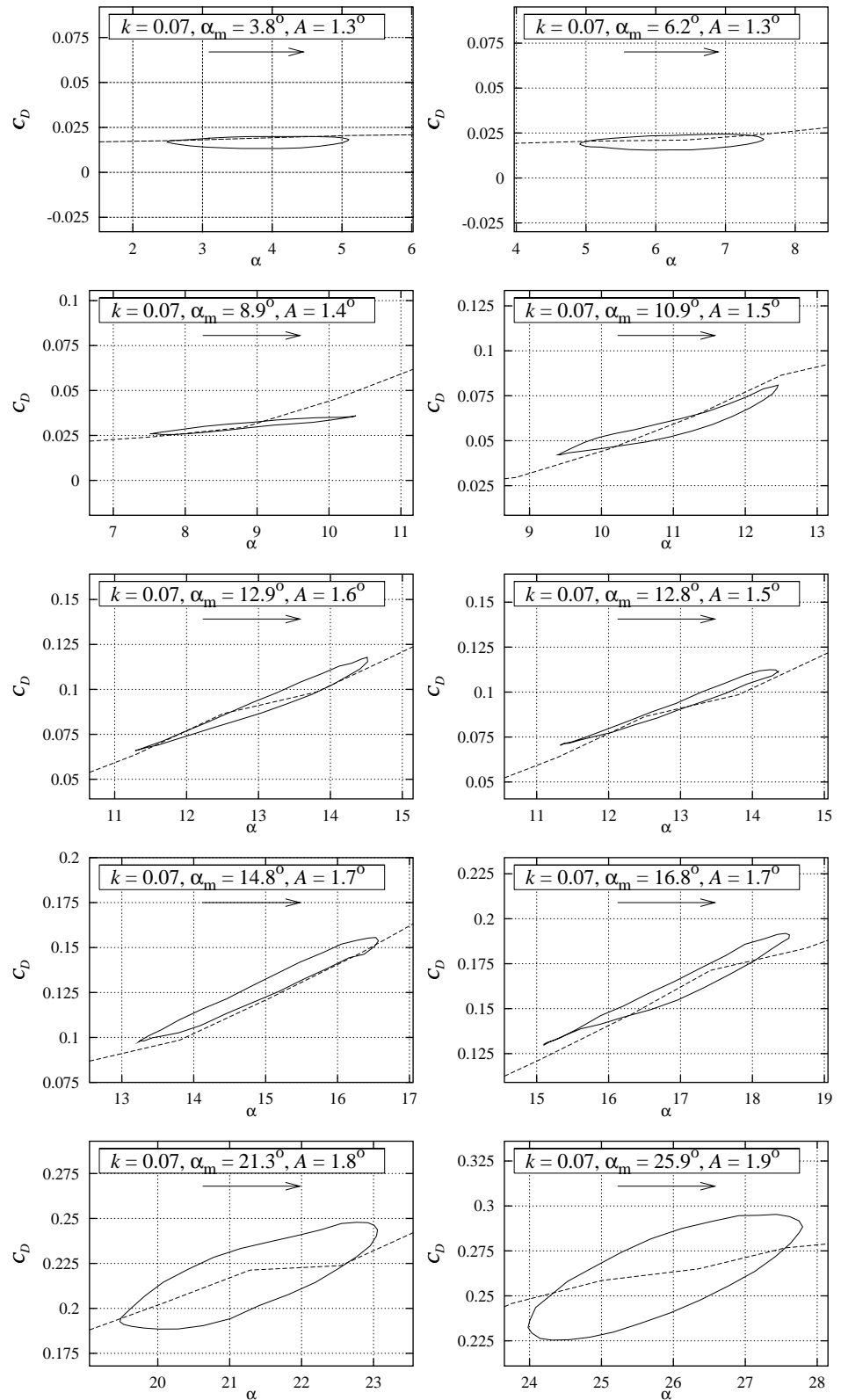
Figure G-5 Measured C_D hysteresis loops for smooth leading edge flow at k = 0.070, A between 1.3° and 1.9°, Re = 1.6×10⁶ (FFAW3301PITCH091297V2).
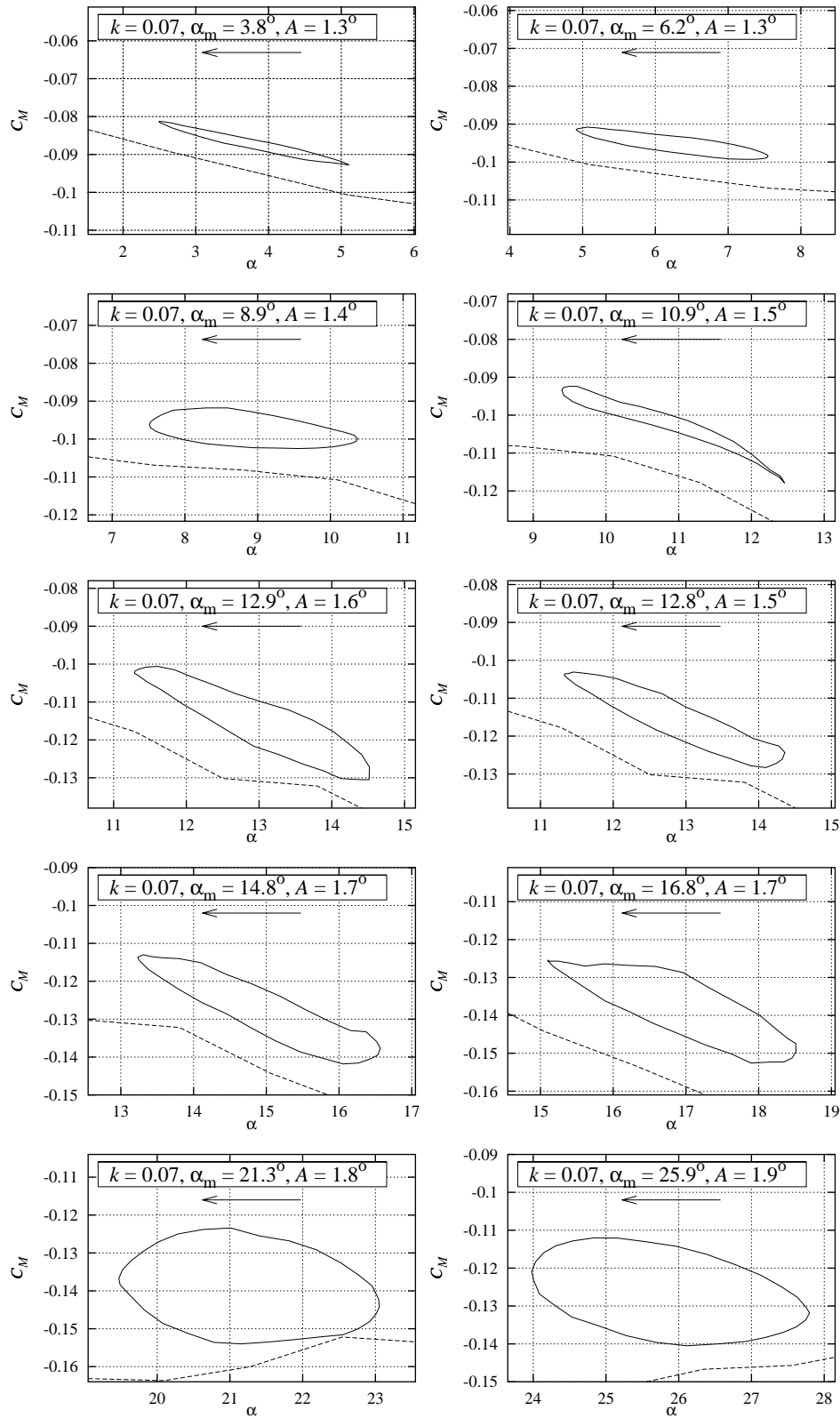
Figure G-6 Measured C_M hysteresis loops for smooth leading edge flow at $k = 0.070$, A between $1.3°$ and $1.9°$, $Re = 1.6×10^6$ (FFAW3301PITCH091297V2).

H NACA 63-430 Vortex generators

H.1 Delft vortex generators, *h* = 6 mm at *x/c* = 0.2

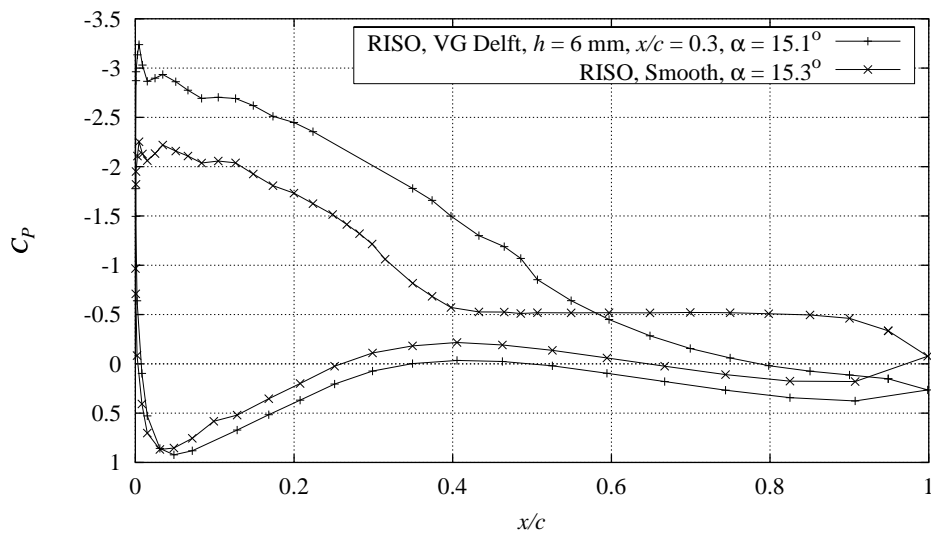*Figure H-1 Measured C_P distribution with Delft vortex generators, h = 6 mm, x/c = 0.2, compared with smooth measurement, Re = 1.6×10⁶, α = 10.0° (NACA63430CONT091297V5).*

Figure H-2 Measured C_P distribution with Delft vortex generators, h = 6 mm, x/c = 0.2, compared with smooth measurement, Re = 1.6×10⁶, α = 18.1° (NACA63430CONT091297V5).
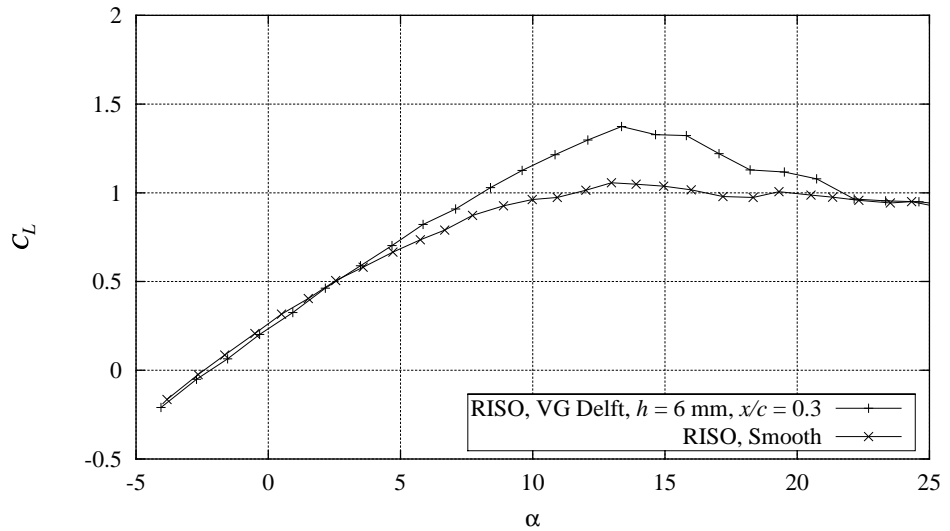
Figure H-3 Measured C_L curve with Delft vortex generators, h = 6 mm, x/c = 0.2, compared with smooth measurement, Re = 1.6×10⁶, (NACA63430CONT091297V5).
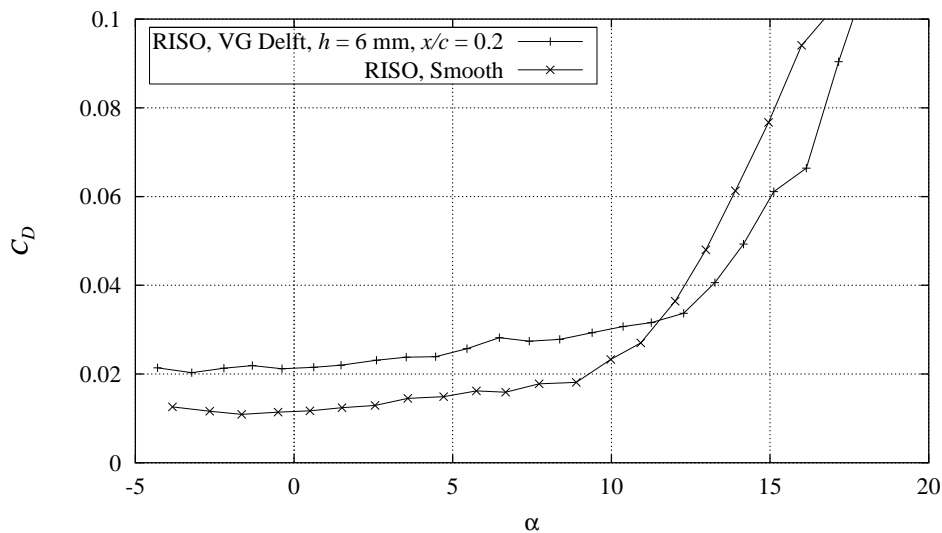
Figure H-4 Measured C_D curve with Delft vortex generators, h = 6 mm, x/c = 0.2, compared with smooth measurement, Re = 1.6×10⁶, (NACA63430CONT091297V5).
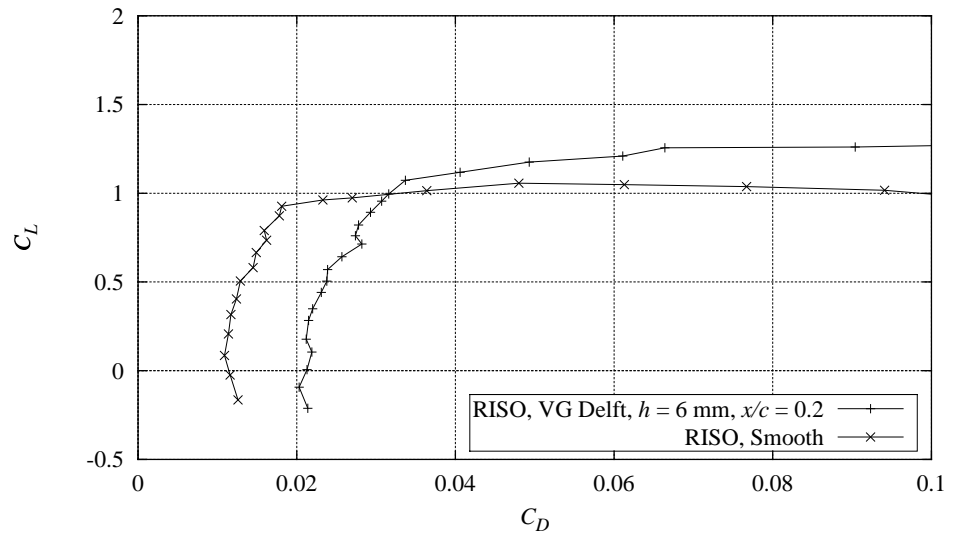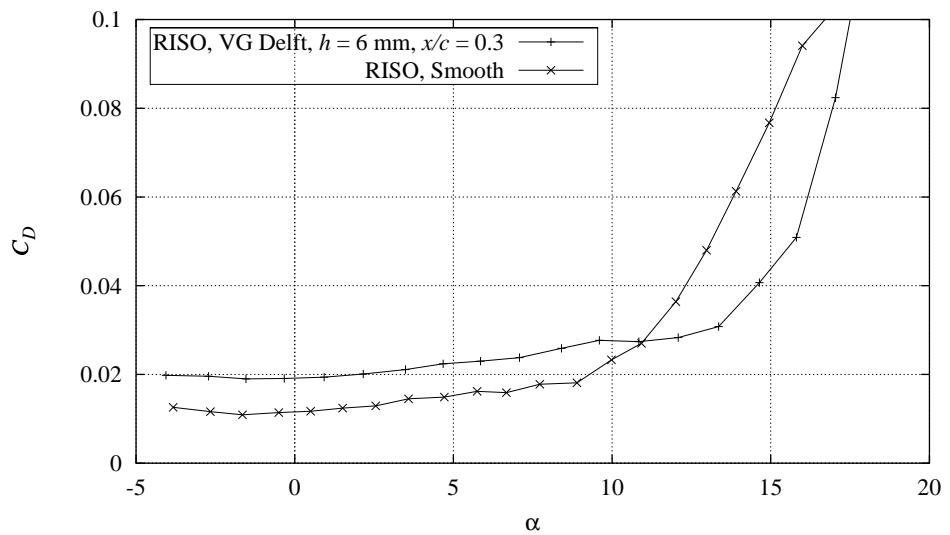
Figure H-5 Measured C_L-C_D curve with Delft vortex generators, h = 6 mm, x/c = 0.2, compared with smooth measurement, Re = 1.6×10^6, (NACA63430CONT091297V5).
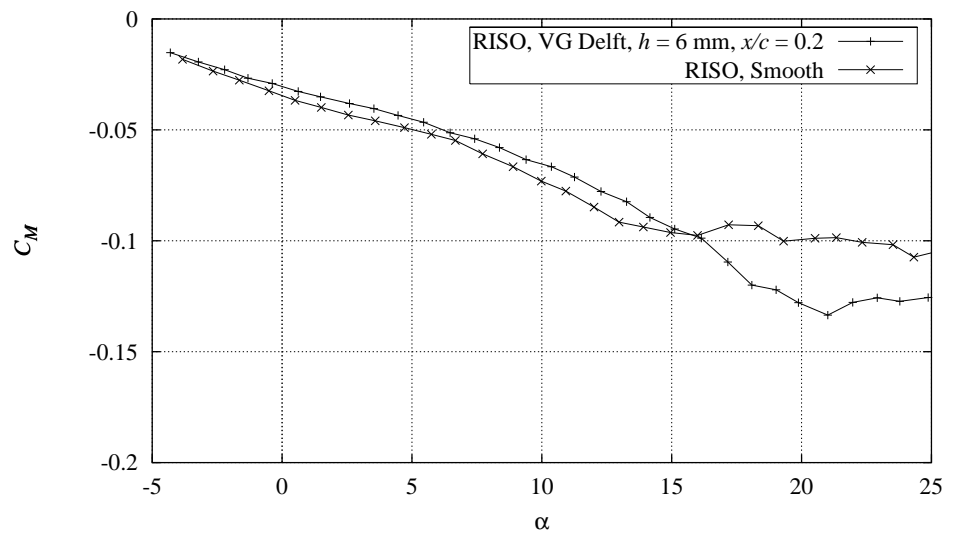
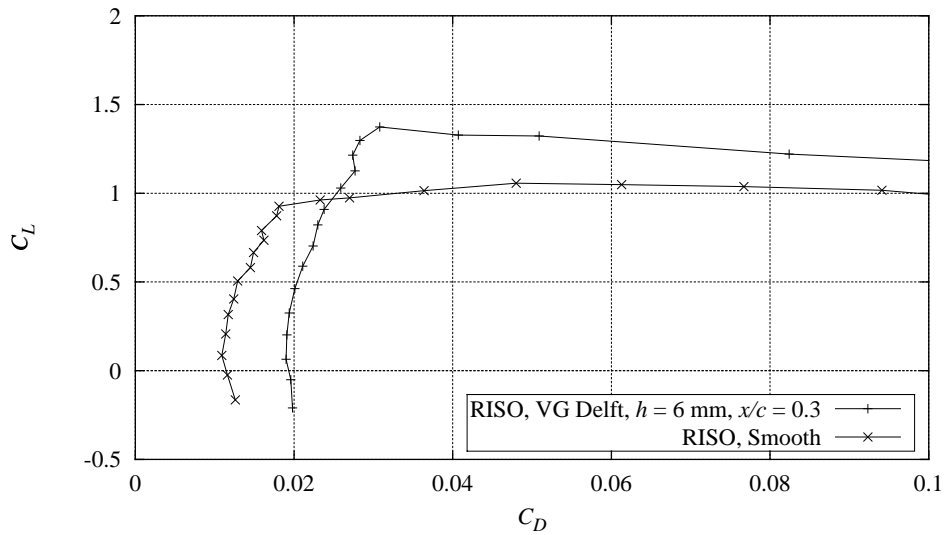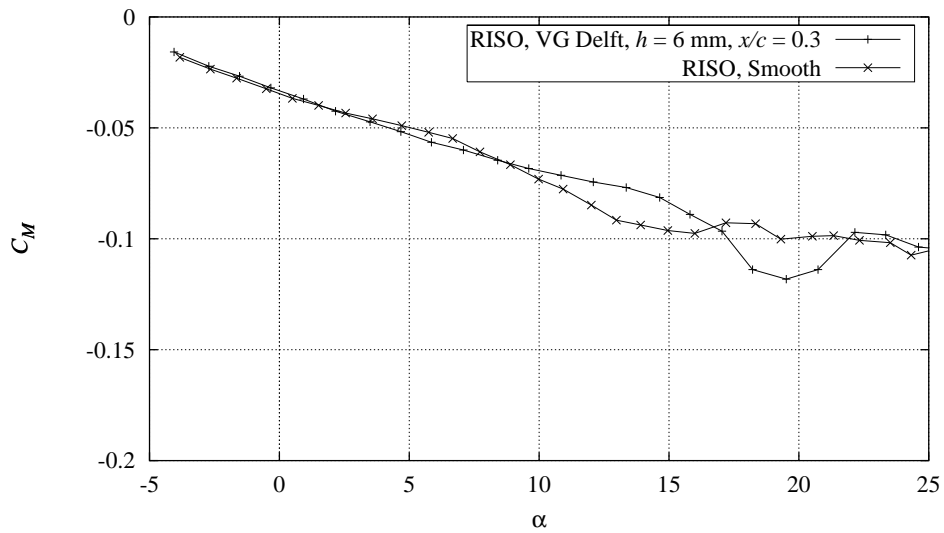*Figure H-6 Measured C_M curve with Delft vortex generators, h = 6 mm, x/c = 0.2, compared with smooth measurement, Re = 1.6×10^6, (NACA63430CONT091297V5).*

H.2 Delft vortex generators, *h* = 6 mm, at *x/c* = 0.3
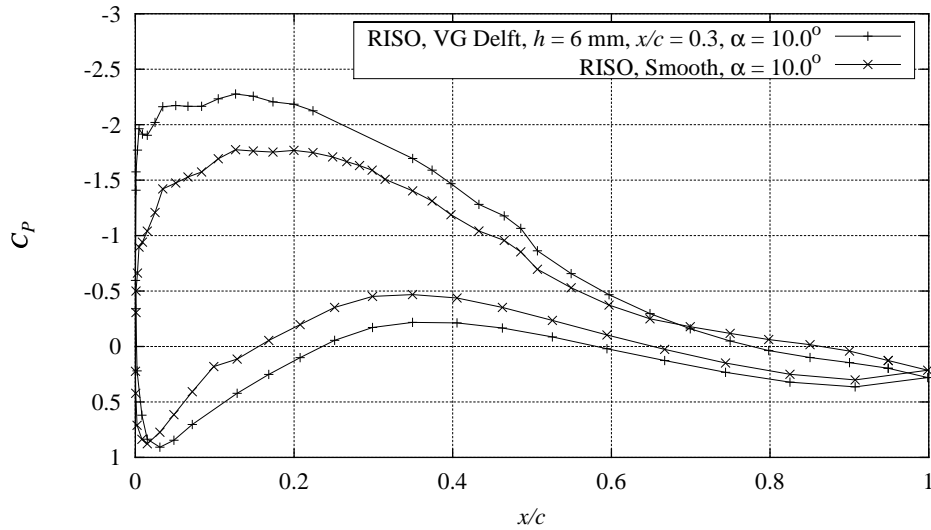
Figure H-7 Measured C_P distribution with Delft vortex generators, h = 6 mm, x/c = 0.3, compared with smooth measurement, Re = 1.6×10^6, α = 10.0° (NACA63430CONT091297V1).

Figure H-8 Measured C_P distribution with Delft vortex generators, h = 6 mm, x/c = 0.3, compared with smooth measurement, Re = 1.6×10^6, α = 15.1° (NACA63430CONT091297V1).

Figure H-9 Measured C_L curve with Delft vortex generators, h = 6 mm, x/c = 0.3, compared with smooth measurement, Re = 1.6×10⁶, (NACA63430CONT091297V1).

Figure H-10 Measured C_D curve with Delft vortex generators, h = 6 mm, x/c = 0.3, compared with smooth measurement, Re = 1.6×10⁶, (NACA63430CONT091297V1).

Figure H-11 Measured C_L-C_D curve with Delft vortex generators, h = 6 mm, x/c = 0.3, compared with smooth measurement, Re = 1.6×10^6, (NACA63430CONT091297V1).

Figure H-12 Measured C_M curve with Delft vortex generators, h = 6 mm, x/c = 0.3, compared with smooth measurement, Re = 1.6×10^6, (NACA63430CONT091297V1).

I NACA 63-430 Dynamic stall

I.1 *k* = 0.093
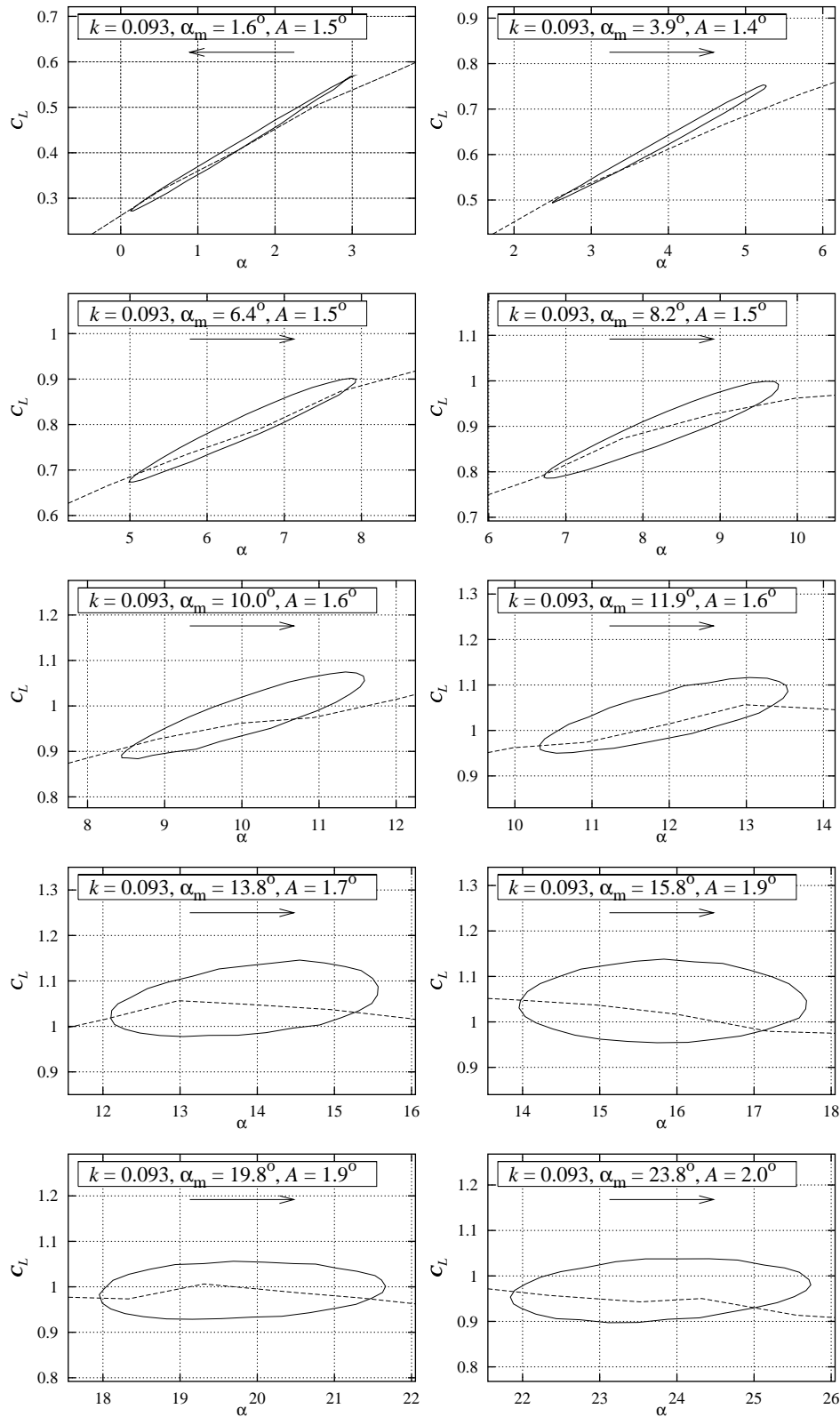
Figure I-1 Measured C_L hysteresis loops for smooth leading edge flow at k = 0.093, A between 1.4° and 2.0°, Re = 1.6×10⁶ (NACA63430PITCH091297V1).
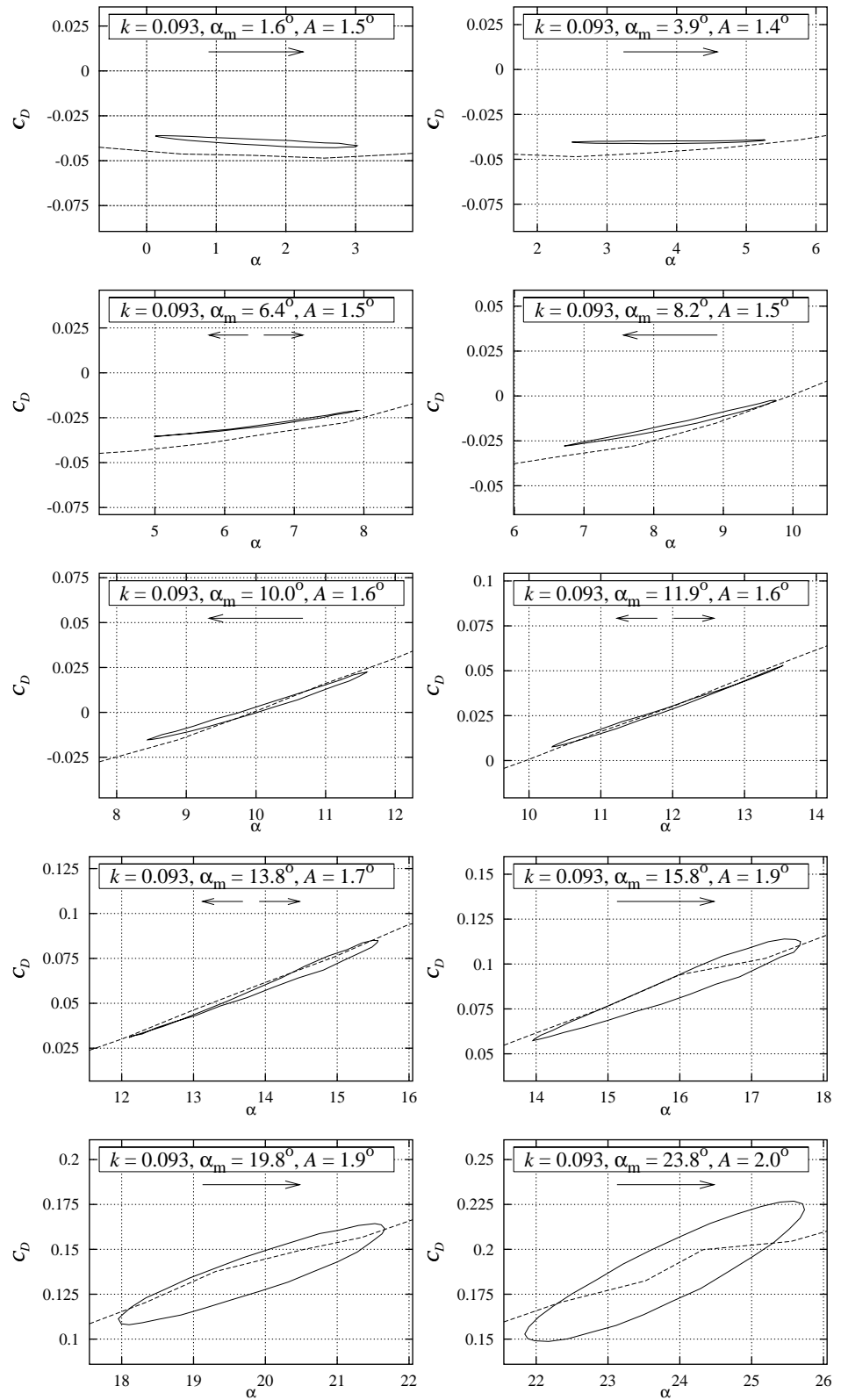
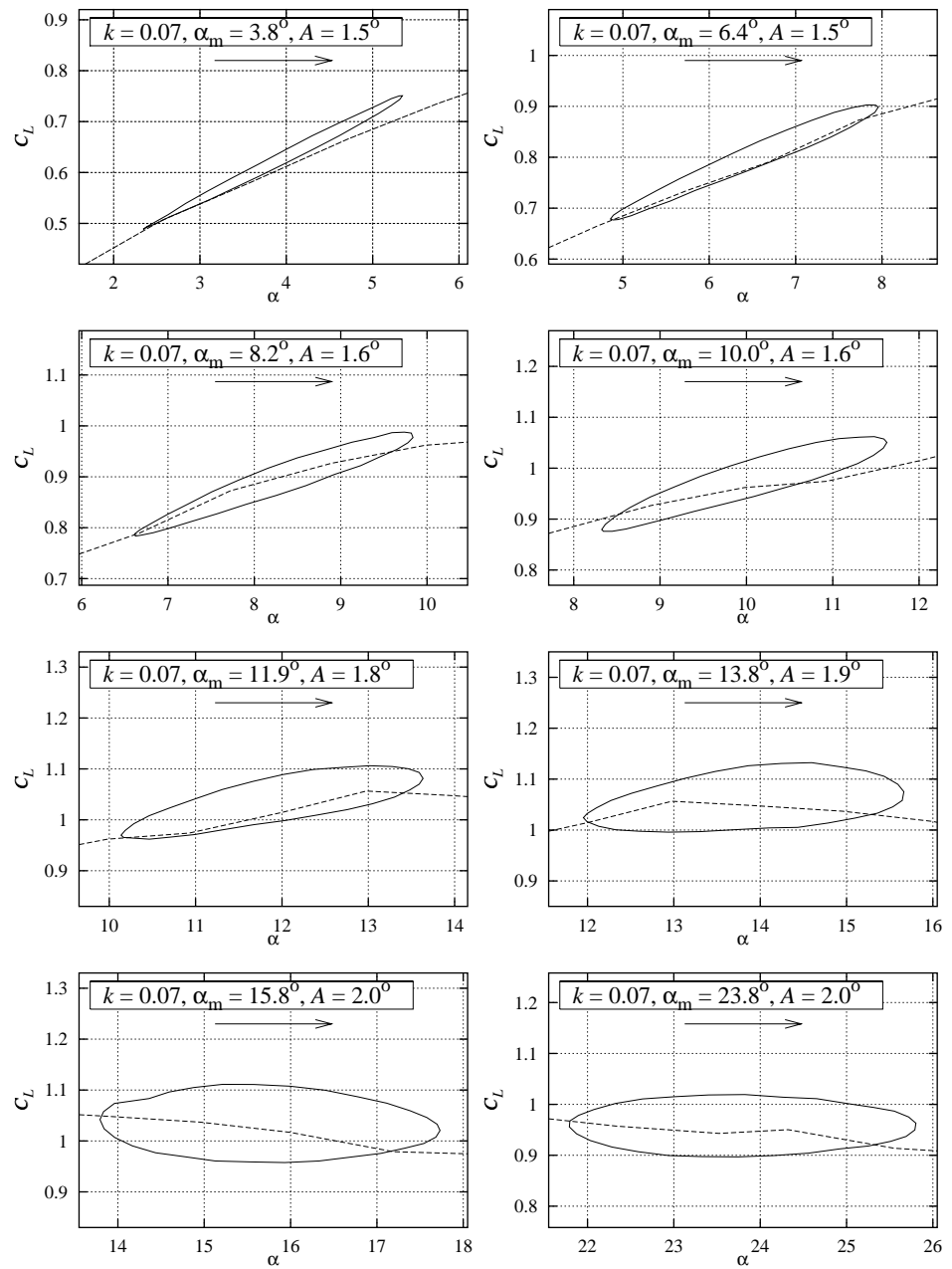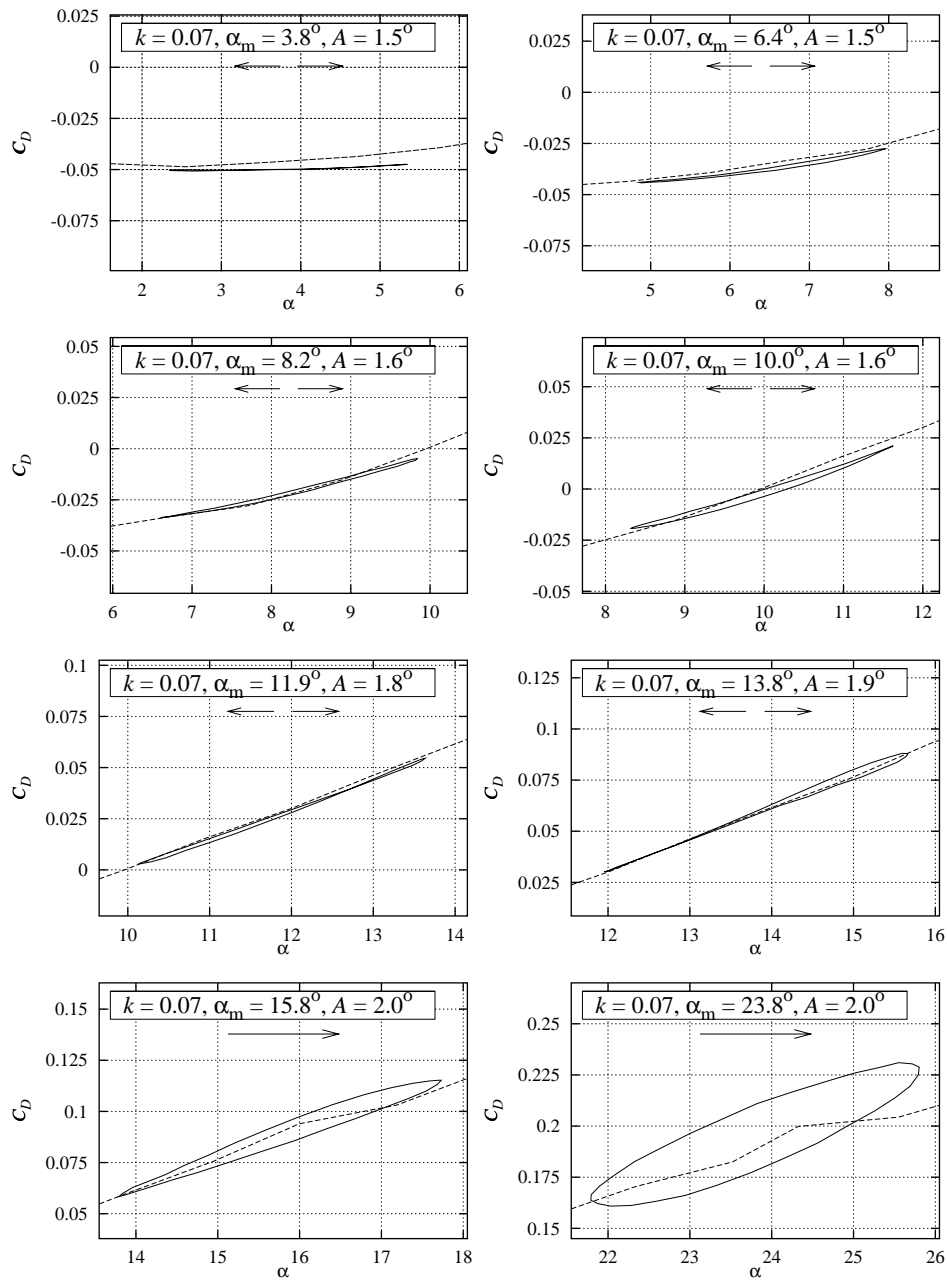*Figure I-2 Measured C_D hysteresis loops for smooth leading edge flow at $k = 0.093$, A between 1.4° and 2.0°, Re = 1.6×10⁶ (NACA63430PITCH091297V1).*
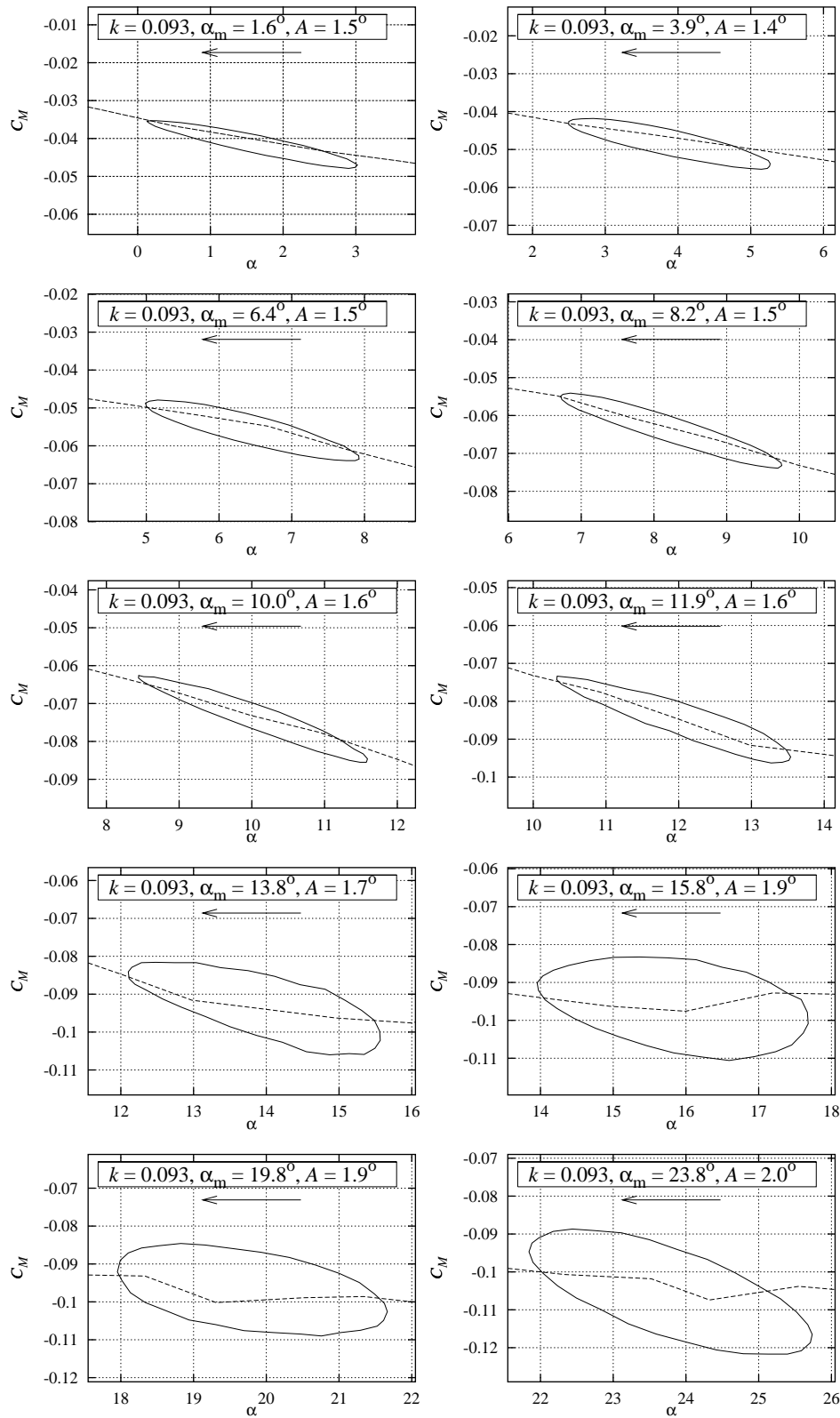
Figure I-3 Measured C_M hysteresis loops for smooth leading edge flow at k = 0.093, A between 1.4° and 2.0°, Re = 1.6×10⁶ (NACA63430PITCH091297V1).

I.2 $k = 0.070$

Figure I-4 Measured C_L hysteresis loops for smooth leading edge flow at $k = 0.070$, A between $1.4°$ and $2.0°$, $Re = 1.6 \times 10^6$ (NACA63430PITCH091297V2).
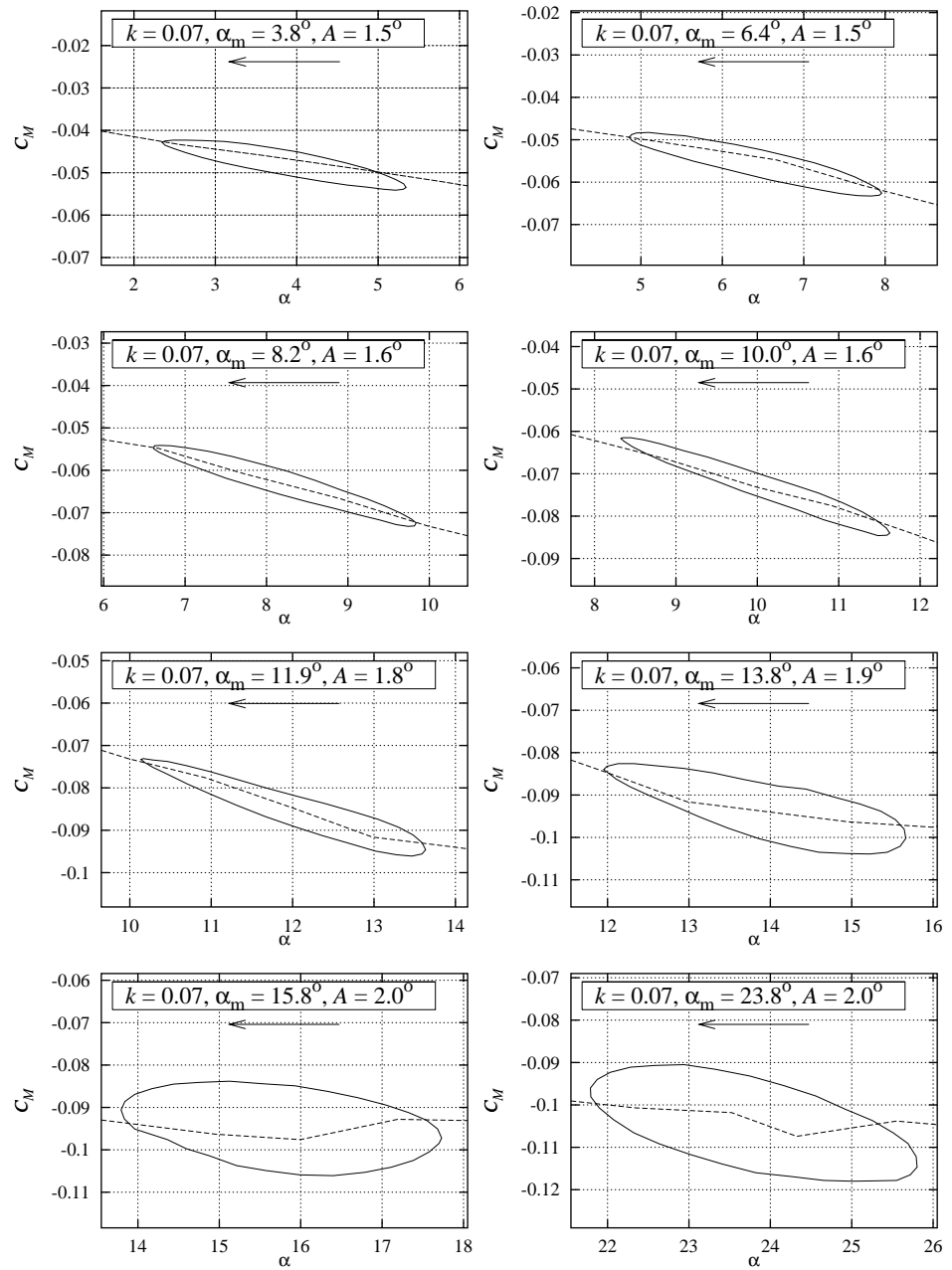
Figure I-5 Measured C_D hysteresis loops for smooth leading edge flow at $k = 0.070$, A between $1.4°$ and $2.0°$, $Re = 1.6×10^6$ (NACA63430PITCH091297V2).

Figure I-6 Measured C_M hysteresis loops for smooth leading edge flow at $k = 0.070$, A between 1.4° and 2.0°, Re = 1.6×10^{6} (NACA63430PITCH091297V2).

Abstract (max. 2000 characters)

This report deals with 2D measurements of the FFA-W3-241, FFA-W3-301 and NACA 63-430 airfoils. The aerodynamic properties were measured at $Re = 1.6 \times 10^6$. The VELUX open jet wind tunnel with a background turbulence intensity of 1% was used. The airfoil sections had a chord of 0.60 m and a span of 1.9 m and end plates were used to minimize 3D flow effects. The measurements comprised both static and dynamic inflow where dynamic inflow was obtained by pitching the airfoil in a harmonic motion. We tested the influence from vortex generators and leading edge roughness both individually and in combination.

The aerodynamic characteristics were measured and the agreement between calculations and measurements was fair for FFA-W3-241 but not good for FFA-W3-301 and NACA 63-430. In general calculations overestimated maximum C_L and sometimes underestimated minimum C_D. Maximum C_L for smooth flow was in good agreement with calculated maximum C_L for leading edge transition flow and this could serve as a worst case calculation. We determined the influence from vortex generators and they should always be applied on thick airfoils to increase maximum C_L. We determined the influence from leading edge roughness, which reduced maximum C_L and increased minimum C_D. Compared with the NACA 63-4xx airfoils, the FFA-W3 airfoils were found better suited for the inboard part of a wind turbine blade both with and without vortex generators.